Numerical simulation of silicon solar cells with novel cell structures

Dissertation

zur Erlangung des akademischen Grades
des Doktors der Naturwissenschaften
(Dr. rer. nat.)
an der Universität Konstanz
Fakultät für Physik

vorgelegt von

Jürgen Otto Schumacher

Fraunhofer-Institut für
Solare Energiesysteme
Freiburg

2000

Referenten: Prof. Dr. Wolfram Wettling
Prof. Dr. Ernst Bucher

Abstract

This thesis examines the detailed modelling of monocrystalline silicon solar cells.

- The first part of the thesis forms an introduction to the numerical simulation of silicon solar cells.

The device physics of solar cells is presented in steps of increasing complexity. The simplest analytical model of a *p-n* junction cell consisting of an emitter and a base is taken as a starting point. This can be considered as offering a basic skeleton of equations that govern the device physics of solar cells. This helps us to understand and interpret the numerical simulation results explained in the following parts of the thesis.

More refined analytical models are then described in order to include the front and rear surfaces, the influence of non-ideal dark current components and escape reflectance due to multiple internal reflection in the infrared wavelength range. The analytical calculation of the saturation current density of diffused emitters with a doping profile is also discussed.

A numerical discretisation method for device simulation is briefly outlined. The one-dimensional numerical solution for a simple solar cell structure is discussed and compared with the simplified analytical approach. Ray tracing simulation of optical reflection and absorption in textured silicon solar cells is explained, including the simulation of optical carrier generation rates in textured silicon solar cells. The first part of the thesis ends with a description of the circuit simulation method that accounts for distributed resistive losses in the metal grid, non-generation losses, and perimeter losses present in actual solar cells.

- An object oriented simulation environment for solar cell modelling, called *PVObjects*, is presented. It is implemented using the *Mathematica* programming language. The object oriented approach permitted the construction of the simulation tool and its data in the same way as our knowledge about solar cells is structured. This knowledge is represented in terms of object categories, allowing us to add specialised categories, reflecting existing objects found in a solar cell laboratory as semiconductor materials, solar cells, and measurement facilities.

PVObjects also includes a basic set of models describing the solar cell physics. This allows an easy focusing on the parameter dependencies of the physical models used in solar cell simulation.

Simulations are conducted using analytical models implemented in *Mathematica* or by interfacing with the numerical simulation programs *RAYN*, *MESH*, and *DESSIS*. All input files for numerical device simulations are generated by *PVObjects*, and the simulation output is evaluated. A solar cell structure to be investigated by numerical device simulation with *DESSIS* can be efficiently implemented in two and three dimensions, varied and enhanced by using *PVObjects*.

- The commonly used band gap narrowing (BGN) models for crystalline silicon do not describe heavily doped emitters with sufficient precision. One of the reasons for this is that

the applied BGN models were empirically derived from measurements that assumed Boltzmann statistics.

In contrast to previous studies – which used Boltzmann statistics and empirical apparent BGN data - Fermi-Dirac statistics and a quantum mechanically derived band gap narrowing model are employed here. This new emitter model is applied to the numerical simulation of the recombination properties of phosphorous-doped silicon emitters. It is demonstrated that carrier degeneracy and the new BGN model substantially affect the electron-hole (*p-n*) product within the emitter region.

Using the new emitter model to simulate heavily doped emitters, lower values for the hole density near the front surface of the emitter are obtained. Thus, the surface and Auger recombination fractions of the emitter are both reduced. As a consequence, (a) simulated saturation current densities of heavily phosphorous doped emitters, calculated with the new BGN model, are lower than results obtained with the empirical BGN model of del Alamo; and (b) significantly higher values for the surface recombination *velocities* of heavily doped emitters have to be specified in combination with the new emitter model to obtain the same surface recombination *currents*.

The recombination velocity of minority carriers at the surface of phosphorous doped emitters is re-extracted from published measurements of the emitter saturation current. In conclusion, emitters with dopant densities higher than 3×10^{19} cm^{-3} can be described with a considerably higher level of precision than has been previously possible.

- A detailed analysis of silicon on insulator (SOI) thin film cells is presented. An analytical model for the external reflection of planar SOI cells is developed, including multiple internal reflection in the epitaxially-grown layer and in the substrate. The optical properties of textured SOI cells are described employing ray tracing simulation. These optical baseline models are verified experimentally by reflection measurements. Textured (planar) SOI baseline cells absorb 82 % (71 %) of the incident photon flux in the epi-layer for illumination with the AM1.5 spectrum. The influence of epi-layer thickness on the reflection and absorption properties of planar and textured SOI cells are examined. A strong dependence of the maximum achievable short circuit current density $J_{sc,max}$ of the planar cell on epi-layer thickness is found. Increasing the epi-layer thickness from 15 to 100 µm leads to a relative increase of $J_{sc,max}$ of 18 % for the planar cell, compared to only 10 % for the textured cell.

Accurate numerical baseline models for the simulation of the electrical performance of SOI cells were established. The recombination parameters are determined from simulated contours of constant V_{oc} by comparison with the measured V_{oc}. This method yields a higher accuracy than the extraction of the effective diffusion length from spectral response measurements.

The influence of epi-layer thickness and the recombination parameters on the electrical performance of planar and textured SOI cells was investigated. A gain in V_{oc} can be achieved by a surface texture in comparison to a planar cell front. J_{sc} of a textured SOI cell can be increased for low minority carrier base diffusion lengths if the epi-layer thickness is reduced. This is a result of the efficient light confinement achieved by inverted pyramids. Opposite

trends in the influence of epi-layer thickeness on J_{sc} are found comparing planar and textured surfaces for a base diffusion length of L_b = 50 µm. J_{sc} can be slightly increased for reduced epi-layer thickness if the front surface is textured whereas J_{sc} decreases for the planar cell.

Measured fill factor values of a batch of SOI solar cells tend to display substantial variation. The origins of these deviations were investigated by taking measurements from two batches of solar cells processed using comparable conditions. The realised cross sectional area of the metal fingers plays a dominant role in determining the value of the fill factor. Hence, variations in the electroplating process, used to increase the cross-sectional area of the contact fingers, cause deviations in the measured fill factor values of different cells. The asymmetric shape of the relative fill factor frequency distribution can be understood by appeal to a simple statistical approach. The obtained probability distribution is in accordance with the frequency distribution of the fill factor. It is concluded that one should not compare the mean fill factor value of a solar cell batch to simulation results.

- 21.4 % efficient rear-contact cells (RCC) with interdigitated contact grids processed at Fraunhofer ISE on 1.25 Ωcm float zone silicon are analysed in detail. The numerical simulation model employs optical ray tracing, two-dimensional electrical device simulation, and circuit simulation. In addition to previous models for the RCC optical carrier generation, distributed metal resistance losses and perimeter losses were accounted for numerically.

A new approach to separate bulk- and surface recombination losses is presented combining photoconductance decay and open circuit voltage measurements with numerical device simulation. The interface surface recombination velocity of the thermal oxidised emitter covering the front surface is deduced to be 1500 cm/s, while the bulk diffusion length is 1200 µm.

The simulations reveal that at maximum power point, 80 % of the total recombination is due to Shockley-Read-Hall recombination in the base.

A shunt effect at the floating emitter junction at the front side is shown to cause a strongly reduced spectral response for low illumination levels as well as a hump in the dark *I-V* curve. Both effects could be modelled quantitatively assuming the same shunt resistance.

Losses due to the distributed metal resistance (including non-generation losses) were determined to cause a fill factor decrease of 1% absolute. Recombination at the cell's perimeter led to an additional fill factor loss of 1.5% absolute.

In addition, parameter variations were performed. The optimum cell thickness is located in the thickness range from 100 µm to 150 µm. A relative increase of 2% in cell efficiency results from a reduced thickness in comparison to the baseline value of 250 µm for the realised cell. The metal finger spacing of the highly efficient RCC mainly affects the fill factor. Internal series resistance losses in the semiconductor cause a 3 % relative drop in the fill factor by increasing the metal finger spacing from 300 µm to 800 µm.

When changing the surface concentration of the front and rear emitter diffusion from 5×10^{18} to 1×10^{18} cm^{-3} (for constant sheet resistance), a relative improvement in efficiency of

3 % was predicted. This modification has lead to an increase in the realised cell efficiency from 21.4 % to 22.1 %, which is a 3.3 % relative improvement.

Acknowledgements

Firstly, I would like to express my special gratitude to Prof. Wolfram Wettling for his continuous help and support throughout my studies. His faith in my abilities and recommendation allowed me the exciting opportunity to spend a year of my Ph.D. working at the University of New South Wales (UNSW) in Australia. His valuable input is also particularly evident in the chapter 'Device physics of silicon solar cells' of the completed thesis.

I am grateful to Prof. Bucher from the University of Konstanz for his generosity to review and examine this thesis.

I would also particularly like to thank Jochen Dicker. He was a fantastic colleague during the time we spent working together on the characterisation of solar cells. His enthusiasm for new ideas was particularly inspirational. Thanks are also due to Jens Sölter for contributing numerous ideas to our object oriented simulation tool. The friendly atmosphere in our simulation group at Fraunhofer ISE has meant that I have enjoyed an extremely pleasant working environment throughout my studies.

Special thanks must also go to Dr. Stefan Glunz. His speedy problem-solving and comprehensive experience of measurement methods and solar cell technology was invaluable for all the characterisation work on solar cell structures presented in this thesis. Also, I would like to thank Dr. Wilhelm Warta for sharing his extensive knowledge on the characterisation of solar cells with me and for our many fruitful discussions.

The following people of Fraunhofer ISE also deserve special mention:

Dr. Bernd Wagner for his extensive insights into ray tracing simulation and into hard- and software details;

Dr. Christopher Hebling for our fruitful collaboration on the characterisation of silicon on insulator solar cells;

Daniel Biro for his implementation of a sizeable part of *PVObjects* and for our many interesting discussions on lifetime measurements;

Ralf Preu for our informative and stimulating conversations on the fabrication of silicon solar cells;

I have also much appreciated the reviews and comments that Anne Kovach-Hebling, Peter Koltay, Dominik Huljic, Martin Schnell and Sebastian Schäfer have offered on this text and am further indebted to Elisabeth Schäffer for numerous measurements.

In addition I would like to express my gratitude to Dr. Pietro Altermatt from UNSW in Sydney. I learnt a huge amount from Pietro on the numerical simulation of emitters and working with him was a privilege. I would also like to thank Dr. Armin Aberle, Dr. Gernot Heiser and Holger Neuhaus of UNSW for making many constructive suggestions.

I have also benefited greatly from the suggestions of Dr. Mary Archer and Tamsin Mather of Cambridge University who have read parts of this thesis and made constructive suggestions.

Funding support for the emitter modelling was provided by the German Academic Exchange Service (DAAD, HSP III, international support for doctoral and postdoctoral students).

Contents

Abstract i

Acknowledgements v

Contents vii

1 Introduction 10

1.1 A new energy paradigm including renewable energy based on price competition 10

1.2 The value of lowering the cost of solar power 11

1.3 Different routes in Photovoltaics research 12

1.4 Motivation and thesis structure 13

2 Device physics of silicon solar cells 17

2.1 Semiconductor device equations 17

2.2 The p-n junction model of Shockley 19

2.2.1 The p-n junction at equilibrium 19

2.2.2 The junction under bias in the dark 22

2.2.3 The superposition principle 25

2.2.4 Carrier density solutions for dark conditions 26

2.2.5 The illuminated I–V curve 31

2.3 Real diode characteristics 34

2.3.1 Solar cell parameters 34

2.3.2 Assumptions regarding the majority carrier concentration 34

2.3.3 Charge carrier lifetime 35

2.3.4 Surface recombination 36

2.3.5 Series and shunt resistance 37

2.3.6 Non-ideal dark current components 38

2.3.7 Photogeneration and quantum efficiency 40

2.3.8 External reflection 44

2.3.9 Accounting for doping profiles 45

3 Numerical solar cell modelling 49

3.1 Previous work on multidimensional solar cell modelling 49

3.2 Solving the semiconductor device equations numerically 50

3.3 Comparison of numerical and analytical solution 54

3.4 Ray tracing 61

3.4.1 Light trapping investigations 61

3.4.2 The ray tracing program *RAYN* 62

3.4.3 Simulation of normalised generation function 64
3.5 Numerical modelling of differential spectral response 65
3.6 Circuit simulation 67
3.7 Chapter summary 69

4 An object oriented approach to modelling of silicon solar cells 70

4.1 Introduction 70
4.2 The purpose of PVObjects 70
4.3 Object oriented programming with application to solar cell simulation 71
4.3.1 Abstraction and inheritance 72
4.3.2 Polymorphism and reusable code 72
4.3.3 Embedding of objects and autonomous objects 73
4.4 An object class for the simulation of optical properties 76
4.4.1 Light trapping geometries 76
4.4.2 Example: Optical characterisation of thin silicon solar cells 78
4.5 Solar cell models 80
4.5.1 An abstract class for the simulation of silicon solar cells 80
4.5.2 Numerical device simulation tools 80
4.5.3 Two and three-dimensional solar cell geometries 81
4.5.4 Baseline models 84
4.6 A virtual measurement laboratory 84
4.6.1 Characterisation facilities 85
4.6.2 Example characterisation 85
4.7 Conclusion and outlook 88

5 Numerical simulation of recombination properties of phosphorous doped emitters 89

5.1 Introduction 89
5.2 Band gap narrowing 89
5.3 Simulation method 91
5.4 Emitter saturation current density 94
5.5 Electron-hole product in heavily doped emitters 95
5.6 Recombination fractions of a heavily doped emitter 96
5.6.1 Low injection conditions 97
5.6.2 High injection conditions 98
5.7 Simulated J_{0e} of Gaussian doping profiles 98
5.8 Extraction of surface recombination velocities 99
5.8.1 Conclusion 103

6 Silicon on insulator solar cells with interdigitated front contacts 104

6.1 Structure and technology of silicon on insulator (SOI) cells 104

6.2 Optical baseline models 105
6.2.1 Analytical calculation of the external reflection of a planar cell 105
6.2.2 Ray tracing simulation of the optical properties of a textured cell 106
6.2.3 Optical baseline models for planar and textured cell 108

6.3 Influence of the epi-layer thickness on reflection and absorption 111

6.4 Electrical baseline models 114

6.5 Influence of the epi-layer thickness and the recombination parameters 119

6.6 Comparison of simulated and measured fill factor 125

6.7 Performance of simplified SOI cells 130

6.8 Summary of results 132

7 Analysis of one sun mono-crystalline rear contacted silicon solar cells 134

7.1 Introduction 134

7.2 Rear contact cells for one-sun application at Fraunhofer ISE 136

7.3 A comprehensive electrical and optical numerical model for the rear-contacted cell 138

7.4 Optical properties of random pyramid texture 140

7.5 Determination of recombination parameters 141

7.6 Injection level dependence of the floating emitter 144

7.7 Resistive losses 149

7.8 Perimeter losses 152

7.9 Comparison of simulated and measured *I-V* output parameters 156

7.10 Parameter studies 158
7.10.1 Wafer thickness 158
7.10.2 Metal finger spacing (n-p contact spacing) 159
7.10.3 Emitter coverage fraction 160
7.10.4 Emitter profiles 161
7.10.5 Recombination parameters 162

7.11 Summary of results 165

List of symbols 167

Author's publications 171

Bibliography 173

1 Introduction

Photovoltaics (PV), the direct conversion of sunlight into electric energy, is one component of an evolving energy mix. This technology provides several attractive features, such as pollution-free operation, relatively low maintenance costs, and modularity. In future energy scenarios solar cells (or PV cells) may well occupy an increasingly prominent role in global electricity generation in order to limit environmental pollution and to slow down the rate at which greenhouse gas concentration is rising.

1.1 A new energy paradigm including renewable energy based on price competition

The economic and social dimensions of the present climate change are threatening. According to the Intergovernmental Panel on Climate Change Assessment, global carbon dioxide emissions have risen by 3.3% per year since 1950, average global temperatures have increased from 0.3 to 0.6 °C since the late 1800's, and recent years have been among the warmest since the 1860's [1]. The average global temperature is likely to rise by 2 degrees C during the next century (range: 1° to 3.5° C), and in the same period the sea level is expected to rise by 50 cm. [1]

Nevertheless, one has to keep in mind that modelling future climate change is based on Global Circulation Models (GCM's). There are problems with the current state of GCM's, including inaccuracies due to a lack of understanding of the global carbon cycle and atmospheric chemistry. Thus, there is considerable debate in the literature surrounding both the possibility of these predicted impacts and their likely scale.

Apart from environmental concerns, several authors state that implementing renewable, carbon-emission free energy techniques is of great economic value. Today's dominant power supply system is centralised, large-scale, and focused on increasing consumption. Its successor could be decentralised, downsized and directed toward meeting demand [3]. The forthcoming decentralised energy mix will be supplied by small modular generation units such as combined-cycle gas turbines, wind turbines, photovoltaic panels and fuel cells. Electricity from large power plants will soon prove too expensive for it to maintain its traditional dominant role. As Lovins points out, 'environmental problems due to energy use

[1] A partial list of potential impacts of climate change on selected natural systems includes: altered growth and regeneration capacity of forests; altered ocean tidal range due to sea level rise; change in regional precipitation level affecting surface and groundwater supply for drinking and industrial use; substantial changes in coastal areas; increased mortality and illness due to intensity and duration of heat waves; and increased exposure of humans to certain infectious diseases (malaria, dengue, etc.) [2].

are unnecessary and only increase business costs. Specifically, meeting and surpassing the Kyoto Protocol climate-protection targets will not be costly but profitable, because saving fuel costs less than buying fuel, let alone burning it' [4].

Major oil and electricity companies have already realised the opportunities offered by renewable energy. Both BP Amoco and the Royal Dutch/Shell company have launched significant research programs and investments in the solar energy field. Furthermore, Shell is working on biomass fuels. The Shell scenario predicts a half-renewable world energy supply by 2050, based on price competition and granting solid commercial profit [5].

1.2 The value of lowering the cost of solar power

Kim *et al* [6] investigated the cost for implementing PV and the likelihood of PV making a significant contribution to the global energy system. Their model considers the interaction between population, economy, energy, agriculture, land-use, greenhouse gas emissions, and atmospheric dispositions. The approach compares a reference energy system over time with an alternative policy path. It is assumed that the global population will eventually stabilise at approximately 11 billion people. Fossil energy forms are defined as resource-constrained technologies. In addition, the model considers solar power, nuclear power, hydroelectric power, and biomass-derived power. Nuclear power is assumed to have been phased out in Western Europe and North America.

The reference model assumes a transition from the present conventional oil and gas-based world to a future world dominated by coal. It exhibits continued growth in fossil fuel emissions. This growth is inconsistent with eventual stabilisation of CO_2 concentrations. This is a common vision of the future [7]. Assuming no carbon constraints, the highest PV-cost trajectory under the reference's assumptions predicts a 10 % contribution to global electricity generation in 2095. This contribution rises to around 40 % for the lowest PV-cost trajectory.

An alternative policy path would impose carbon constraints in order to stabilise atmospheric CO_2 concentrations significantly. This, in turn, alters the evolution of the global energy system. PV helps to lower the required emission reduction necessary to comply with any carbon constraint. Once the carbon constraints are in place, PV technology offers a carbon-free option for electricity. In this case, PV substitutes not only for fossil fuel technologies, but also for expensive conservation measures.

Assuming a 750 parts per million by volume (ppmv) carbon constraint ceiling, savings of over US$59 billion (1996) until 2095 would result in the highest PV-cost trajectory. This rises to US$4500 billion in the lowest PV-cost trajectory under a 450 ppmv carbon constraint ceiling [6]. It is not surprising that these results depend on the cost evolution of the utilised PV technology. However, the authors of the study come to the conclusion, that the value of solar technologies is *robust* across a wide range of sensitivities.

1.3 Different routes in Photovoltaics research

R&D investments in alternative technologies will help to reduce costs. A wide range of solar cell structures on the basis of different semiconductor materials are being investigated in laboratories around the world.

- *Single- and multicrystalline silicon cells processed on wafers*

Mature cell concepts include the standard screen printed cell or the buried contact approach. Crystalline silicon solar cells can be produced on a large scale already, resulting in cell efficiencies in the 15-18 % range [8]. Rear contacted cells are presently being developed with a view to low cost production. Chapter 7 of this thesis presents a detailed analysis of rear contacted cells on monocrystalline silicon.

The highest efficiency levels for one sun application were reported for the local back surface field (or passivated emitter rear locally diffused) cell structure made of single crystalline float zone silicon. The evolution of silicon solar cells is depicted in [9], while the present state in research on crystalline silicon solar cells is resumed in [10].

- *Crystalline silicon thin-film solar cells*

Major advantages of the crystalline silicon thin-film (CSiTF) cell are a reduction in material costs compared to wafered cells and the option for integrated series interconnection of the module. As silicon is an indirect semiconductor absorbing light only weakly in the infrared wavelength range, light confinement in thin silicon solar cells is crucial (Section 6.2).

Depositing thin silicon layers on substrates that withstand processing temperatures higher than 1000 °C is called the ‘high-temperature approach’ [11]. An interesting model system for a thin-film cell is the SOI cell investigated in detail in Chapter 6. If the highest processing temperatures are restricted to temperatures lower than 600 °C, inexpensive substrates such as glass can be used. This is called the low temperature approach, reviewed in [12].

- *Amorphous silicon alloy*

Amorphous silicon alloy (a-Si) technology offers a way to reduce material costs, as only a very thin (less than 500 nm) film is needed. However, a disadvantage with this is the presence of dangling bonds and other defects that impede carrier transport. Exposure to light also creates metastable states in the gap, which degrade material and cell performance. The present status of amorphous silicon alloy research is reviewed in [13].

- *Cadmium telluride*

Cadmium telluride-based thin-film technologies are seen as one viable option for low cost PV. The thin films and the back contact electrodes can be deposited onto a glass superstrate and the cells can be interconnected by monolithic integration. Current activities in CdTe solar cell research are focused on the development of a low cost, reliable, high throughput manufacturing technology [14].

- *Copper indium (gallium) diselenide (CIGS)*

High performance PV modules in a laboratory stage were demonstrated using heterojunction cells made of $Cu(In,Ga)Se_2$ (CIGS). The cell performance was optimised on an intuitive basis and by empirical optimisation of the deposition process. Future research will address an improvement in the understanding of the defect chemistry and the structure of the CIGSS absorber. An up-to-date review on CIGS research can be found in [15].

- *Solar cells made of III-V compound semiconductors*

III-V compound semiconductors are grown by liquid phase epitaxy (LPE) and by metal organic vapour phase epitaxy (MOVPE), and allow to realise various band gaps. This technology - more expensive than silicon based solar cells - is mainly used for space solar cells, concentrator solar cells, and in thermophotovoltaic generators. Growing III-V compounds lattice matched on GaAs or Ge substrates allows the fabrication of monolithic multi-junction cells boosting the cell efficiency beyond 30 %. The application of III-V compound semiconductors to solar cell fabrication is reviewed in [16].

This list of solar cell approaches is by no means complete. However, the emerging PV market will incorporate different cell concepts and semiconductor materials.

1.4 Motivation and thesis structure

Optimising cell efficiency is a major challenge in terms of reducing costs. Solar cell simulation as outlined in this thesis is a powerful tool for quantifying and minimising the losses that limit the cell efficiency. The quantification of limiting losses in crystalline silicon solar cells was made possible by applying numerical semiconductor simulation techniques and advanced models for the physical properties of silicon. These were either developed or improved in the past few years, thereby allowing us to understand and optimise the performance of monocrystalline silicon solar cell structures.

This thesis provides substantial contributions to several areas of solar cell modelling, improving the basis for device optimisation.

In Chapter 2 the device physics of solar cells is presented in steps of increasing complexity. Starting from the fundamental equations that describe semiconductor devices (Section 2.1), solutions are first discussed for the most simple cell model. The device equations are solved for a simple *p-n* junction cell consisting of an emitter and a base, each with a constant doping profile, with no boundaries taken into account (Section 2.2). In this most simple model, the ideal current-voltage characteristic of a solar cell is obtained. This can be seen as a basic skeleton of equations governing the device physics of solar cells. A knowledge of these equations helps to understand and interpret the numerical simulation results explained in the following parts of the thesis

.

In Section 2.3 the most critical assumptions used in the derivation of the current-voltage characteristics are discussed, and the ideal solar cell model is extended to include both the front and rear surfaces (Section 2.3.4). The influence of non-ideal dark current components such as depletion region recombination and injection-level dependent surface recombination on the solar cell's current-voltage characteristics are briefly discussed in Section 2.3.6.

The optical properties of planar cells, including multiple internal reflection in the infrared wavelength range, can still be handled analytically. Section 2.3.7 outlines the derivation of an expression for the optical charge carrier generation in planar silicon cells. Using the same basic approach, the external reflection of planar cells, including escape reflectance, can be described (Section 2.3.8). The concept is elaborated upon in the latter part of this thesis in order to describe the optical properties of thin planar silicon cells on insulating substrates.

The analytical calculation of the saturation current density of diffused emitters with a doping profile - as is the case in most solar cells - is discussed in Section 2.3.9. The analytical approach is sufficiently accurate for non-degenerated emitters.

The semiconductor device equations can be solved with a higher level of accuracy by applying numerical methods. In Section 3.2, it is briefly explained how the basic equations governing carrier transport in a solar cell are solved numerically in a commercial device simulation program using a discretisation method. The one-dimensional numerical solution for a simple solar cell structure is compared with the simplified analytical approach of Chapter 2. However, to describe modern high-efficiency solar cells, two- and three-dimensional features like surface texturisation, point contacts and selective emitters have to be included in the calculation. Accordingly, 2D- and 3D-numerical models must be used.

In Section 3.4, the 3D ray tracing simulation of optical reflection and absorption in textured silicon solar cells is discussed. The simulation of optical carrier generation rates in textured high-efficiency silicon solar cells is described in Section 3.4.3.

The fill factor of a silicon solar cell is limited by series resistance losses in the base, at the contacts and in the metal grid. These losses are naturally of a distributed nature; that is, one has to account for the 2D (or 3D) carrier distribution in the semiconductor and for distributed resistance losses in the metal grid. Furthermore, the fill factor is influenced by so-called non-generation losses (Section 7.7). Charge carriers recombining at the cells perimeter further degrade the fill factor. The performance of an entire solar cell can be modelled in such a way that explains distributed resistive losses in the metal grid by applying the circuit simulation method, as outlined in Section 3.6.

Numerical simulation techniques can be used to model a wide range of solar cell structures. Implementing two or three different solar cell structures as numerical models, including ray tracing and device simulation, proves to be difficult when editing input files manually. Section 4 presents an *object oriented approach* for 2D and 3D solar cell simulation. The basic mechanisms (abstraction, inheritance, polymorphism and embedding of objects) to control complexity in object oriented programs are outlined in Section 4.3 with application to solar cell modelling. Objects representing the optical properties of textured thick silicon

wafers and silicon-on-insulator thin film solar cells are discussed in Section 4.4. Objects representing the optical and electrical properties of entire solar cells were implemented as well. Solar cell models for rear contact cells (including emitter wrap-through cells and buried base rear-contacted cells), high-efficient silicon on insulator thin film cells, and thin film cells on a perforated intermediate layer are presently available (Section 4.5.4).

Heavily doped emitters are found in most industrially relevant silicon solar cells. These emitters cannot be described accurately using the same models as those for lowly doped emitters of high-efficiency cells. When modelling heavily doped emitters, many relevant silicon parameters and device models come into play. These are: the intrinsic carrier density of silicon n_i, the statistics for the energy distribution of free carriers, band gap narrowing (BGN), Auger recombination, minority carrier mobility, the density of states (DOS) affected by doping, and the incomplete ionisation of dopants. Apart from n_i, all these items are effects caused by carrier-carrier and carrier-dopant interactions. The improvements in the understanding of the emitter over the past few years can be regarded as a development from the ideal-gas to many-body theory.

Chapter 5 is a contribution towards a *realistic emitter model*. A new BGN model was used here, which is described in Section 5.2. The characteristic entity of the emitter, the saturation current density, is calculated numerically from the electron recombination current under open-circuit conditions in the diode (Section 5.4). It is crucial to realise that application of the enhanced models modifies the position dependent electron-hole product (Section 5.5), leading to an altered distribution of the recombination in the emitter and in the base (Section 5.6). Extracting the recombination velocity at the surface of phosphorous-doped emitters is discussed in Section 5.8.

A detailed analysis of *silicon on insulator* (SOI) *thin film cells* is presented in Chapter 6. An analytical model for the external reflection of planar SOI cells is developed (Section 6.2.1). The model proved to be advantageous in extracting optical parameters of crystalline silicon thin-film cells on a perforated SiO_2 intermediate layer as well. The optical properties of textured SOI cells are described employing ray tracing simulation (Section 6.2.2). These baseline models are verified experimentally by reflection measurements. The influence of epi-layer thickness on reflection and absorption properties of planar and textured SOI cells is examined in Section 6.3.

In addition, the electrical performance of SOI cells is modelled by means of numerical device simulation. The recombination parameters of the planar and textured SOI cells must be extracted in order to establish electrical baseline models (Section 6.4). These baseline models show agreement with measurements under both short circuit and open circuit conditions, using the same set of recombination parameters. The employed optical generation rate functions are based on ray tracing simulations. In Section 6.5 the electrical baseline models are used to investigate, the influence of epi-layer thickness and recombination parameters on the SOI cell performance. The dependency of the short circuit current and the open circuit voltage on epi-layer thickness is modelled to a high degree of accuracy. Deviations of the measured fill factor values from simulation results are observed. In Section 6.6 a statistical

approach is used to investigate the origins of these deviations by taking a measurement series of fill factor values.

Rear contact cells for one-sun application are analysed in Chapter 7. As this cell type has been previously fabricated and analysed (especially at Stanford University), the literature on it is reviewed in Section 7.1.

An accurate baseline model is established: A new approach to separating bulk- and surface recombination losses in high efficiency cells is presented in Section 7.5. The floating emitter at the front of the rear contact cells at Fraunhofer ISE causes a strong bias light-dependency in the spectral response at low illumination levels. This behaviour can be modelled quantitatively, as outlined in Section 7.6. Distributed resistive losses are described by applying the circuit simulation method (Section 7.7), which helps to understand and quantify perimeter losses in rear contact cells (Section 7.8). Finally, the detailed numerical simulation model reproduces the measured illuminated *I-V* output parameters (7.9).

The baseline model is utilised to perform parameter studies investigating the influence of wafer thickness, metal finger spacing, emitter coverage fractions, emitter profiles and recombination parameters on the cell performance, as presented in Section 7.10.

2 Device physics of silicon solar cells

As shown in this section, a semiconductor solar cell is based on a simple *p-n* junction. A qualitative description of cell performance can therefore be given in terms of a very simple model based on the Shockley diode equation in the dark and under illumination. This model is sufficient for understanding the basic carrier transport mechanisms in the cell, and for roughly predicting the performance parameters of a solar cell.

2.1 Semiconductor device equations

Five equations describe the behaviour of charge carriers in semiconductors under the influence of an electric field and/or light, both of which cause deviations from thermal equilibrium conditions. These equations are therefore called the basic equations for semiconductor device operation. In the following they are simplified to one dimension. The Poisson equation relates the static electric field $\mathcal{E}$ to the space-charge density ρ

$$\frac{d^2\phi(x)}{dx^2} = -\frac{d\mathcal{E}(x)}{dx} = -\frac{\rho(x)}{\epsilon_0\epsilon_s} \tag{2.1}$$

where ϕ is the electrostatic potential, ϵ_0 is the permittivity of free space and ϵ_s is the static relative permittivity of the medium. The electron current density J_e and the hole current density J_h are given by Eqs. 2.2 and 2.3

$$J_e(x) = +q D_e \frac{dn(x)}{dx} + q \mu_e n(x) \mathcal{E}(x) \tag{2.2}$$

$$J_h(x) = -q D_h \frac{dp(x)}{dx} + q \mu_h p(x) \mathcal{E}(x) \tag{2.3}$$

where n and p are electron and hole densities, μ_e and μ_h are the electron and hole mobilities and D_e and D_h are the electron and hole diffusion constants. The first terms on the right hand side of Eqs. 2.2 and 2.3 are diffusion currents driven by a concentration gradient, and the second terms are drift currents driven by the electric field $\mathcal{E}$.

The divergence of the current density J is related to the recombination and generation rates of charge carriers by the *continuity equation*. The electron and hole continuity equations may be written as

$$+\frac{1}{q}\frac{dJ_e(x)}{dx} - r_e(x) + G_e(x) = 0 \tag{2.4}$$

$$-\frac{1}{q}\frac{dJ_h(x)}{dx} - r_h(x) + G_h(x) = 0 \tag{2.5}$$

where $r(x)$ and $G(x)$ are the position-dependent volume recombination and photogeneration rates, respectively.

Substitution of the current densities Eqs. 2.2 and 2.3 into the continuity equations 2.4 and 2.5 gives a coupled set of differential equations, the *transport equations*

$$D_e\frac{d^2n}{dx^2} + \mu_e\mathcal{E}\frac{dn}{dx} + n\mu_e\frac{d\mathcal{E}}{dx} - r_e(x) + G_e(x) = 0 \tag{2.6}$$

$$D_h\frac{d^2p}{dx^2} - \mu_h\mathcal{E}\frac{dp}{dx} - p\mu_h\frac{d\mathcal{E}}{dx} - r_h(x) + G_h(x) = 0. \tag{2.7}$$

The electron and hole transport equations 2.6 and 2.7 are coupled by the electric field $\mathcal{E}$. The coupled set of differential equations 2.1, 2.6 and 2.7 can be solved with different degrees of accuracy. The most basic approach will be discussed in the next section.

2.2 The p-n junction model of Shockley

2.2.1 The p-n junction at equilibrium

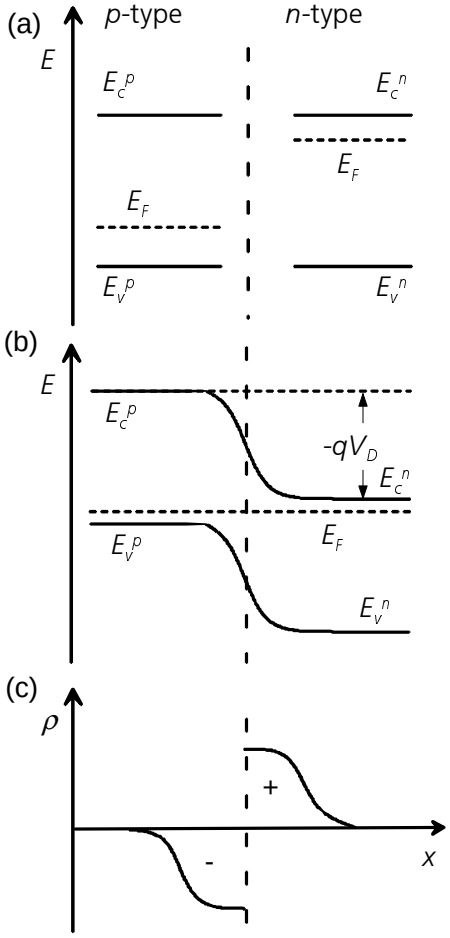

Fig. 2.1: (a) Conduction and valence band-edge energies of separated p- and n-type semiconductors; (b) band bending of the *p-n* junction. The Fermi level is constant at equilibrium; (c) space-charge density ρ across the junction.

For a dark unbiased *p-n* junction, thermal equilibrium conditions are fulfilled. In this section the density of mobile charge carriers, the electric field and the electrostatic potential at thermal equilibrium are discussed. For now, the most simple case is assumed, *i.e.* a constant doping in the *p*- and *n*-regions with an abrupt doping step at the transition. This is a good model for a *p-n* junction grown by epitaxy. If an *n*-region is formed by diffusion of donor atoms from the surface into a *p*-doped material, the model is too simple and must be refined.

The Fermi levels E_F of two separated *p*- and *n*-doped semiconductors are different, as shown in Fig. 2.1a.

If the two materials are brought into contact, the Fermi levels become identical. Fig. 2.1b shows a *p-n* junction which is in equilibrium, so that it has a constant Fermi level E_F achieved by diffusion of mobile charge carriers from one side of the junction to the other. This causes band bending of the conduction band-edge energy E_c and the valence band-edge energy E_v. A transient diffusion current of electrons from the *n*-doped to the *p*-doped semiconductor leads to a positively charged region in the *n*-type semiconductor, while hole diffusion from the *p*-doped to the *n*-doped semiconductor causes a negative space-charge in the *p*-type region. The space-charge region is almost completely depleted of mobile charge carriers, so that n and p are negligibly small compared to the donor and acceptor densities there. The resulting electric field produces a drift force that opposes the diffusion force. The diffusion and drift forces are equal at equilibrium conditions.

In the quasineutral regions that lie beyond the space-charge region the donor and acceptor charges are compensated by electrons and holes, so the space-charge density is zero. For *low-injection conditions*, *i.e.* when the majority carriers are the dominant carrier type

($n_n >> p_n$; $p_p >> n_p$) and at room temperature the majority carrier concentrations n_n and p_p in the quasineutral regions are given by the density of ionised dopants

$$n_n \approx N_D \tag{2.8}$$

$$p_p \approx N_A . \tag{2.9}$$

For Eqs. 2.8 and 2.9 to be valid it is assumed that the dopants are fully ionised. The validity of this assumption will be discussed in Section 2.3.2. For a non-degenerate semiconductor at thermal equilibrium the free carrier concentrations are given by the Boltzmann expressions

$$n = N_c \exp\left(-\frac{E_c - E_F}{kT}\right) \tag{2.10}$$

$$p = N_v \exp\left(-\frac{E_F - E_v}{kT}\right) \tag{2.11}$$

where N_c and N_v are the effective densities of states of the conduction band and of the valence band, respectively.

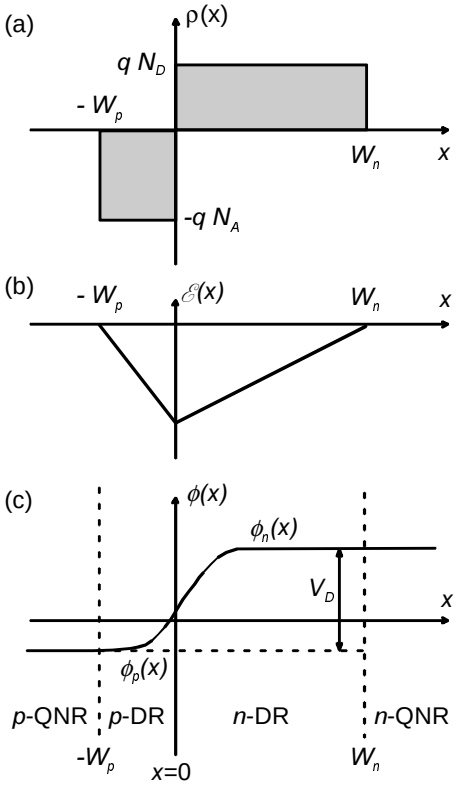

Fig. 2.2: (a) Space-charge density ρ(x); (b) electric field $\mathcal{E}$(x); (c) inner potential ϕ(x) across a p-n junction.

For thermal equilibrium conditions the semiconductor mass-action law $n_i^2 = n(x)p(x)$ holds, and using Eqs. 2.10 and 2.11 this can be written as

$$n_i^2 = n\ p = N_c\ N_v \exp\left(-\frac{E_g}{kT}\right) \tag{2.12}$$

where E_g is the energy gap ($E_c - E_v$) between the conduction and valence band edges.

A simple model for the space-charge region, the *exhaustion region* approximation, was introduced by Schottky assuming rectangular charge density distributions as shown in Fig. 2.2a.

The space-charge region is depleted of mobile charge carriers. Hence the space-charge density here is given by

$$\rho(x) = qN_D \qquad (0 \le x \le W_n). \tag{2.13}$$

$$\rho(x) = -qN_A \quad (-W_p \le x \le 0) \tag{2.14}$$

The electric field in the space-charge region can be found by integrating Poisson's equation, Eq. 2.1, from $x = 0$ to the edges of the depletion region with the constant charge densities Eqs. 2.14 and 2.13.

This gives

$$\mathcal{E}(x) = -\frac{qN_A}{\varepsilon_0 \varepsilon_s}(W_p + x) \qquad (-W_p \le x \le 0) \tag{2.15}$$

$$\mathcal{E}(x) = -\frac{qN_D}{\varepsilon_0 \varepsilon_s}(W_n - x) \qquad (0 \le x \le W_n)\ . \tag{2.16}$$

Fig. 2.2b shows the linear dependence of the electric field on position in the space charge region. The electric field vanishes outside this region.

Defining the Debye length L_D as

$$L_D^p = \left(\frac{\varepsilon_0 \varepsilon_s kT}{q^2 N_A} \right)^{1/2} \tag{2.17}$$

$$L_D^n = \left(\frac{\varepsilon_0 \varepsilon_s kT}{q^2 N_D} \right)^{1/2} \tag{2.18}$$

the electric field can be expressed as

$$\mathcal{E}(x) = -\frac{V_{th}}{(L_D^p)^2}(W_p + x) \qquad (-W_p \le x \le 0) \tag{2.19}$$

$$\mathcal{E}(x) = -\frac{V_{th}}{(L_D^n)^2}(W_n - x) \qquad (0 \le x \le W_n) \tag{2.20}$$

where

$$V_{th} = kT / q \tag{2.21}$$

is the so-called thermal voltage.

The Debye length is a characteristic length of the *p*-*n* junction. At thermal equilibrium the depletion-layer widths of abrupt junctions are about $8L_D$ for silicon. For doping densities higher than 10^{16} cm^{-3}, the Debye length for silicon is less than ~40 nm.

The electrostatic potential in the depletion region is found by integrating Eqs. 2.15 and 2.16 along x to be

$$\phi_p(x) = \frac{qN_A}{2\varepsilon_0 \varepsilon_s} x(2W_p + x) \qquad (-W_p \le x \le 0) \tag{2.22}$$

$$\phi_n(x) = \frac{qN_D}{2\varepsilon_0 \varepsilon_s} x(2W_n - x) \qquad (0 < x \le W_n)\ . \tag{2.23}$$

At the depletion region edge and in the quasineutral regions beyond, the potential takes the constant values $\phi_p(-\infty)$ for the *p*-type region and $\phi_n(\infty)$ for the *n*-type region, respectively.

The potential difference at the depletion region edges is denoted with

$$V_j = \phi_n(\infty) - \phi_p(-\infty) = \phi_n(W_n) - \phi_p(-W_p)\,. \tag{2.24}$$

For *equilibrium conditions* V_j is called the *diffusion voltage* or *built-in potential* V_D of the *p-n* junction (Fig. 2.2). Substituting $\phi_n(W_n)$ and $\phi_p(-W_p)$ into Eq. 2.24 yields

$$V_D = \frac{q}{2\varepsilon_0\varepsilon_s}\left(N_D W_n^{\,2} + N_A W_p^{\,2}\right). \tag{2.25}$$

The interface as a whole must be electrically neutral so

$$N_A W_p = N_D W_n\,. \tag{2.26}$$

Using Eqs. 2.25 and 2.26 the depletion region widths for equilibrium conditions follow as

$$W_n = \left(\frac{2\varepsilon_0\,\varepsilon_s V_D}{q}\,\frac{N_A/N_D}{N_A+N_D}\right)^{1/2} \tag{2.27}$$

$$W_p = \left(\frac{2\varepsilon_0\,\varepsilon_s V_D}{q}\,\frac{N_D/N_A}{N_A+N_D}\right)^{1/2}. \tag{2.28}$$

2.2.2 The junction under bias in the dark

At thermal equilibrium the diffusion current of one carrier type is compensated by a drift current of the same carrier type so the net current flow vanishes. The diffusion of electrons from the *n*-doped region to the *p*-doped region can be expressed as a recombination current: electrons recombine with holes in the *p*-doped region creating a current density $J_{e,rec}$. Similarly the drift current of the electrons from the *p*-doped to the *n*-doped region is supplied by thermally generated electrons in the *p*-region, creating a current density $J_{e,gen}$. When the junction is unbiased

$$J_{e,rec}(V_{ja}=0) - J_{e,gen}(V_{ja}=0) = 0 \tag{2.29}$$

is valid.

An externally applied bias voltage V_{ja} disturbs equilibrium conditions and shifts the potential barrier across the *p-n* junction.[2] A forward bias $V_{ja} > 0$ decreases the potential barrier and the recombination current $J_{e,rec}(V_{ja})$ increases with the Boltzmann factor exp (qV_{ja}/kT)

[2] For simplicity we do not account for a voltage drop due to the series resistance of a solar cell here; V_{ja} denotes the portion of the *applied voltage that appears* across the junction.

$$J_{e,rec}(V_{ja}) = J_{e,rec}(V_{ja} = 0)\exp\left(\frac{qV_{ja}}{kT}\right). \tag{2.30}$$

The rate of thermally generated charge carriers $J_{e,gen}$ is not influenced by the external voltage, therefore

$$J_{e,gen}(V_{ja}) = J_{e,gen}(V_{ja} = 0). \tag{2.31}$$

The analogous equations for holes are

$$J_{h,rec}(V_{ja} = 0) = J_{h,gen}(V_{ja} = 0) \tag{2.32}$$

$$J_{h,rec}(V_{ja}) = J_{h,rec}(V_{ja} = 0)\exp\left(\frac{qV_{ja}}{kT}\right) \tag{2.33}$$

$$J_{h,gen}(V_{ja}) = J_{h,gen}(V_{ja} = 0). \tag{2.34}$$

The external electron and hole current densities are given by

$$J_e = J_{e,rec} - J_{e,gen} \tag{2.35}$$

$$J_h = J_{h,rec} - J_{h,gen}. \tag{2.36}$$

The net current density is the sum of electron and hole currents

$$J = J_e + J_h. \tag{2.37}$$

Using Eqs. 2.30 to 2.37 the net current density is therefore given by

$$J(V_{ja}) = J_0\left[\exp\left(\frac{qV_{ja}}{kT}\right) - 1\right] \tag{2.38}$$

where J_0 is the *saturation current density* of the *p-n* junction, given by

$$J_0 = J_{e,gen} + J_{h,gen}. \tag{2.39}$$

For forward bias, the current increases exponentially with the applied voltage. For high reverse voltages $V_{ja} < 0$ the Boltzmann factor in Eq. 2.38 can be neglected and the external current corresponds to the flux of thermally generated charge carriers as follows

$$J \approx -J_0 = -\left(J_{e,gen} + J_{h,gen}\right). \tag{2.40}$$

Equation 2.38 is known as the *Shockley equation* [17]. Note that it was derived without considering any special semiconductor characteristics such as charge carrier lifetime. The current-voltage behaviour of this idealised *p-n* junction is simply governed by the recombination current as a function of the Boltzmann factor $\exp(qV_{ja}/kT)$. The Shockley equation describes the ideal *rectifier diode* and is thus a fundamental equation for microelectronic device physics.

For a quantitative discussion of the idealised *p-n* junction the charge carrier densities at *non-equilibrium* have to be calculated. The device works under non-equilibrium conditions if charge carriers are either injected by an applied voltage or optically generated. For this purpose, one can derive boundary conditions for the charge carrier densities at the junction edges $-W_p$ and W_n, respectively, as follows: at thermal equilibrium the charge carrier densities are given by the Boltzmann distribution Eqs. 2.10 and 2.11 based on the energy difference between the band-edge energies E_c and E_v and the Fermi energy E_F (Fig. 2.1). A similar dependence can be stated for non-equilibrium conditions by introducing separate Fermi energies for electrons and holes, the *quasi-Fermi energy levels* E_{fc} and E_{fv}. These are defined so that replacement of the single equilibrium Fermi energy E_F in the equilibrium expressions on the left side of Table 2.1 by the quasi-Fermi energy levels E_{fc} and E_{fv} yields the non-equilibrium carrier densities on the right hand side of Table 2.1.

Equilibrium	Non-equilibrium
$n_0 = N_c \exp\left(-\frac{E_c - E_F}{kT}\right)$ (2.41)	$n = N_c \exp\left(-\frac{E_c - E_{fc}}{kT}\right)$ (2.42)
$p_0 = N_v \exp\left(-\frac{E_F - E_v}{kT}\right)$ (2.43)	$p = N_v \exp\left(-\frac{E_{fv} - E_v}{kT}\right)$ (2.44)
$n_0 p_0 = n_i^2 = N_c N_v \exp\left(-\frac{E_c - E_v}{kT}\right)$ $= N_c N_v \exp\left(-\frac{E_g}{kT}\right)$ (2.45)	$np = N_c N_v \exp\left(-\frac{E_c - E_v}{kT}\right)\exp\left(\frac{E_{fv} - E_{fc}}{kT}\right)$ $= n_0 p_0 \exp\left(\frac{E_{fv} - E_{fc}}{kT}\right)$ (2.46)

Table 2.1: Charge carrier density for equilibrium and non-equilibrium. Left: The charge carrier densities for equilibrium are given by the difference of the band-edge energy and the Fermi energy. Right: For non-equilibrium conditions the quasi-Fermi levels E_{fc} and E_{fv} are introduced.

At the edges of the space-charge regions the minority and majority carrier quasi-Fermi levels are separated by the bias $q\,V_{ja}$ imposed across the *p-n* junction

$$qV_{ja} = E_{fv}(-W_p) - E_{fc}(W_n)\,. \tag{2.47}$$

Here, the validity of the Boltzmann approximation for the charge carriers (Table 2.1) and low-injection conditions is assumed. More general expressions for the separation of carrier quasi-Fermi levels were derived by Marshak and van Vliet [18]. With respect to our assumptions, the separation of the quasi-Fermi levels V_{ja} is related to the potential difference V_j across the junction (Eq. 2.24) by

$$V_{ja} = V_D - V_j \,. \tag{2.48}$$

Under low-injection conditions, the majority carrier concentrations are unperturbed throughout the quasineutral regions, so that

$$p_p(-W_p) = p_{p,0} \tag{2.49}$$

$$n_n(W_n) = n_{n,0} \tag{2.50}$$

where $p_{p,0}$ and $n_{n,0}$ are the majority carrier concentrations in the quasineutral *p*- and *n*-type regions, respectively.

Using Eqs. 2.46 to 2.50 the boundary conditions for the minority carrier concentrations at the edges of the space-charge regions (Fig. 2.3) are found as

$$n_p(-W_p) = n_{p,0} \exp\left(\frac{qV_{ja}}{kT}\right) \tag{2.51}$$

$$p_n(W_n) = p_{n,0} \exp\left(\frac{qV_{ja}}{kT}\right). \tag{2.52}$$

With these boundary conditions the transport equations can be solved to find quantitative expressions for the saturation current density of the *p*-*n* junction.

2.2.3 The superposition principle

The transport equations for electrons and holes Eqs. 2.6 and 2.7 contain the electric field $\mathcal{E}$, thus forming a coupled set of differential equations for the carrier concentrations *n* and *p*. If the spatial dependence of the electric field and the carrier concentrations is known the current densities can be calculated with the help of Eqs. 2.2 and 2.3.

With the approximations discussed in Section 2.2.1 it was found that the electric field in the quasineutral region vanishes, and therefore the transport equations 2.6 and 2.7 decouple in these regions. In this case the carrier transport is purely diffusive and the minority carrier concentrations can be calculated separately for both quasineutral regions. Under low-injection conditions the perturbation of the majority carrier concentration due to generation and recombination processes can be neglected. The recombination rate of minority carriers is then proportional to the excess minority carrier concentration ($n - n_0$) on the *p* side and ($p - p_0$) on the *n* side. Therefore the minority carrier recombination rate *r* is given by

$$r_e = \frac{n - n_0}{\tau_e} \tag{2.53}$$

$$r_h = \frac{p - p_0}{\tau_h} \tag{2.54}$$

where τ_e and τ_h are the minority carrier lifetimes of electrons and holes, respectively.

The transport equations 2.6 and 2.7 simplify to the following decoupled linear differential equations for the quasineutral regions if the minority carrier lifetimes do not depend on the carrier concentrations

$$D_e \frac{d^2 n}{dx^2} - \frac{n - n_0}{\tau_e} + G_e(x) = 0 \tag{2.55}$$

$$D_h \frac{d^2 p}{dx^2} - \frac{p - p_0}{\tau_h} + G_h(x) = 0 . \tag{2.56}$$

In addition it is assumed that the photogeneration rates $G_e(x)$ and $G_h(x)$ are independent of the carrier concentrations and depend only on distance x from the illuminated surface. For dark conditions [$G(x) = 0$] Eqs. 2.55 and 2.56 are then homogeneous differential equations. The carrier concentrations under illumination are found by adding particular solutions of the inhomogeneous differential equations to the general homogeneous solutions. For electrons in the *p*-type region this may be expressed as

$$n^{Lt} = n^{Dk} + n^{ph} \tag{2.57}$$

where n^{Dk} is the solution for dark conditions, n^{ph} is the photogenerated electron density and n^{Lt} is the electron concentration under illumination. This implies that the illuminated *I–V* curve can be found simply by adding the photogenerated current to the dark *I–V* curve (shifting approximation)—the model cell is said to exhibit *superposition*.

This is shown schematically in Fig. 2.4, where the dark diode *I–V* characteristic is shifted from the first quadrant to the fourth quadrant by adding the photogenerated current density $J^{Lt} = -J_{sc}$. In a circuit diagram as shown in Fig. 2.7 the superposition of currents means that the diode and the photogenerated current flow is parallel.

2.2.4 Carrier density solutions for dark conditions

The Shockley equation 2.38, for the current-voltage characteristic of a *p-n* junction was found in Section 2.2.2 with the help of a qualitative discussion. A quantitative expression for the saturation current density J_o in the Shockley equation can be calculated by solving the diffusive carrier transport equations in the quasineutral regions.

If the superposition principle discussed in Section 2.2.3 applies, the carrier density solutions in the quasineutral regions can be found by solving Eqs. 2.55 and 2.56 separately. Under dark conditions Eqs. 2.55 and 2.56 reduce respectively to

$$D_e \frac{d^2 n}{dx^2} - \frac{n - n_0}{\tau_e} = 0 \qquad (x \le -W_p) \tag{2.58}$$

$$D_h \frac{d^2 p}{dx^2} - \frac{p - p_0}{\tau_h} = 0 \qquad (x \ge W_n). \tag{2.59}$$

The general solution of Eq. 2.58 can be expressed as

$$n - n_0 = A \cosh\left(\frac{x}{L_e}\right) + B \sinh\left(\frac{x}{L_e}\right) \tag{2.60}$$

where the distance

$$L_e \equiv \sqrt{D_e \tau_e} \tag{2.61}$$

is the *diffusion length* of electrons in the *p*-doped side. The diffusion length is the average length a minority carrier can diffuse between generation and recombination, *i.e.* during its lifetime τ.

If it is assumed that there is no recombination loss at the surface of the *p*-quasineutral region, the boundary condition

$$\frac{dn}{dx}\Big|_{x \to -\infty} = 0 \tag{2.62}$$

applies. Applying Eqs. 2.62 and 2.60 it is found that $A = B$ so the concentration of electrons in the *p*-QNR is given by

$$n - n_0 = A \exp\left(\frac{x}{L_e}\right). \tag{2.63}$$

The boundary condition Eq. 2.51 yields

$$A = n_0 \left[\exp\left(\frac{qV_{ja}}{kT}\right) - 1\right] \exp\left(\frac{W_p}{L_e}\right). \tag{2.64}$$

Note that the exponential excess carrier concentration decays (Eq. 2.63) from position $x = -W_p$ in the *p*-QNR with the diffusion length L_e as characteristic length.

The electric field in the quasineutral region vanishes because of the exhaustion region approximation, so the current flow is driven by diffusion only. At the edge of the *p*-doped depletion region the current density is given by

$$J_e(-W_p) = qD_e \frac{d}{dx}(n - n_0)\Big|_{x=-W_p} \tag{2.65}$$

and from Eqs. 2.63 and 2.64 it is found that

$$J_e(-W_p) = \frac{q D_e n_0}{L_e}\left[\exp\left(\frac{qV_{ja}}{kT}\right)-1\right]. \tag{2.66}$$

Similar arguments give the excess hole concentration in the *n*-QNR as

$$p - p_0 = p_0\left[\exp\left(\frac{qV_{ja}}{kT}\right)-1\right]\exp\left(\frac{W_n - x}{L_h}\right) \tag{2.67}$$

and the current density of the diffusive hole carrier flow at $x = W_n$ as

$$J_h(W_n) = \frac{q D_h p_0}{L_h}\left[\exp\left(\frac{qV_{ja}}{kT}\right)-1\right]. \tag{2.68}$$

To derive analytical expressions for the electron and hole carrier densities in the *n*-doped depletion region it is assumed in this Section that the recombination loss in the depletion region can be neglected, *i.e.* $r = 0$ for $-W_p \le x \le W_n$.

The transport equation 2.6 then reduces to

$$D_e \frac{d^2 n}{dx^2} + \mu_e \mathcal{E}(x)\frac{dn}{dx} + n\mu_e \frac{d\mathcal{E}}{dx} = 0. \tag{2.69}$$

Using Schottky's model for the space-charge region discussed in Section 2.2.1 and the Nernst–Einstein relation

$$D_e = \frac{kT}{q}\mu_e \tag{2.70}$$

the electric field can be expressed in terms of the characteristic Debye length L_D^n (Eq. 2.18) of the space-charge region

$$\frac{d^2 n}{dx^2} - \frac{1}{\left(L_D^n\right)^2}(W_n - x)\frac{dn}{dx} + n(x)\frac{1}{\left(L_D^n\right)^2} = 0. \tag{2.71}$$

At $x = W_n$ the carrier concentrations must match the solutions for the quasineutral regions, and therefore

$$n(W_n) = n_0 \tag{2.72}$$

$$p(W_n) = p_0 \exp\left(\frac{qV_{ja}}{kT}\right). \tag{2.73}$$

Under low-injection conditions the majority carrier concentration gradient vanishes at $x = W_n$, *i.e.*

$$\left.\frac{dn}{dx}\right|_{x=W_n} = 0\,. \tag{2.74}$$

The boundary condition for the hole gradient at the depletion region edge follows from Eq. 2.67 as

$$\left.\frac{dp}{dx}\right|_{x=W_n} = -\frac{p_0}{L_h}\left[\exp\left(\frac{qV_{ja}}{kT}\right)-1\right]. \tag{2.75}$$

Integrating Eq. 2.71 from W_n to x using the boundary condition Eq. 2.74 yields

$$\frac{dn(x)}{dx} + \frac{x-W_n}{L_D^{n\,2}}\,n(x) = 0\,. \tag{2.76}$$

The differential equation for the hole carrier density in the *n*-doped depletion region can be found by using the boundary condition Eq. 2.75. The same steps are used as for the derivation of Eq. 2.76, leading to

$$\frac{dp(x)}{dx} - \frac{x-W_n}{(L_D^n)^2}\,p(x) = -\frac{p_0}{L_h}\left[\exp\left(\frac{qV_{ja}}{kT}\right)-1\right]. \tag{2.77}$$

The electron carrier density in the *n*-doped depletion region is found by integrating Eq. 2.76 subject to the boundary condition Eq. 2.72, thus

$$n(x) = n_0\,\exp\left(-\frac{(x-W_n)^2}{2\,(L_D^n)^2}\right) \qquad (0 \le x \le W_n). \tag{2.78}$$

Integrating Eq. 2.77 using the boundary condition Eq. 2.73 gives the hole carrier density in the *n*-doped depletion region as

$$\begin{aligned} p(x) = {} & \left\{\left[\exp\left(\frac{q\,V_{ja}}{kT}\right)-1\right]\frac{L_D^n}{L_h}\left(\frac{\pi}{2}\right)^{1/2}\,\mathrm{erf}\left(\frac{W_n-x}{\sqrt{2}\,L_D^n}\right)+\exp\left(\frac{qV_{ja}}{kT}\right)\right\}\cdot \\ & \cdot\, p_0\,\exp\left(\frac{(x-W_n)^2}{2\,(L_D^n)^2}\right) \qquad (0 \le x \le W_n). \end{aligned} \tag{2.79}$$

The Debye length L_D introduced in Eq. 2.17 and 2.18 is several orders of magnitude smaller than typical diffusion lengths L_e, L_h. Thus the first term in Eq. 2.79 can be neglected and this equation reduces to

$$p(x) = p_0\,\exp\left(\frac{qV_{ja}}{kT}\right)\exp\left[\frac{(x-W_n)^2}{2\,(L_D^n)^2}\right] \qquad (0 \le x \le W_n). \tag{2.80}$$

The depletion-region concentration profiles predicted by Eqs. 2.78 and 2.80 are illustrated in Fig. 2.3. These equations are sometimes known as the quasiequilibrium expressions. They

indicate that, although there is a net carrier flux across the biased junction, the carrier concentrations are, to a very good degree of approximation, still related to those at the depletion region edges by Boltzmann expressions. Physically this is because the net hole and electron currents in the depletion regions arise from the small difference between very large opposed drift and diffusion forces. These are exactly balanced at equilibrium (Section 2.2) and only slightly unbalanced when the junction is subjected to moderate bias, so the carrier profile remains quasistatic, that is, solely determined by the local electric potential and independent of any transport properties, such as carrier mobility (Archer *et al.*, Ref. [19]).

An expression for the saturation current density J_0 can be found as follows. Since the hole and electron currents are constant across the dark, biased junction, it follows that all majority carriers injected into the junction at one depletion region edge must emerge as minority carriers from the other depletion region edge. The saturation current from Eqs. 2.66 and 2.68 can therefore be calculated as the sum of the minority carrier currents emerging from the depletion edges into the quasineutral regions, which gives

$$J(V_{ja}) = J_e(-W_p) + J_h(W_n) = J_0\left[\exp\left(\frac{qV_{ja}}{kT}\right) - 1\right] \tag{2.81}$$

where

$$J_0 = \frac{q\,D_e n_0}{L_e} + \frac{q\,D_h p_0}{L_h}\ . \tag{2.82}$$

Comparing Shockley's current–voltage characteristic Eq. 2.38 with Eq. 2.81 and using also Eqs. 2.8, 2.9 and 2.12, the saturation current density of the *p-n* junction can be written as

$$J_0 = q\,n_i^2\left(\frac{D_e}{L_e\,N_A} + \frac{D_h}{L_h\,N_D}\right). \tag{2.83}$$

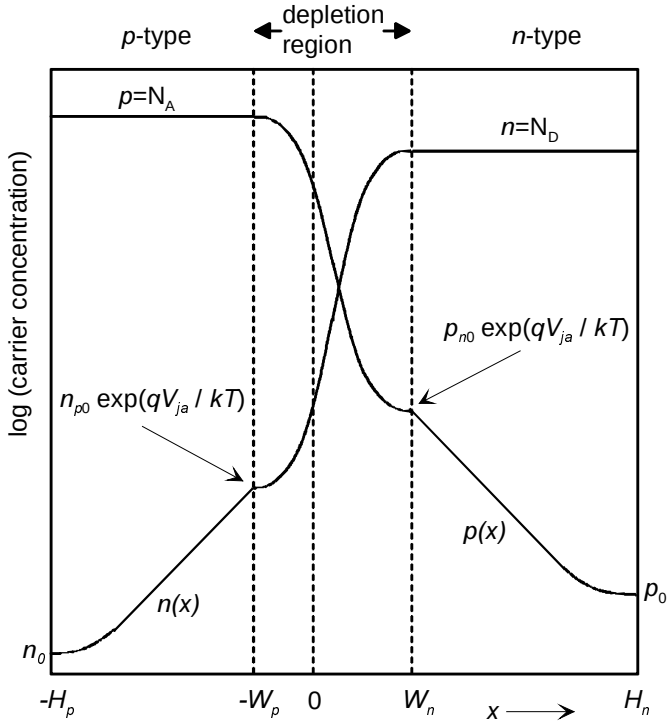

Fig. 2.3: Electron and hole carrier concentrations across the dark forward biased *p-n* junction. Arrows indicate the points where the boundary conditions 2.51 and 2.52 apply.

2.2.5 The illuminated I–V curve

To find the carrier concentration under illumination the superposition principle (Section 2.2.3) is used. The electron concentration in the illuminated *p*-type quasi-neutral region is found by solving Eqs. 2.55 and 2.56, where the position-dependent photogeneration rate $G_e(x)$ has now to be considered. For mathematical simplicity the case of spatially homogeneous generation G of electron hole pairs is assumed (see Ref. [20]). This means we assume weakly absorbing material so photogeneration of charge carriers does not fall off with x. This assumption simplifies the treatment and does not alter the essential conclusions. From the superposition principle one obtains

$$D_e \frac{d^2 n^{Lt}}{dx^2} - \frac{D_e \left(n^{Lt} - n_0\right)}{L_e^{\,2}} + G = 0 \qquad (x \le -W_p) \tag{2.84}$$

and

$$n^{ph} = n^{Lt} - n^{Dk}. \tag{2.85}$$

Substracting Eq. 2.58 from Eq. 2.84 gives

$$D_e \frac{d^2 n^{ph}}{dx^2} - \frac{D_e n^{ph}}{L_e^{\,2}} + G = 0 \qquad (x \le -W_p)\,. \tag{2.86}$$

The photogenerated charge carrier density at the edge of the space-charge region is considered to be negligible, and therefore

$$n^{ph}(-W_p) = 0\ . \tag{2.87}$$

Assuming no recombination loss at the surface of the *p*-type region the boundary condition Eq. 2.62 holds also for n^{ph}, *i.e.*

$$\frac{dn^{ph}}{dx}\Big|_{x\to-\infty} = 0\,. \tag{2.88}$$

The general solution to Eq. 2.86 is

$$n^{ph} = G\tau_e + C\exp\left(\frac{x}{L_e}\right) + D\exp\left(-\frac{x}{L_e}\right) \tag{2.89}$$

where the constants *C* and *D* can be determined from the boundary conditions. Using Eq. 2.87 gives

$$G\tau_e + C\exp\left(\frac{-W_p}{L_e}\right) + D\exp\left(\frac{W_p}{L_e}\right) = 0\,. \tag{2.90}$$

The boundary condition Eq. 2.88 implies that $D = 0$ for a physically meaningful solution; thus

$$C = -G\tau_e \exp\left(\frac{W_p}{L_e}\right) \tag{2.91}$$

and the photogenerated carrier density in the *p*-QNR is found as

$$n^{ph}(x) = G\tau_e\left\{1 - \exp\left(\frac{W_p + x}{L_e}\right)\right\}. \tag{2.92}$$

Substituting Eqs. 2.63, 2.64 and 2.92 in Eq. 2.85 the electron concentration in the *p*-QNR under illumination is calculated as

$$n^{Lt} = n_0 + G\tau_e + \left[\exp\left(\frac{W_p + x}{L_e}\right)\right]\left[n_0\left\{\exp\left(\frac{qV_{ja}}{kT}\right) - 1\right\} - G\tau_e\right] \quad (x \le -W_p)\,. \tag{2.93}$$

The diffusive electron flow in the *p*-type quasineutral region follows by differentiating Eq. 2.93 with respect to *x* as

$$J_e(x) = q n_0 \frac{D_e}{L_e}\left\{\exp\left(\frac{W_p + x}{L_e}\right)\right\}\left\{\exp\left(\frac{qV_{ja}}{kT}\right) - 1\right\} - qGL_e \exp\left(\frac{W_p + x}{L_e}\right)(x \le -W_p) \qquad (2.94)$$

with a similar expression for the diffusive hole current flow in the *n*-type quasineutral region

$$J_h(x) = q p^0 \frac{D_h}{L_h}\left\{\exp\left(\frac{W_n - x}{L_h}\right)\right\}\left\{\exp\left(\frac{qV_{ja}}{kT}\right) - 1\right\} - qGL_h \exp\left(\frac{W_n - x}{L_h}\right)(x \ge W_n)\,. \qquad (2.95)$$

The total current density is found by adding the diffusive minority carrier flow at the edges of the depletion regions as in Section 2.2.4. Including the change in current density $q\,G\,W$ arising from the generation of electron-hole pairs in the depletion region of width $W = W_n + W_p$ yields

$$J_{total} = J_e(-W_p) + J_h(W_n) - qG\,W\,. \qquad (2.96)$$

Substituting Eqs. 2.94 and 2.95 in Eq. 2.96 yields the *ideal diode equation under illumination*

$$J_{total} = J_0\left[\exp\left(\frac{qV_{ja}}{kT}\right) - 1\right] - J^{Lt} \qquad (2.97)$$

where i_o is the saturation current density Eq. 2.82 and

$$J^{Lt} = qG\left[W + L_e + L_h\right] \qquad (2.98)$$

is the light-generated current.

The most important simplifying assumptions used to obtain the ideal diode equation are:

- the exhaustion region approximation.
- low-injection conditions.
- the superposition principle.
- the cell is wide enough that no surface recombination has to be taken into account, *i.e.* $L_e << H_n$ and $L_h << H_p$.
- spacially homogeneous photogeneration of electron hole pairs.
- no parasitic losses due to series and parallel resistances.

With these assumptions simple expressions for the charge carrier distribution in an illuminated *p-n* junction were derived. The saturation current density was found from the diffusive current flow at the edges of the QNRs.

2.3 Real diode characteristics

Though the ideal diode equation 2.97 takes account of the basic physical principles of charge carrier transport that can be found in real devices, silicon solar cells in general can exhibit strong deviations from this ideal characteristic. In the following sections the parameters that characterise a 'real' solar cell are discussed.

2.3.1 Solar cell parameters

For a practical analysis of solar cell performance the dark and light *I–V* characteristics shown in Fig. 2.4 are investigated.

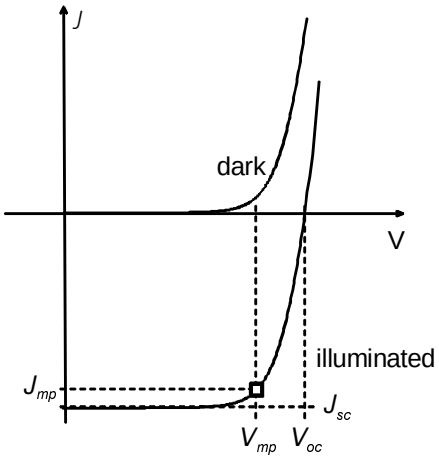

Fig. 2.4: Typical dark and illuminated solar cell *I-V* curves

Prominent parameters of the illuminated *I–V* characteristics include the open-circuit voltage V_{oc}, the short-circuit current density J_{sc}, the maximum power voltage V_{mp} and the current density for maximum power J_{mp}. The maximum power P_{mp} is given by the product $V_{mp}\,J_{mp}$. The efficiency of the cell at the maximum power point is the ratio of output power P_{mp} to the incident solar power E_o

$$\eta = \frac{P_{mp}}{E_0} = \frac{V_{mp}\,J_{mp}}{E_0} = \frac{V_{oc}\,J_{sc}\,\eta_{fill}}{E_0} \tag{2.99}$$

where η_{fill} is the fill factor

$$\eta_{fill} = \frac{J_{mp}\,V_{mp}}{J_{sc}\,V_{oc}}, \tag{2.100}$$

i.e. the ratio of the two rectangular areas shown in Fig. 2.4.

By setting J_{total} in Eq. 2.97 to zero, the relation between the open-circuit voltage V_{oc} and the saturation current density J_o is found as

$$V_{oc} = V_{th}\,\ln\left(1 + \frac{J^{Lt}}{J_0}\right). \tag{2.101}$$

2.3.2 Assumptions regarding the majority carrier concentration

In Eqs. 2.8 and 2.9 it was assumed that the majority carrier concentration was equal to the density of the dopants throughout the QNRs. For this to be so, low-injection conditions have to be fulfilled: that is, the perturbation of the majority carrier concentration due to light generation or carrier injection is small and therefore

$$n \approx N_{D^+} \text{ (in } n\text{-type material)} \tag{2.102}$$

$$p \approx N_{A^-} \text{ (in } p\text{-type material).} \tag{2.103}$$

In other words, the density of free charge carriers is equal to the density of ionised dopants. This approximation is not valid under illumination by concentrated sunlight or high forward bias voltages.

If, in addition, the energy level of the dopant lies near the relevant band edge, *all* the dopants will be ionised at room temperature, and in this case

$$n \approx N_D \approx N_{D^+} \tag{2.104}$$

$$p \approx N_A \approx N_{A^-} \ . \tag{2.105}$$

2.3.3 Charge carrier lifetime

For the superposition principle to be valid, the minority carrier lifetimes in Eqs. 2.53 and 2.54 must be constant, as noted in Section 2.2.3. These lifetimes are determined by the dominant recombination mechanism. For an *n*-type semiconductor, the upper bound on the hole lifetime, namely the radiative recombination lifetime τ_h^r, is given by

$$\tau_h^r = \frac{1}{k_1^r \ N_D} \tag{2.106}$$

where k_1^R is the radiative recombination rate constant.

Often the minority carrier lifetime is determined by recombination through traps. For the simple model of recombination centres of a single energy, the Shockley–Read–Hall (SRH) hole carrier lifetime expression in an *n*-type semiconductor is given by

$$\tau_h^T = \frac{1}{k_h^T \ N_T} \tag{2.107}$$

where N_T is the trap concentration and k_h^T is the hole capture rate constant.

In other cases, minority carrier lifetimes are determined by Auger recombination. In this case, the hole lifetime for low-injection conditions is given by

$$\tau_h^A = \frac{1}{C_n \ N_D^2} \tag{2.108}$$

where C_n is the Auger band-to-band recombination rate constant.

Shockley–Read–Hall and Auger recombination are the two dominant recombination mechanisms in Si solar cells. The minority carrier lifetime τ_h of holes in *n*-doped silicon is then given by

$$\frac{1}{\tau_h} = \frac{1}{\tau_h^T} + \frac{1}{\tau_h^A} . \tag{2.109}$$

The $1/N_D^2$-dependence of the Auger lifetime causes the minimum carrier lifetime to be smaller in heavily doped regions (*e.g.* the emitter) than in lightly doped regions (*e.g.* the base). Also, the doping dependence of τ_h^A leads to a position-dependent lifetime in the emitter region of cells with a doping profile. The saturation current density of emitters with position-dependent carrier lifetimes can be calculated analytically as demonstrated in Section 2.3.9.

If low-injection conditions are not fulfilled, the recombination rates for electrons, r_e and r_h, depend on both the electron and hole concentrations, *i.e.* the superposition principle does not apply. This is the case in solar cells working under illumination by concentrated sunlight. The coupled set of differential equations 2.1, 2.6 and 2.7 have then to be solved numerically, as described in Section 3.

2.3.4 Surface recombination

In the discussion of the dark diode characteristics in Section 2.2.4 it was assumed that there was no recombination loss at the cell surfaces. A boundary condition that includes the surface recombination of electrons at the surface of the *p*-type region (at $x=-H_p$) can be expressed as

$$D_e \left.\frac{dn}{dx}\right|_{x=-H_p} = S_e \left(n - n_0\right)\Big|_{x=-H_p} \tag{2.110}$$

where S_e is the surface recombination velocity of electrons. Introducing a similar boundary condition for the recombination of holes at the surface of the *n*-type region and performing the same steps as in Section 2.2.4 gives a modified expression for the saturation current density (compare with Eq. 2.82)

$$J_0 = \left(\frac{q\, D_e\, n_{p,0}}{L_e}\, \Xi_p + \frac{q\, D_h\, p_{n,0}}{L_h}\, \Xi_n \right). \tag{2.111}$$

The geometric factor Ξ_n is given by

$$\Xi_n = \frac{\sinh\left(\frac{Q_n}{L_h}\right) + \frac{S_h L_h}{D_h}\cosh\left(\frac{Q_n}{L_h}\right)}{\cosh\left(\frac{Q_n}{L_h}\right) + \frac{S_h L_h}{D_h}\sinh\left(\frac{Q_n}{L_h}\right)} \tag{2.112}$$

where $Q_n = H_n - W_n$ is the thickness of the *n*-doped quasineutral region, S_h is the surface recombination velocity of holes at the surface of the *p*-doped region, L_h is the hole diffusion length and D_h is the hole diffusion constant as introduced before.

A similar expression can be found for the geometric factor Ξ_p. The effect of surface recombination on the saturation current density can be studied by plotting the geometric factor as a function of Q/L for various values of SL/D, as shown in Fig. 2.5. For $L < Q$, (*i.e.* $Q/L > 1$) the surface does not contribute to the saturation current density J_o.

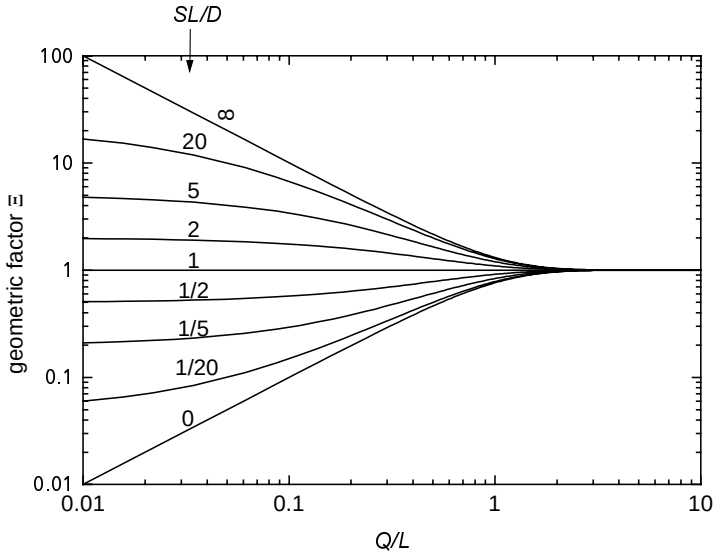

Fig. 2.5: Geometric factor as a function of the ratio of the width of the quasineutral region Q to the minority carrier diffusion length L. Each curve represents a fixed ratio SL/D.

A thin quasineutral region of width Q in combination with a high surface recombination velocity results in a high saturation current density, and consequently a low open-circuit voltage (see Eq. 2.101). On the other hand, good surface passivation can reduce J_o considerably at low values of Q/L. This is particularly important for thin solar cells.

2.3.5 Series and shunt resistance

In the real device a series resistance R_s and a shunt (or parallel) resistance R_p may be present. Accounting for series and shunt resistance losses, the illuminated *I–V* characteristic Eq. 2.97 becomes

$$J(V) = J_0\left[\exp\left(\frac{q\left(V - J(V)R_s\right)}{kT}\right) - 1\right] + \frac{V - J(V)R_s}{R_p} - J^{Lt} \tag{2.113}$$

where V is the voltage at the cell terminals.

The series resistance of a solar cell is composed of the resistance of the metal grid, the contact resistance and the base and emitter sheet resistances. Shunt conductive losses can arise from imperfections on the device surface as well as leakage currents across the edge of the cell.

The influence of the series and shunt components on the illuminated and dark I–V characteristics, according to Eq. 2.113, is plotted in Fig. 2.6. The dark I–V curves in the lower half are shown on a logarithmic scale; the ideal I–V characteristic Eq. 2.97 gives a straight line on this scale. For high current densities the deviation from straight line behaviour is caused by the series resistance, while low shunt resistances cause deviations from the ideal I–V characteristic for small current densities.

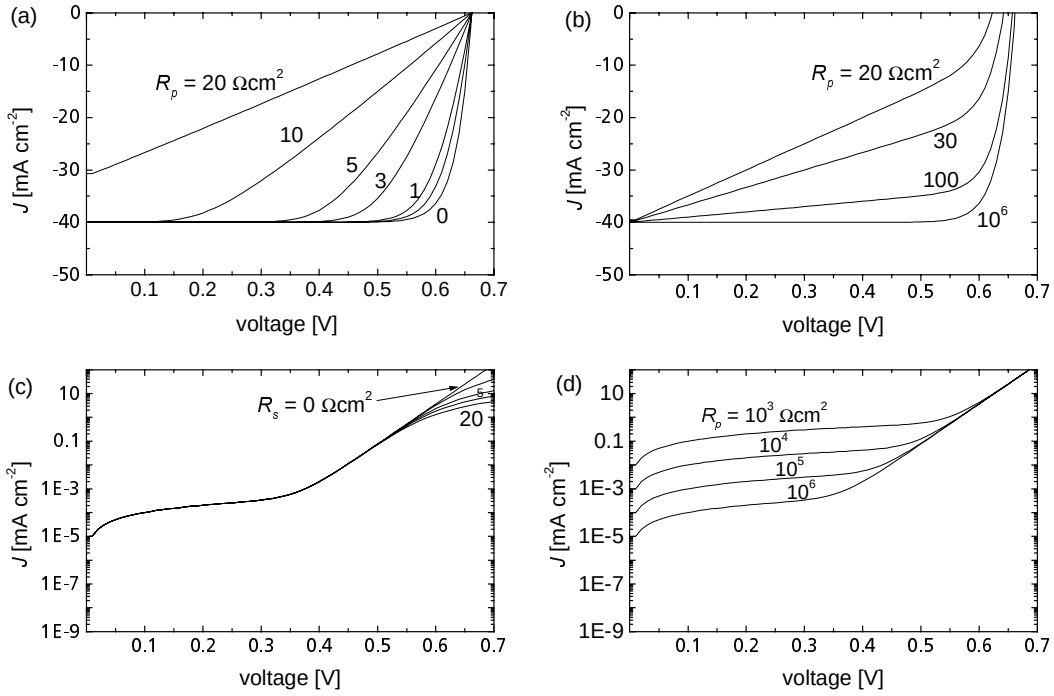

Fig. 2.6: Influence of series resistance R_s and parallel resistance R_p on the I–V characteristic: (a) Illuminated, R_s varied; (b) illuminated, R_p varied; (c) dark, R_s varied; (d) dark, R_p varied.

2.3.6 Non-ideal dark current components

It has so far been assumed that there is no recombination loss in the depletion region. However, in real solar cells, depletion-region recombination represents a substantial loss mechanism. An analytical expression for the ‘space-charge layer recombination current’ was first given by Sah *et al.* [21], for the simplified case of a single recombination centre located within the forbidden gap. Traps located in the vicinity of the gap give a dominating

contribution to the Shockley–Read–Hall recombination rate. It was further assumed that the recombination rate is constant across the space-charge region. The resulting recombination rate can be expressed as a recombination current J_{DR} in the depletion region

$$J_{DR} = J_{02}\left[\exp\left(\frac{qV}{2kT}\right)-1\right]. \tag{2.114}$$

Adding this space-charge layer recombination current to Eq. 2.113 gives the '*two diode model*' expression

$$J(V) = J_{01}\left[\exp\left(\frac{q\left(V-J(V)R_s\right)}{kT}\right)-1\right]+J_{02}\left[\exp\left(\frac{q\left(V-J(V)R_s\right)}{2kT}\right)-1\right]+\frac{V-J(V)R_s}{R_p}-J^{Lt} \tag{2.115}$$

Sah also derived an analytical expression for J_{DR} with less rigid assumptions as stated above (see Fahrenbruch [22]); for instance, Sah's expression is still valid for unequal electron and hole lifetimes. In general, the recombination current in the depletion region is a function of the applied voltage and is not necessarily of monoexponential form.

A non-ideal *I–V* characteristic can further be caused by an injection-level-dependent surface recombination current. In the boundary condition Eq. 2.110 the surface recombination velocity S was assumed to be independent of the minority carrier concentration. However, Aberle *et al.* [23] found that the origin of the non-ideal diode behaviour of high-efficiency silicon solar cells is a surface recombination velocity at the rear Si/SiO_2 interface that strongly depends on the minority carrier concentration.

In practice, most measured *I–V* curves of solar cells can be approximated by several exponential regions in the dark forward *I–V* characteristic revealing the presence of several dark current components. One can take this behaviour into account by empirically introducing the *ideality factors* β_1 and β_2 so that Eq. 2.115 can be expressed as

$$J(V) = J_{01}\left[\exp\left(\frac{q\left(V-J(V)R_s\right)}{\beta_1 kT}\right)-1\right]+J_{02}\left[\exp\left(\frac{q\left(V-J(V)R_s\right)}{\beta_2 kT}\right)-1\right]+\frac{V-J(V)R_s}{R_p}-J^{Lt}. \tag{2.116}$$

Fig. 2.7 shows the equivalent circuit of Eq. 2.116, consisting of two diodes with different ideality factors β_1 and β_2, the light-generated current J^{Lt} and the series and parallel resistances R_s and R_p.

By varying J_{o1}, J_{o2} β_1, β_2, R_p, and R_s, a wide range of experimentally observed *I–V* curves can be fitted. As outlined above, different recombination components may be lumped in

numerical fit values of the model parameters J_{o1}, J_{o2} β_1 and β_2 of Eq. 2.116. Therefore a unique assignment of fit results corresponding to the physical origin of one recombination mechanism is in general difficult.

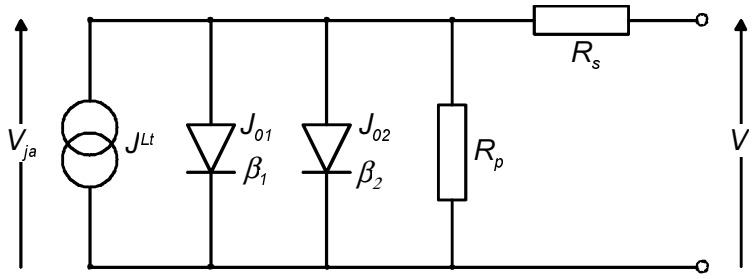

Fig. 2.7: Equivalent circuit of a solar cell described by the two-diode model, Eq. 2.116.

2.3.7 Photogeneration and quantum efficiency

In Section 2.2.5 an expression for the *I–V* curve of a *p-n* junction under illumination was derived under the assumption of a spatially homogeneous generation rate. This is rather unrealistic, since good solar cells must absorb the incident light strongly. For illumination with the solar spectrum the spatially dependent generation rate of electron-hole pairs can be calculated with respect to a wavelength-dependent absorption coefficient $\alpha(\lambda)$.

A photon of wavelength λ penetrating the surface of the solar cell is absorbed with the probability $\alpha(\lambda)$ per unit length. Each absorbed photon creates one electron-hole pair.[3] Thus the generation rate $G_\lambda(x)$ of electron-hole pairs per unit volume with respect to wavelength λ (spectral generation rate) is given by

$$G_\lambda(x) = \alpha(\lambda)\, j_\lambda(x) \tag{2.117}$$

where $j_\lambda(x)$ is the spectral photon flux at depth x. For steady-state conditions the continuity equation for photons gives

$$div\, j_\lambda = -G_\lambda(x) \tag{2.118}$$

or

$$\frac{dj_\lambda}{dx} = -\alpha(\lambda)\, j_\lambda(x)\ . \tag{2.119}$$

This leads to an exponential decay of the photon flux

[3] For photon energies exceeding twice the bandgap energy E_g it is possible to create two electron-hole pairs by impact ionisation. However, the number of photons with energies exceeding $2E_g$ can be neglected for silicon solar cells illuminated by terrestrial sunlight.

$$j_\lambda(x) = j_\lambda(0)\exp\left[-\alpha(\lambda)\,x\right]. \tag{2.120}$$

From Eq. 2.117 the spectral generation rate is found as

$$G_\lambda(x) = j_\lambda(0)\;\alpha(\lambda)\exp\left[-\alpha(\lambda)\,x\right]. \tag{2.121}$$

The total generation rate of electron-hole pairs per unit volume can be found by integrating Eq. 2.121 over wavelength

$$G(x) = \int G_\lambda(x)\;d\lambda\,. \tag{2.122}$$

The electron and hole current densities can still be calculated analytically for the generation rate expression Eq. 2.122, following the same steps as described in Section 2.2. The complete current expressions can be found in a book by Sze [24].

The normalised generation function

It is convenient to normalise the generation rate function $G_\lambda(x)$ to the incident photon flux $j_\lambda(0)$

$$g(\lambda,x) \equiv \frac{G_\lambda(x)}{j_\lambda(0)} \tag{2.123}$$

where $g(\lambda,x)$ is the normalised generation function. Using the continuity equation for photons (Eq. 2.118), $g(\lambda,x)$ can be rewritten as

$$g(\lambda,x) = -\frac{1}{j_\lambda(0)}\vec{\nabla}\vec{j}_\lambda(x)\,. \tag{2.124}$$

By calculating the generation rate of electron-hole pairs with Eq. 2.121, losses due to reflection at the front and rear cell surfaces are neglected. These losses can be calculated analytically in the case of planar cell surfaces. This will be outlined in the following in order to illustrate the concept of the normalised generation function. Fig. 2.8 shows a planar silicon wafer illuminated with light under normal incidence. The external reflectivity, the reflectivity of the rear cell surface and the internal reflectivity are denoted by R_{fe}, R_b and R_{fi}, respectively. The spectral photon flux of light travelling the n-th time from front to rear of the wafer is

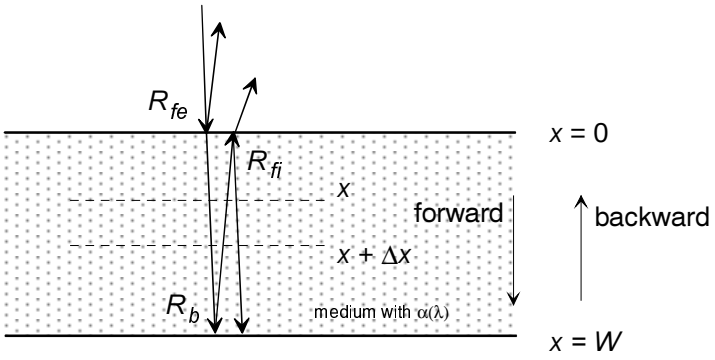

Fig. 2.8: Multiple light reflections in a planar wafer.

$$\vec{j}_{\lambda,n}^{\,forw}(x) = \vec{e}_x \, j_\lambda(0)(1-R_{fe})\, R_{fi}^m \, R_b^m \exp(-2m\alpha W)\exp(-\alpha x) \tag{2.125}$$

where W is the wafer thickness, $\vec{e}_x$ is the unit vector pointing towards the rear side and $m = n - 1$. In analogy the spectral photon flux of light passing through the wafer from rear to front the n-th time can be expressed as

$$\vec{j}_{\lambda,n}^{\,back}(x) = -\vec{e}_x \, j_\lambda(0)(1-R_{fe}) R_{fi}^m \, R_b^m \exp(-2m\alpha W) R_b \exp(-2\alpha W)\exp(\alpha x). \tag{2.126}$$

Thus, the total photon flux at position x is

$$\begin{aligned} \vec{j}_\lambda(x) &= \sum_{n=1}^{\infty}\left(\vec{j}_{\lambda,n}^{\,forw}(x) + \vec{j}_{\lambda,n}^{\,back}(x)\right) \\ &= \vec{e}_x \, j_\lambda(0)(1-R_{fe})\left[\exp(-\alpha x) - R_b \exp(\alpha(x-2W))\right]\sum_{m=0}^{\infty} R_{fi}^m \, R_b^m \exp(-2m\alpha W). \end{aligned} \tag{2.127}$$

The geometric series in Eq. 2.127 converges because $\left|R_{fi} \, R_b \exp(-2\alpha W)\right| < 1$ and therefore

$$\vec{j}_\lambda(x) = \vec{e}_x \, j_\lambda(0)(1-R_{fe})\frac{\exp(-\alpha x) - R_b \exp(\alpha(x-2W))}{1 - R_{fi} \, R_b \exp(-2\alpha W)}. \tag{2.128}$$

From Eq. 2.124 the normalised generation function of a planar solar cell is found as

$$\begin{aligned} g(\lambda, x) &= -\frac{1}{j_\lambda(0)}\left(\vec{e}_x \frac{d}{dx}\right)\vec{j}_\lambda(x) \\ &= (1-R_{fe})\,\alpha \frac{\exp(-\alpha x) + R_b \exp(\alpha(x-2W))}{1 - R_{fi} R_b \exp(-2\alpha W)} \end{aligned} \tag{2.129}$$

where R_{fe}, R_b, R_{fi} and α are in general functions of wavelength.

The normalised generation function describes the absorption properties of the solar cell. Important solar cell device characteristics can be derived from $g(\lambda,x)$ by integration above the cell depth and/or the incident photon flux $j_\lambda(0)$. These characteristics are summarised in Tab. 2.1.

Solar cell characteristic	Units	Explanation
$G(x)=\int d\lambda\, j_\lambda(0)\, g(\lambda,x)$ (2.130)	$\frac{1}{s\,cm^3}$	Generation rate function used for electrical device simulation
$f_{abs}(\lambda)=\int d\xi\, g(\lambda,\xi)$ (2.131)	dimension-less	Spectral dependent fraction of light absorbed in silicon, that is, the maximum achievable external quantum efficiency (recombination neglected)
$J_{sc,\max}=q\int d\lambda\int d\xi\, j_\lambda(0)\, g(\lambda,\xi)$ (2.132)	$\frac{mA}{cm^2}$	Maximum achievable short circuit current density (recombination neglected)

Tab. 2.1: Important solar cell characteristics derived from the normalised generation function *g(λ,x)*.

Quantum efficiency and differential spectral response

The *spectral response* of a solar cell is defined as

$$s(\lambda)=\frac{J_{sc}(\lambda)}{E(\lambda)} \tag{2.133}$$

where $J_{sc}(\lambda)$ is the short circuit current density of the cell illuminated with irradiance $E(\lambda)$.

The *quantum efficiency* $\eta_{QE}(\lambda)$ is defined as

$$\eta_{QE}(\lambda)=\frac{n_q(\lambda)}{n_{ph}(\lambda)} \tag{2.134}$$

where $n_q(\lambda)$ equals the rate of charge carriers collected at the cell terminals under short circuit conditions and $n_{ph}(\lambda)$ is the photon rate illuminating the cell. Therefore, spectral response and quantum efficiency are related by

$$\eta_{QE}(\lambda)=\frac{J_{sc}(\lambda)/q}{E(\lambda)/h\nu}=s(\lambda)\frac{hc}{q\lambda}. \tag{2.135}$$

In other words, the quantum efficiency is the probability that charge carriers are generated and collected at the cell terminals if the cell is illuminated with photons of wavelength λ. If

both incidences, charge carrier generation and collection of a generated electron-hole pair, are independent events[4], the quantum efficiency can be expressed as

$$\eta_{QE}(\lambda) = f_{abs}(\lambda)\,\eta_c(\lambda) \tag{2.136}$$

where $f_{abs}(\lambda)$ is the spectral dependent fraction of light absorbed in the cell (Eq. 2.131) and η_c is the carrier collection efficiency [27].

The *differential spectral response* [28] is the derivative of the short circuit current density with respect to irradiance

$$\tilde{s}(\lambda) = \left.\frac{dJ(\lambda)}{dE(\lambda)}\right|_E . \tag{2.137}$$

Here, $\tilde{s}(\lambda)$ is determined at operating conditions given by illumination with irradiance *E*. The differential spectral response equals the (absolute) spectral response if the superposition principle (Section 2.2.3) is fulfilled. High-efficiency silicon solar cells can exhibit strong current-irradiance non-linearities, as can be seen in Fig. 7.9.

A numerical method of simulating the differential spectral response is developed in this thesis, and is discussed in Section 3.5.

2.3.8 External reflection

The total external reflection of a planar silicon solar cell, including escape reflectance, can be calculated analytically by considering multiple light reflections, as plotted in Fig. 2.8. In analogy to the derivation of the normalised generation function in Section 2.3.7, a geometric series is obtained where each addend represents internally trapped light which is coupled out of the wafer. The resulting expression for the external reflection is

$$R_{ext}^{nm} = R_{fe} + \frac{T_{fe}\,T_{fi}\,R_b \exp\left(-2\,\alpha\,W\right)}{1 - R_b\,R_{fi} \exp\left(-2\,\alpha\,W\right)} \tag{2.138}$$

where $R_{fe}(\lambda)$ is the external reflection of the front surface, $T_{fe}(\lambda)$ is the transmission through the front surface, R_b is the rear surface reflection, and $R_{fi}(\lambda)$ is the internal front surface reflection. Equation 2. is plotted in Fig. 2.9, assuming a double layer antireflection coating on the front surface and $R_b = 0.72$. In order to compare the calculation with a reflection measurement, the reflection of the metal grid has to be accounted for

$$R_{ext}(\lambda) = A_{metal}\,R_{metal} + (1 - A_{metal})\,R_{ext}^{nm}(\lambda) . \tag{2.139}$$

[4] For light with wavelength λ>1130 nm, free carrier absorption in silicon enhances the absorption coefficient [25], [26]. In this case Eq. 2. is only a rough approximation because light absorption and carrier collection are not independent of each other.

It is assumed that an area fraction of A_{metal} = 0.06 is covered by the metal grid and the metal reflection is R_{metal} = 0.95 for the case plotted in Fig. 2.9.

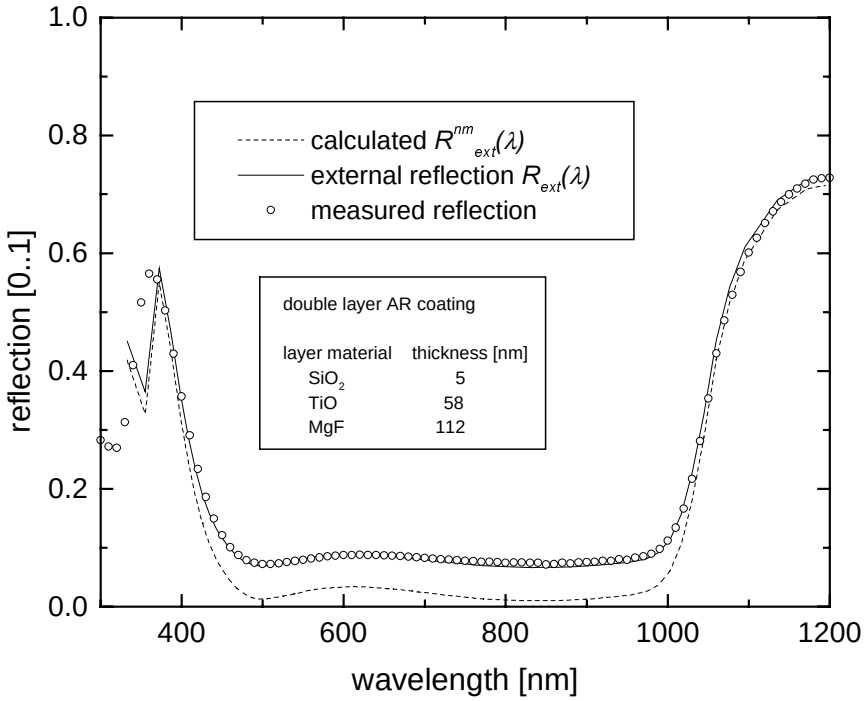

Fig. 2.9: External reflection of a solar cell with a double layer antireflection coating on the front. The analytically calculated reflection coincides with the measurement if it is corrected by the reflectivity of the metal grid.

2.3.9 Accounting for doping profiles

The dopant concentrations were assumed to be constant through the *n*- and *p*-type regions, but this is an oversimplification.

The emitter of a silicon solar cell has a spatially dependent donor profile since it is manufactured by diffusion of phosphorous atoms into a *p*- (boron) doped wafer. This donor profile can often be approximated by an error or Gaussian function.

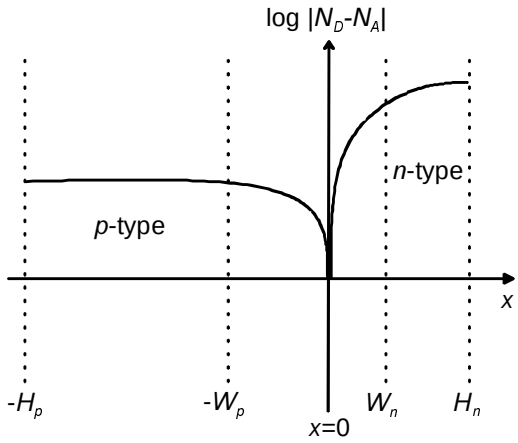

Fig. 2.10: Schematic doping profile of a solar cell with an *n*-type emitter diffused into a *p*-doped substrate.

Where the dopant concentration varies with depth *x*, the assumption of a constant mobility (Section 2.2) is not in general justified. For example, ionised impurities in the semiconductor cause carrier scattering, which significantly affects the mobility. In more heavily doped regions of the semiconductor the average time between collisions of the charge carriers with ionised impurity atoms decreases and thus the mobility decreases. Additionally, the Auger lifetime in emitters with a non-uniform doping profile becomes position-dependent due to Eq. 2.108.

An analytical approach to the calculation of the emitter saturation current density in semiconductors with position-dependent doping profiles has been given by Park *et al*. [29]. Consider a *p*-*n* junction formed by diffusing *n*-type impurities of concentration $N_D(x)$ into a uniform *p*-type substrate, as illustrated in Fig. 2.10.

To find the emitter saturation current density, the hole recombination current density in the *n*-QNR is calculated. Using Eqs. 2.5 and 2.54, the hole continuity equation for dark conditions can be written as

$$\frac{dJ_h}{dx} = -q\,r_h(x) = -\,q\,\frac{p(x)-p_0(x)}{\tau_h(x)}\,. \tag{2.140}$$

At thermal equilibrium the hole drift current and hole diffusion current balance. Thus, a quasi-electric field for the diffusion component can be expressed as

$$\mathcal{E} = \frac{kT}{q}\frac{d}{dx}\ln(N_D(x))\,. \tag{2.141}$$

Substituting this *hole quasi-field* into Eq. 2.3 gives

$$J_h(x) = -q\,D_h(x)\left[p\frac{d}{dx}\{\ln N_D(x)\} + \frac{dp}{dx}\right]. \tag{2.142}$$

The first term on the right side of Eq. 2. is the drift current and the second term is the diffusion current. Note that the effective diffusion constant $D_h(x)$ of the holes is now position-dependent

$$D_h(x) = \frac{kT}{q}\mu_h(N_D(x))\,. \tag{2.143}$$

The boundary condition for the hole concentration at the edge of the space-charge region is given by Eq. 2.52. The boundary condition for the recombination of holes at the emitter surface at $x = H_n$ is

$$J_h(H_n) = q\,S_h\left(p - p_0\right)\Big|_{x=H_n} \approx q\,S_h\,p\Big|_{x=H_n}. \tag{2.144}$$

Integrating Eqs. 2. and 2. from W_n to x gives

$$p'(x) = p_0(x)\left[1 - \frac{1}{q}\int_{W_n}^{x} dx'\frac{1}{D_h(x')p_0(x')}J'(x')\right] \tag{2.145}$$

and

$$J'(x) = J'(W_n) - q\int_{W_n}^{x}\frac{p'(x')}{\tau_h(x')}dx' \tag{2.146}$$

where $J'(x)$ and $p'(x)$ are the normalised hole current and hole density expressions

$$J'(x) = \frac{J_h(x)}{\exp(qV_{ja}/kT) - 1} \tag{2.147}$$

$$p'(x) = \frac{p - p_0(x)}{\exp(qV_{ja}/kT) - 1} \; . \tag{2.148}$$

The second term on the right hand side of Eq. 2. contains the current flow in the emitter region, which causes the hole concentration to differ from the local equilibrium value $p_o(x)$. Substituting the hole current density expression Eq. 2. into Eq. 2. gives an integral equation for the hole density. Successive substitution of Eqs. 2. and 2. into each other yields an iterative scheme for the calculation of the hole carrier distribution. Depending on the number of iteration steps, different approximation orders for $p'(x)$ can be gained. The innermost integral of the approximation is taken over the equilibrium hole carrier distribution, which can be found from Eqs. 2.45 and 2.104 as

$$p_0(x) = \frac{n_i^2}{N_D(x)} \; . \tag{2.149}$$

The *emitter* saturation current density J_{oe} is composed of the surface and bulk components

$$J_{0e} = J'(W_n) = J'(H_n) + J'_{bulk} \; . \tag{2.150}$$

Using Eq. 2. and the calculated hole density $p'(x)$ leads to

$$J_{0e} = q\,S_h\,p'(H_n) + q\int_{W_n}^{H_n} \frac{p'(x)}{\tau_h(x)}\,dx \; . \tag{2.151}$$

The integral in Eq. 2. is taken over the volume recombination rate in the quasineutral emitter region and represents the recombination current in this region. Here the minority carrier lifetime $\tau_h(x)$ is given by Eq. 2.109.

Equation 2. can be solved for different combinations of surface recombination velocities S_h and doping profiles $N_D(x)$ as demonstrated by King *et al.* [30]. From the emitter saturation current density a maximum open-circuit voltage can be obtained by applying Eq. 2.101.

The surface recombination velocity S_h depends on processing conditions. For high S_h a low minority carrier concentration at the surface $p(H_n)$ is advantageous. This can be achieved with a heavily doped emitter so that the first term in Eq. 2. is minimised. Fig. 2.11b shows an example for an unpassivated emitter surface with $S_h = 10^6$ cm s^{-1} (Preu *et al.*, [31]). The highest open-circuit voltage is found for a deep doping profile with a high peak doping concentration. Here, gaussian-shaped doping profiles were assumed.

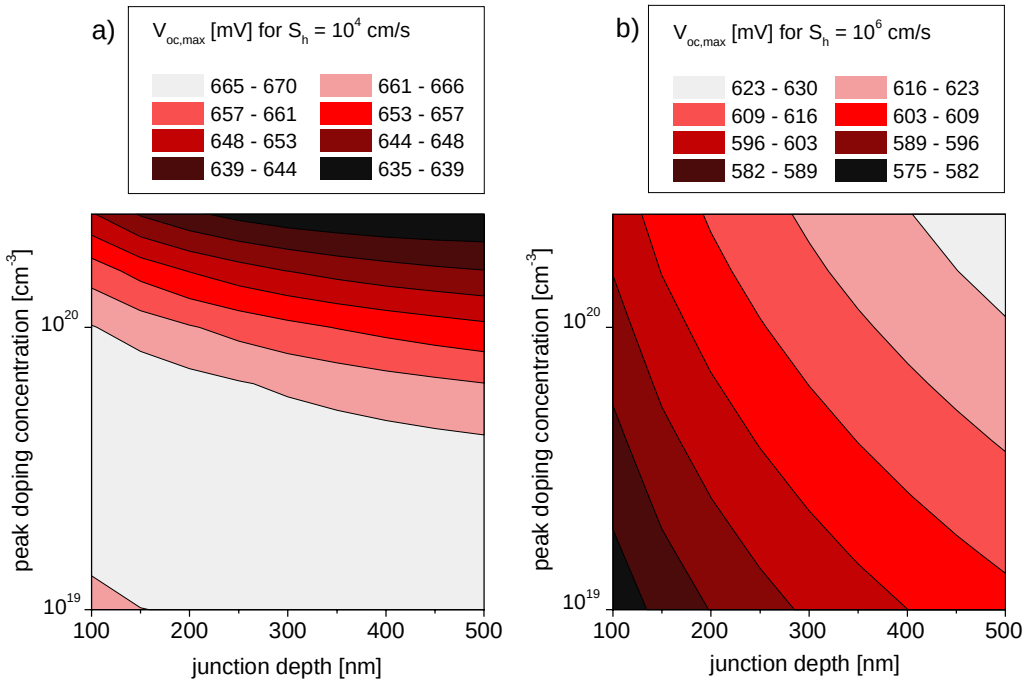

Fig. 2.11: Maximum achievable open-circuit voltages for emitters with different Gaussian doping profile shapes. The graphs were calculated with the Park model discussed in this section. (a) Surface recombination velocity $S_h = 10^4$ cm s^{-1}; (b) $S_h = 10^6$ cm s^{-1}.

The second term in Eq. 2. represents the bulk recombination contribution to the emitter saturation current density. Varying an emitter profile, an optimum profile is found if an increase in the bulk recombination contribution balances the decrease of the surface recombination component. An example can be found in Fig. 2.11a for a surface recombination velocity of $S_h = 10^4$ cm s^{-1}. In this case, optimum open circuit voltages are found for peak doping concentrations around 5×10^{19} cm^{-3}.

More detailed models require numerical calculations, as described in the next chapter.

3 Numerical solar cell modelling

Up till now, the solar cell has been treated analytically in one dimension. In practice more sophisticated numerical models must be used to describe a 'real' solar cell and to allow for a quantitative comparison of simulation results with solar cell measurements. More accurate models require two- or three-dimensional solar cell simulations, particularly with regard to the lateral current density flow, which may be substantial, to describe most of the high efficiency solar cell structures.

3.1 Previous work on multidimensional solar cell modelling

Numerical simulation techniques have been extensively used to quantify optical and electrical losses for many solar cell structures. Aberle *et al.* [32] presented a numerical optimisation study of high-efficiency silicon solar cells with rear point-contact patterns. This cell type shows low minority carrier recombination losses at the rear surface due to the small rear-surface metallisation fraction. This 2D parameter study took lateral current components due to the point contacts into account.

Recombination losses at the cell perimeter of solar cells which either stay embedded in the wafer or are sawn from the wafer can also be described using numerical methods, as described in this chapter (Altermatt *et al.*, [33]).

Distributed resistive losses in the semiconductor material and in the front metal grid of high-efficiency silicon solar cells have been investigated using a combination of device simulation and circuit simulation. Such a combination allows the simulation of complete solar cells, instead of the usually restricted simulation domain, which is kept to a geometrically irreducible minimum. With the inclusion of the whole device domain, the predictions became so precise as to contribute significantly to an increase in the world record efficiency of silicon solar cells (Altermatt *et al.,* [34]).

Optical and electrical losses of silicon-on-insulator thin-film solar cells with interdigitated front contacts are analysed in Chapter 6. These cells have two- and three-dimensional current flow patterns as well as a textured front surface for light trapping. Their performance was modelled by a combination of 3D optical ray tracing with 2D electrical device simulation.

Using ray tracing programs, the spatially dependent photogeneration rate of cells with textured surfaces can be calculated numerically (Section 3.4.3). For example, mechanically textured silicon solar cells were investigated by Zechner *et al.* by means of ray-tracing simulation [35].

Another solar cell structure with pronounced lateral current flow is the rear-contact cell of Swanson [36]. As both the emitter and the base of this cell are contacted at the back side,

there are no front-surface shading losses. Furthermore, this cell type allows for simplified module assembly because of the single-sided metallisation. The numerical simulation of rear-contacted silicon cells is discussed in detail in Chapter 7.

To describe current transport in metal–insulator–semiconductor silicon solar cells, a quantum mechanical model describing the tunnelling of charge carriers through the tunnel insulator of the metal-insulator contact is needed. The resulting set of equations cannot be solved analytically without making severe simplifying assumptions. A detailed numerical model utilising two-dimensional device simulation and circuit simulation was presented by Kuhlmann *et al.* [37].

3.2 Solving the semiconductor device equations numerically

For the numerical calculation of solar cell performance, the device equations 2.1, 2.6 and 2.7 are solved at discrete mesh-points in space. A comprehensive treatment of discretisation methods for semiconductor device simulation can be found in Selberherr [38]. In order to solve the Poisson equation plus the electron and hole continuity equations numerically, the box scheme as described by Bürgler [39] and Heiser [40] is discussed. The device volume is discretised. In other words, a symmetry element of the device is divided into boxes.

Fig. 7.3 shows an example of the discretisation of a symmetry element for a rear contact cell. A simple discretisation mesh can be constructed of rectangular boxes. However, a more efficient approach which is computationally less expensive is to use triangular boxes. Such triangular boxes can be seen around the enlarged *n*-contact in Fig. 7.3. A single box Ω_i of this two-dimensional discretisation mesh for one node *i* (mesh-point) of the symmetry element is shown in Fig. 3.1. The boxes must be constructed such as to cover the whole symmetry element. Therefore, box boundaries (dashed lines) are chosen that are the perpendicular bisectors of the lines between neighbouring nodes.

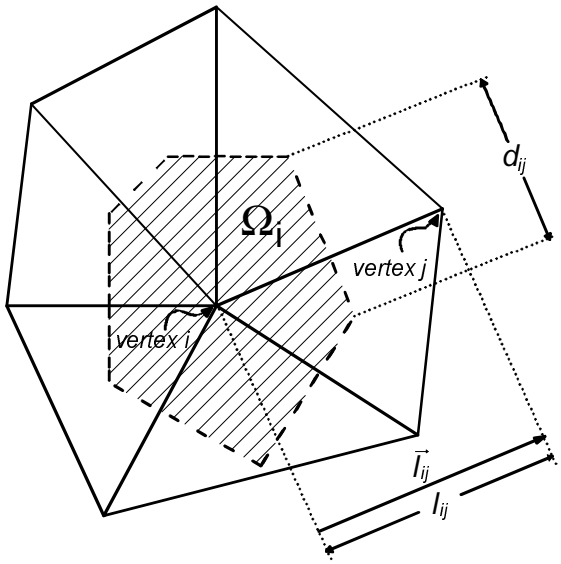

Fig. 3.1: The graph shows part of a discretisation mesh for the electrical device simulation; solid lines are drawn between neighbouring mesh-points. The shaded area represents the volume Ω_i of a single box for a triangular discretisation mesh in two dimensions.

We shall now continue by deriving the discretised form of the Poisson equation (Eq. 2.1). In this derivation, the fact that an electrostatic electric field $\mathcal{E}$ is a conservative field is vital.[5]

More generally, the partial differential equations treated here can be stated in a conservation law

$$\nabla\vec{\Gamma}(\vec{x}) = \Lambda(\vec{x}) \tag{3.1}$$

where $\vec{\Gamma}(\vec{x})$ is a vector field and $\Lambda(\vec{x})$ is a position-dependent scalar field. To obtain an equation for vertex *i*, Eq. 3.1 is integrated over the volume of box Ω_i using Gauss's theorem

$$\int_{\Omega_i} \left[\nabla\vec{\Gamma}(\vec{x}) - \Lambda(\vec{x})\right] dV = \int_{\partial\Omega_i} \vec{\Gamma}(\vec{x})\, d\vec{n}(\vec{x}) - \int_{\Omega_i} \Lambda(\vec{x})\, dV = 0\,. \tag{3.2}$$

The first term on the right hand side of Eq. 3.2 is integrated over the boundary $\partial\Omega_i$ of the box, *i.e.* $\vec{n}(\vec{x})$ denotes the normal vector of the box boundary. The discretised form of Eq. 3.2 can be written as

$$\sum_{j\neq i} \Gamma_{ij}\, d_{ij} - \Lambda_i\, V_i = 0 \tag{3.3}$$

where Γ_{ij} is the projection of the vector field $\vec{\Gamma}(\vec{x})$ onto the edge $\vec{l}_{ij}$ from node *i* to node *j* (Fig. 3.1). Here d_{ij} denotes the length of the perpendicular bisector on this edge. Λ_i is the value of the scalar field $\Lambda(\vec{x})$ at node *i.* In two dimensions V_i is the area of box Ω_i, in three dimensions it is the box volume. The sum in Eq. 3.3 extends over all nodes *j* that neighbour node *i*. Applying Eq. 3.3 to the Poisson equation 2.1 yields

$$\sum_{j\neq i} \mathcal{E}_{ij}\, d_{ij} - \rho_i\, V_i = 0\,. \tag{3.4}$$

The electric field $\mathcal{E}$ in Eq. 3.4 can be expressed as the differential quotient $\mathcal{E}_{ij} = -(\phi_i - \phi_j)/l_{ij}$, thus

$$F_i^{\phi} \equiv -\sum_{j\neq i} \frac{d_{ij}}{l_{ij}} \phi_{ij} \; - V_i\,(p_i - n_i + N_i) = 0 \tag{3.5}$$

where $\phi_{ij} = \phi_i - \phi_j$ is the potential difference along $\vec{l}_{ij}$.

A thorough derivation of the discretised electron and hole continuity equations 2.4 and 2.5 is given in a thesis by Heiser [40]. The discretised continuity equations are

---

[5] This means that Gauss's theorem is valid, and the surface integral of $\mathcal{E}$ over a closed surface is equal to the volume integral over the total amount of charges enclosed by the surface.

$$F_i^n \equiv -\sum_{j \neq i} \frac{d_{ij}}{l_{ij}} \mu_{ij}^n \left[n_j \, B(\phi_{ji}) - n_i \, B(\phi_{ij}) \right] + V_i \left(r_i - G_i \right) = 0 \tag{3.6}$$

$$F_i^p \equiv -\sum_{j \neq i} \frac{d_{ij}}{l_{ij}} \mu_{ij}^p \left[p_j \, B(\phi_{ij}) - p_i \, B(\phi_{ji}) \right] + V_i \left(r_i - G_i \right) = 0 \tag{3.7}$$

where B is the Bernoulli function

$$B(x) = \frac{x}{\exp(x) - 1} \; . \tag{3.8}$$

The mobility is denoted as μ_{ij}, and is assumed to be constant on the box edge perpendicular to $\vec{l}_{ij}$.

To solve the discretised differential equations 3.5–3.7 by computer, the physical entities have to be scaled. For example, carrier concentrations are scaled by the intrinsic carrier concentration, the electrostatic potential ϕ is scaled by the thermal voltage V_{th}, and the electric field is scaled by V_{th}/L_D, where L_D is the Debye length (Eq. 2.18). This scaling is essential for the numerical calculation because the potential typically varies by one or two orders of magnitude whereas the carrier densities vary over ten to twenty orders of magnitude.

Eqs. 3.5–3.7 give rise to $3N$ partial differential equations from the N nodes of the discretisation mesh. These have solution variables ϕ, n and p. These differential equations can be abbreviated as

$$\begin{aligned} F_i^{\phi}(\phi, n, p) &= 0 \\ F_i^{n}(\phi, n, p) &= 0 \\ F_i^{p}(\phi, n, p) &= 0 \end{aligned} \; . \tag{3.9}$$

These equations can be solved by the Newton method. Given the non-linear system of equations 3.9 written as

$$\vec{F}(\vec{z}) = 0 \tag{3.10}$$

the Newton procedure iteratively computes a new solution

$$z_i^{k+1} = z_i^k + \delta s^k z_i^k \tag{3.11}$$

from the old one z^k. The update $\delta s^k \; z^k$ is found as the solution of the equation

$$\sum_j \frac{\partial F_i(\vec{z}^{\,k})}{\partial z_j^k} \delta s^k z_j^k = -F_i(\vec{z}^{\,k}) \; . \tag{3.12}$$

To achieve numerical convergence of the Newton iteration, a damping factor $0 < s^k \leq 1$, determined in each iteration step from the last successful one, is used in Eq. 3.12.

Equations 3.3–3.12 can be stated for one, two and three dimensions as discussed in ISE-TCAD [41]. An example of the one-dimensional solution of Eq. 3.10 is given in the next section, and applications for the two-dimensional case are treated in Chapters 6 and 7.

In modern device simulators, different solution methods can be chosen. It is possible to solve all *3N* partial differential equations 3.10 together ('coupled solution'). Another method with less demand on memory and faster convergence for low and intermediate injection conditions is the 'plug-in method': First the *N* Poisson equations $F_i^{\phi}(\phi, n, p) = 0$ are solved. The resulting potential $\phi(\vec{x}_i)$ is inserted into the electron continuity equations $F_i^{n}(\phi, n, p) = 0$, and iteration by the Newton method then yields a new electron density distribution $n(\vec{x}_i)$. Both $\phi(\vec{x}_i)$ and $n(\vec{x}_i)$ are then used to solve the hole continuity equation $F_i^{p}(\phi, n, p) = 0$.

3.3 Comparison of numerical and analytical solution

As an example of how Eq. 3.10 may be solved numerically, a *p-n* junction solar cell with diffused doping profiles will be modelled in one dimension. The cell model is shown in Fig. 3.2. The base material consists of homogeneously doped *p*-type silicon of 250 µm thickness. In order to reduce the surface recombination velocity at the rear surface a back-surface field was built into the cell. The doping profiles for the emitter and the back surface field are of Gaussian form (Fig. 3.2b).

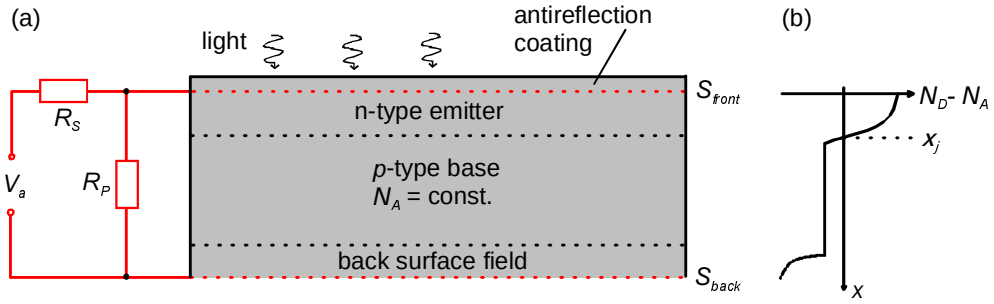

Fig. 3.2: A one-dimensional model of a planar silicon solar cell with Gaussian doping profiles: (a) A back surface field and the series and shunt resistances are accounted for; (b) doping density distribution. For this simulation a doping profile of Gaussian shape with a peak doping density of 5×10^{18} cm^{-3} and a junction depth of 1.4 µm was assumed. The base diffusion length was taken as L_b = 350 µm and the cell thickness as 250 µm; the surface recombination velocity was set to S = 800 cm s^{-1} at the front and $S = 10^6$ cm s^{-1} at the rear. The calculated solar cell output parameters are i_{sc} = 37.6 mA cm^{-2}, V_{oc} = 626 mV, η_{fill} = 73 % and a conversion efficiency of η = *17.2 %*. One-Sun (AM 1.5) illumination was assumed.

Most of the restrictions of the analytical models can be overcome by solving the transport equations numerically. The doping dependence of charge carrier mobility, mentioned in Section 2.3.9, and band gap narrowing in heavily doped regions of the cell, arising from many-body interactions of the charge carriers, can both be incorporated (Chapter 5). Moreover, the coupled set of differential equations 3.10 can be solved for intermediate- and high-injection conditions, whereas for low-injection conditions only analytical solutions can be found.

The simulations presented in this section were performed with the program PC1D, which is commonly used for one-dimensional solar cell simulations ([42]; [43]; [44]).

Fig. 3.3 shows the simulated space-charge density, the electric field and the inner potential across the *p-n* junction for this particular cell. The curves were calculated for three terminal voltages: $V = 0$, $V = V_{mpp}$, and $V = V_{oc}$. Note the difference between the results shown in Fig. 2.2 and Fig. 3.3. The numerically simulated space-charge density distribution is smooth in comparison to the sharp analytical case. The highest space-charge density is found for short-circuit conditions. Applying a forward bias to the *p-n* junction injects carriers into the depletion region and reduces the space-charge density.

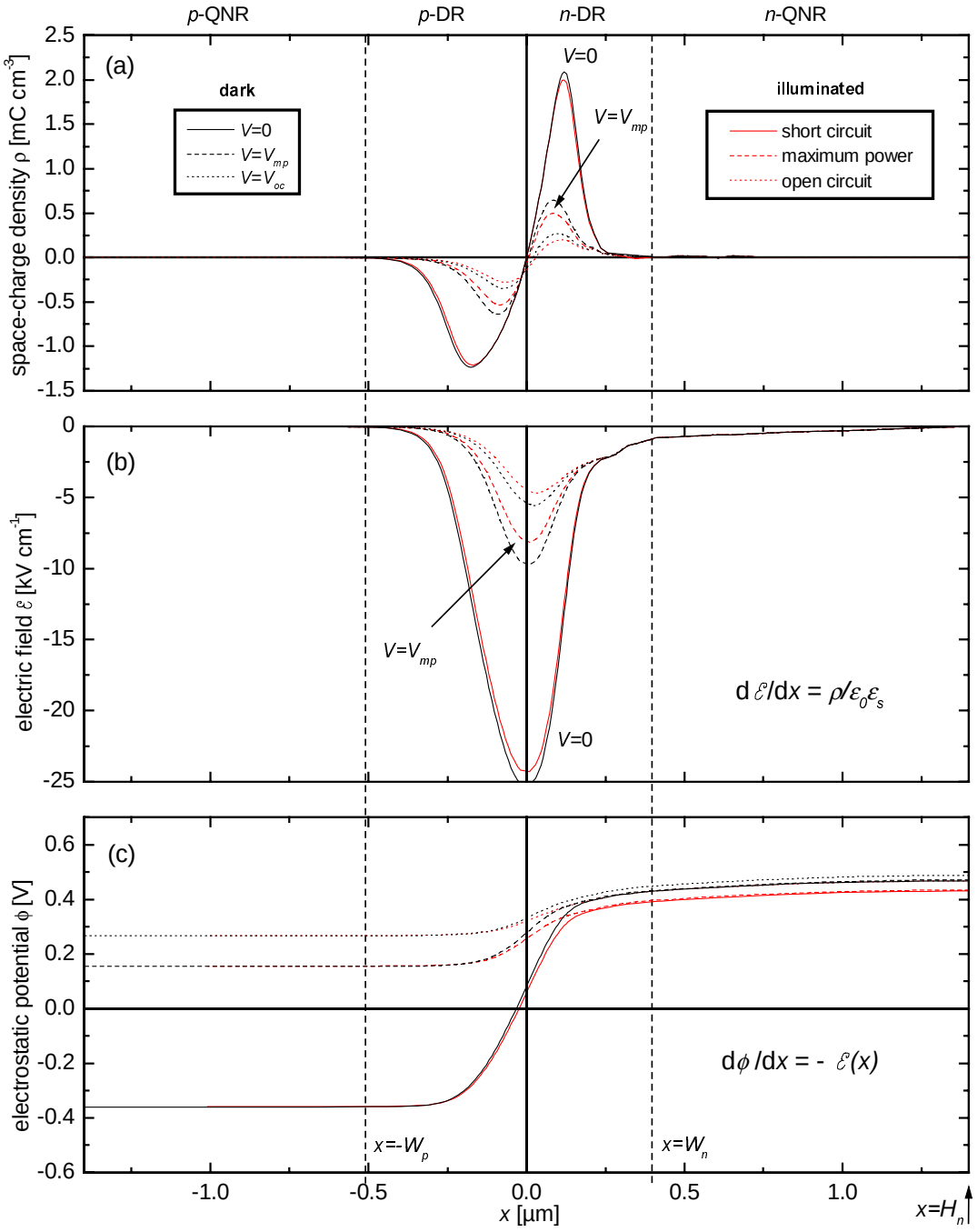

Fig. 3.3: (a) Space-charge density $\rho(x)$; (b) electric field $\varepsilon(x)$; (c) inner potential $\phi(x)$ across the *p-n* junction of the sample cell drawn in Fig. 3.1. Compare with the idealised Schottky exhaustion layer case shown in Fig. 2.2.

The electric field in the space-charge region is also reduced by forward bias, as shown in Fig. 3.3b. In contrast with the abrupt-doping case, the electric field does not vanish in the *n*-type quasineutral region. The net force on an electron is given by

$$F_e = q\,\mathcal{E}(x) + kT\,\frac{d[\ln n(x)]}{dx} \tag{3.13}$$

where the first term of Eq. 3.13 is the drift force and the second term is the diffusive force. For equilibrium conditions the net force on an electron is zero. Substituting the Gaussian doping profile with the electron density *n*(x)

$$N_D(x) = N_D(H_n)\exp\left[-\frac{(x-H_n)^2}{2\sigma^2}\right] \tag{3.14}$$

where σ is the standard deviation and setting $F_e = 0$ yields

$$\mathcal{E}(x) = V_{th}\,\frac{x-H_n}{\sigma^2}\ . \tag{3.15}$$

Thus, a doping gradient of Gaussian shape produces the linear dependence of the electric field on position shown in the *n*-QNR of Fig. 3.3b.

Fig. 3.4 shows the numerically calculated band-edge energies, quasi-Fermi potentials, carrier densities and current densities for short-circuit conditions. Cell parameters are listed in the caption in Fig. 3.2. The equilibrium carrier densities shown as black curves in Fig. 3.5b can be compared with Fig. 2.3. Again, the electron majority concentration in the quasineutral region is given by the doping profile. The small electron minority concentration gradient in the *p*-type quasineutral region is due to the long diffusion length of $L_b = 350$ µm (see Eq. 2.63), which is greater than the cell thickness of 250 µm. This is typical for high-performance c-Si cells.

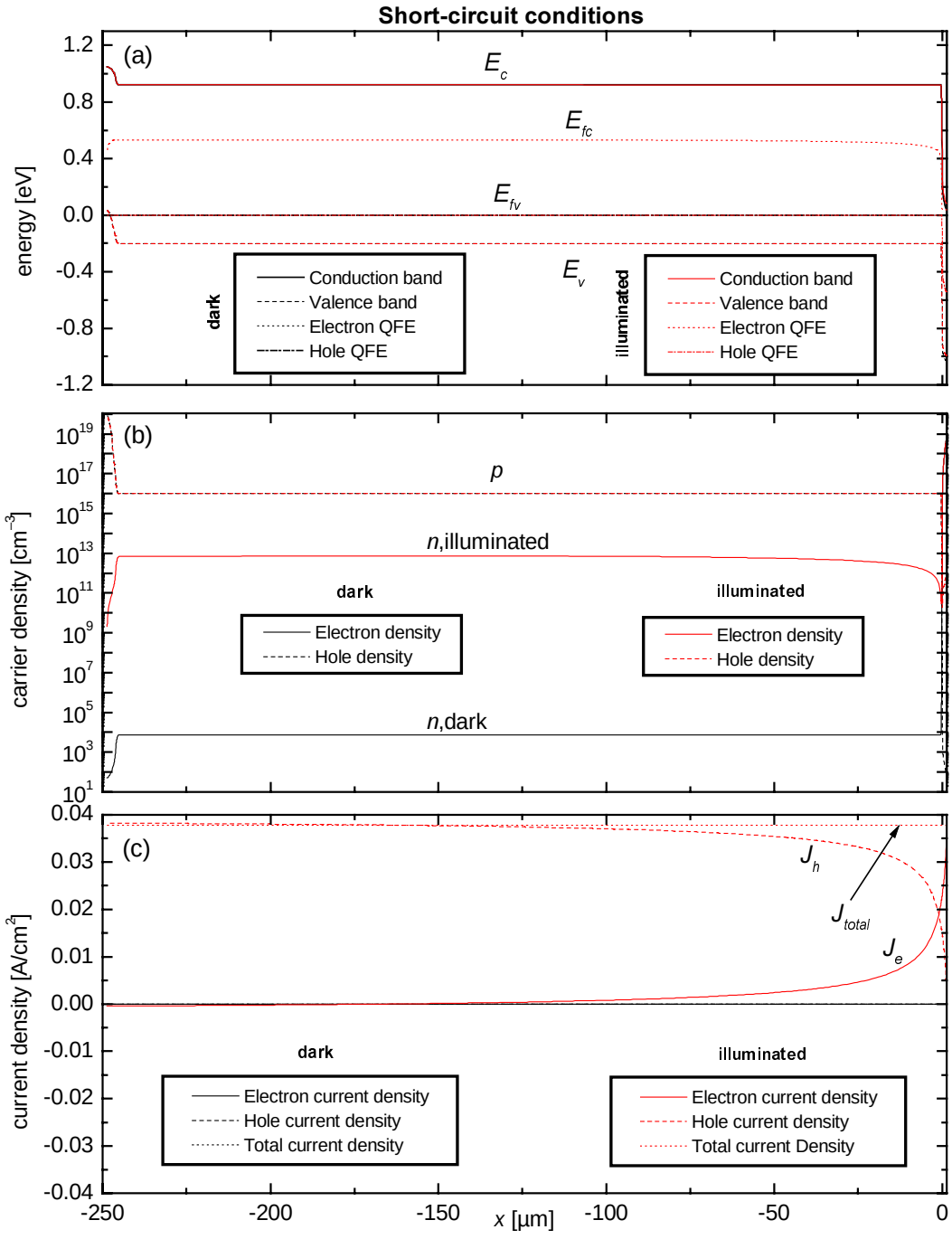

Fig. 3.4: A cut through the whole cell for short–circuit conditions. The black curves are calculated for dark conditions, the red curves for illuminated conditions. (a) Band-edge energies and quasi-Fermi energies (QFE); (b) electron density and hole density; (c) electron current density, hole current density and total current density.

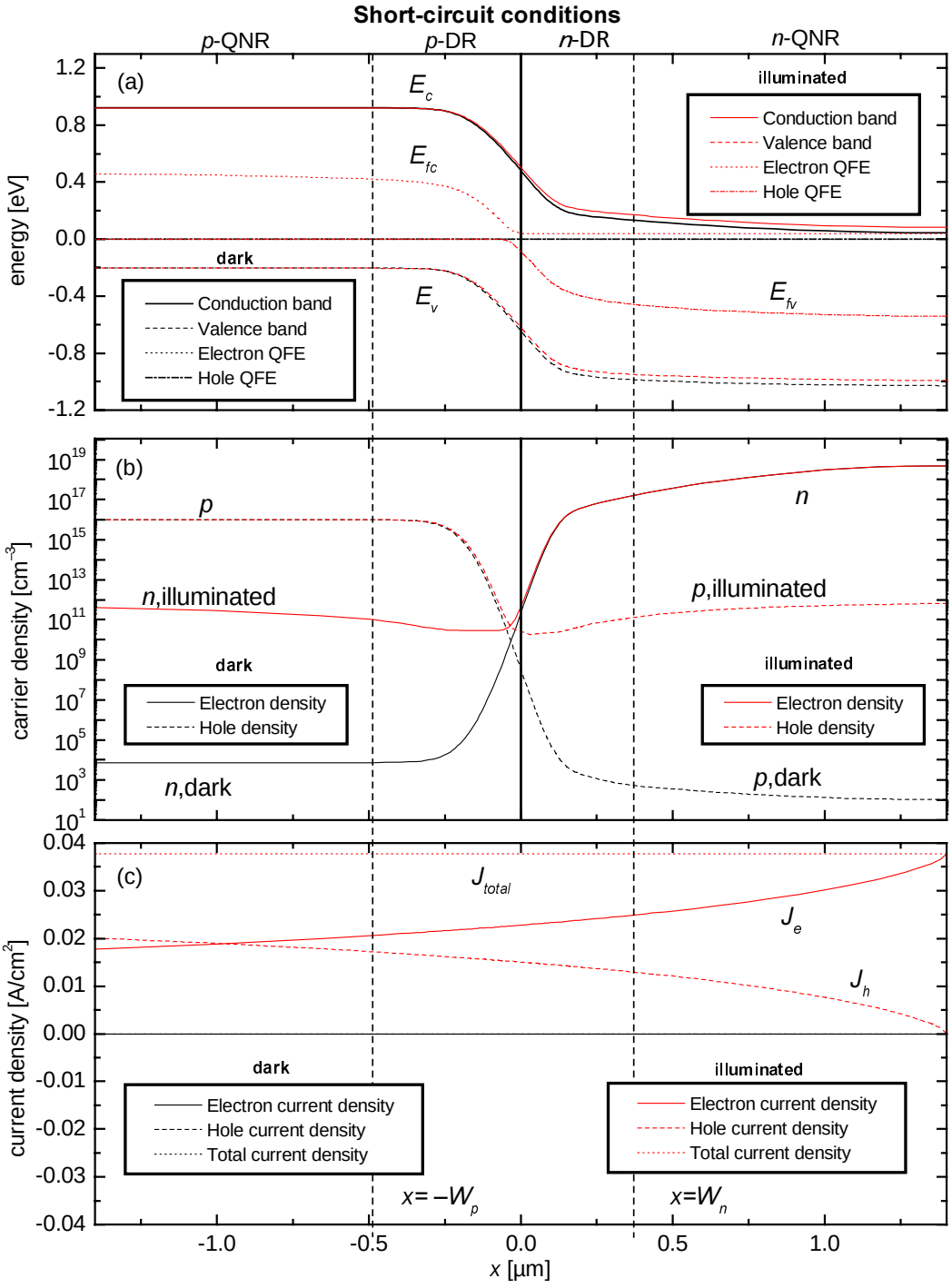

Fig. 3.5: Enlargement of the emitter region for short–circuit conditions.

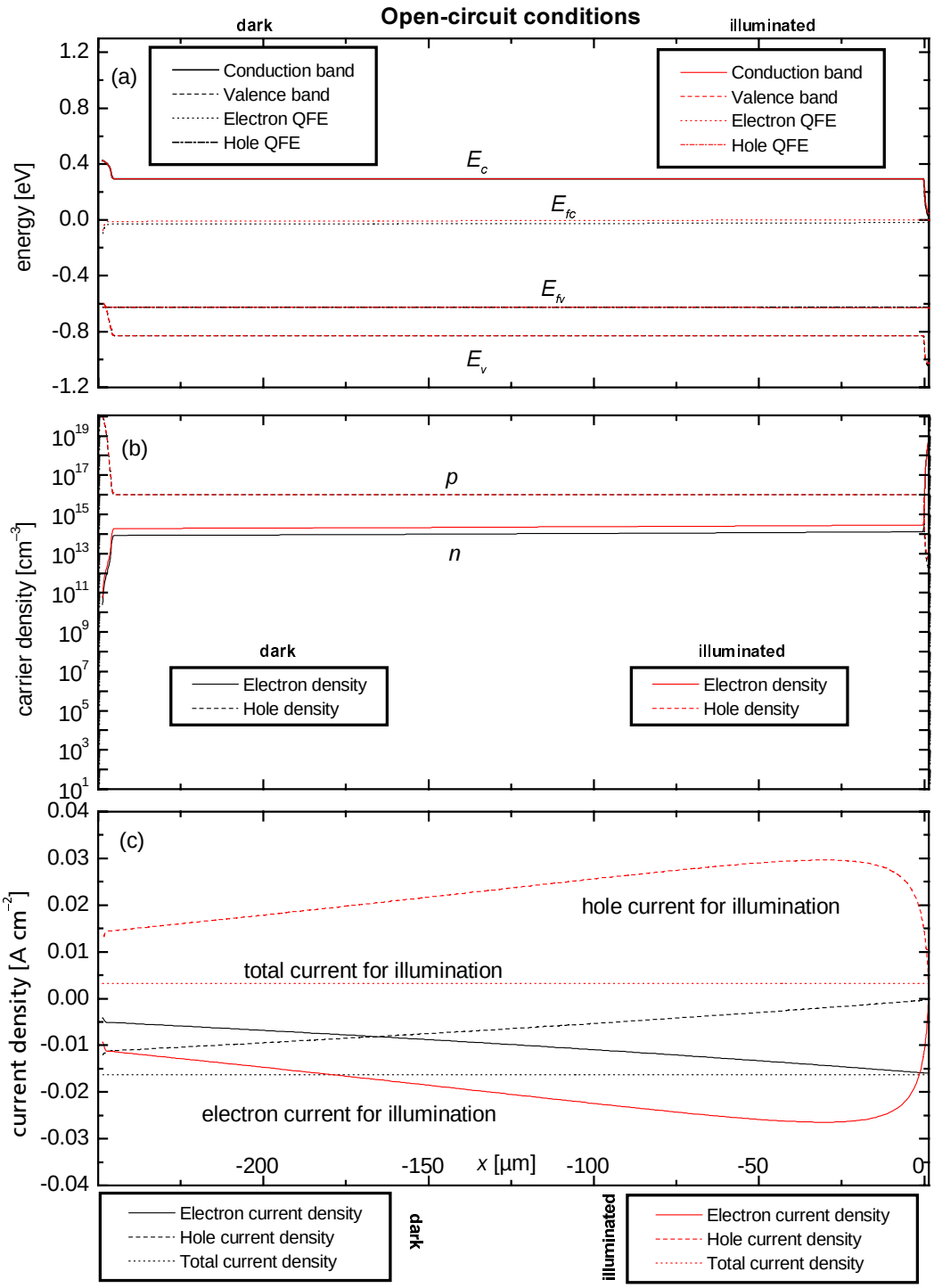

Fig. 3.6: A cut through the whole cell is drawn for open-circuit conditions ($V = V_{oc}$). The black curves are calculated for an applied voltage equal to V_{oc} of the illuminated cell.

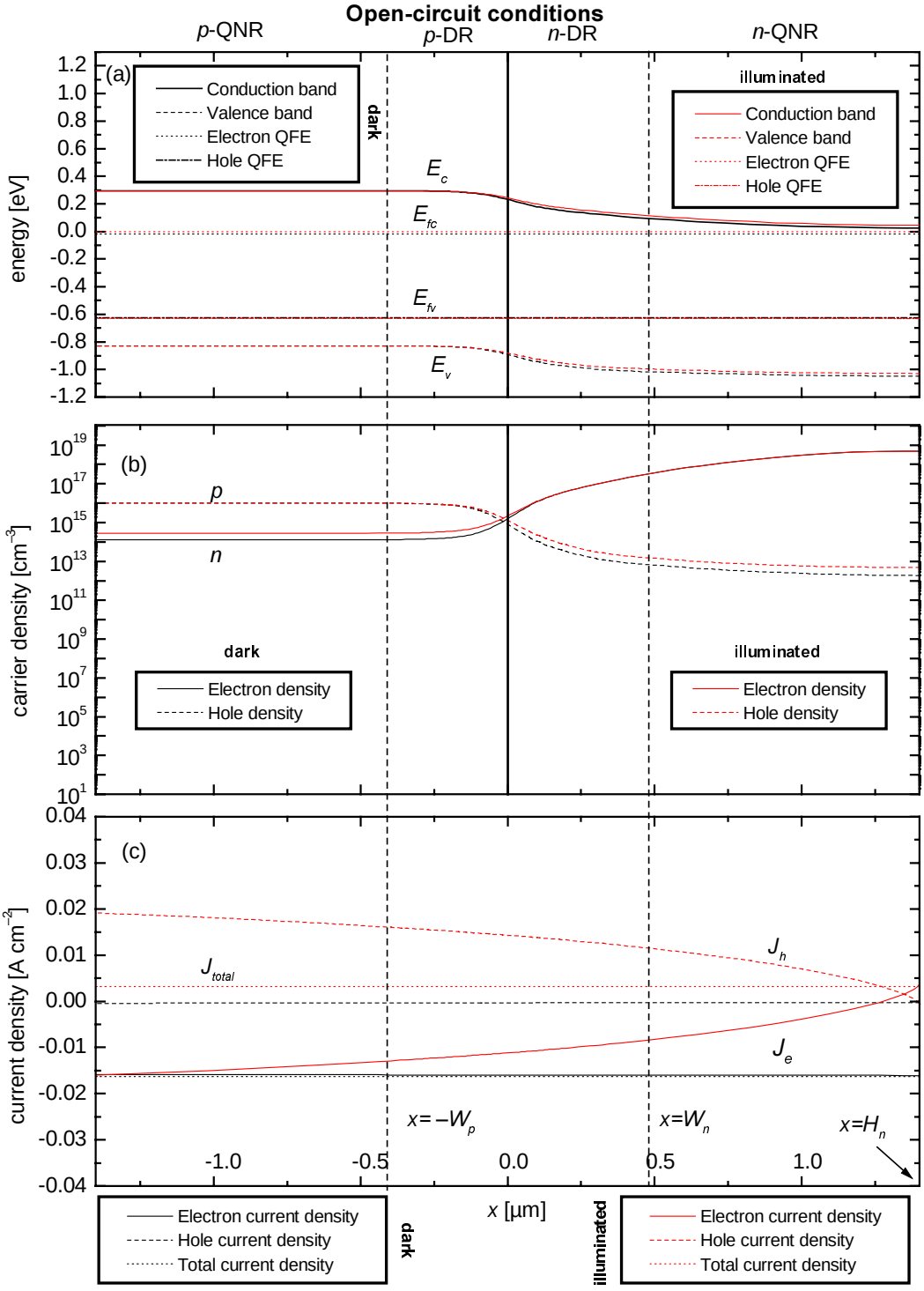

Fig. 3.7: Enlargement of the emitter region for open-circuit conditions.

To solve the differential equations for the carrier densities, it was assumed that the photogenerated carrier density vanishes at the edge of the depletion region. In Section 2.2.5, this was expressed by the boundary condition $n^{ph}(-W_p)=0$ (Eq. 2.87). That is to say, *in the analytical approximation* the space-charge region serves as a perfect sink for minority carriers, *i.e.* minority carriers at one edge of the space charge region are transferred to the opposite edge where they emerge as majority carriers. This boundary condition can be checked by looking at Fig. 3.4b, which shows the dark and illuminated charge carrier densities for short-circuit conditions. The numerical simulation reveals that the boundary condition 2.87 is an idealisation for short-circuit conditions. However, this assumption can be justified as giving a good degree of accuracy for open-circuit conditions; the differences between dark and illuminated minority carrier concentrations at the edges of the depletion region are small for $V = V_{oc}$, as can be seen in Fig. 3.6b.

The quasi-Fermi levels are separated by the simulated open-circuit voltage of 626 mV, given by Eq. 2.47. This can be seen in Fig. 3.6a. Under illumination the electron and hole currents J_e and J_h are mainly recombination currents at open-circuit conditions. The small total current density depicted by the red dotted line in Fig. 3.5c is a result of the current feeding into the external shunt resistance R_p.

3.4 Ray tracing

The external reflection of a textured silicon surface is minimised by the multiple reflections of the incoming light at the front surface. Furthermore, the light trapping quality of a texturisation scheme can be enhanced by the rough rear cell surface [27]. These effects cannot accurately be described using analytical approaches as in Section 2.3.7.

Ray tracing procedures allow the calculation of optical properties of silicon solar cells with textured surfaces. This is especially important for the investigation of light confinement in thin silicon solar cells. The ray tracing programs *TEXTURE* [45], *SUNRAYS* [46], *SONNE* [35] and *RAYN* (Section 3.4.2) are based on geometrical optics. These programs account for the wavelength, the angle of incidence, the optical constant of antireflection layers and contacting metals[6].

3.4.1 Light trapping investigations

Light confinement in thin planar silicon cells was studied by Goetzberger in 1981 using an analytical approach [47]. Ideal diffuse reflection at the rear surface was assumed. With such a

[6] Although the mentioned programs allowed the investigation of a wide range of surface textures, there is still no ‘general purpose‘ ray tracing program publicly available. Typically, the source code of an existing ray tracing program has to be modified in order to define sufficiently realistic simulation conditions to match new problems (*e.g.* round shapes, non-standard illumination conditions, polarisation of light, non-Lambertian surface roughness, absorbing antireflection coatings, 3D-spatially distributed absorption *etc.*). Various laboratories (Fraunhofer ISE, University of New South Wales, University of Konstanz and others) have developed their own ray tracing software suitable for handling special cases of interest.

perfect rear reflector, a fraction of the light equal to $1/n^2$ is lost each time a ray strikes the top surface, assuming unity transmittivity of the front surface. Here, n refers to the ratio of internal to external refractive indices.

The maximum optical pathlength enhancement of such a randomising scheme was calculated as $4\,n^2$ by Yablonovitch [48]. This is equivalent to a pathlength enhancement factor of around 50 for silicon, that is, the average pathlength of a light beam is enhanced by 50 times the cells thickness.

Substrates with pyramidally textured surfaces were analysed by Campbell using ray tracing [49]. Light trapping schemes with front surface texture and a planar rear surface were investigated. Random pyramids were shown to provide superior light confinement compared to a regular pyramid texture. The weakness of the single sided pyramidally textured schemes is the high proportion of light coupling out after only two passes. Enhanced light confinement can be achieved by arranging pyramids in groups as regular square arrays (‘tylers pattern’). Campbell also studied double-sided textures, which revealed enhanced light trapping properties compared to single sided textures. A comprehensive overview on light trapping investigations was compiled by Thorp [50].

The optical path length enhancement of light trapping schemes using inverted pyramids on the front side was investigated by Wagner and the author of this thesis at Fraunhofer ISE [51]. The ray tracing program *RAYN* was used which is described in detail in Section 3.4.2. A textured structure with a planar reflector at the back enhances the optical path length 9 times. This value is much smaller than that for an ideal diffuse back reflector, which yields a pathlength enhancement factor of 25. Therefore, structures with an ideal diffuse back reflector are better suited for textured thin silicon solar cells than those with a planar rear surface.

The above mentioned investigations assumed ideal diffuse reflection according to Lambert’s law. This law states that the intensity of light reflected from a surface is proportional to the cosine of the angle between the vector to the light source and the normal vector perpendicular to the surface. Assuming ideal diffuse reflection, the amount of reflected light is independent of the observer's position.

However, experimentally observed scattering patterns from semi-circular silicon probes, sandblasted (rough) on the planar part, do not exhibit ideal diffuse reflection [52]. The observed scattering pattern of internally reflected light shows a symmetrical distribution around the direction of direct reflection. The width of the scattering cone depends on the surface roughness. Realistic light scattering can be modelled using *RAYN* as outlined in Section 3.4.2.

3.4.2 The ray tracing program *RAYN*

The ray tracing modelling in this work was performed with the program *RAYN* which was originally developed by Wagner in order to optimise the illumination homogeneity in rapid thermal processing ovens [53]. It is written in the programming language C. The program was extended by the author of this thesis for the simulation of the optical properties of silicon solar

cells [26]. *RAYN* has also been used by R. Preu [54] and P. Koltay [55] to investigate the absorption enhancement resulting from the structuring of cell interconnectors in solar modules.

In *RAYN*, rays are randomly generated and geometrically traced through a geometrical structure until the intensity of a ray is below a threshold value. This threshold value must be set very low (especially for long wavelengths above 1000 nm) since only a small fraction of the ray is absorbed in each pass through the structure. This is due to the low absorption by silicon of photons with an energy close to the bandgap energy. Since for each ray a reflected and a refracted ray have to be traced, the total number of rays to be computed becomes higher than in the visible wavelength range. Polarisation of light is not considered by this program. An average over *p*- and *s*-type polarisation is taken for oblique light incidence. This average is a good approximation for unpolarised incident light [56].

Structures investigated with *RAYN* are composed using several types of optical surface:

Light emitting surfaces are used to illuminate the ray tracing geometry (Fig. 3.8a). The starting points for rays are generated randomly with equal distribution over the emitting surface. An angular distribution can be specified as well.

Absorbing surfaces are used to model a light detector or a non-transparent surface in a solar cell (Fig. 3.8b). Additionally, reflecting boundary conditions of the ray tracing geometry can be modelled using this surface type by specifying zero absorptivity.

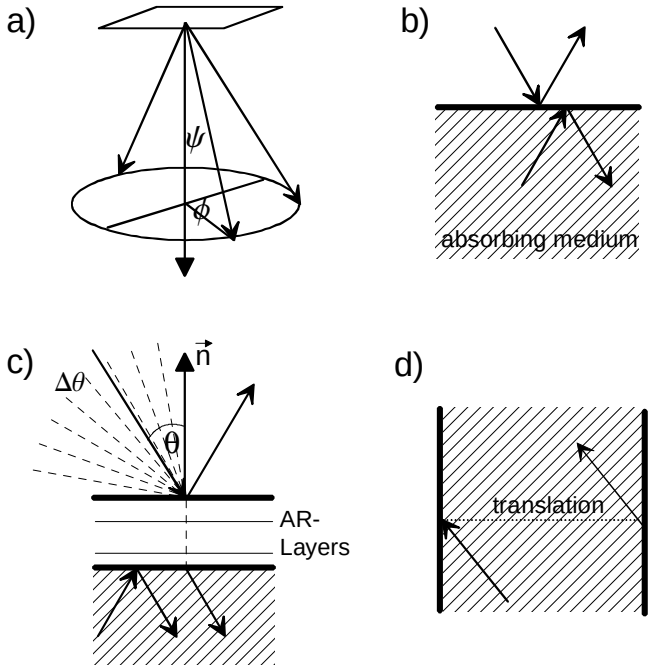

Fig. 3.8: Optical surfaces available in the ray tracing program *RAYN:* (a) Light emitting surfaces; (b) absorbing surfaces; (c) multilayer-surfaces for the simulation of AR-coatings; (d) virtual surfaces

Antireflection coatings are modelled with *multilayer surfaces* (Fig. 3.8c). The angular and wavelength dependent reflectivity of a surface covered with thin antireflection layers is calculated using Born's matrix method [57]. To monitor the light flux through a plane, *virtual surfaces* are implemented in *RAYN* (Fig. 3.8d). Such virtual surfaces are also needed to model closed surfaces of boxes. This allows the application of the divergence theorem: the total absorption in the box volume enclosed by the surfaces is equal to the light flux through all surfaces limiting the box.

Diffusive reflection from the bright etched surfaces used on the rear of the Fraunhofer ISE high efficiency solar cells was realistically modelled by a model of Phong [58]. The scattering of light with initial intensity I_0 is expressed as a symmetrical scattering pattern about the direction of direct reflection. $I(\alpha)$, where α is the angle off the direction of direct reflection (see Fig. 3.9) is given as an angular distribution

$$I(\alpha) = I_0 \cos^w(\alpha). \tag{3.16}$$

The "Phong exponent" w determines the width of the scattering cone. With Phong reflection the direction of beam propagation is not fully randomised, but essentially remains close to the angle of direct reflection. This can be modelled by adding a random angle offset to reflected rays. The angular distribution of a large number of traced rays is computed using an angular scattering probability as to fit the chosen distribution $I(\alpha)$. Phong reflection gives a more realistic description of the observed scattering pattern of bright etched silicon surfaces than a superposition of direct and Lambertian reflection.

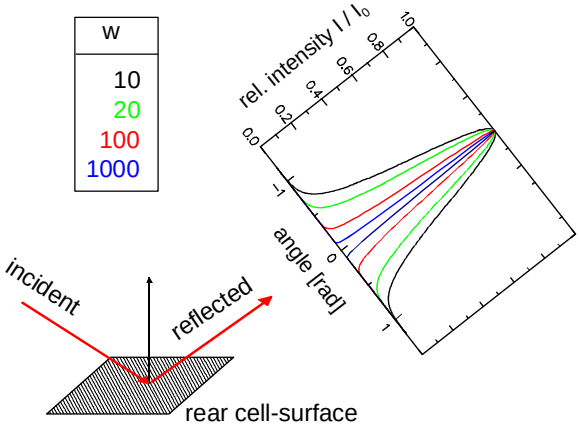

Fig. 3.9: Phong model for the description of diffusive reflection

3.4.3 Simulation of normalised generation function

Numerical device simulation programs cannot handle the 3D-distribution of optical charge carrier generation due to the surface texture. Spatial resolution within a single optical symmetry element of for example 10 µm width is not compatible with the wide contact spacing of about 800 µm. Thus, a 1D projection of the three-dimensionally simulated charge carrier generation rates is necessary. A simple parallel projection leads to an unrealistic generation function with $g(\lambda,z) = 0$ of a textured surface.

In this work the depth dependence of the normalised generation function $g(\lambda,z)$ is obtained via a projection technique to give the 3D generation function adapted specifically for textured surfaces as shown in Fig. 4.5. The volume close to the surface is divided into layers parallel to the surface. Carriers generated within each layer are attributed to the respective 1D depth coordinate, since they have approximately equal probability of reaching the surface.

Utilising the normalised generation function provided by *RAYN,* counteracting optical and electrical loss mechanisms can be described by combining realistic optical modelling with semiconductor device simulation (Section 6.5). This is an advantage over the ray tracing programs mentioned previously.

3.5 Numerical modelling of differential spectral response

The differential spectral response of a solar cell can be simulated by a numerical approach which was developed during the course of this thesis.

Below, E denotes the total irradiance (W m^{-2}) and E_λ is the spectral irradiance at a given wavelength (W m^{-2} nm^{-1}).

The differential spectral response (Eq. 2.) can be approximated by

$$\tilde{s}(\lambda) \approx \frac{J(G_0 + G_\lambda) - J(G_0)}{E(G_0 + G_\lambda) - E(G_0)} \tag{3.17}$$

where $J(G_0)$ is the short circuit current density determined for illumination with the bias light generation profile $G_0(x)$ and $E(G_0)$ is the bias light irradiance. By analogy, $J(G_0 + G_\lambda)$ and $E(G_0 + G_\lambda)$ are the short circuit current density and irradiance, respectively, determined for illumination with added monochromatic light of wavelength λ. $G_0(x)$ is determined from the normalised generation function $g(\lambda, x)$ (Eq. 2.130) simulated using *RAYN*.

To avoid numerical errors in solving the integral, the solar spectral irradiance for AM1.5 conditions is divided into m wavelength intervals each containing $1/m$ of the total irradiance E. The centroid wavelengths λ_i for $m = 100$ equal irradiance intervals ΔE of the AM1.5 spectrum are tabulated in Ref. [59]. Each irradiance interval ΔE contains $\Delta E = \frac{1}{m} E = E_{\lambda_i} \Delta\lambda_i = 10 \frac{W}{m^2}$ and thus

$$\begin{aligned} G_0(x) &= \int d\lambda \, E_\lambda \frac{\lambda}{hc} g(\lambda, x) \\ &= \frac{1}{hc} \sum_{i=1}^{m} \Delta\lambda_i \, E_{\lambda_i} \, \lambda_i \, g(\lambda_i, x) \\ &= \frac{1}{hc} \frac{E}{m} \sum_{i=1}^{m} \lambda_i \, g(\lambda_i, x). \end{aligned} \tag{3.18}$$

In order to simulate the differential spectral response, monochromatic light of wavelength λ_k is added to the bias light generation profile $G_0(x)$

$$G_k(x) = \frac{1}{hc} \frac{E}{m} \left(\sum_{i=1}^{m} (1 + b\,\delta_{ki}) \, \lambda_i \, g(\lambda_i, x) \right) \tag{3.19}$$

where $\delta_{ki} = {}^{1\ for\ k=i}_{0\ for\ k\neq i}$ and the intensity of monochromatic light is given by $b\frac{E}{m}$ (*i.e.* b=1 equals 10 W/m^2 added monochromatic light for m =100 and E =1000$\frac{W}{m^2}$ using the mentioned AM1.5 spectrum).

The differential spectral response at wavelength λ_k is found by numerical simulation to be

$$\tilde{s}(\lambda_k) = \frac{J(G_k) - J(G_0)}{b\frac{E}{m}} \tag{3.20}$$

where $J(G_k)$ is the short circuit current density for illumination with the generation profile $G_k(x)$. Thus, modelling a numerical semiconductor device according to Eq. 3.20 allows the direct simulation of the measurement technique introduced by Metzdorf [28] for determining the differential spectral response.

This simulation technique can be used to numerically investigate the origins of current-irradiance non-linearities as observed for rear-contact silicon solar cells (Fig. 7.9).

3.6 Circuit simulation

A discretisation mesh of the entire solar cell device volume could not be constructed, using state-of-the-art simulation software nor could the device equations be solved on such a huge mesh. Therefore, semiconductor device simulation as described in Section 3.2 is restricted to a symmetry element representing an irreducible section of the solar cell. Considering a solar cell with single sided contacts this symmetry element of the interior cell part typically consists of one *n*- to *p*-contact finger distance multiplied by the wafer thickness for a 2D simulation.

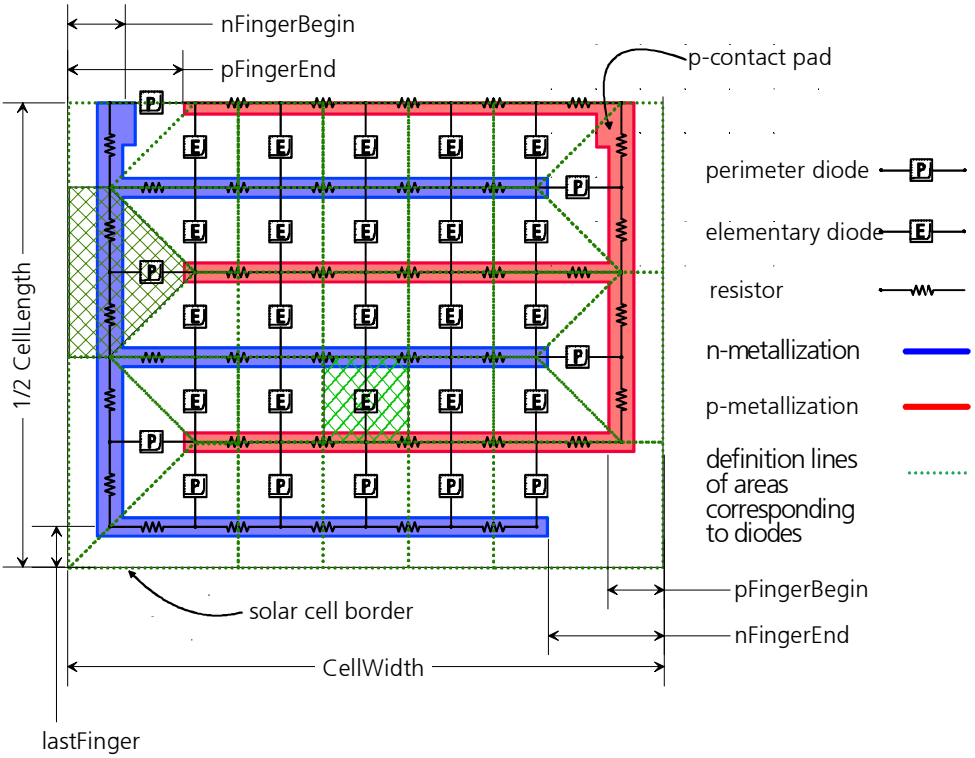

Fig. 3.10: Electrical circuit for the circuit simulation consisting of half of the solar cell. The small boxes denote the elementary diodes (E) and the perimeter diodes (P). The resistors are arranged in order to describe the interdigitated metal grid indicated as dark areas.

Losses arising from the ohmic metal resistance and recombination losses at the cell perimeter can not be included using a symmetry element of the interior cell part. These losses can be accounted for by using the circuit simulation method [60].

An equivalent circuit of a solar cell with single sided interdigitated contact grid is shown in Fig. 3.10. It consists of elementary diodes (E) and perimeter diodes (P) which are connected by Ohmic resistors. Contact pads of the solar cell are located in the upper corners of the graph. The *I-V* curve of each diode is simulated by semiconductor device simulation and tabulated. These tabulated *I-V* curves are considered as voltage controlled current sources in the subsequent circuit simulation [41]. Each current density value of a diode is scaled by an associated area fraction shown as hatched areas in Fig. 3.10. For symmetry reasons only half of the metal grid has to be resolved in the circuit simulation in order to describe the *I-V* curve of an entire solar cell.

The total current flow causes a voltage drop along the metal grid. Thus, different cell regions (represented by the tabulated *I-V* curves in the circuit) are driven by different voltages to that at the contact pads. The resulting losses are known as *non-generation losses* [61].

3.7 Chapter summary

This chapter has presented an overview of numerical methods of silicon solar cell simulation. It has briefly explained how the basic equations that govern carrier transport in solar cells can be solved numerically using a discretisation method.

One-dimensional numerical solutions of the semiconductor device equations using the program *PC1D* are presented for a *p-n* junction solar cell with a diffused emitter. The position dependent carrier- and current densites for short-circuit, maximum power and open-circuit conditions have been compared to the analytical Shockley model.

Early analytical light trapping investigations were performed for planar cells with ideal diffuse reflectors on the rear side of the wafer. Modelling light trapping in textured silicon solar cells requires numerical ray tracing techniques. This led B. Wagner and the author of this thesis to develop the ray tracing program *RAYN*. This program is capable of handling textured surfaces, antireflection coatings, non-Lambertian surface roughness (Phong model), and spatially distributed absorption. *RAYN* represents an improvement compared to other ray tracing software as it has achieved a more realistic description of surface roughness: Modelled scattering patterns of rough silicon surfaces are observed to match those determined by experiment.

RAYN was used to simulate the external reflection and absorption of silicon solar cells textured with inverted pyramids and random pyramids. In addition, the absorption enhancement due to structuring of cell interconnectors in solar modules has been investigated by R. Preu and P. Koltay using *RAYN*.

Using *RAYN*, the normalised generation function of a solar cell with textured surfaces can be simulated. This is essential in order to realistically simulate the short circuit current of textured cells, especially textured thin silicon solar cells. Furthermore, the normalised generation function calculated by *RAYN* provides the basis for modelling the differential spectral response of solar cells with injection level-dependent recombination mechanisms. This feature is not provided by other ray tracing programs.

Distributed resistive losses in the metal grid can be accounted for by applying the circuit simulation method. Moreover, this method accounts for non-generation losses: when the entire cell is operating at maximum power, different cell parts work at different voltages. Therefore, the maximum power point of the entire cell deviates from the maximum power point of the elementary diodes constituting the circuit.

Losses due to recombination of charge carriers at the solar cell perimeter can be quantified as well by introducing *I–V* curves of the perimeter region into the circuit simulation.

Both distributed Ohmic losses in the metal grid and perimeter losses influence the solar cell’s fill factor (this will be exemplified in Sections 7.7 and 7.8).

4 An object oriented approach to analytical and numerical modelling of silicon solar cells

4.1 Introduction

A two- or three-dimensional computer simulation of a solar cell is often considered as an attempt to estimate the cell output parameters by feeding black boxes (executable programs) with several independent input parameters. The input parameters specify the optical properties of antireflection coatings, the surface texture, the device geometry, and the doping profiles. Furthermore, details of physical models like those for carrier recombination and minority carrier mobility etc. have to be specified.

However, when solving a scientific problem, researchers communicate in abstract terms, rather than exchanging numerous lists of numbers.

Accordingly, how can our knowledge of the physical properties of solar cells be organised in terms of a hierarchy of categories reflecting the way we formulate problems when discussing them in a research group? In this study the problem is solved by using the *object oriented paradigm*, which is a new way of thinking about the process of decomposing problems and developing programming solutions.

4.2 The purpose of PVObjects

The design of *PVObjects* allows us to examine a wide variety of solar cell-related problems. Some examples of this are outlined in the following:

- Reflection and absorption of a textured silicon wafer or encapsulated solar module can be simulated using ray tracing techniques.
- Models describing the solar cell physics can be accessed separately, *e.g.* mobility, band gap, and recombination models. This is useful in gaining insight into the physical dependencies without having to perform a complete device simulation.
- The electrical symmetry element of device simulations is based on a simple set of two- and three-dimensional geometrical elements implemented as objects. All geometrical and doping parameters determining the topology of the device can be varied.

Solar cells are represented by complex objects (solar cell models), in which all of the above-mentioned objects are embedded. A solar cell model includes several interfaces with commercial device simulation programs.

All the standard measurement procedures of a characterisation laboratory for solar cell analysis can be simulated: the external reflection, the spectral response, the dark- and

illuminated *I-V* curve, and the J_{sc}-V_{oc} curve. This is achieved by passing a solar cell model to an object representing a measurement apparatus in a virtual laboratory.

4.3 Object oriented programming with application to solar cell simulation

In the following, the basic principles of object oriented programming are outlined with application to the analytical and numerical modelling of silicon homo-junction solar cells.

Object oriented programs can be seen as a collection of largely autonomous agents, called *objects* [62]. These objects encapsulate both the data values and the operation information. Operations that an object can perform are called *methods*. Writing an object oriented program means first of all defining the *object classes*. The object classes determine the object's behaviour; that is, the data structure and the methods are defined in the classes. Every object is an *instance* of a class. To illustrate the meaning of class and object think of the class "solar car" and of the object "Dream" as an instance (or one realisation with this name) of the class solar cars.

PVObjects was implemented in the scientific software tool *Mathematica* [63] using an object oriented extension [64]. *PVObjects* is designed according to the way we think when analysing solar cells: there are specialists involved in the characterisation process. The main

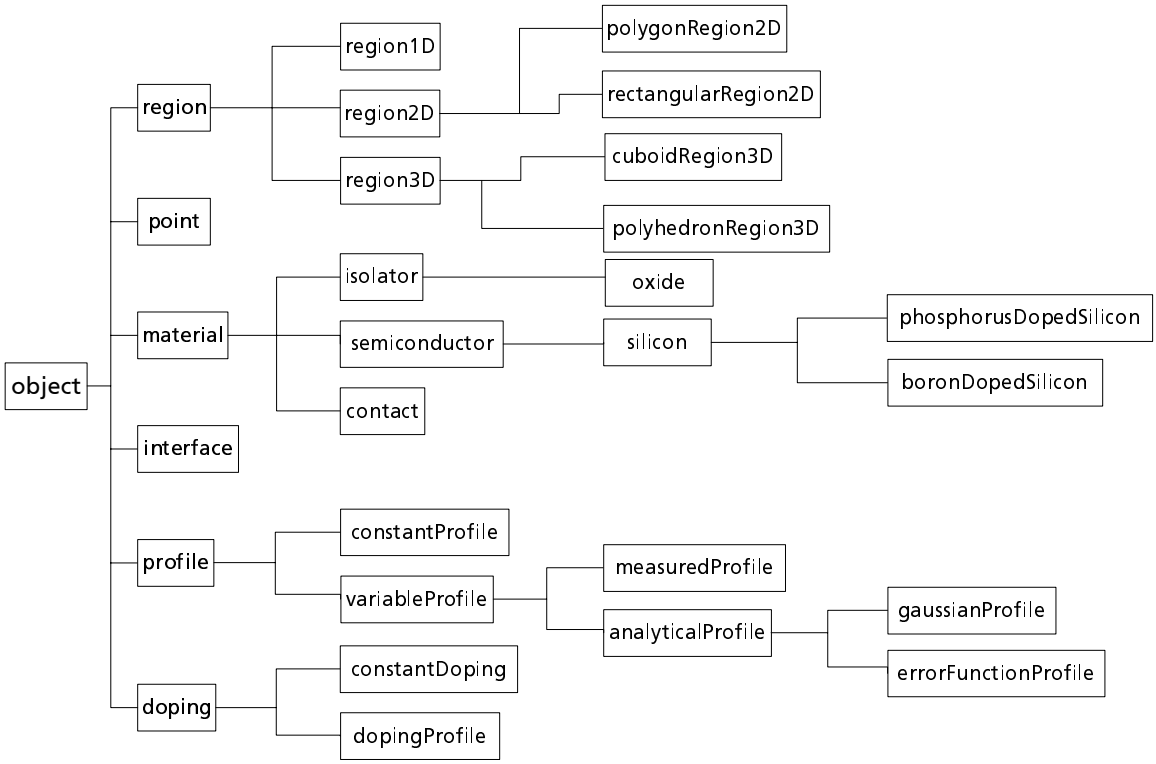

Fig. 4.1: The object tree called SemiconductorPhysicist'Material is shown. The degree of specialisation increases to the right in the tree. The concept of inheritance can be illustrated with the class semiconductor, which represents an abstract base class. The more specialised class silicon inherits attributes of the class semiconductor.

specialists are the *OpticSpecialist*, the *SemiconductorPhysicist* and the *SolarCellResearcher*. Each object tree, to be described in the following, belongs to one of these three specialists.

4.3.1 Abstraction and inheritance

Abstraction is a mechanism to control complexity: if a number of related data types share some common characteristics, they are isolated and encapsulated in an abstract object class. Specialisations of the abstract class are implemented as subclasses *inheriting* the characteristics of the superclass. Only the aspects in which a class differs from its superclass, have to be implemented. Therefore much of the program code needs to be written only once. This ensures consistency and reduces development time. Constructing object trees using the mechanisms of abstraction and inheritance allows us to create categories of object classes that reflect the structure of terms in our natural human language. This can be illustrated by the object tree shown in Fig. 4.1 including material objects needed for the simulation of silicon solar cells.

Isolators, semiconductors and contacts are implemented as subclasses of the abstract class material. For instance, an abstract class *semiconductor* provides the material features common to all semiconductors; it contains methods for the definition of a band gap model, a model for the charge carrier mobility, and so on.

4.3.2 Polymorphism and reusable code

When simulating solar cells, a basic consideration is how to represent their physical dependencies in a computer model. Often one has to compare the influence of different physical models on the cell's characteristics. Consider different models for the minority carrier mobility, *e.g.* the model of Masetti [65] and that one of Cuevas [66]. The temperature dependency of the mobility is included in Masetti's model, whereas Cuevas' parameterisation is given for a fixed temperature only. Therefore, in a functional implementation one has to deal with different numbers of arguments for the calculation of the mobility. As a consequence, the code for the calculation of the mobility as a function of doping density has to be written twice. This leads to a tight interconnectedness of the software, which was a major problem in past implementations, insofar as the extraction of elements of the software from one project to another, unrelated project was difficult.

One tool for writing "reusable" software is *polymorphism*. It permits a code to be written once, at a high level of abstraction, and to be tailored as required to fit a variety of situations.

An example of the calculation of the minority carrier mobility with a reusable code is given in Fig. 4.2. The function *calculateMobility* accepts an object of type *mobilityModel*, regardless of the detailed dependency hidden in the model. Applying the polymorphic method *electronMinorityPar* to the mobility, the mobility parameters are switched to a parameter set describing electrons as minority charge carriers. This parameter set is hidden in the object; in other words, the data defining the model's dependency on electrons as minority carriers are part of the object.

a)
```
Needs["PVObjects`SemiconductorPhysicist`CarrierMobility`"];

masetti = new[masettiMobilityModel]; electronMinorityPar [masetti];
setDonorDensity [masetti, 10^16];
mobility [masetti]

1429.68
```

b)
```
pc1d = new[pc1dv51MobilityModel]; electronMinorityPar [pc1d];
setDonorDensity [pc1d, 10^16];
mobility [pc1d]

1417.
```

c)
```
calculateMobility[model_, doping_] :=
 (electronMinorityPar [model]; setDonorDensity [model, doping]; mobility [model])

calculateMobility[masetti, 10^16]

1429.68

calculateMobility[pc1d, 10^16]

1417.
```

Fig. 4.2: An example of the calculation of the minority carrier mobility of phosphorous-doped silicon using the polymorphic methods *electronMinorityPar*, *setDonorDensity* and *mobility*: (a) Masetti's model is used; (b) using the model implemented in PC1D [67]; (c) polymorphic methods allow us to write a reusable code without the need for modification even if the dependencies of the models on the physical entities are changed.

4.3.3 Embedding of objects and autonomous objects

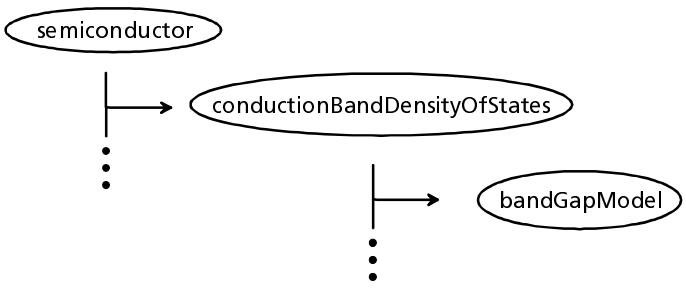

Fig. 4.3: Schematic diagram of the embedding of object classes for physical models. Arrows indicate embedding of classes: the class semiconductor embeds a model for the density of states, which itself embeds a band gap model.

Instances of object classes *embedding* in other objects are a powerful tool for structuring object oriented programs. Fig. 4.3 shows part of the structure of the abstract base class *semiconductor* with an embedded model for the density of states in the conduction band. Furthermore, the model for the density of states contains an embedded class for the calculation of the silicon band gap.

Each embedded object can be used autonomously. This allows us to immediately focus on specific physical dependencies, without any further programming effort. An example is given in Fig. 4.4. The effective intrinsic carrier density of silicon is calculated depending on the donor density for two different models of the effective intrinsic density. The object *delAlamo* shows a constant effective intrinsic density value for donor densities lower than 7×10^{17} cm^{-3} whereas the object *schenk* shows a smooth curve (Fig. 4.4a). The shape of the two effective

intrinsic density curves can be understood by looking at the embedded band gap narrowing models. As each model for the effective intrinsic density embeds a band gap narrowing model it is easy to investigation this. The method *giveBandGapNarrowingModel* in Fig. 4.4b extracts the objects for the band gap narrowing. Plotting the band gap narrowing model depending on the donor density yields the curves shown in Fig. 4.4b which explains the effective intrinsic density curves. The band gap narrowing model of Schenk [68] is derived from quantum mechanics, leading to a smooth curve; whereas del Alamo [69] gave an empirical fit expression, leading to the dash-dotted curve with the kink in Fig. 4.4b.

The object oriented approach is superior to functional programming, where complex functions are behaving like a black box: as explained in the introduction, due to the high level of interconnectedness in functional software, specific physical dependencies cannot easily be accessed.

```
Needs["PVObjects`SemiconductorPhysicist`BandGap`"];

schenk = new[schenkEffIntrinsicDensityModel];
delAlamo = new[delAlamoEffIntrinsicDensityModel];

makeDataList[g_] := Map[g, logTabFkt[10^15, 10^21, 50]] ;

niEff[model_] := Function[doping,
  (setElectronConcentration[model, doping]; setDonorDensity[model, doping];
   {doping, effectiveIntrinsicDensity[model]})]

data[f_, Σ_, Γ_] := Map[makeDataList, {f[Σ], f[Γ]}];

multipleLogListPlot[{"Schenk", "del Alamo"},
  data[niEff, schenk, delAlamo], < graphics options discarded >];
```

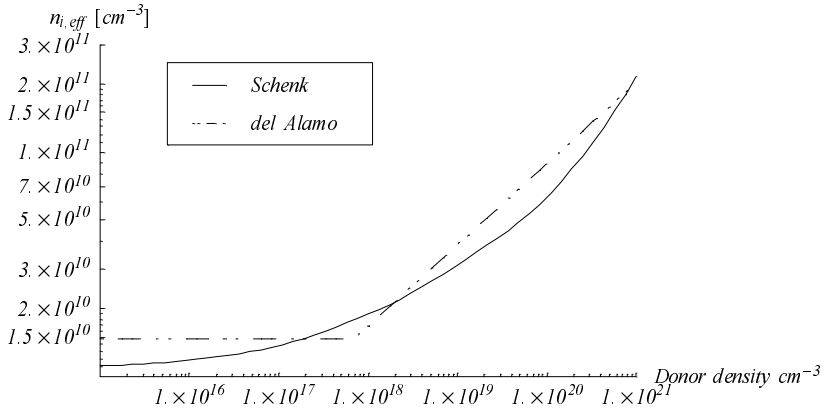


```
bgnSchenk  = giveBandGapNarrowingModel  [schenk ];
bgnDelAlamo  = giveBandGapNarrowingModel  [delAlamo ];

bgn[model_] := Function[doping,
  (setElectronConcentration[model, doping]; setDonorDensity[model, doping];
   {doping, bandGapNarrowing[model]})]

multipleLogListPlot[{"Schenk", "del Alamo"},
  data[bgn, bgnSchenk, bgnDelAlamo], < graphics options discarded >];
```

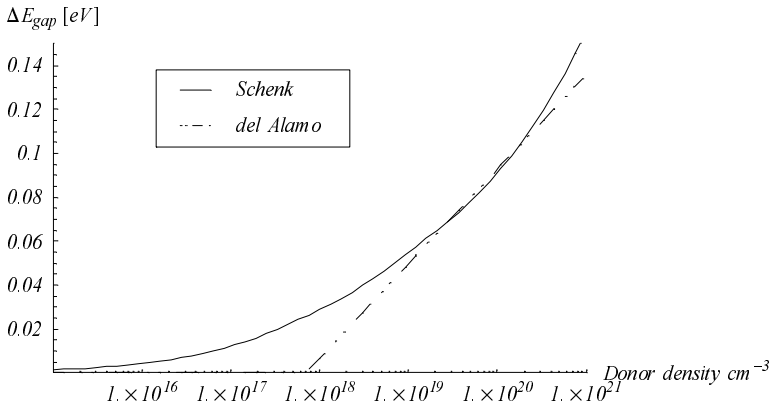

Fig. 4.4: Focusing on model dependencies is easy because each object can be used autonomously: (a) Effective intrinsic density $n_{i,eff}$ of silicon as a function of doping for two different models; (b) focusing on band gap narrowing models to explain differences in $n_{i,eff}$.

4.4 An object class for the simulation of optical properties

This section describes optical models for silicon solar cells. From an abstract point of view, the most important spectrally dependent properties of any silicon solar cell structure are the external reflection and the light trapping quality; that is, the fraction of incident light absorbed in the electrically active part of the solar cell. Moreover, it is important to calculate the charge carrier generation profile in the solar cell structure to realistically simulate the short circuit current density using an electrical device simulation program.

Fig. 4.5 shows an object tree for the optical simulation of silicon solar cells. Methods for the above-mentioned optical properties are implemented in the object class *opticalGeneration*. The optical properties can be calculated analytically in the case of a planar front and rear surface of a silicon wafer (Section 2.3.8). This model is implemented in the object class *analyticalOpticalGeneration*.

A numerical approach to the simulation of textured silicon solar cells is achieved by interfacing with the ray tracing program *RAYN* which is described in detail in Section 3.4.

4.4.1 Light trapping geometries

Models for the most important light trapping geometries realised at Fraunhofer ISE are implemented in *PVObjects* as subclasses of the object class *opticalGenerationStack* (Fig. 4.5). This class represents optical symmetry elements with stacked optical boundaries. An optical boundary consists of optical surfaces, which are shown in Fig. 3.8.

Three examples of optical symmetry elements are shown in Fig. 4.5a - d.

Optical properties of regular inverted pyramids etched in monocrystalline silicon are modelled with the object class *invertedPyramidGeneration* [27]. It embeds the optical symmetry element shown in Fig. 4.5a, b. The inverted pyramid on the front side is composed of four triangular-shaped multi-layered surfaces. Therefore, antireflection coatings on textured surfaces can be simulated as well.

Optical properties of random upright pyramids can be approximated by an optical symmetry element composed of one upright pyramid [70]. This optical symmetry element is embedded in the object class *uprightPyramidGeneration* shown in Fig. 4.5c.

Light trapping in thin film silicon solar cells can be simulated with the object classes *planarThinFilmGeneration* and *invertedThinFilmGeneration*. The optical symmetry element shown in Fig. 4.5d describes a thin-film layer deposited on a substrate. Light trapping in the thin silicon layer is achieved using inverted pyramids on the front side and an intermediate oxide layer, which acts as a backside reflector. The intermediate oxide is modelled by a multi-layered surface [71].

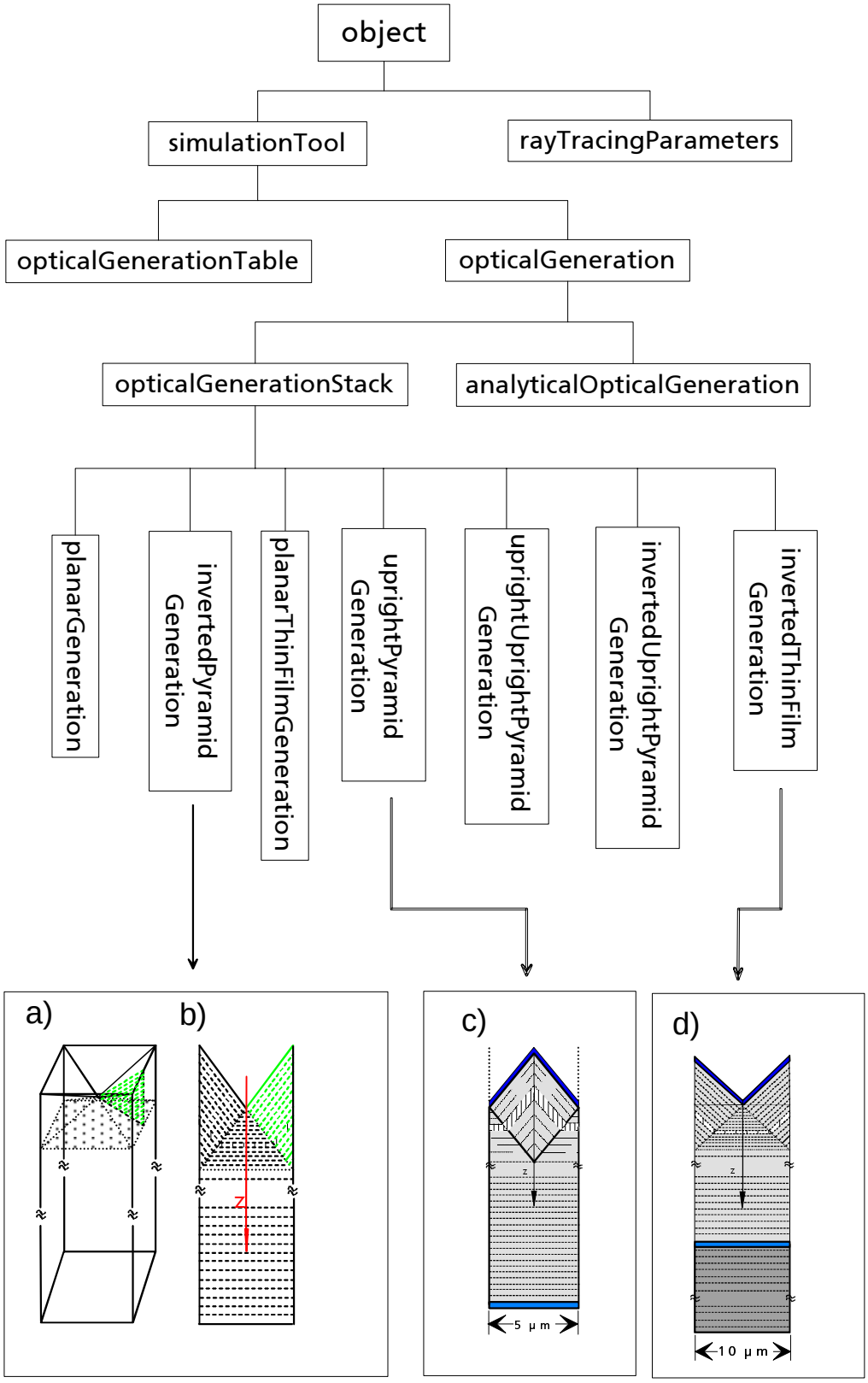

Fig. 4.5: The graph shows objects of the package *OpticSpecialist`OpticalGeneration* describing the optical properties of textured monocrystalline silicon solar cells: (a) The optical symmetry elements are implemented in three dimensions, graphs b - d are 2D-cuts through the respective 3D-symmetry element; (b) front texture with inverted pyramids; (c) upright pyramid; (d) inverted pyramid texture of a thin film cell on an insulating substrate.

4.4.2 Example: Optical characterisation of thin silicon solar cells

This section presents an example ray tracing calculation of the optical properties of a planar silicon on insulator (*SOI*) solar cell [72]. The modelling was performed with the object *planarThinFilmGeneration*. The complete code for the simulation and graphical output is shown in Fig. 4.6.

The external reflection of the SOI cell is plotted as a solid line in Fig. 4.6a. In the example the object of class *planarThinFilmGeneration* assumes a default thickness of the surface passivation oxide of 105 nm. The external quantum efficiency of a solar cell with these optical features cannot exceed the upper limit plotted as a dash-dotted line in Fig. 4.6a (active absorption). Maximum transmission of light through the intermediate oxide layer occurs at 1050 nm: 40 % of light at this wavelength is transmitted through the intermediate oxide layer and absorbed mostly in the supporting substrate (dotted line in Fig. 4.6a).

Another interesting feature of the class *opticalGeneration* is its ability to simulate mixtures of white light illumination and additional monochromatic illumination. Different mixtures can be simulated where the ray tracing procedure is invoked only once. An example calculation is shown in Fig. 4.6b. The incident light intensity is varied from 0.001 suns to 10 suns. Additional monochromatic illumination with 1100 nm wavelength and an intensity of 10 W/m^2 was set. The curves in Fig. 4.6b show depth-dependent optical generation profiles. A discontinuity of the generation profile is found at a depth of 30 µm. This is due to reflection of light at the intermediate oxide layer.

The example discussed above illustrates the autonomous use of complex objects in *PVObjects*. Only a few parameters have to be specified, differing from default settings to obtain reasonable results. This ensures a short and clear code. Data generated by the objects can immediately be displayed with *Mathematica*, as demonstrated in Fig. 4.6.

a)

```
Needs["PVObjects`OpticSpecialist`OpticalGeneration`"];

G = new[planarThinFilmGeneration];

setOpticalThickness[G, 30(*μm*)]; setRearPhongExponent[G, 20];
setIntermediateOxideThickness[G, 200(*nm*)];

request[G];

data = {externalReflection[G], frontSurfaceBalance[G], cumulativeAbsorption[G], activeAbsorption[G],
   intermediateOxideBalance[G]};
descriptor = {"externalReflection", "frontSurfaceBalance", "cumulativeAbsorption",
   "activeAbsorption", "intermediateOxide"};

multipleLogListPlot[descriptor, data, < graphics options discarded >]
```

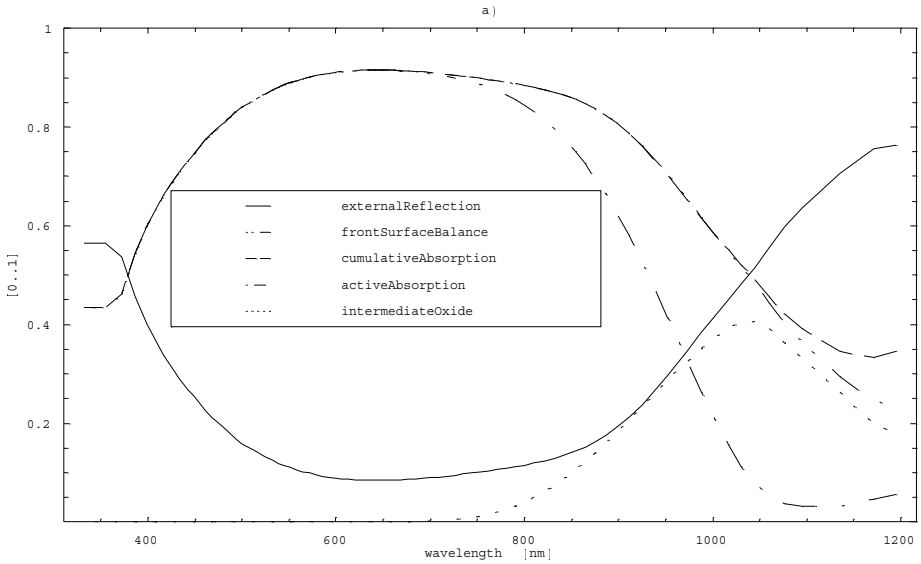

b)

```
setMeasLightWavelength[G, 1100(*nm*)]; setMeasLightIntensity[G, 10(*W/m^2*)];

generationForGivenSuns[suns_] := (setSuns[G, suns]; giveGenerationList[G])

data = generationForGivenSuns /@ {0.001, 0.01, 0.1, 1, 10};
descriptor = ToString /@ {0.001, 0.01, 0.1, 1, 10};

multipleLogListPlot[descriptor, data, < graphics options discarded >]
```

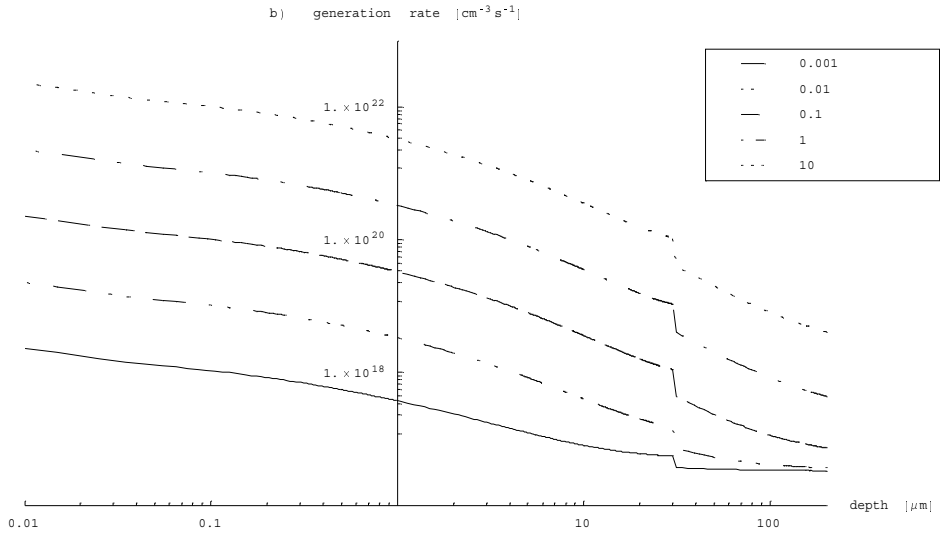

Fig. 4.6: *Mathematica* input and output for the simulation of the optical properties of a 30 µm thick planar SOI solar cell on a 200 nm thick insulating intermediate oxide layer. The intermediate oxide layer is assumed to be rough.

4.5 Solar cell models

This section presents an object oriented implementation of models describing solar cells. A solar cell is represented by an object of class *solarCellModel*. The object class *solarCellModel* can be associated with the prototype of a solar cell: if no further details of the term solar cell are explained, the author thinks of a homo-junction silicon solar cell with a boron-doped base and a phosphorous-doped emitter. Therefore, the abstract base class *solarCellModel* collects material properties of this solar cell prototype by means of embedded material objects which are independent of the device geometry. The definition of subclasses is based on the distinction between analytical solar cell models and numerical solar cell models.

4.5.1 An abstract class for the simulation of silicon solar cells

A *p-n* junction silicon solar cell consists of a base, an emitter and two contact types. Therefore, these shared characteristics are isolated in an abstract class - the object class called *solarCellModel*. The objects for the base and emitter are embedded in the solar cell model, and are sub-objects of the *silicon* class including the doping type (Fig. 4.1). It provides methods of calculating all important semiconductor properties such as the effective intrinsic density, doping dependent mobility, charge carrier dependent recombination rates etc.

Another feature common to all solar cells is that they are illuminated with light, causing charge carriers generated in the base and emitter. To subsume the optical properties of the device, the solar cell model embeds an object *opticalGeneration* describing the optical charge carrier generation as explained above.

4.5.2 Numerical device simulation tools

For exact solar cell simulations, numerical device simulation programs have to be involved. The most important steps for the device simulation are ray tracing simulation, construction of a discretisation mesh, and numerical device simulation, performed with the programs *RAYN* (Section 3.4.2), *MESH* and *DESSIS* [41], respectively. The objects involved in the numerical simulation process are shown in the object tree of Fig. 4.7. The *Mathematica* objects *mesh* and *DESSIS* provide interface methods for the programs *MESH* and *DESSIS*. The operating system-specific code is collected in the class *computer*, which is embedded in the class *simulationTool*. Objects of the class *computer* for the operating systems Linux and HP-Unix have been implemented so far.

The device simulation program *DESSIS* allows us to use different solution algorithms. The selection of the solution algorithm and details concerning the order of solving the Poisson equation and the electron and hole continuity equations are embedded in subclasses of *dessisSolveScheme* (Fig. 4.7).

An object of type *dessisSolveStrategy* provides interface methods specifying the voltage applied to the solar cell device within *DESSIS*. For example, an instance of *dessisSolveStrategyQuasistationary* can be used to ramp the voltage applied to the solar cell contacts to a given level assuming quasistationary conditions in the device.

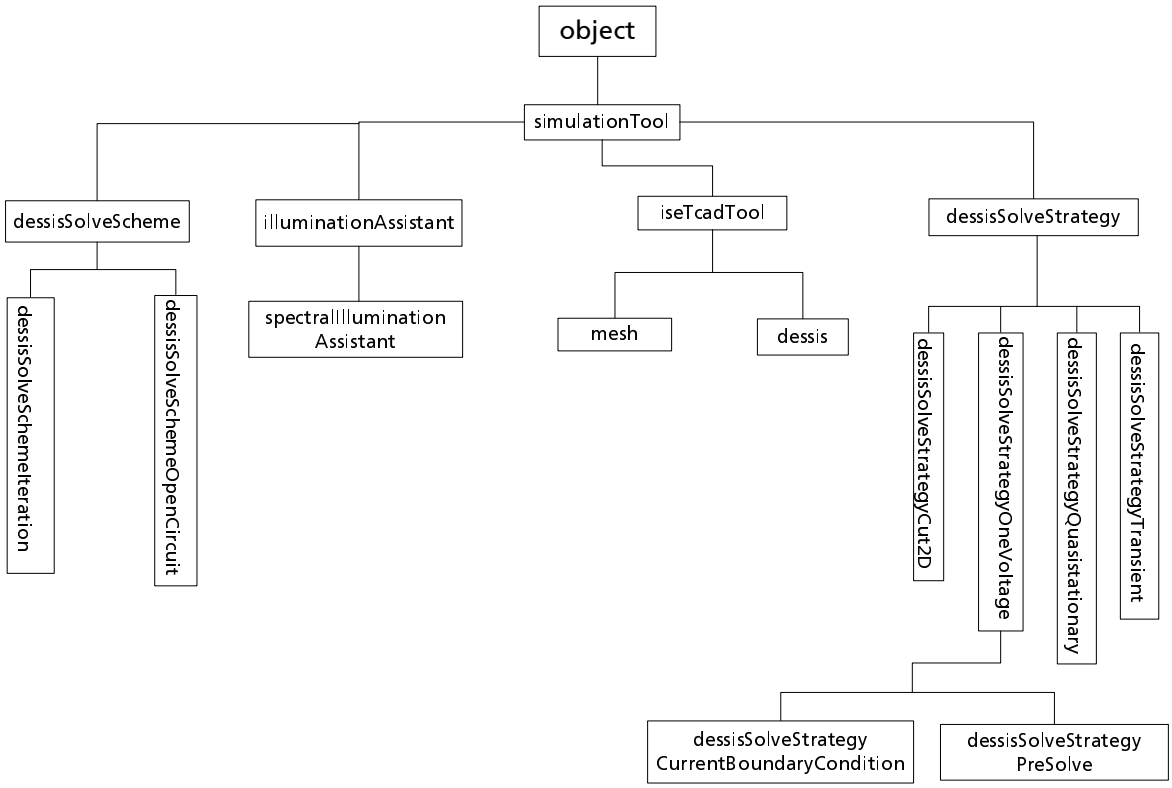

Fig. 4.7: Object tree *SolarCellResearcher`IseTcadTools* for interfacing with numerical device simulation tools.

Finally, the optical generation rates at the nodes of a discretisation mesh have to be specified. This is achieved by using an object of type *illuminationAssistant*. Files specifying optical generation rates can be generated with this object for white light illumination and for added monochromatic light (see Fig. 4.6b). The last case is important for the simulation of the spectral response of a solar cell.

The class *numericalSolarCellModel* embeds all simulation tools shown in Fig. 4.7. Details concerning the device geometry are specified in subclasses of the class *numericalSolarCellModel*; this will be discussed in the following section.

4.5.3 Two and three-dimensional solar cell geometries

In order to numerically simulate the electrical characteristics of a solar cell with a device simulation program, a geometrically irreducible symmetry element of the cell has to be constructed.

In *PVObjects* all physical dimensions and doping profiles are encapsulated in a subclass of *electricalSymmetryElement.* Fig. 4.8 shows two examples of geometrically irreducible symmetry elements with reflecting boundary conditions: (a) two-dimensional symmetry element of a silicon on insulator thin film cell with both contacts on the front side; (b) three-dimensional symmetry element of an emitter wrap-through cell. The front and rear emitters are connected by a diffusion through holes (called hole emitter). Due to the current collecting

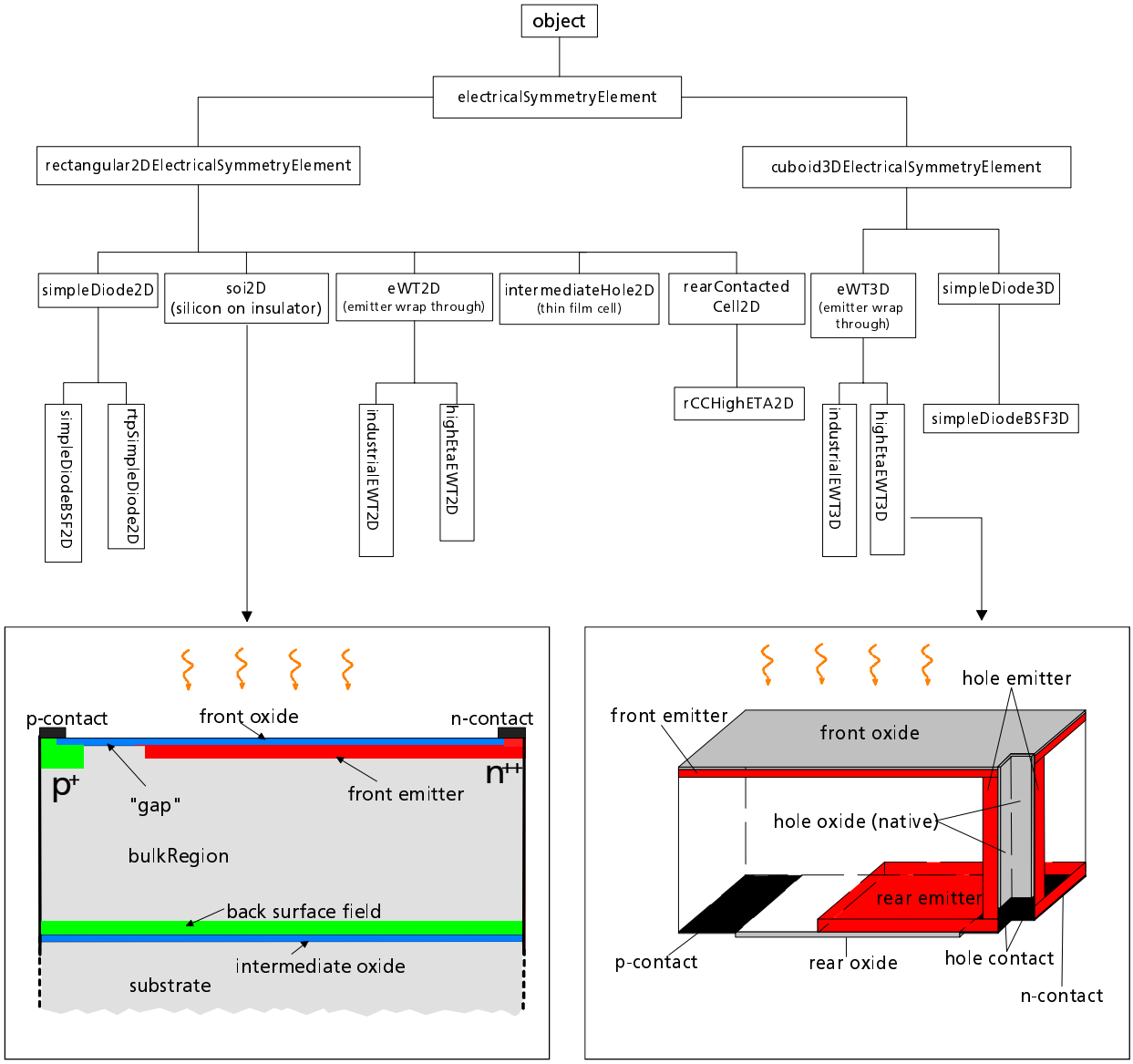

Fig. 4.8: Object tree *SolarCellResearcher`ElectricalSymmetryElements* for two- and three-dimensional device simulation.

activity of the hole emitter, the current flow patterns found in an emitter wrap-through cell cannot accurately be described by a two-dimensional model.

The conception of the object class *electricalSymmetryElement* minimises the implementation effort for the simulation of a new solar cell geometry: the coordinates of all cell regions are calculated from a few fundamental dimensions, *e.g.* from the cell thickness, the spacing of the metal contact fingers, etc. This allows for variation of the size or thickness of the symmetry element without having to draw the symmetry element anew with a CAD tool.

An electrical symmetry element is constructed from subobjects of the classes *region* and *profile* shown in Fig. 4.1.

An object of type *refinementAssistant* helps to construct discretisation meshes for the electrical device simulation in two and three dimensions. The regions of a semiconductor device have to be refined differently. A high density of mesh points in device regions with a

steep doping gradient is needed for the convergence of the numerical device simulation. Therefore, refinement regions used by the *refinementAssistant* are distinguished as follows: bulk refinement, optical refinement at illuminated surfaces with high gradients of optically generated charge carriers, emitter refinement, space charge region refinement and contact refinement. Typically, a device region is given as an argument to the *refinementAssistant* and the type of refinement is specified. The *refinementAssistant* automatically provides the output for the program *MESH* which is used for the construction of the electrical discretisation mesh.

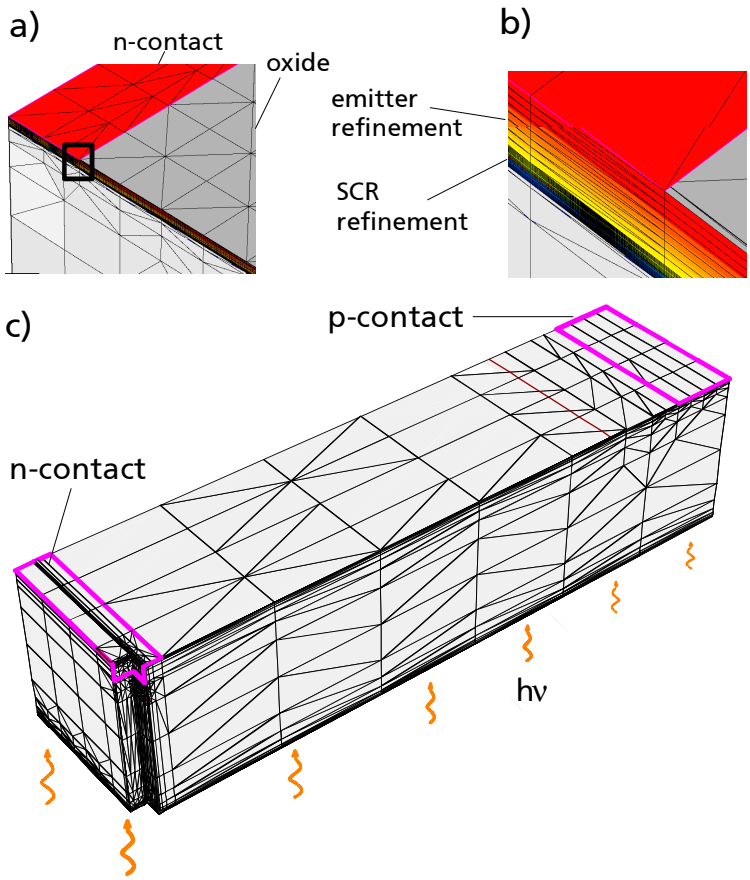

Fig. 4.9: Discretisation meshes created by the *refinementAssistant*; (a) Emitter refinement at the front surface of a three-dimensional cell structure; (b) enlargement of the black square in a): the *refinementAssistant* automatically generates a dense space charge region (SCR) refinement for each emitter refinement; (c) discretisation mesh for three-dimensional simulation of an emitter wrap-through cell.

4.5.4 Baseline models

Fig. 4.10 shows baseline models of solar cells representing realised solar cells. Models for the following solar cells are implemented in *PVObjects* so far:

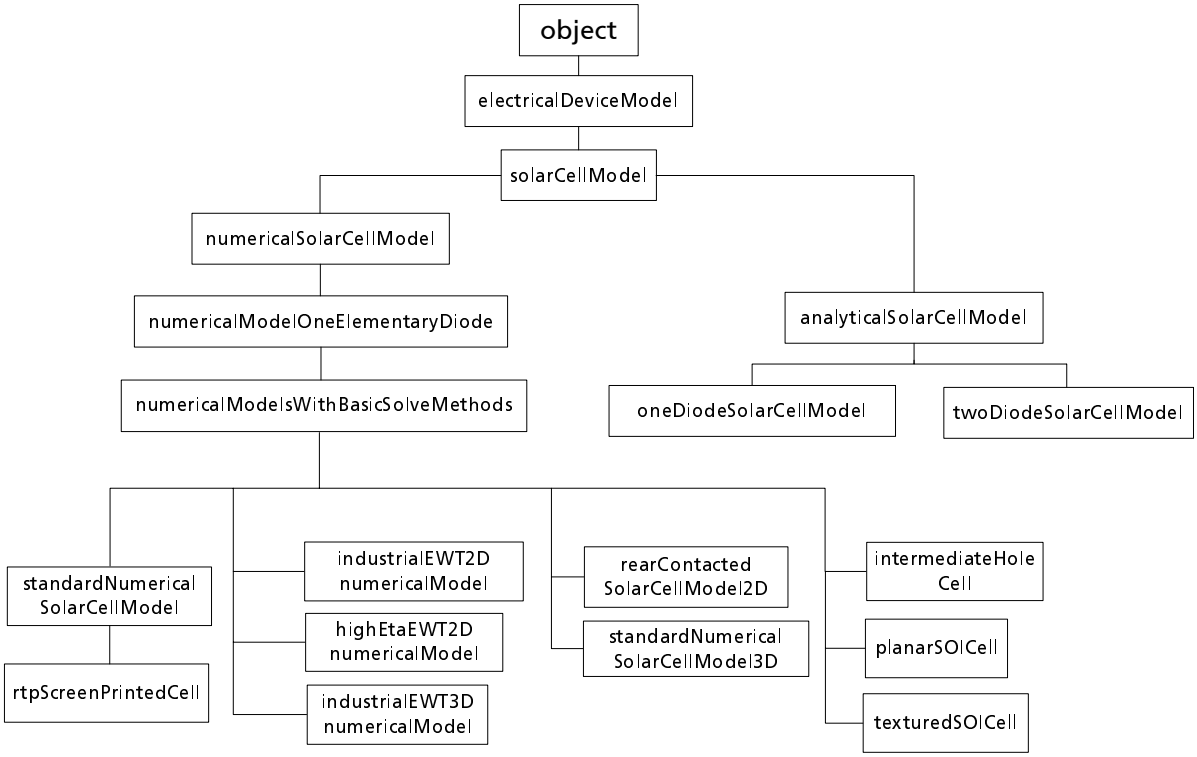

Fig. 4.10: The object tree *SolarCellResearcher`SolarCellModels* contains models for analytical and numerical solar cell simulation.

- Silicon on insulator solar cells (Chapter 6)
- Highly efficient rear contacted solar cells (Chapter 7)
- Cells with an emitter from rapid thermal processed (RTP) phosphorous dopants and evaporated contacts [31]
- The emitter wrap-through cell [73]
- Crystalline silicon thin film cells on low cost substrates [74], [75]

4.6 A virtual measurement laboratory

In a real laboratory situation a solar cell is carried to a measurement apparatus to be measured. The illumination conditions and specific electrical boundary conditions at the cell terminals are controlled by the measurement apparatus. This situation is reflected in the objects responsible for the device characterisation: in the virtual laboratory a solar cell model is passed to an object of type *measurementApparatus*. The abstract base class

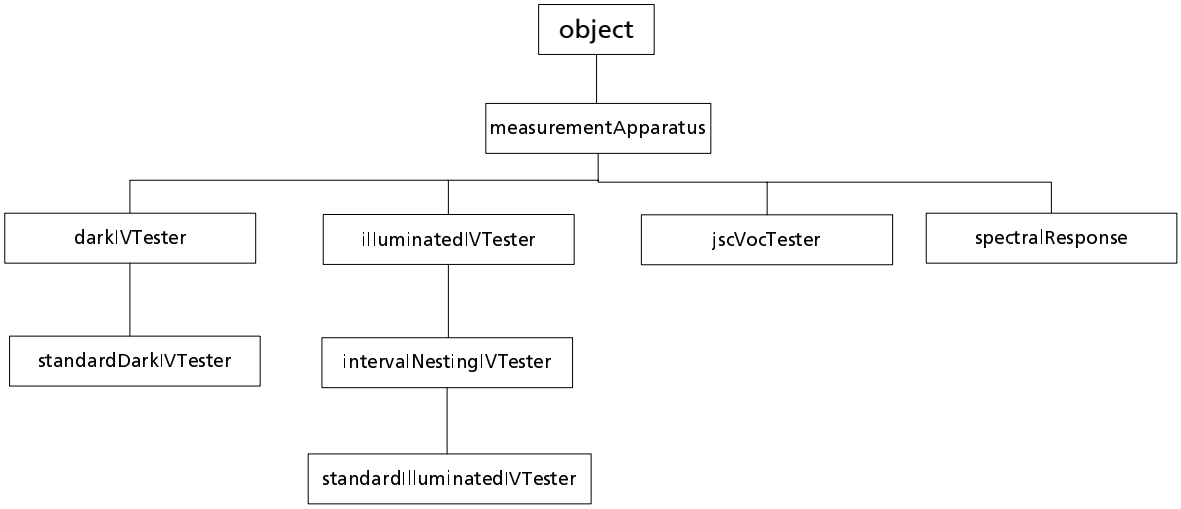

Fig. 4.11: *SolarCellResearcher`MeasurementLab*: a virtual measurement laboratory for the characterisation of solar cells implemented in *PVObjects*.

measurementApparatus represents all standard characterisation facilities. Illumination conditions and the applied voltage are controlled via polymorphic methods by the measurement apparatus. Therefore, it was possible to implement measurement-objects, which can be used to characterise analytical *and* numerical solar cell models using the *same* code. As long as the solar cell model provides all polymorphic methods to realise illumination and injection conditions it can be "measured" by the *measurementApparatus*.

4.6.1 Characterisation facilities

Using the abovementioned polymorphic methods for the simulation of illumination and injection conditions it is a straightforward procedure to implement all standard solar cell measurement facilities at a high level of abstraction. Fig. 4.11 shows the object tree of a virtual measurement laboratory implemented in *PVObjects*. The series resistance-corrected J_{sc}-V_{oc} *curve* [76] can be simulated with the object *jscVocTester*. The object *spectralResponse* is capable of simulating the differential spectral response as described in Section 3.5.

4.6.2 Example characterisation

One application of the characterisation facilities is shown in Fig. 4.12. The model of a planar silicon on insulator cell (class *planarSOICell* in Fig. 4.10) is passed to the virtual measurement apparatus *spectralResponse*. Applying the method *evaluateSpectralResponse* to the instance of class spectralResponse causes all numerical simulation tools to be executed automatically: first, a request to an object of class *planarThinFilmGeneration* (Fig. 4.5) causes the ray tracing procedure to calculate the generation function using *RAYN*. In the next step, an object of type *mesh* (Fig. 4.7) generates the discretisation mesh for the SOI-structure (Fig. 4.8) using default values for all physical dimensions and doping profiles. Optical generation rates with white bias light and added monochromatic measurement light are calculated (Fig. 4.6b) for several wavelengths. The difference between simulated short circuit

current densities with and without monochromatic light added to the white bias light results in the differential spectral response. This is achieved by an instance of type *dessis*.

```
Needs["PVObjects`SolarCellResearcher`MeasurementLab`"];

solarCellModelVar = new[planarSOICell];

monochromatorVar = new[spectralResponse, solarCellModelVar];

evaluateSpectralResponse[monochromatorVar];

eqeSimulated = giveExternalQuantumEfficiency[monochromatorVar];

eqeMeasured = sR2QE[readSrWimo["simox4_2c1.dat"]];

multipleLogListPlot[{"simulated", "measured"}, {eqeSimulated, eqeMeasured},
  < graphics options discarded >]
```

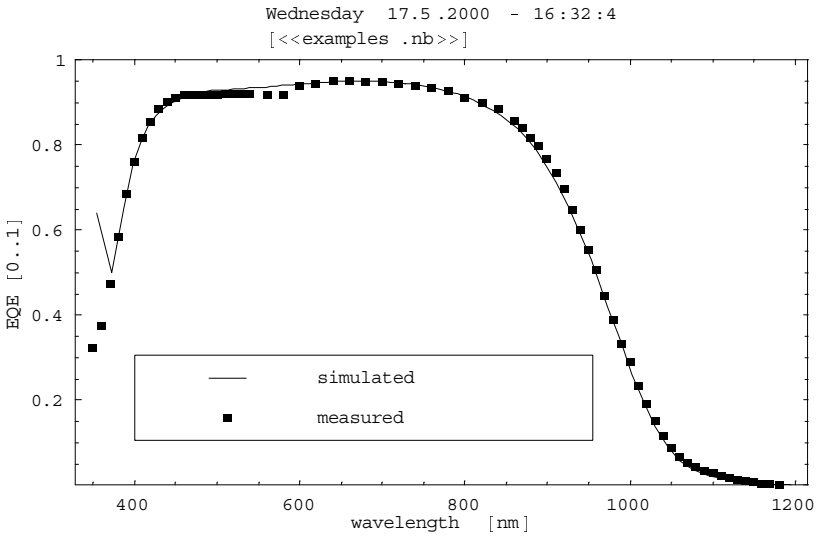

Fig. 4.12: Simulation of external quantum efficiency of a silicon on insulator solar cell with planar front. The complete code for the simulation is shown including a comparison with measured data.

Since all requests to numerical tools are handled by *Mathematica*, numerous operations on objects can easily be combined to higher level functions. Thus, the powerful set of mathematical functions built into *Mathematica* [63], [77] can be used to process the simulation input and evaluate simulation results. An example is shown in Fig. 4.13. The influence of the *n*- to *p*- metal finger distance of a textured silicon on insulator structure on the solar cell output parameters is examined. The function *variation*, which is defined in the example, performs a complete simulation of an illuminated *I-V* curve for a given *n*- to *p*- finger distance.

```
Needs["PVObjects`SolarCellResearcher`MeasurementLab`"];

solarCellModelVar = new[planarSOICell];

elem = giveElementaryDiode[solarCellModelVar];

myMesh = giveMesh[solarCellModelVar];

myIVTester = new[standardIlluminatedIVTester, solarCellModelVar];

variation[dsym_] := (setElectricalSymmetryElementWidth[elem, dsym];
  reset[myMesh]; request[myMesh];
  ivSweep[myIVTester];
  {ivOutput -> giveIVOutputParameters[myIVTester], d → dsym}
 )

result = variation /@ Table[i, {i, 400, 1000, 100}];

selectIVOutput[dataSet_] := Transpose[{d /. result, Abs[dataSet] /. (ivOutput /. result)}];

jscPlot = multipleLogListPlot[{"Jsc"}, {selectIVOutput[isc]}, < graphics options discarded >]

ffPlot = multipleLogListPlot[{"FF"}, {selectIVOutput[ff]}, < graphics options discarded >]

vocPlot = multipleLogListPlot[{"Voc"}, {selectIVOutput[voc]}, < graphics options discarded >]

etaPlot = multipleLogListPlot[{"efficiency"}, < graphics options discarded >]

Show[GraphicsArray[{{jscPlot, vocPlot}, {ffPlot, etaPlot}}]]
```

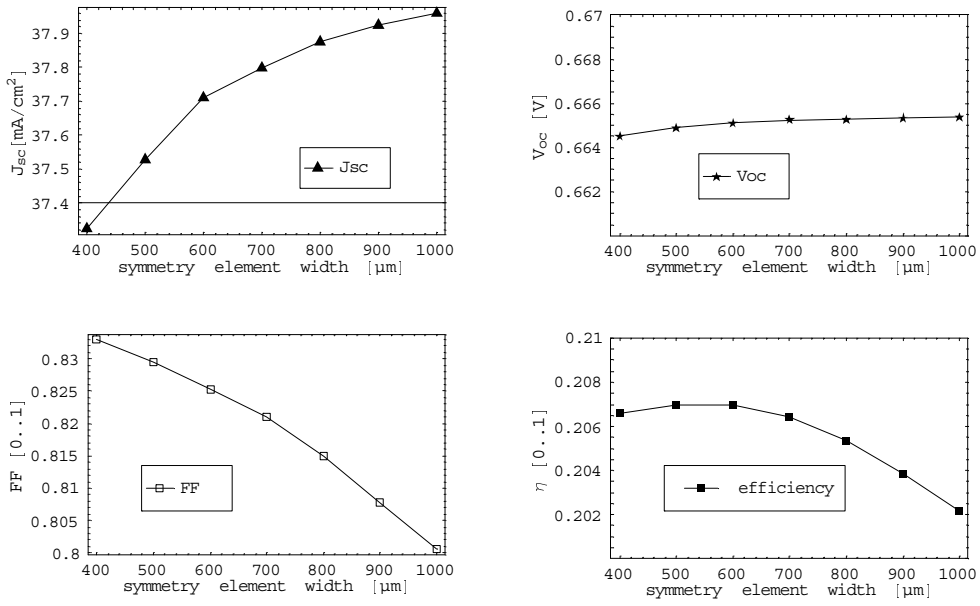

Fig. 4.13: Influence of the *n*- to *p*- finger distance on the solar cell output parameters calculated for the textured SOI cell.

4.7 Conclusion and outlook

A new simulation environment for solar cell characterisation is presented: *PVObjects* unifies analytical physical models, interfaces with elaborate commercial simulation software and the corresponding evaluation methods. Furthermore, prototypes of existing solar cells are implemented in terms of measured values and material data.

The tool can be enhanced by new material objects, physical models and solar cell models. New solar cell structures resembling implemented structures can easily be implemented using the mechanism of inheritance. Therefore, *PVObjects* provides a system for solar cell knowledge representation, achieved by objects having default values corresponding to realised materials and solar cells.

The code of *PVObjects* is written in the *Mathematica* programming language, which is based on system independent commands. This assures compatibility on a wide variety of computer operating systems without the need to compile the code. The simulation code can be published at a high level of abstraction, as shown in this chapter. Simulation results can be reproduced by the reader if the short source code is attached to publications.

PVObjects is highly suitable for teaching purposes: predefined examples can be executed and modified interactively by students.

5 Numerical simulation of recombination properties of phosphorous doped emitters

5.1 Introduction

The commonly used band gap narrowing (BGN) models for crystalline silicon do not describe heavily doped emitters with desirable precision. One of the reasons is that the applied BGN models were empirically derived from measurements assuming Boltzmann statistics. A new BGN model derived by Schenk [68] from quantum mechanical principles is applied to the numerical simulation of recombination properties of phosphorous doped silicon emitters. It is demonstrated that carrier degeneracy and the new BGN model substantially affect the electron-hole product within the emitter region. Simulated saturation current densities of heavily phosphorous doped emitters, calculated with the new BGN model are lower than results obtained with the empirical BGN model of del Alamo [69].

5.2 Band gap narrowing

Many-body interactions among the free carriers and between free carriers and dopants lead to a shrinkage of the silicon band gap, called band gap narrowing (BGN): In *n*-type silicon, free electrons are attracted by ionised donor atoms. This *electron-impurity interaction* leads to a shift of the conduction band to lower energies. The Fermion nature of the electrons tends to keep the ones with parallel spin orientation away from each other. This spatial exclusion principle reduces the repellant Coulomb forces between electrons and hence is equivalent to an attractive *exchange energy*. Free electrons screen the Coulomb forces between holes. This shifts the valence band upwards by the so called *correlation energy*. The electrons in the conduction band allow the valence holes to relax around positively charged donor centres and thus gain in energy. This *hole-impurity interaction* causes a rise in the energy of the valence band.

The emitter models for silicon commonly found in the literature are not able to describe highly doped emitters (obtained, for instance, with rapid thermal annealing) with satisfactory precision. Such models use empirical (or apparent) BGN data ΔE_g^{app} derived from transport measurements of highly doped silicon, and are parameterised as a function of doping density N_D. Hence, physical effects like carrier-impurity or carrier-carrier interactions are not separated from each other. Moreover, empirical BGN data represent a conglomeration of various physical effects; these are degeneracy effects at high doping levels, the change in the density-of-states due to the formation of an impurity band at medium to high doping densities, and the asymmetry in gap shrinkage [78]. The emitter model developed in this thesis

considers these effects separately and is therefore a more precise one. It goes beyond the application of empirical BGN models.

The BGN model of Schenk [68] is applied here, which is a comprehensive silicon BGN model that is entirely derived from quantum mechanical principles. This model provides the band gap energies E_v and E_c separately, and hence is compatible with Fermi-statistics. It also distinguishes between dopant- and free-carrier induced gap shrinkage. This is a fundamentally different approach from the determination of ΔE_g^{app}. Hence, it is generally insufficient to compare solely the resulting ΔE_g of Schenk's model with the ΔE_g^{app} values. However, at low dopant densities and under low-level injection conditions, the BGN model of Schenk can be directly compared with ΔE_g^{app}. Fig. 5.1 shows that there is good agreement between the two approaches. In the high doping range, the model of Schenk provides a similar ΔE_g as photoluminescence measurements (crosses in Fig. 5.1). They give a slightly higher ΔE_g than the model of Schenk due to band tails, which host immobile carriers and therefore do not contribute to BGN relevant to electronic devices.

Gernot Heiser from the University of New South Wales in Sydney implemented the new BGN model of Schenk into a developer version of the device simulator *DESSIS* [41]. This version was used for all simulation results presented in this chapter. The developer version of *DESSIS* numerically solves the complete set of coupled semiconductor equations, and uses Fermi-Dirac statistics for the charge carriers. Hence, using this program version, BGN can be simulated for any doping and injection condition relevant to electronic devices.

In the simulations discussed here, the BGN model of Schenk is compared with the widely used empirical BGN model of del Alamo [69]. With del Alamo's model, Boltzmann statistics must be used for the calculation of the charge carrier distribution [78]. The application of Fermi statistics would overestimate the degeneracy effects, because they are already contained in del Alamo's $\Delta E_g(N_D)$ data.

When comparing these two BGN models, care has to be taken as to the choice of the intrinsic carrier density, n_i. In analogy to the law of mass action for ideal gases, the relation $n_i^2 = n_o p_o$ holds only if the carriers do not interact strongly with each other, *i.e.* in weakly doped silicon. The validity of this law is extended to the heavy doping range by introducing the *effective* intrinsic carrier density, $n_{i,eff}$, using the expression

$$n_{i,eff}^{\ 2} = n_o p_o = n_i^{\ 2} \exp\left[\frac{\Delta E_g}{kT}\right] = n_i^{\ 2}\, \gamma_{BGN}^{\ 2} \tag{5.1}$$

where n_o and p_o are the equilibrium carrier densities in the heavy doping range. The BGN model of del Alamo was derived from electrical measurements using $n_i = 1.45\times10^{10}$ cm^{-3} at 300 K. In 1991, the value of n_i was revised to be 1.00×10^{10} cm^{-3} at 300 K [79]. Hence, in order to achieve comparability, $n_i=1.45\times10^{10}$ cm^{-3} is used for simulations with the BGN model of del Alamo and $n_i=1.00\times10^{10}$ cm^{-3} in combination with the BGN model of Schenk.

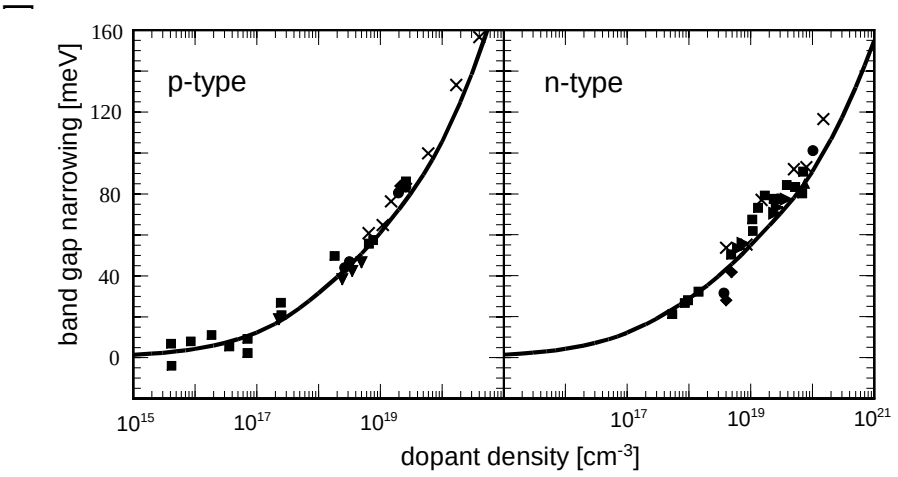

Fig. 5.1: Band gap narrowing as a function of phosphorous concentration under low-injection conditions. Symbols indicate measured data [80], the solid lines show the model dependency as obtained from Ref. [68].

5.3 Simulation method

In order to determine the recombination properties (*i.e.*, J_{oe}) of *n*-type emitters, steady-state photoconductance (PCD) measurements [81] of n^+p structures with a perfectly passivated rear surface are simulated. A schematic doping profile of an *n*-type emitter is shown in Fig. 5.2.

In contrast to the commonly treated case of an abrupt *p*-*n* junction with a quasi neutral emitter, a Gaussian doping profile is used. Thus, the electric field at the front surface and in the bulk of the emitter is non-zero (see Fig. 5.3) due to the doping gradient. It is considered that the edge of the space charge region x_e is to be located towards the base side of the *p*-*n* junction, where the electric field has dropped to 1 ‰ of its maximum value. Therefore, the emitter saturation current density J_{oe} is determined at the edge of the space charge region at position x_e, shown as dotted line in Fig. 5.2 and Fig. 5.3.

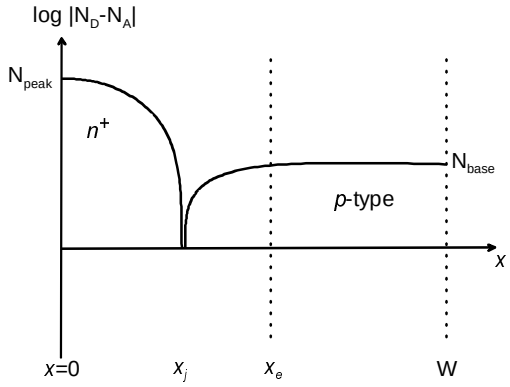

Fig. 5.2: Schematic doping profile of an *n*-type emitter diffused into a *p*-doped substrate of thickness *W*. The dotted line with position x_e is the edge of the space charge region to be located towards the base side of the junction.

In order to determine J_{oe} as a function of injection level, the intensity of the incoming light is varied, so that the simulation approach is equivalent to the commonly used PCD measurements.

All simulation results shown in this chapter are obtained illuminating the sample with blue light from the rear side. Comparison with simulations, using illumination of white light from the front, showed that the influence on J_{oe} of such variations in steady state illumination can be neglected in comparison to the deviations between the BGN models. The simulation parameters are listed in Tab. 5.1.

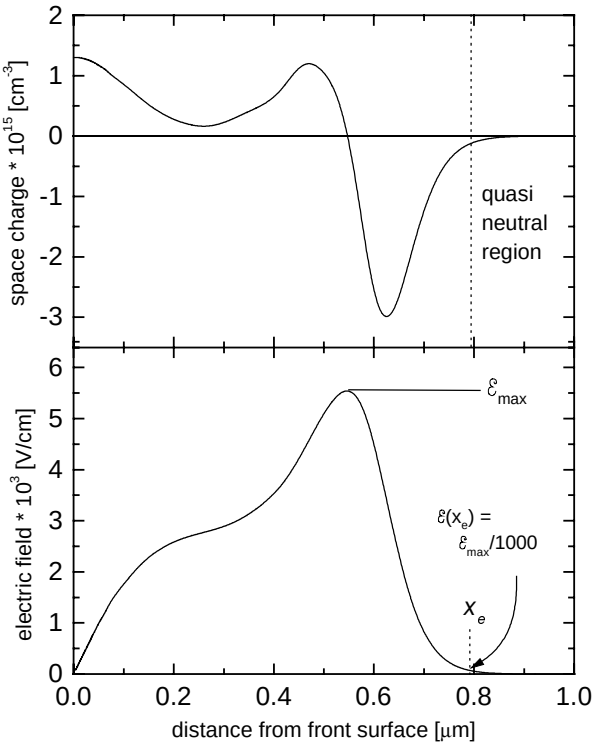

Fig. 5.3: Space charge density and electric field across a heavily doped emitter with a Gaussian doping profile.

For a fixed injection level, the averaged electron density $\overline{n}$ in the base is calculated by numerical integration of the simulated local electron density *n(x)* over the *p*-type region

$$\overline{n} = \frac{1}{W - x_e} \int_{x_e}^{W} n(x)\, dx \,. \tag{5.2}$$

The averaged generation rate is calculated as

$$\overline{G} = \frac{1}{W} \int_{x_e}^{W} G(x)\, dx \tag{5.3}$$

where $G(x)$ is the optical generation profile. Given the generation current-density as $J_{gen} = q\overline{G}$, we define the effective minority carrier lifetime in the base for steady state conditions by [82]

$$\tau_{eff} = \frac{\Delta\overline{n}}{\overline{G}} \,. \tag{5.4}$$

The Shockley-Read-Hall (SRH) and Auger recombination currents in the emitter and the base are found by integration over the simulated local recombination rates

$$J_{Auger,em} = q\int_0^{x_e} R_{Auger}(x)\,dx; \qquad J_{Auger,base} = q\int_{x_e}^{W} R_{Auger}(x)\,dx \tag{5.5}$$

$$J_{SRH,em} = q\int_0^{x_e} R_{SRH}(x)\,dx; \qquad J_{SRH,base} = q\int_{x_e}^{W} R_{SRH}(x)\,dx\,. \tag{5.6}$$

The hole recombination current density at the emitter surface is given by

$$J_{surf} = q\left(p(0) - p_0(0)\right)S_h \tag{5.7}$$

where S_h is the surface recombination velocity of holes at the emitter surface, and p_0 is the hole density at thermal equilibrium. For steady state conditions, the generation current density (Eq. 2.) equals the sum of all recombination currents

$$J_{gen} = J_{Auger,base} + J_{Auger,em} + J_{SRH,base} + J_{SRH,em} + J_{surf}\,. \tag{5.8}$$

Dividing Eq. 5.8 by J_{gen} gives the relative recombination fraction for each recombination 'channel'

$$f_{Auger,base} + f_{Auger,em} + f_{SRH,base} + f_{SRH,em} + f_{surf} = 1\,. \tag{5.9}$$

Finally, the emitter transparency factor α_t is defined as the minority-carrier current reaching the front surface divided by the current injected into the emitter [83]

$$\alpha_t = \frac{J_{surf}}{J_h(x_e)}\,. \tag{5.10}$$

If all carriers injected from the *p-n* junction reach the surface, the emitter is called "transparent" [84]. A transparent emitter has transparency factor near one. For a vanishing transparency factor the emitter is said to be "opaque" and, in this case, most of the emitter recombination occurs in the bulk of the emitter.

Investigated structure	Gaussian shaped n^+ diffusion on p-type substrate
Substrate	Intrinsic with $N_{base} = 10^{13}$ cm^{-3} or $N_{base} = 10^{16}$ cm^{-3}
Temperature	300 K
SRH bulk recombination	Midgap traps with equal capture cross sections for electrons and holes, $\tau_{bulk} \approx 600$ µs
Radiative recombination	Neglected
Auger recombination	$C_n = C_{n,lli}\left(1 + H_n \exp\left[-\frac{n}{N_{0,n}}\right]\right)$; C_p similar $C_{n,lli}$=2.8×10^{-31} cm^6/s; $C_{p,lli}$=0.99×10^{-31} cm^6/s; H_n=1.96; H_p=7.38 $N_{0,n}$=5×10^{17} cm^{-3}; $N_{0,p}$=5×10^{17} cm^{-3} $R_{Auger} = \left(C_n n + C_p p\right)\left(n p - n_{i,eff}^2\right)$
Surface recombination	Oxidised front surface, $S_e = S_h$ Oxidised rear surface, $S_e = S_h = 0$
Intrinsic carrier density	n_i = 1.00 10^{10} cm^{-3} [85] for simulations with the BGN model of Schenk and n_i = 1.45 10^{10} cm^{-3} in combination with the apparent BGN model of del Alamo
Mobility model	Klaassen unified mobility model [80]

Tab. 5.1: Simulation parameters used for the emitter modelling in this chapter.

5.4 Emitter saturation current density

A general definition of the emitter saturation current density is given as

$$J_{0e} \equiv \frac{J_e(x_e)}{n(x_e)\,p(x_e) - n_{i,eff}^2(x_e)}\, n_{i,eff}^2(x_e), \tag{5.11}$$

i.e. J_{0e} is determined (at open-circuit conditions of the diode) by the electron recombination current $J_e(x_e)$ at the edge x_e of the space charge region, divided by the normalised excess *p-n* product.

Assuming non-degenerated holes, the *p-n* product in Eq. 5.11 can be expressed as [18]

$$n(x)\,p(x)=n_i^2\,\gamma_{BGN}^2(x)\,\gamma_{\mathrm{deg}}\big(z(x)\big)\exp\left(\frac{E_{fc}(x)-E_{fv}(x)}{kT}\right) \tag{5.12}$$

where the degeneracy factor γ_{deg} is given by

$$\gamma_{\mathrm{deg}}(z)=\frac{F_{1/2}(z)}{\exp(z)};\qquad z=\frac{E_{fc}(x)-E_c(x)}{kT}. \tag{5.13}$$

$F_{1/2}$ is the Fermi integral of order ½, describing Fermi-Dirac statistics. The degeneracy factor γ_{deg} is a measure of how much the electron density deviates from its classical value. The quasi-Fermi levels $E_{fc}(x)$ and $E_{fv}(x)$ are found with *DESSIS* from a self-consistent solution of the coupled semiconductor differential equations.

Pietro Altermatt from UNSW has proved that simulating J_{oe} in this way gives results which are consistent with J_{oe} measurements [86]. Cuevas et al. measured the J_{oe} values of planar emitters after applying various surface passivation treatments, and also after covering the surfaces with metal. These samples served to test the consistency of the simulation method described above as in the case of metal covered surfaces S is limited by the thermal velocity of free carriers, *i.e.* $S\approx 1\times10^7$ cm/s.

5.5 Electron-hole product in heavily doped emitters

The simulated, position dependent *p-n* product (Eq. 5.12) is visualised in Fig. 5.4 for a Gaussian shaped phosphorous diffusion with $N_{peak} = 1.2\times10^{20}$ cm^{-3}. In this simulation, the device is illuminated with blue light from the rear with constant intensity.

Schenk's model yields lower ΔE_g-values for high doping densities than the model of del Alamo. One has to keep in mind that del Alamo measured ΔE_g at $N_{dop} < 7\times10^{19}$ cm^{-3}. At higher doping densities, an extrapolation of his expression, given in Ref. [69], is used. This extrapolation has been commonly used to simulate heavily doped emitters. However, for $z=\frac{E_{fc}-E_c}{kT}\gtrsim -2$ the electron gas becomes degenerated [87]. Hence, Fermi statistics becomes important at doping densities above 10^{18} cm^{-3} (Fig. 5.4c).

Band gap narrowing increases the *p-n* product towards the emitter surface (Fig. 5.4b). For very high doping densities, the degeneracy factor (Fig. 5.4c) tends to decrease the *p-n* product, leading to a maximum value at a certain distance below the emitter surface (solid line in Fig. 5.4d). The counteracting effect between band gap narrowing and carrier degeneracy cannot be quantified using the model of del Alamo, as this BGN data was extracted from electrical at $N_D < 7\times10^{19}$ cm^{-3} where no strong degeneracy occurs [88].

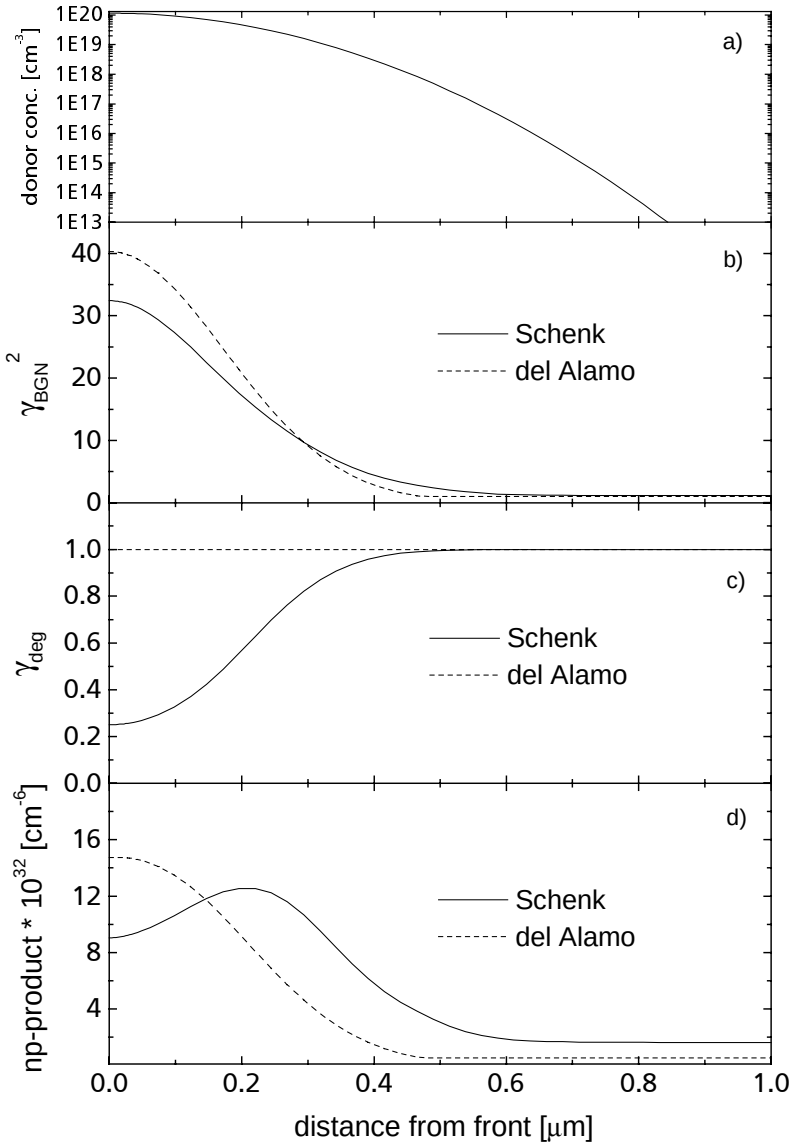

Fig. 5.4: The *p-n* product within a heavily doped *n*-type emitter with respect to the two investigated BGN models. Solid lines show the results using the BGN model of Schenk, and Fermi-Dirac statistics for the charge carriers. The dashed lines are obtained with the BGN model of del Alamo and Boltzmann statistics. (a) Doping profile; (b) influence of band gap narrowing on *p-n* product, *i.e.* $\gamma_{BGN}^2 = exp(\Delta E_g/kT)$; (c) degeneracy factor due to the use of Fermi-Dirac statistics in the model of Schenk; (d) resulting *p-n* product in steady state condition, given by Eq. 5.12.

5.6 Recombination fractions of a heavily doped emitter

As an example of the application of the numerical emitter model developed in this thesis, the recombination properties of a heavily phosphorous doped emitter is analysed. The emitter was fabricated by King *et al.* [89] (emitter M4X, peak doping density $N_{peak}=1.2\times10^{20}$ cm^{-3}, junction depth=0.64 µm). A surface recombination velocity of $S_{no} = S_{po} = 10^4$ cm/s and a wafer thickness of 260 µm is assumed. Numerical simulations with *DESSIS* reveal the

recombination current within each region, using equations 5.5, 5.6 and 5.7. The relative recombination fractions (Eq. 5.9) are shown in Fig. 5.5 as a function of Δn.

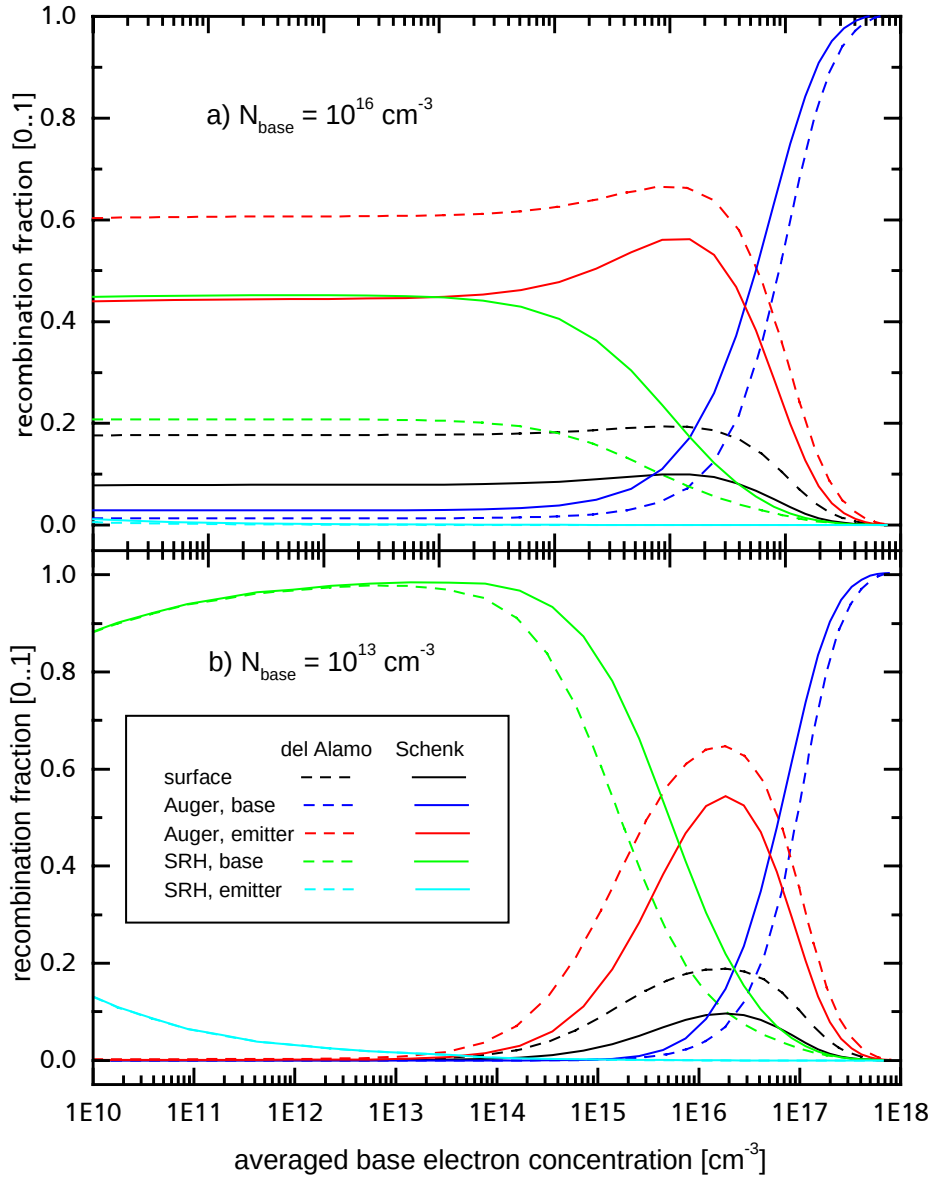

Fig. 5.5: Recombination fractions of sample M4X as a function of the averaged electron concentration in the base. The solid curves were calculated using the BGN model of Schenk, and the dashed curves using the BGN model of del Alamo; (a) N_{base} = 10^{16} cm^{-3} ($\rho_{sheet} \approx 1.5$ Ωcm); (b) N_{base} = 10^{13} cm^{-3} ($\rho_{sheet} > 1000$ Ωcm).

5.6.1 Low injection conditions

Fig. 5.5 indicates that SRH recombination in the emitter (occuring mainly in the space charge region) can be neglected for sample M4X, as the emitter recombination is dominated by Auger- and surface recombination. Under low injection conditions, 79% (52%) of the recombination occurs in the emitter, using the BGN model of del Alamo (Schenk). This difference arises because the BGN model of Schenk is used in conjunction with Fermi statistics, leading to a decreasing *p-n* product towards the emitter's front surface (Fig. 5.4d).

Lower values of the *p-n* product lead to lower values of the hole density near the front surface of the emitter. Thus, both the surface and Auger-recombination fractions are reduced. Due to the difference in the hole density at the front surface, significantly different values for the surface recombination *velocities* have to be specified to obtain the same surface recombination *currents*. This explains why surface recombination velocity values, extracted from J_{0e} measurements, depend on the applied simulation models, as will be discussed in further detail below.

5.6.2 High injection conditions

A strong injection dependence of the recombination fractions is found for high injection conditions. At $\overline{n}=2\times10^{16}\,cm^{-3}$, the emitter recombination fractions are at a maximum of 83 % (63%), using the BGN model of del Alamo (Schenk). At this injection level, maximum sensitivity for the extraction of the surface recombination velocity from PCD measurements is reached.

5.7 Simulated J_{0e} of Gaussian doping profiles

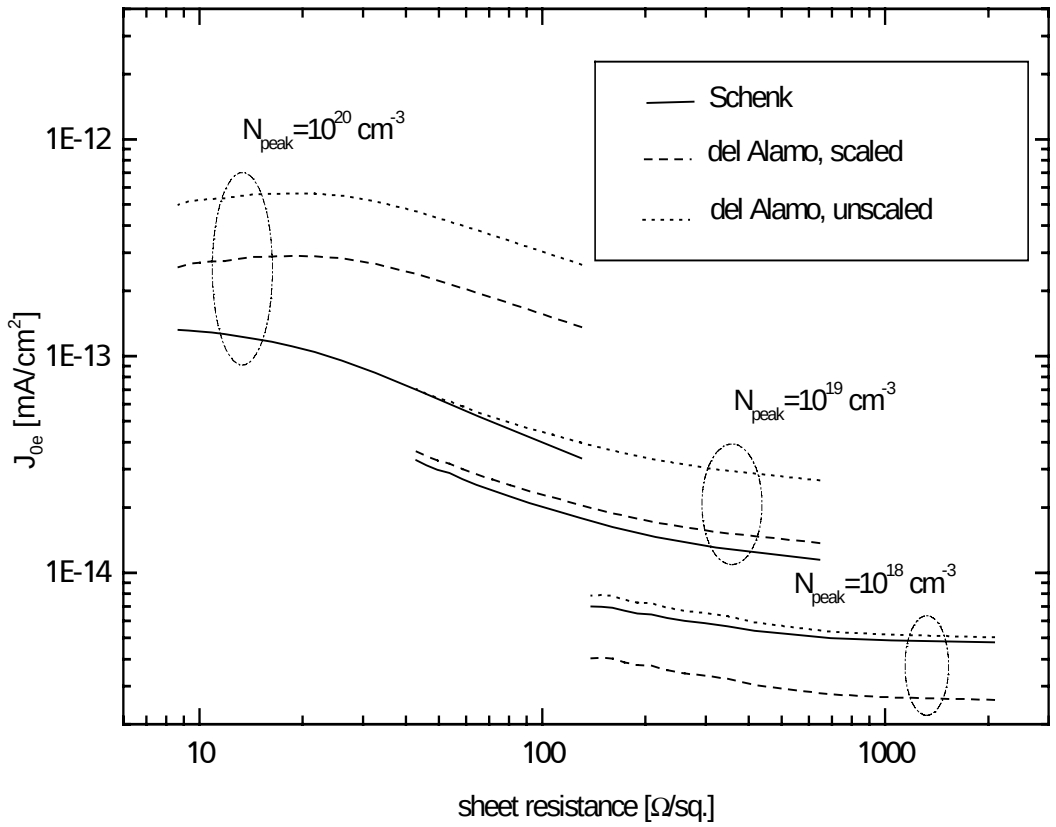

Fig. 5.6 shows J_{0e} of various Gaussian shaped doping profiles, simulated as described above. The sheet resistance is varied by changing the junction depth. For comparison of J_{0e}-values, results obtained with the BGN model of del Alamo are scaled to n_i=1.00×10^{10} cm^{-3} as described in [89], namely using $J_{0e}=J_{0e,delAlamo}\left(1.0/1.45\right)^2$. At $N_{peak}=10^{18}\,cm^{-3}$, the Schenk model yields double the J_{0e}-value than the model of del Alamo, because the latter was derived

from measurements using the old (and excessively large) value of $n_i = 1.45\times10^{10}$ cm^{-3}. Nearly identical results are obtained with the two models at $N_{peak} = 10^{19}\ cm^{-3}$.

The largest differences between the two models occur in heavily doped emitters where carrier degeneracy becomes important. J_{0e}-values obtained with the BGN model of Schenk are five times *lower* for small junction depths. The difference in J_{0e} between the two models becomes less pronounced at large junction depths (*i.e.* at a low sheet resistance), because the surface recombination losses become small compared to the bulk recombination losses in the emitter.

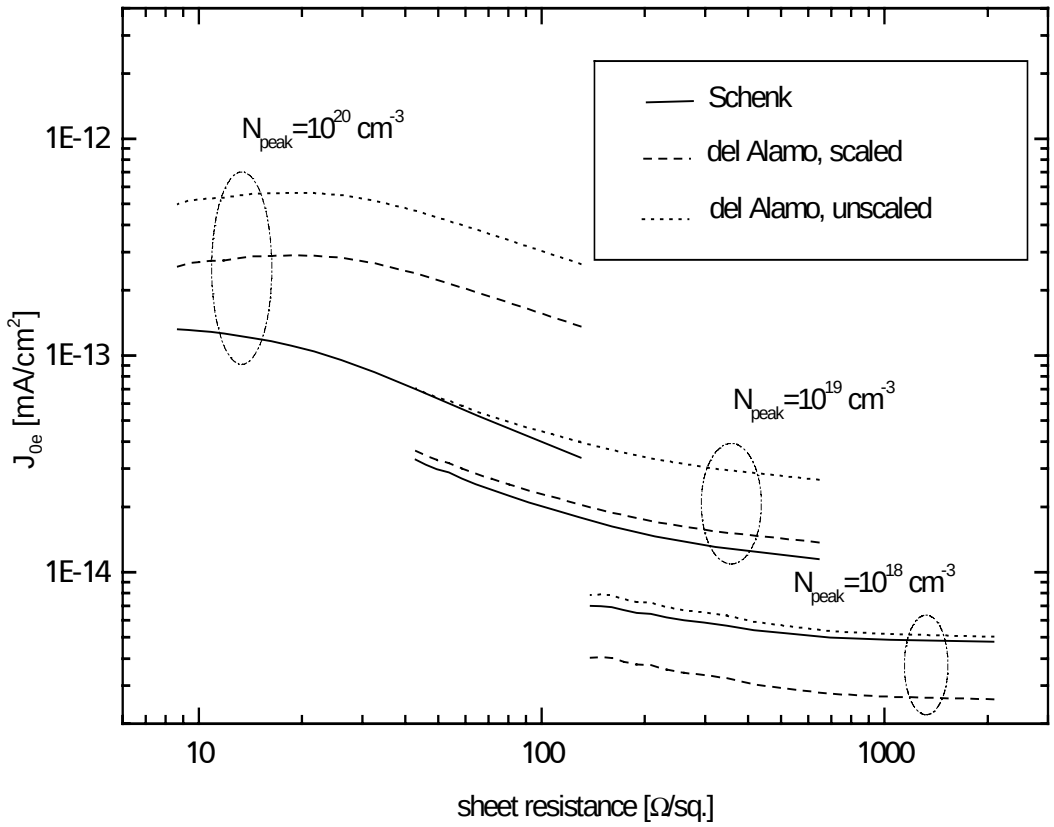

Fig. 5.6: Simulated J_{0e}-values, using Gaussian doping profiles with a fixed peak doping density. Simulation results obtained with the BGN model of del Alamo are shown as short dashed curves. The long dashed curves were obtained by scaling these simulation results to the currently accepted value for the intrinsic carrier density of silicon. To allow comparison between curves of constant peak doping concentration the same S_p-values were used for both BGN models: $S_{p0} = 10^4$ cm/s for $N_{peak} = 10^{20}$ cm^{-3}; $S_{p0} = 10^3$ cm/s for $N_{peak} = 10^{19}$ cm^{-3}; $S_{p0} = 10^2$ cm/s for $N_{peak} = 10^{18}$ cm^{-3}.

5.8 Extraction of surface recombination velocities

To the author's knowledge, the surface recombination velocity S of heavily doped emitters cannot be measured directly. S is commonly extracted by reproducing J_{0e} measurements with a theoretical model, assuming that the boundary condition for the recombination current at the surface is $J_{surf} = q\ S\ \Delta p$, where q is the electronic charge and Δp is the excess minority carrier density at the surface. Thus, the extracted value of S depends in a complex way on carrier mobility, Auger recombination, BGN and carrier statistics. Only if the simulation model

describes the recombination fractions at the surface, in the bulk of the emitter and in the base realistically, can meaningful values of S be extracted (by comparing Eq. 5.11 with measurements of J_{0e}). Otherwise, the extracted S value represents solely a fit factor, and may have no physical meaning.

Using *DESSIS*, J_{0e} of some selected emitters fabricated by King [89] was simulated, and compared with King's J_{0e} measurements. It is assumed that the base was highly injected ($\Delta n = 10^{16}\ cm^{-3}; N_{base} = 10^{13}\ cm^{-3}$) in King's experiment. J_{0e} is simulated as a function of S_h in the SRH formula (mid gap traps). The simulated $J_{0e}(S_h)$ values are shown in Fig. 5.7 for a wide range of S_h, using the BGN model of Schenk (solid curves) and del Alamo (dashed curves), respectively. The measured J_{0e}-values, indicated by dotted horizontal lines, are scaled to $n_i = 1.00\times10^{10}\text{cm}^{-3}$. A 10 % error for J_{0e} smaller than 10^{-13} A/cm^2 is assumed, and 20 % for sample M4X [89].

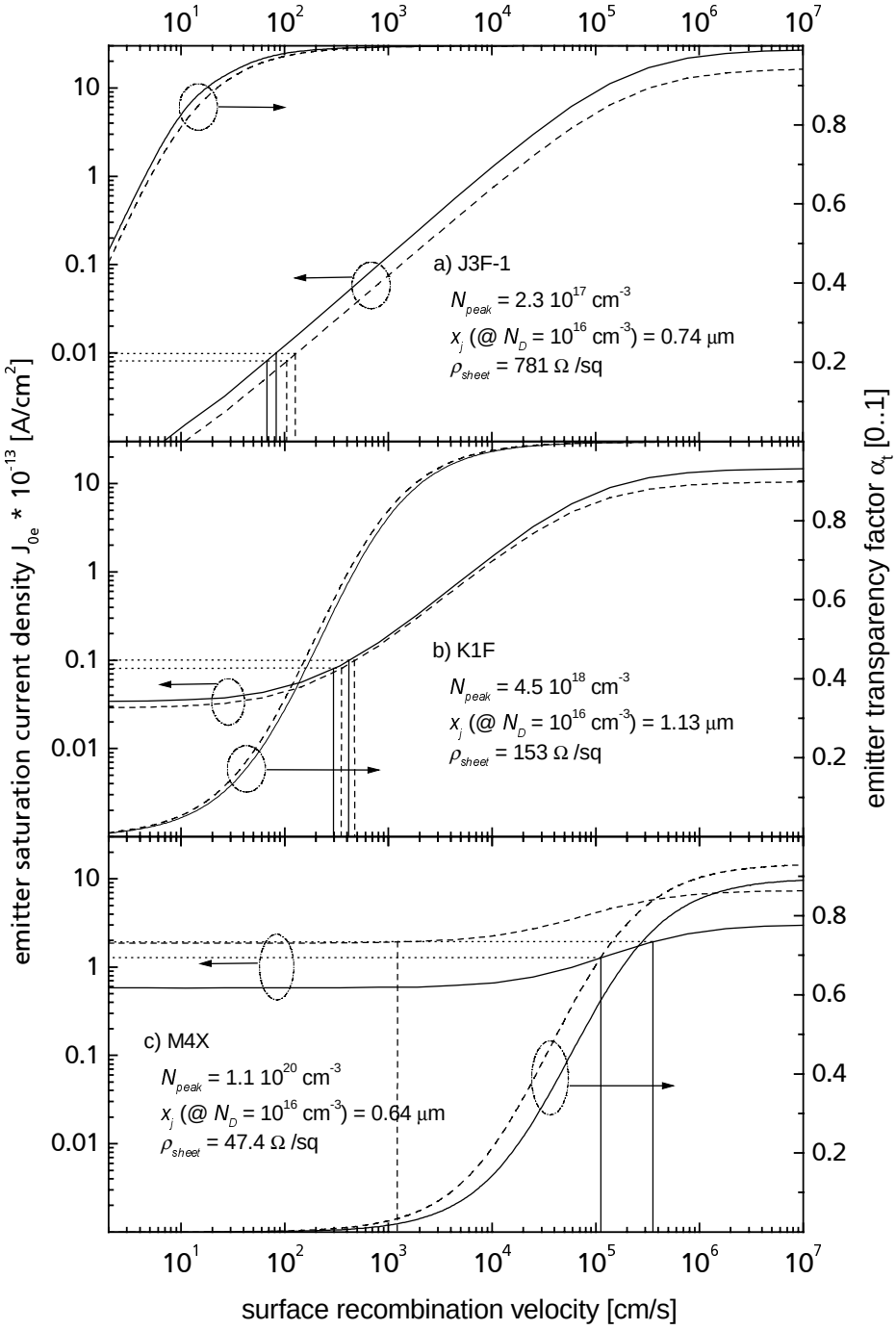

Fig. 5.7: J_{0e} as a function of the surface recombination velocity for three different emitter doping profiles. J_{0e}-values, measured by King are scaled to match $n_i = 1.0\times10^{10}$ cm^{-3} and shown as horizontal lines with respect to the estimated measurement errors [89]. Solid curves: simulations using the BGN model of Schenk; dashed curves: BGN model of del Alamo. Emitter transparency factors are plotted on the right y-axis.

Fig. 5.8 compares simulations with the outlined emitter model with the S_{p0}-values extracted by King. King oxidised the samples at 1000°C (without TCA), followed by a forming gas anneal. The simulated S_h values, shown in Fig. 5.8, can be understood with Fig. 5.7, representing simulation results for a lightly doped emitter (J3F-1), a medium doped

emitter (K1F) and a heavily doped emitter (M4X). In the lightly doped emitter, the extracted S_h values differ significantly between the two BGN models (65 cm/s < $S_{h,Schenk}$ < 80 cm/s and 100 cm/s < $S_{h,delAlamo}$ < 110 cm/s). The reason for this is that the Schenk model provides a considerable amount of BGN at low doping densities, while the del Alamo model yields no BGN at $N_D < 7\ 10^{17}$ [78], [68]. At medium doping levels, the extracted S_h values are similar for both BGN models (300 cm/s < $S_{h,Schenk}$ < 400 cm/s and 330 cm/s < $S_{h,delAlamo}$ < 480 cm/s). In this doping range, the Schenk model yields a slightly larger gap shrinkage, but its effect on the *p-n* product is compensated by a decreasing γ_{deg}, as degeneracy effects become significant.

Finally, in the case of heavily doped emitters, completely different S_h values are obtained (Fig. 5.7c). Using the BGN model of del Alamo, the heavily doped emitter M4X is predicted to be opaque (emitter transparency factor $\alpha_t \approx 0$) [84], *i.e.* most of the recombination occurs in the bulk of the emitter. J_{0e} values that are consistent with King's measurement can only be obtained (dotted horizontal lines in Fig. 5.7) if $S_{h,delAlamo}$ < 2000 cm/s is chosen, which seems unrealistically low. However, using the BGN model of Schenk, $\alpha_t \approx 0.7$ is obtained, implying that 70 % of the emitter recombination occurs at the front surface, resulting in $S_{h,Schenk} = 10^5$ cm/s. As discussed above, Fermi statistics is used here in conjunction with the Schenk model, which lowers the *p-n* product (Fig. 5.4). This explains the smaller contribution of volume recombination to the total recombination in the emitter, resulting in higher S_h-values.

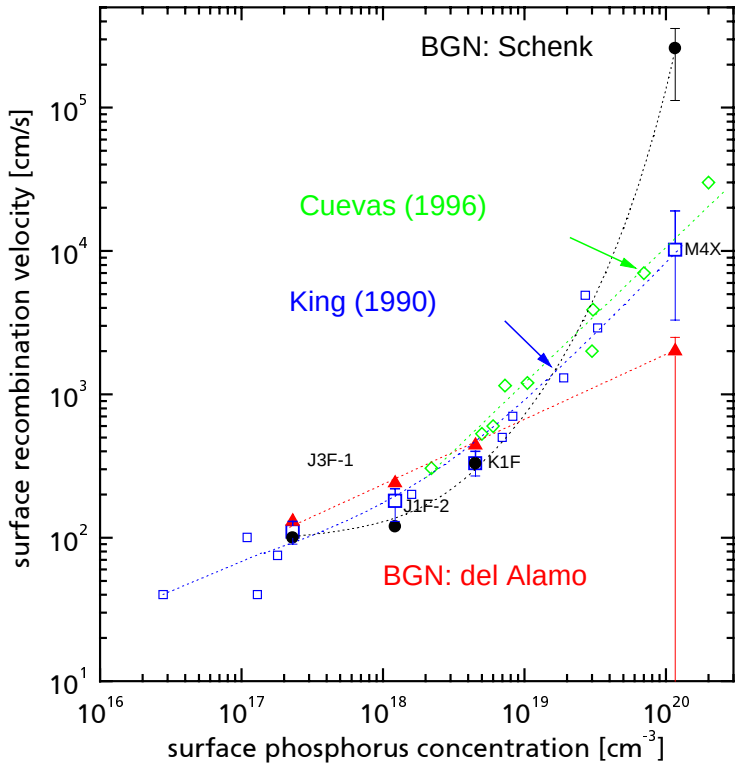

Fig. 5.8: Values of the surface recombination velocity, extracted from J_{0e} measurements of oxide passivated phosphorous emitters. The data shown was extracted from samples which received a forming gas anneal; ❒) extracted by King [89] using a numerical procedure of del Alamo [90]; ●) this work, using *DESSIS*, the BGN model of Schenk and Fermi-Dirac statistics for charge carriers; ▲) this work, using *DESSIS*, the BGN model of del Alamo and Boltzmann statistics for charge carriers; ◊) extracted by Cuevas [91] using an analytical emitter model of Park [29], solid source diffusion; ∇) Cuevas [91], $POCl_3$-diffusion.

The extraction of surface recombination velocity S_h with the method described above was also applied to the J_{0e} measurements of Cuevas [91] and Glunz [92]. An examination of the S_h-values extracted from these measurements can be found in Ref. [86].

5.8.1 Conclusion

A comprehensive numerical emitter model was applied in this thesis describing heavy doping effects accurately. The emitter model uses a new BGN model derived from quantum mechanical principles formulated by Schenk. To obtain the *p-n* product in a heavily doped emitter, the BGN model has to account for carrier-carrier and carrier-impurity interactions separately. Moreover, degeneracy effects become important, and these can only be described using Fermi-Dirac statistics. Taking into account carrier degeneracy, lower values are obtained for the minority carrier density near the front surface of a heavily doped emitter in comparison to results obtained using the Boltzmann approximation and apparent BGN data.

As carrier degeneracy lowers the *p-n* product near the front surface of heavily doped emitters, significantly different S_h values are obtained with the two BGN models in the high doping regime. For example, a difference of two orders of magnitude is obtained at $N_D = 1.2\times10^{20}$ cm^{-3}. The Schenk model yields more realistic values of S_h than the model of del Alamo. This is relevant for both experiment and simulation.

6 Silicon on insulator solar cells with interdigitated front contacts

6.1 Structure and technology of silicon on insulator (SOI) cells

Silicon on insulator (SOI) cells with interdigitated front metal grid are investigated in this chapter. This SIMOX-technology (Separation by Implanted Oxygen) uses high-dose oxygen implantation in order to achieve a buried oxide layer on single crystalline silicon wafers [93]. After an annealing step, a 200 nm thick silicon seeding layer of high crystal quality remains on top of the SiO_2 layer. A subsequent epitaxial CVD step is performed to achieve the final layer thickness of the electrically-active thin silicon layer [94].

prepared with an additional highly doped p^+ -layer between the SiO_2-layer and the electrically-active silicon film in order to study the influence of a back surface field on the cell's performance.

Fig. 6.1 shows the solar cell structure, including the physical dimensions of the SOI cell with the highest conversion efficiency level of 19% (SIMOX5-2c). This cell structure shows all the features of a high-efficiency LBSF-PERL cell, *i.e.* texturisation with inverted pyramids, a double-step emitter, a local p^+-diffusion under the front base contacts, passivation of the surface with a high-quality SiO_2-layer, grid metallisation with Ti/Pd/Ag and electroplating of the grid structure. The fabrication process relies heavily on the process sequences which have been developed for the LBSF cells at Fraunhofer ISE [95]. A more detailed description of the processing sequence for the SOI cells can be found in [72].

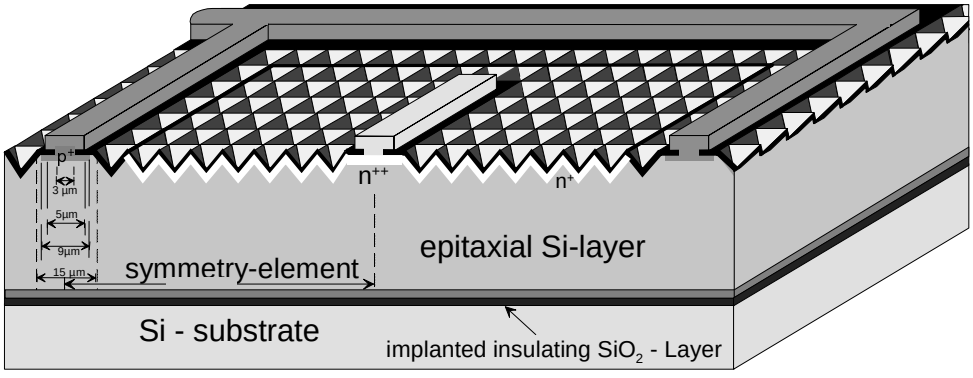

Fig. 6.1: Structure of textured SOI solar cell with interdigitated front contact.

6.2 Optical baseline models

6.2.1 Analytical calculation of the external reflection of a planar cell

The performance of thin silicon solar cells is restricted by loss of light with long wavelengths. In order to understand the limiting loss mechanisms in SOI cells it is therefore particularly important to develop an accurate model of light trapping.

Assuming planar surfaces, the external reflection including escape reflection can be approximated by

$$R_{ext}^{nm} = R_{fe} + \frac{T_{fe}\, T_{fi} \exp\left(-2\alpha H_{epi}\right)}{1 - R_{\text{int}}\, R_{fi} \exp\left(-2\alpha H_{epi}\right)} \left(R_{\text{int}} + \frac{T_{\text{int}}^2\, R_b \exp\left(-2\alpha W\right)}{1 - R_b\, R_{\text{int}} \exp\left(-2\alpha W\right)} \right), \qquad (6.1)$$

where $R_{fe}(\lambda)$ is the external reflection of the front surface, $R_{fi}(\lambda)$ is the internal front surface reflection, $T_{fe}(\lambda)$ is the transmission through the front surface, $T_{fi}(\lambda)$ is the internal front surface transmission, $R_{int}(\lambda)$ is the reflectivity of the intermediate oxide layer, R_b is the reflectivity at the rear side of the substrate, H_{epi} is the thickness of the epi-layer and W is the substrate thickness. Equation 6.1 was derived in the same way as Eq. 2. Escape reflectance from the substrate is also included: The term in Eq. 6.1 containing R_b accounts for multiple reflections in the substrate. Light transmitted from the substrate through the intermediate oxide and the epi-layer contributes to the external reflection in the long wavelength regime.

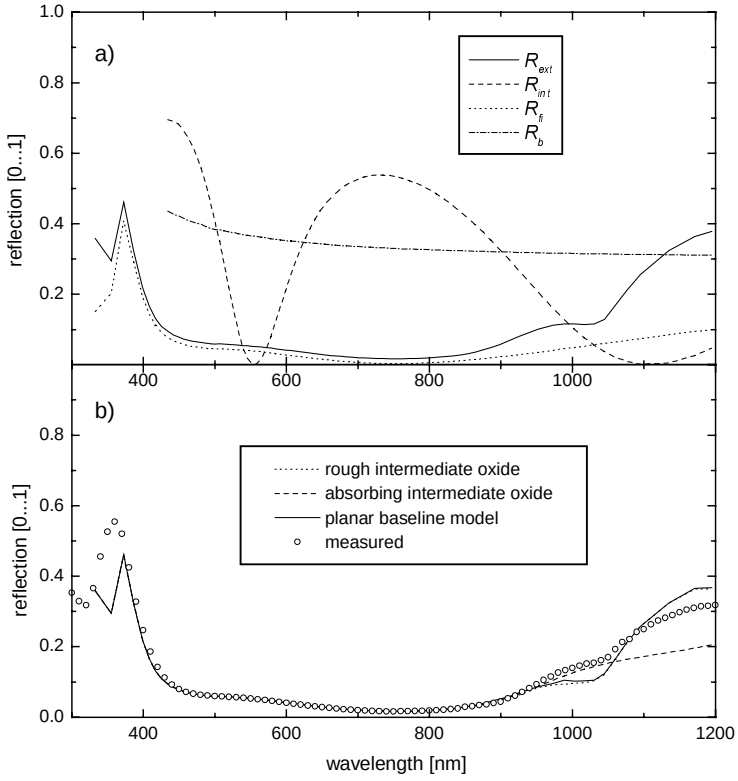

Fig. 6.2: Analysis of external reflection of planar SOI cell. (a) External reflection calculated with Eq. 6.1. (b) comparison of reflection measurement with ray tracing simulation for different assumptions listed in the figure caption.

The reflectivity of the front, intermediate and rear surfaces is plotted in Fig. 6.2a for a planar SOI cell with the surface properties listed in Tab. 6.1. The external reflection calculated with Eq. 6.1 and assuming transparent thin films ($T = 1 - R$) is plotted as a solid line. A characteristic hump in the external reflection is observed at $\lambda = 1030$ nm, due to the decrease in reflectivity at the intermediate oxide (long dashed curve). This hump is seen in the measured external reflectivity of planar SOI cells as well (open circles in Fig. 6.2b).

The intermediate implanted oxide layer of the SIMOX wafer does not have a constant refractive index. The influence of an absorbing intermediate oxide was therefore investigated. Assuming a complex refractive index of $\tilde{n} = 1.46 - i\,0.25$ produces the dashed curve in Fig. 6.2b: less light is retransmitted from the substrate due to absorption in the intermediate oxide layer.

Taking account of the surface roughness of the intermediate oxide does not change the results from the simulation: The dotted curve in Fig. 6.2b was simulated by ray tracing, assuming a Phong exponent of $w = 30$. Essentially the same curve is obtained as with the assumption of a planar intermediate oxide. This is because the scattered light impinges the front surface with angles lower than the critical angle of total internal reflection. Therefore, surface roughness of the intermediate layer is not the reason for the deviation between measurement and simulation in Fig. 6.2b.

6.2.2 Ray tracing simulation of the optical properties of a textured cell

The optical properties of textured SOI cells were simulated using the ray tracing program *RAYN* (Section 3.4.2). Modelling parameters for the textured reference cell are listed on the

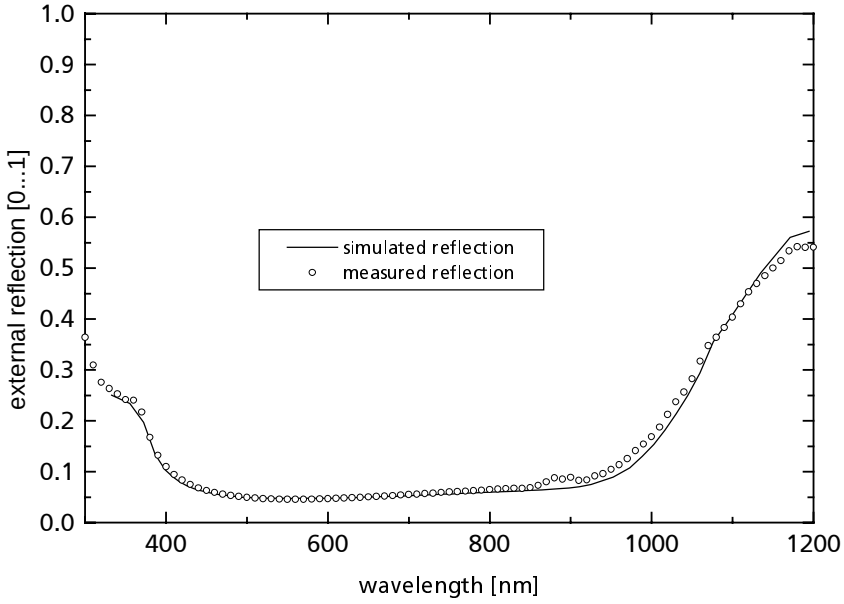

Fig. 6.3: External reflection of textured SOI thin film cell. The open circles show a reflection measurement, the solid line is the simulated external reflection.

right hand side of Tab. 6.1. Using these parameters, the simulated external reflection in

Fig. 6.3 is obtained. The ray tracing result was corrected by the metal grid reflectivity with Eq. 2. The simulated and measured external reflection are in excellent agreement.

Due to the low thickness of the silicon layer it is important to include the angle- and wavelength dependent internal reflectivity at the front- and intermediate oxide in the ray tracing model. Fig. 6.4 shows the reflectance curves of the intermediate oxide used by the ray tracing program *RAYN*. The light trapping properties in the long wavelength range ($\lambda = 800$ to 1200 nm) are determined by internal reflection at the intermediate oxide and the front surface texture. Good light trapping is achieved if the incident angle of light exceeds the critical angle of total internal reflection, that is, 17° at the front surface and 30° at the intermediate oxide layer. The angles are specified relative to the respective plane normals.

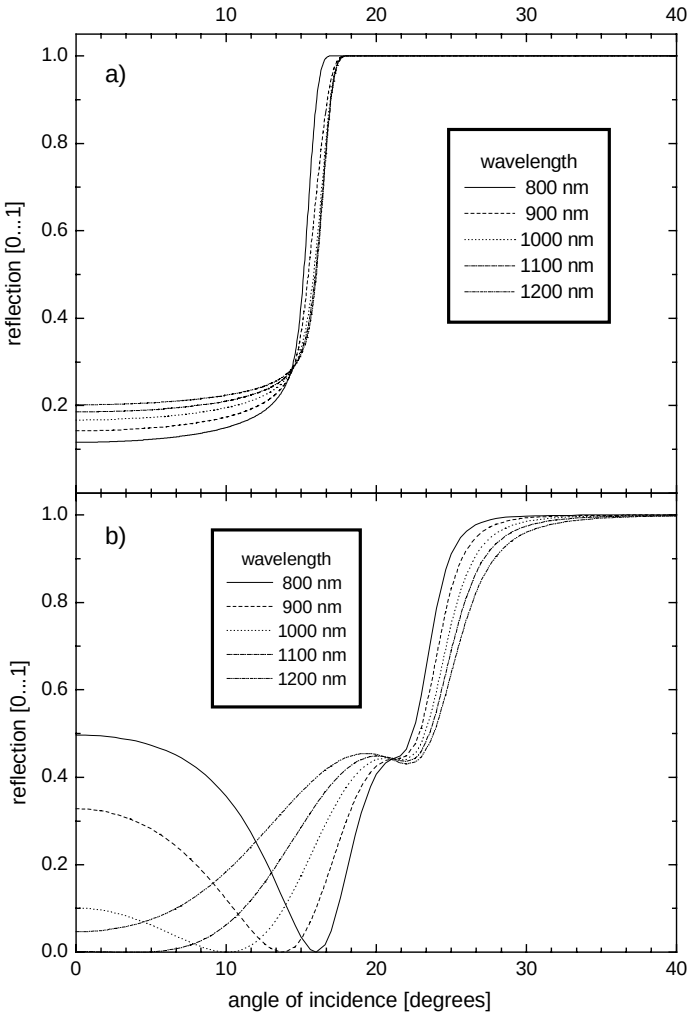

Fig. 6.4: Internal reflection for a textured SOI cell. (a) At front surface; (b) at intermediate oxide with 380 nm thickness. The angle of incidence is specified relative to the plane normal.

The measured external reflection cannot accurately be reproduced by direct reflections at the optical surfaces: The intermediate oxide layer exhibits roughness which is modelled using a Phong exponent of w =60 (Fig. 3.9).

Theoretically, optimum light trapping would be achieved by Lambertian reflection at the intermediate layer. This would lead to total randomisation of the direction of reflected light. This case is not realised in the fabricated SOI cells. For a more detailed discussion see Section 3.4.1.

6.2.3 Optical baseline models for planar and textured cell

As outlined in the previous two sections the simulated external reflection coincides with the measurements. Thereby, the optical baseline parameters listed in Tab. 6.1 were used. This provides the basis for an analysis of the optical loss channels of planar and textured SOI cells.

The planar and textured reference cells exhibit different metal area fractions due to differences in the electroplating process, used to increase the cross-sectional area of the contact fingers after lift-off. The contact grid geometries of the cells investigated displayed significant variation. For the comparison of optical losses in both cell types the metal area fraction for planar and textured cells were assumed to be the same.

	planar front	textured front
reference cell	Simox 4-2c	Simox 5-2c
metal area fraction A_{metal}	1.4%	4.4%
metal reflectivity R_{metal}	96%	96%
Front	double layer AR coating: native oxide (d = 6 nm) TiO (d = 55 nm) MgF (d = 92 nm)	inverted pyramids of 10 µm width, 7.1 µm depth with thermal oxide on top (d = 104 nm)
Epitaxial layer	42 µm	45 µm
intermediate oxide	idealised: transparent oxide with refractive index n = 1.46 (d = 380 nm), roughness of intermediate layer in ray tracing simulation is described by the Phong model (w = 60).	
substrate	W = 525 µm	
rear	native oxide (d = 6 nm)	oxide (d = 104 nm)

Tab. 6.1: Optical baseline parameters for planar and textured reference SOI cells (d denotes layer thickness).

The fraction of incident photon flux transmitted through the intermediate oxide layer, T_{inter} can be calculated by ray tracing simulation. Further, the fraction of incident photon flux absorbed in the thin electrically active silicon layer is given by

$$f_{abs}(\lambda)=1-R_{ext}^{nm}(\lambda)-f_{metal}-T_{inter}(\lambda). \tag{6.2}$$

This is plotted as dashed line in Fig. 6.5. In the last equation, f_{metal} is the photon flux fraction absorbed in the metal grid. T_{inter} can be further split into two parts, the photon flux fraction absorbed in the substrate f_{substr} (dotted line) and the fraction transmitted through the rear surface of the substrate T_{rear} (dash-dotted line), thus

$$f_{abs}(\lambda)=1-R_{ext}^{nm}(\lambda)-f_{metal}-f_{substr}(\lambda)-T_{rear}(\lambda). \tag{6.3}$$

The four terms with negative signs in Eq. 6.3 are the optical loss channels of the SOI thin film cell. Eq. 6.3 can be expressed in terms of current density by integrating over the incident photon flux density. Thereby, it can be assumed that each incident photon equals one generated or lost electron-hole pair. Under this assumption the integral $q\int_{300\,nm}^{1200\,nm} j_\lambda\, d\lambda$ over the AM 1.5 photon flux density equals a current density of 46.14 mA/cm^2. This value can be taken as a reference to express relative absorption, reflection, and transmission fractions, *e.g.* the externally reflected current loss fraction is given by

$$\overline{R}=\frac{\int j_\lambda\, R(\lambda)\, d\lambda}{\int j_\lambda\, d\lambda}. \tag{6.4}$$

These relative absorption, reflection and transmission fractions are plotted in Fig. 6.6 for the textured and the planar reference cells. Assuming 4.4% metal area fraction, a fraction of 82.4% of the incident photon flux is absorbed in the epi-layer in the case of the textured SOI cell. This value compares to 71.1% for the planar cell assuming the same metal area coverage. The spectrally resolved photon flux fraction is plotted in Fig. 6.5 revealing enhanced absorption of light in the long wavelength range for the textured cell. In other words, in the case of the planar cell, more light is transmitted through the intermediate oxide. To be more precisely, 10.5% of the incident photon flux is absorbed in the substrate of the planar cell, whereas this loss is reduced to 2.4% of the incident photon flux in the textured cell, due to light confinement.

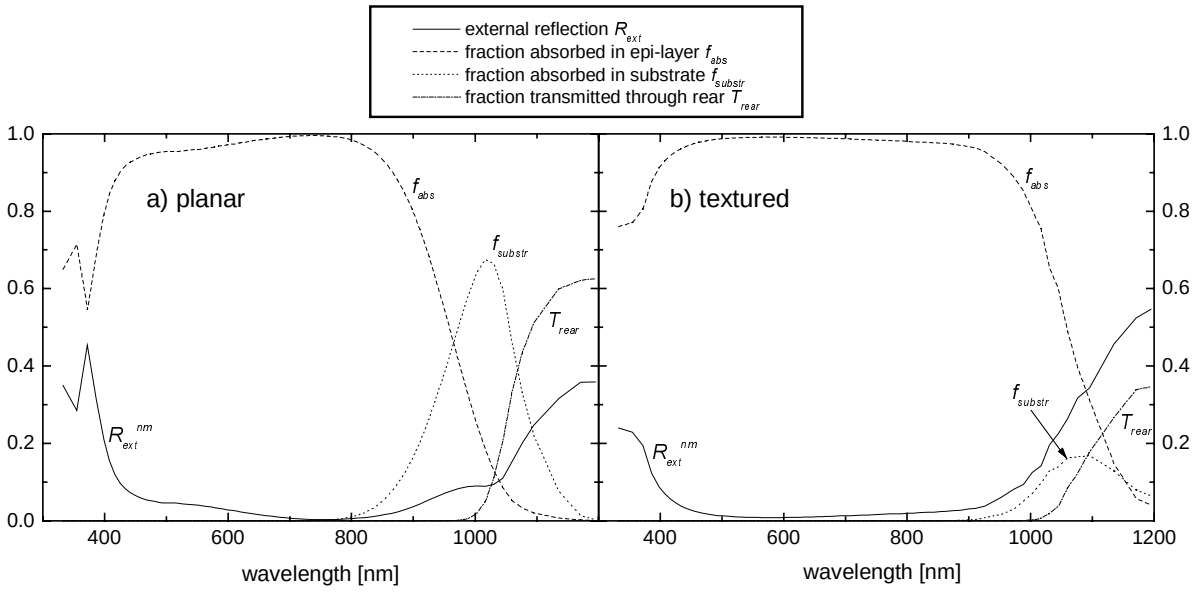

Fig. 6.5: Optical baseline models simulated by ray tracing. (a) Planar front side; (b) inverted pyramids on front side. No reflection or shading due to the metal grid was accounted for in these calculations.

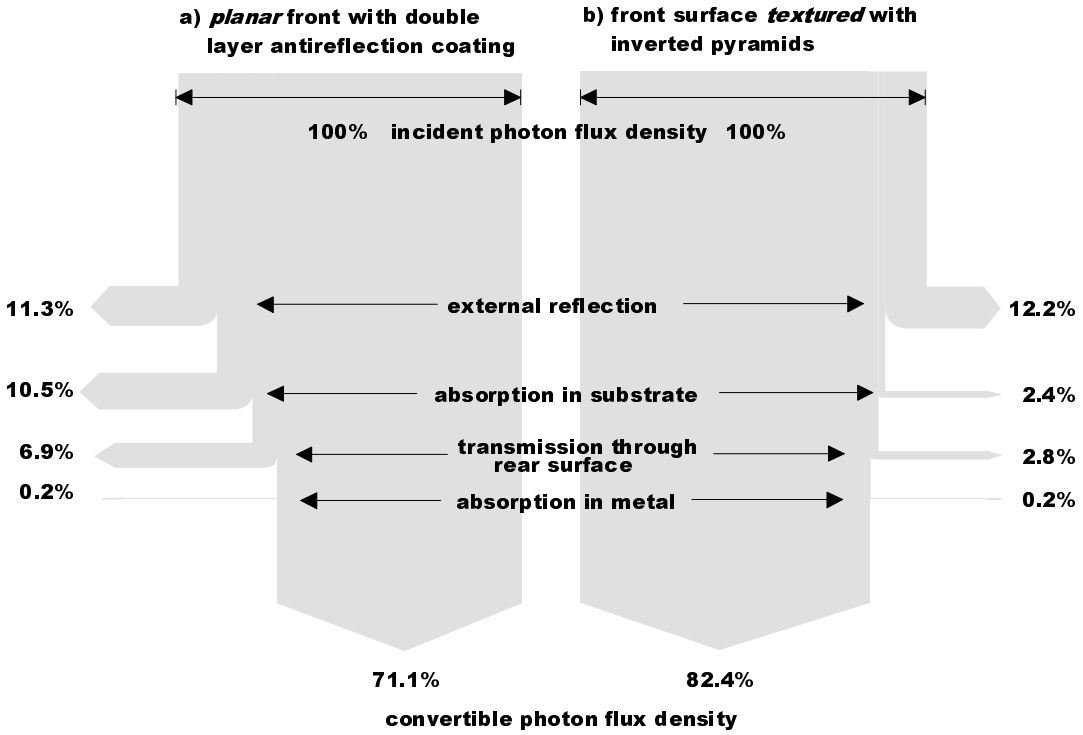

Fig. 6.6: Relative absorption, reflection and transmission fractions of the SOI thin film cells; a) Planar front surface with double layer AR-coating; b) front surface textured with inverted pyramids. A metal area fraction of A_{metal} = 4.4% was assumed for both cell types.

As outlined in Section 3.4.3 *RAYN* provides the spatially resolved optical generation rates. The generation profiles *G(z)* of both planar and textured SOI cells (calculated with Eq. 2.130) are shown in Fig. 6.7. It can be seen that the discontinuity in the generation rate at the z-position corresponding to the intermediate oxide is more pronounced in the case of the textured cell than that of a planar cell. In the textured case most of the light reaches the $Si/SiO_2/Si$-interface with an angle that exceeds the angle of total internal reflection.

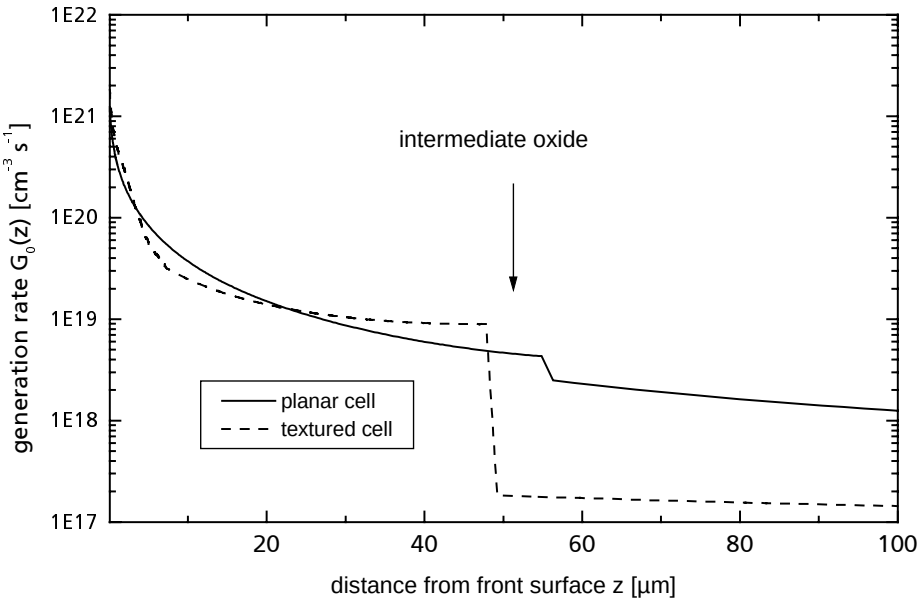

Fig. 6.7: Generation profiles calculated for textured and planar SOI cells.

Therefore, less light is transmitted through the intermediate oxide layer, and thus the rate of generation of uncollectable charge carriers in the substrate is lower.

6.3 Influence of the epi-layer thickness on reflection and absorption

We will now proceed with a discussion of the influence of the epi-layer thickness on the reflection and absorption properties of planar and textured SOI cells. With the exception of the epi-layer thickness and metal area fraction all input parameters were fixed to those of the baseline models listed in Tab. 6.1. As can be seen in Fig. 6.8c and Fig. 6.8d, the absorption in the epi-layer strongly depends on the epi-layer thickness for both cell types. The dependency is much more pronounced for planar cells due to enhanced absorption in the substrate. This can also be seen in Fig. 6.9a: The current loss in the substrate of the planar cell decreases from 7.7 mA/cm^2 to 3.3 mA/cm^2 if the epi-layer thickness is increased from 15 µm to 100 µm. This compares to a decrease from 2 mA/cm^2 to 0.6 mA/cm^2 for the textured cell. Fig. 6.9c and Fig. 6.9d show the same dependency for the optical loss channels of the SOI cell, normalised to the photon flux $\int_{300\,nm}^{1200\,nm} j_\lambda \, d\lambda$ of the AM1.5 spectrum as an upper limit (100%). A fraction of 16.6% of the incident photons is absorbed in the substrate of a 15µm thick planar SOI cell. This loss decreases to 7% for an epi-layer thickness of 100µm. The corresponding values are 4.3% and 1.4%, respectively, for the textured SOI cell.

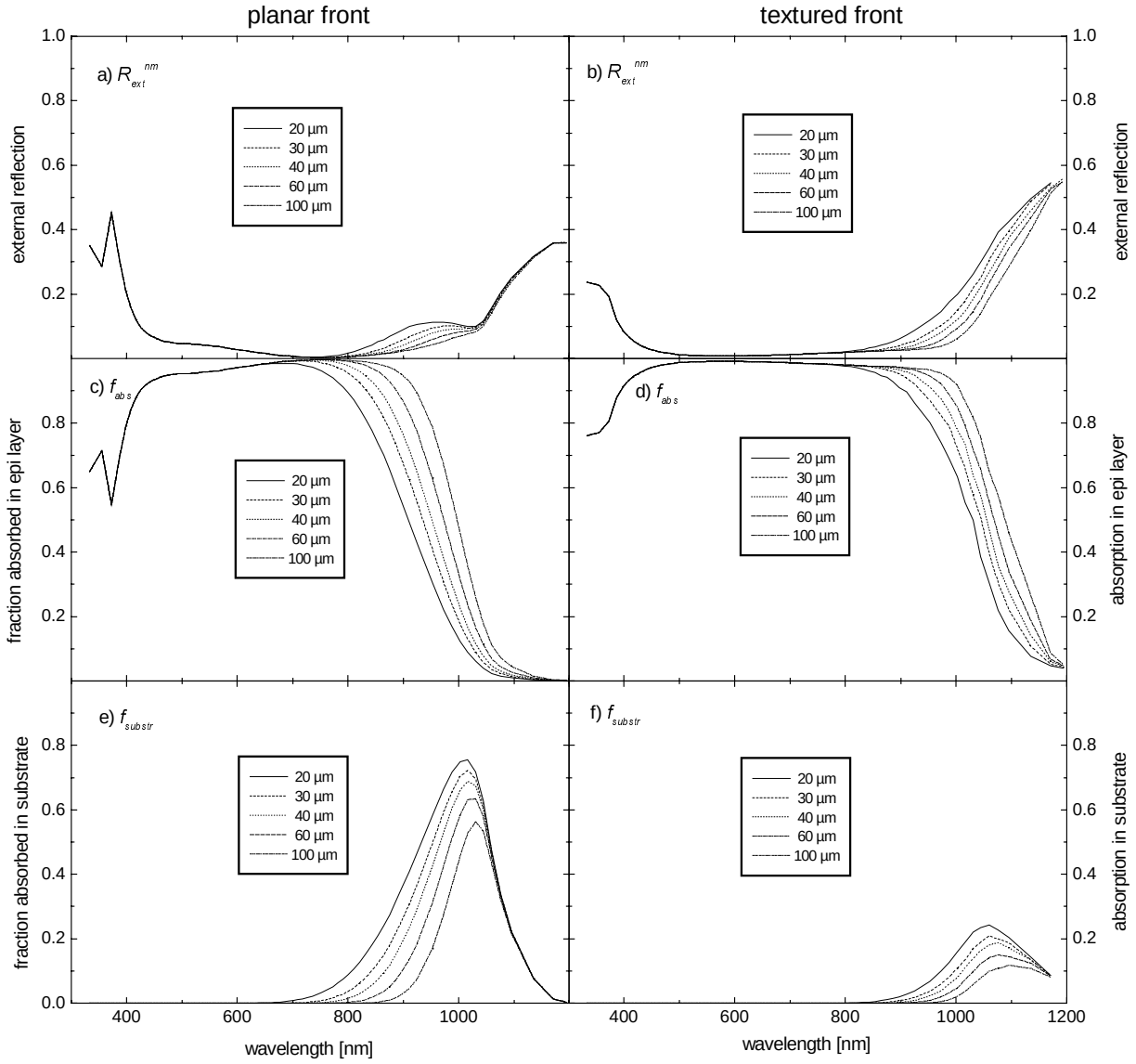

Fig. 6.8: Influence of epi-layer thickness on reflection and absorption in planar and textured SOI cell. The curves are not corrected for reflection (shading) due to the metal grid of the solar cell. (a) External reflection of planar cell; (b) external reflection of textured cell; (c) absorption in epi-layer of planar cell; (d) absorption in epi-layer of textured cell; (e) absorption in substrate of planar cell; (f) absorption in substrate of textured cell.

The maximum achievable short circuit current density $J_{sc,max}$ determined from Eq. 2. is shown in Fig. 6.10a and b as a function of the epi-layer thickness. Assuming no recombination losses, the short circuit current density of a planar SOI cell is limited to $J_{sc,max} = 29.5$ mA/cm^2 for an epi-layer thickness of 15µm. This value increases to $J_{sc,max} = 34.8$ mA/cm^2 for an epi-layer thickness of 100µm. The short circuit current density of the textured cell is limited to $J_{sc,max} = 35.7$ mA/cm^2 for 15µm epi-layer thickness, increasing to $J_{sc,max} = 39.2$ mA/cm^2 for a 100µm thick epi-layer.

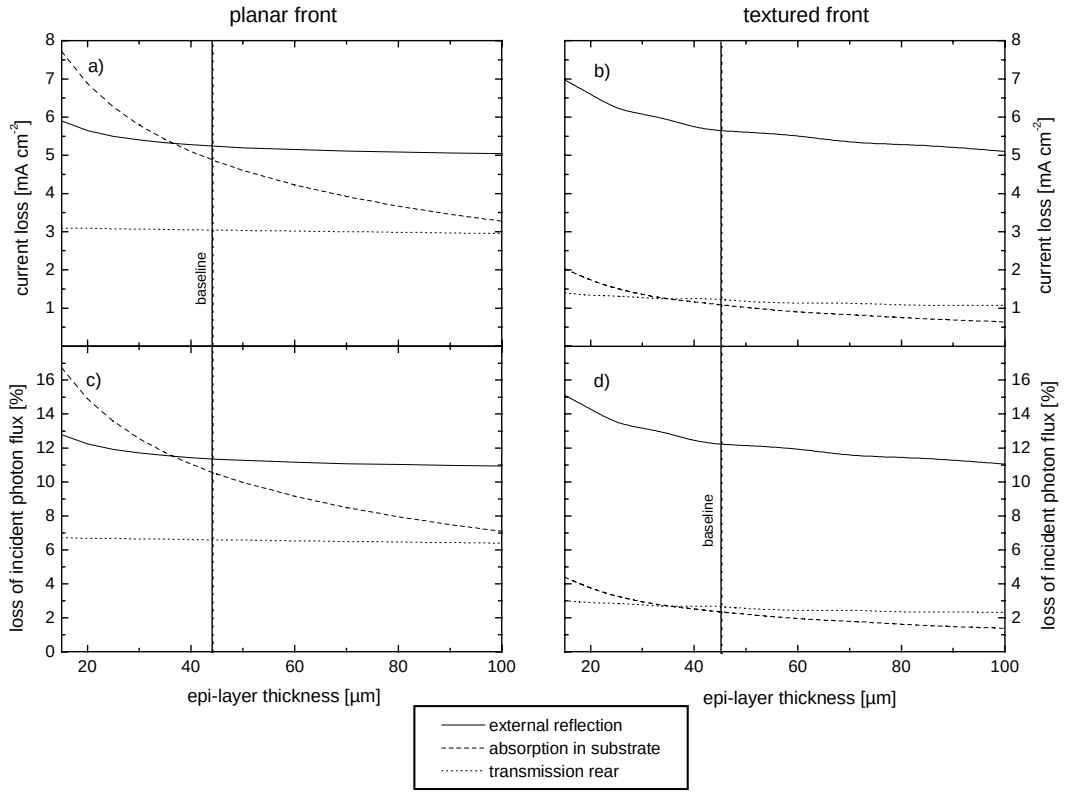

Fig. 6.9: Influence of epi-layer thickness on current loss of planar and textured SOI cell for illumination with the AM1.5 spectrum.

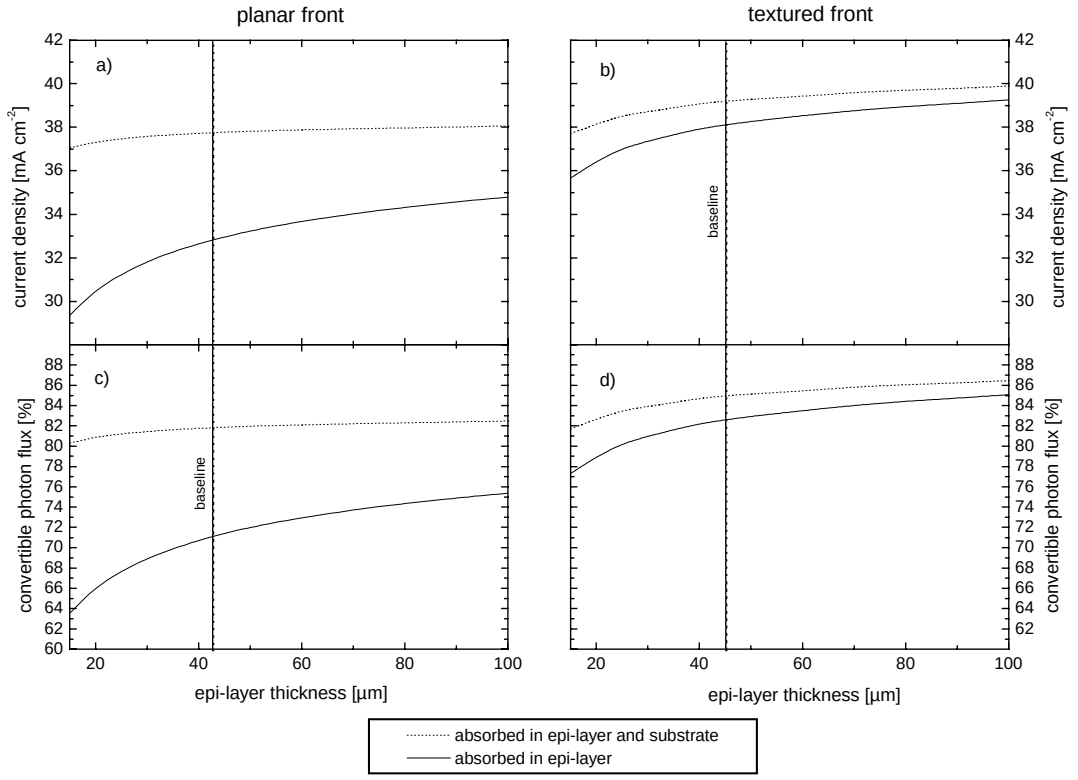

Fig. 6.10: Influence of epi-layer thickness on absorption in planar and textured SOI cell for illumination with the AM1.5 spectrum.

6.4 Electrical baseline models

The same two SOI cells as in the previous section were chosen as reference cells in order to establish realistic baseline models for the electrical performance. Tab. 6.3a summarises the doping parameters of these cells. Their measured *I-V* output parameters are listed in Tab. 6.2.

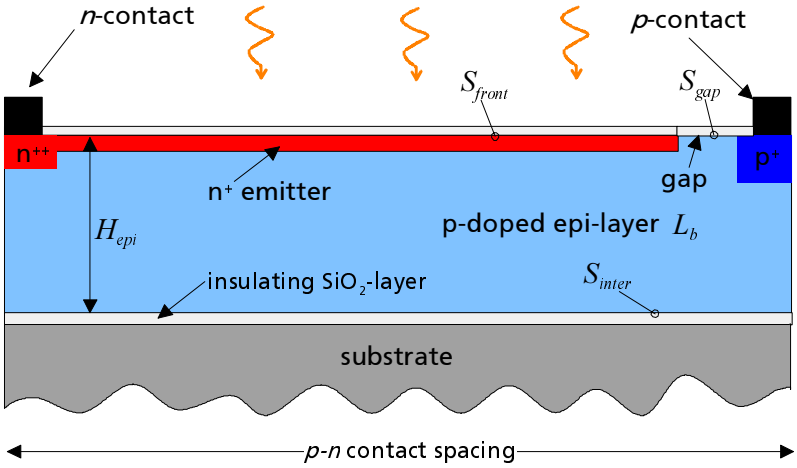

Fig. 6.11: Symmetry element for 2D semiconductor device simulation of SOI cells.

The electrical properties of the SOI cell were modelled using the 2D symmetry element shown in Fig. 6.11. The surface recombination velocity S_{front} of the n^+ doped emitter can be determined with good accuracy from Fig. 5.8. S_{front} is found to be 500 cm/s for the oxide passivated phosphorous doped emitter with peak doping concentration of $5\times10^{18}\,cm^{-3}$. S_{front} of textured oxide passivated phosphorous doped emitters is enhanced by a factor of between 3 and 5 compared to that for a planar surface [86]. Therefore, S_{front} = 1500 cm/s was chosen for the textured reference cell. The influence of the 'gap region' of the front surface, between the emitter and base contacts, on the overall recombination is insignificant compared to the base recombination. Parameter variations clearly show the dominant influence of the effective base diffusion length, L_{eff} on the open circuit voltage V_{oc}.

The back surface field of the SOI cells is accounted for in the electrical model as an effective surface recombination velocity, denoted S_{inter}.

The effective diffusion length of the planar SOI reference cell can be estimated from the measured quantum efficiency and external reflection plotted in Fig. 6.12a. L_{eff} = 160 µm is found from the linear dependence of the inverse internal quantum efficiency on absorption length shown in Fig. 6.12b [96]. The range of L_b-S_{inter} values compatible with L_{eff} = 160±5 µm is plotted as grey area in Fig. 6.13. However, these error bounds do not include systematic errors in the reflection- and quantum efficiency measurements.

	planar front (Simox 4-2c)	textured front (Simox 5-2c)
V_{oc} [mV]	658	671
J_{sc} [mA/cm^2]	33.0	37.1
fill factor [%]	73.5	77.7
efficiency [%]	15.9	19.3

Tab. 6.2: Measured *I-V* output parameters of SOI reference cells.

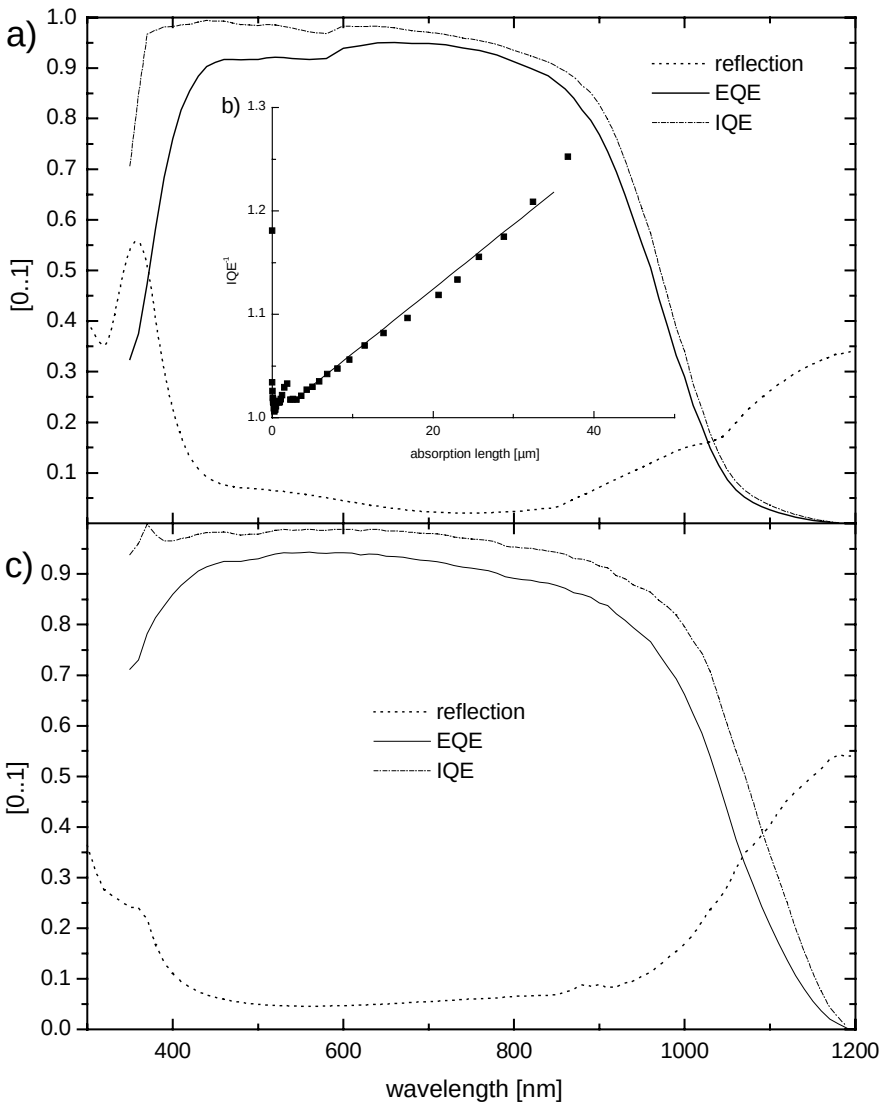

Fig. 6.12: Measured reflection, external quantum efficiency, and internal quantum efficiency of SOI reference cells. (a) Planar cell; (b) the effective diffusion length was extracted from a plot of IQE vs. absorption length; (c) textured cell.

Numerical device simulation allows greater precision in the determination of compatible pairs of recombination parameters L_b and S_{inter} for solar cells with a high base diffusion length. An array of *I-V* curves for different L_b-S_{inter} combinations was determined using *DESSIS*. These were then used to plot the contours of constant J_{sc} and V_{oc} shown in Fig. 6.13a and b, respectively. As V_{oc} can be measured with an accuracy of ±1 mV, the range of possible L_b-S_{inter} values can be determined with higher accuracy from contours of constant V_{oc} than from the internal quantum efficiency or contours of constant J_{sc}.

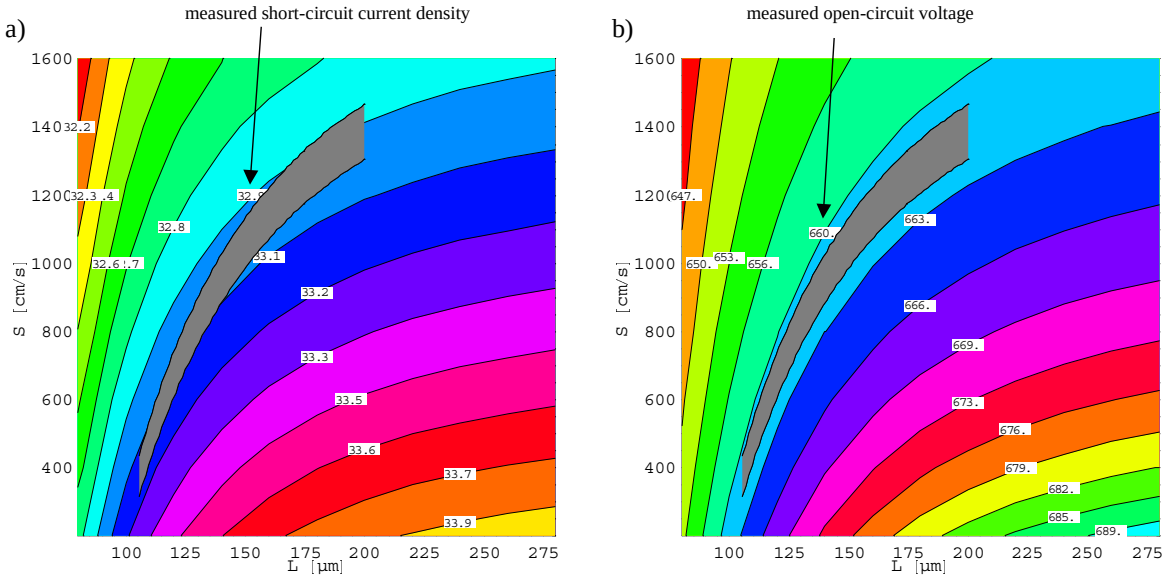

Fig. 6.13: Contours of constant short-circuit current density (left) and open-circuit voltage (right) of the planar SOI cell. The bulk diffusion length L and the effective surface recombination velocity S at the intermediate oxide was varied using *DESSIS* resulting in the labelled lines. The two arrows indicate the measured *I-V* output parameters of the planar reference cell. The numerical model reproduces both the measured J_{sc} = 33.0 mA/cm^2 and V_{oc} = 660 mV using the same set of recombination parameters. In addition, *L-S* combinations corresponding to the same effective diffusion length L_{eff} = 160 µm are plotted within error bounds as grey area. This effective diffusion length was determined from a spectral response measurement.

Using the baseline model for the textured SOI cell, the effective base diffusion length of the textured reference cell was determined to be L_{eff} = 200 µm. Possible L_b-S_{inter} combinations for this diffusion length are shown as solid line in Fig. 6.14.

Bulk recombination (L_b) and surface recombination at the back surface field (S_{inter}) could not be separated accurately due to the high minority carrier lifetime in the base of the SOI

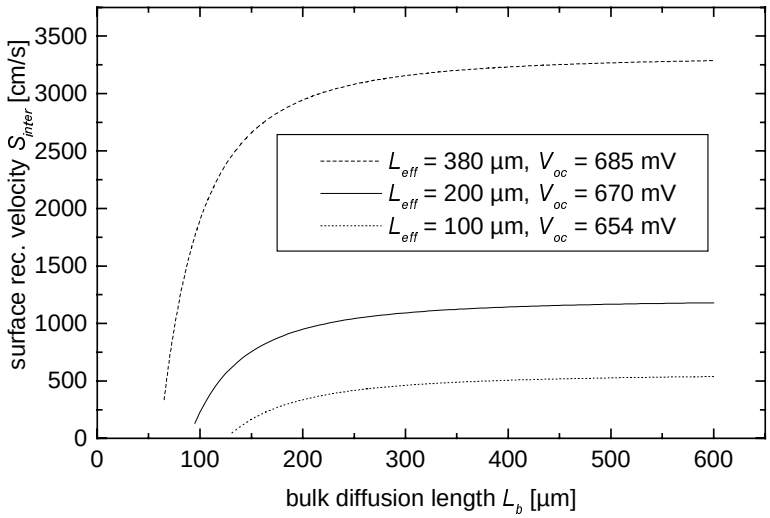

Fig. 6.14: Possible combinations of recombination parameters for different effective diffusion lengths. The measured open circuit voltage of the textured baseline cell is 670 mV (solid line).

reference cells ($L_{eff} / H_{epi} \gtrsim 3$) [96]. Assuming dominating surface recombination at the back surface field of the textured reference cell leads to $S_{inter} \approx 1200$ cm/s and $L_b \approx 470$ µm.

The recombination parameters of the baseline models for the planar and textured SOI cells are listed in Tab. 6.3b. Using these recombination parameters results in the simulated external quantum efficiency curves shown in Fig. 6.15.

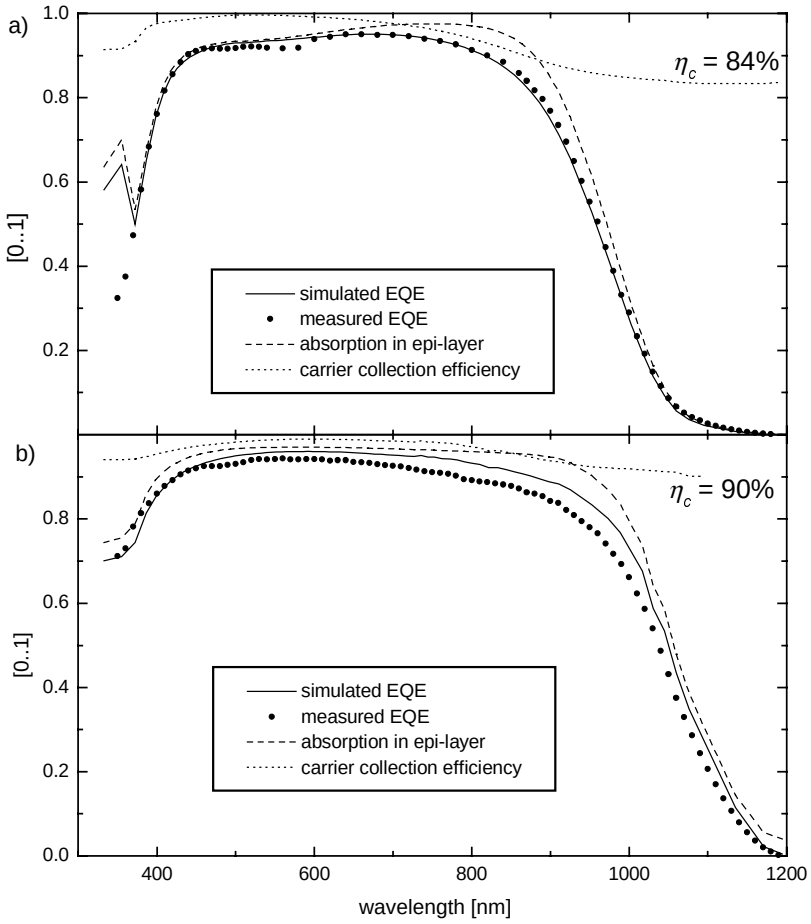

Fig. 6.15: Comparison of the simulated external quantum efficiency with measurements. In addition, the light absorption in the epi-layer and the carrier collection efficiency is shown. (a) Planar SOI reference cell; (b) textured SOI reference cell.

The carrier collection efficiency was determined using Eq. 2. for both cell types. Maximum carrier collection efficiency is found in the wavelength range from λ = 500 to 600 nm; carriers are absorbed in the emitter and collected with $\eta_c = 1$ for these wavelengths. The carrier collection efficiency in the base is 84% and 90% for the planar and textured reference cells, respectively. The higher η_c-value for the textured cell is due to its higher base diffusion length (Tab. 6.3b).

a) Doping

region	peak concentration [cm^{-3}]	depth [µm]
epi-layer	$8\ 10^{16}$	constant doping
n^{++} (phosphorous)	$5\ 10^{19}$	2.3 (Gaussian profile)
n^{+} (phosphorous)	$5\ 10^{18}$	1.15 (Gaussian profile)
p^{+} (boron)	$2\ 10^{19}$	4 (Gaussian profile)
BSF-layer	modelled with effective surface recombination velocity S_{inter}	

b) Recombination parameters

	planar front	textured front
recombination velocity at n^{+} diffused front surface S_{front} [cm/s]	500	1500
recombination velocity at gap region S_{gap} [cm/s]	2000	2000
effective base diffusion length L_{eff} [µm]	160 $(L_{eff}/H_{epi})\approx 3$	200 $(L_{eff}/H_{epi})\approx 4$
base diffusion length L_b [µm]	150	470
recombination velocity at intermediate oxide layer S_{inter} [cm/s] (assumption of dominating surface recombination at BSF)	1200	1200

c) Metal grid and cell geometry

n-p contact spacing: 715 µm

metal resistivity: $1.6\times10^{-6}\ \Omega$ cm

cell area: 4 cm^2

	Length [µm]	height [µm]	width [µm]	shape
Fingers	$1.9\ 10^4$	10	15	constant
bus	$1.9\ 10^4$	20	110	tapered
pad	600	--	400	rectangular

Tab. 6.3: Parameters of electrical baseline models for planar and textured SOI cell. (a) Doping profiles used for semiconductor device simulation; (b) recombination parameters determined from EQE measurements and device simulation; (c) metal grid geometry parameters used to account for correction of fill factor due to Ohmic losses in the metal grid.

6.5 Influence of the epi-layer thickness and the recombination parameters

In this section, the influence of epi-layer thickness H_{epi} on the cell performance of textured and planar SOI cells will be investigated for different combinations of the recombination parameters L_b and S_{inter}. Other cell parameters were fixed to those listed in Tab. 6.3.

Fig. 6.16 reveals that cells with surface texture have a higher V_{oc} compared to those with a planar cell front. The relative gain in V_{oc} due to a textured surface is higher for cells with low diffusion lengths (compare Fig. 6.16a and c). The gain in V_{oc} arising from a surface texture in comparison to a planar cell front can be neglected for high base diffusion lengths L_b. This can be explained using Eq. 2.101. For high L_b and low emitter saturation current densities, $\frac{J^{Lt}}{J_{0b}+J_{0e}} >> 1$ is valid. Thus, V_{oc} in Eq. 2.101 is not sensitive to changes in the light generated current density J^{Lt}.

Since the influence of the back surface field is negligible for $H_{epi} > 3\ L_b$, curves of different recombination velocities, S_{inter} approach each other in this limit (see Fig. 6.16a and b). Reducing the epi-layer thickness increases V_{oc} if base recombination dominates over surface recombination at the back surface field. Conversely, V_{oc} decreases for a poorly passivated intermediate oxide, *e.g.* if no BSF is present.

The impact of recombination parameters on V_{oc} can be understood using the analytical approach visualised in Fig. 2.5. V_{oc} is determined by the influence of the geometric factor Ξ_p on the base saturation current density J_{0b}. Base and surface recombination at the intermediate oxide are balanced for $\frac{S_{inter} L_b}{D_e} = 1$. Thus the geometric factor Ξ_p is independent of the epi-layer thickness when $\tilde{S} \equiv \frac{D_e}{L_b}$. In this case the saturation current density given by Eq. 2.111 is independent of H_{epi}, and it is found from Eq. 2.101 that V_{oc} remains constant. The $\tilde{S}$-values corresponding to the base diffusion lengths of 25 µm, 50 µm, 150 µm and 470 µm of this study are 8010 cm/s, 4005 cm/s, 1330 cm/s and 425 cm/s, respectively.

The influence of H_{epi} on J_{sc} cannot be understood using a simple analytical approach. Here, the results of ray tracing simulations are essential. This is discussed in Section 6.2. A substantial boost in short circuit current density can be achieved by texturing the surface.

Regarding J_{sc} of a textured SOI cell a thin epi-layer is beneficial for low diffusion lengths (Fig. 6.17a). This is a result of the efficient light confinement achieved by inverted pyramids on the front side. Reducing H_{epi} leads to an increase in J_{sc} due to the reduction in base recombination. This effect is not observed for planar cells as any reduction in base recombination is compensated by increasing optical losses (black lines in Fig. 6.17a).

The influence of H_{epi} on J_{sc} is plotted in Fig. 6.17b for a base diffusion length of L_b = 50 µm. Opposite trends are found comparing planar and textured surfaces. J_{sc} can be

slightly increased by reducing the epi-layer thickness if the front surface is textured whereas J_{sc} decreases for the planar cell.

The 21.5% relative improvement in J_{sc}, (indicated as blue arrow in Fig. 6.17a) is due to the surface texture in the case of a base diffusion length of L_b = 25 µm and an epi-layer thickness of H_{epi} = 45 µm.

A gain in V_{oc} due to surface texture has been observed previously. A similar and yet lower *relative* gain in J_{sc} can be achieved for high base diffusion lengths in comparison to low base diffusion lengths. A slightly reduced gain in J_{sc} of 17% and 15% is observed for L_b = 50 µm and L_b = 470 µm, respectively.

The assumption of an excellent surface passivation by the back surface field (S_{inter} = 500 cm/s) and L_b = 470 µm gives the limiting case of negligible recombination in the bulk for short circuit conditions. Here, the carrier collection efficiency η_c of the SOI cell approaches unity. As a result the solid lines in Fig. 6.17d are essentially the same as those in Fig. 6.10a and b, that is, the short circuit current density calculated by semiconductor device simulation approaches the maximum achievable short circuit current density simulated by ray tracing.

The fill factor calculated by *DESSIS* has to be corrected in order to account for resistive losses in the metal grid. The expressions for the fill factor corrections due to the finger and bus geometry are given in detail in [97], the metal grid geometry parameters for the reference cells are listed in Tab. 6.3c.

Decreasing the epi layer thickness enhances the base sheet resistivity. Therefore, the fill factor decreases for lower epi-layer thickness shown in Fig. 6.18. The fill factor is generally lower for textured cells which is due to the higher current density.

Fig. 6.19 shows the potential of planar and textured SOI cells in terms of conversion efficiency under the premise of the theoretical fill factor values. The energy conversion efficiency for planar and textured cells with a base diffusion length of L_b = 25 µm is limited to 14% and 17.5%, respectively. In order to reach this efficiency, the epi-layer thickness must be reduced to 20 µm. The efficiency decreases for a higher epi-layer thickness due to enhanced base recombination as discussed previously.

20% efficiency could be reached for a textured SOI cell with 80 µm epi-layer thickness as shown in Fig. 6.19d, assuming the same recombination parameters as for the textured reference cell. Thereby, the ideal fill factor value of 80.8% must be realised. Although fill factors of 80.4% were reached for textured SOI cells (with lower open circuit voltages), the 19% efficient textured reference cell only showed a fill factor of 77.7%. The origins of these deviations are investigated in the next section based on a statistical approach.

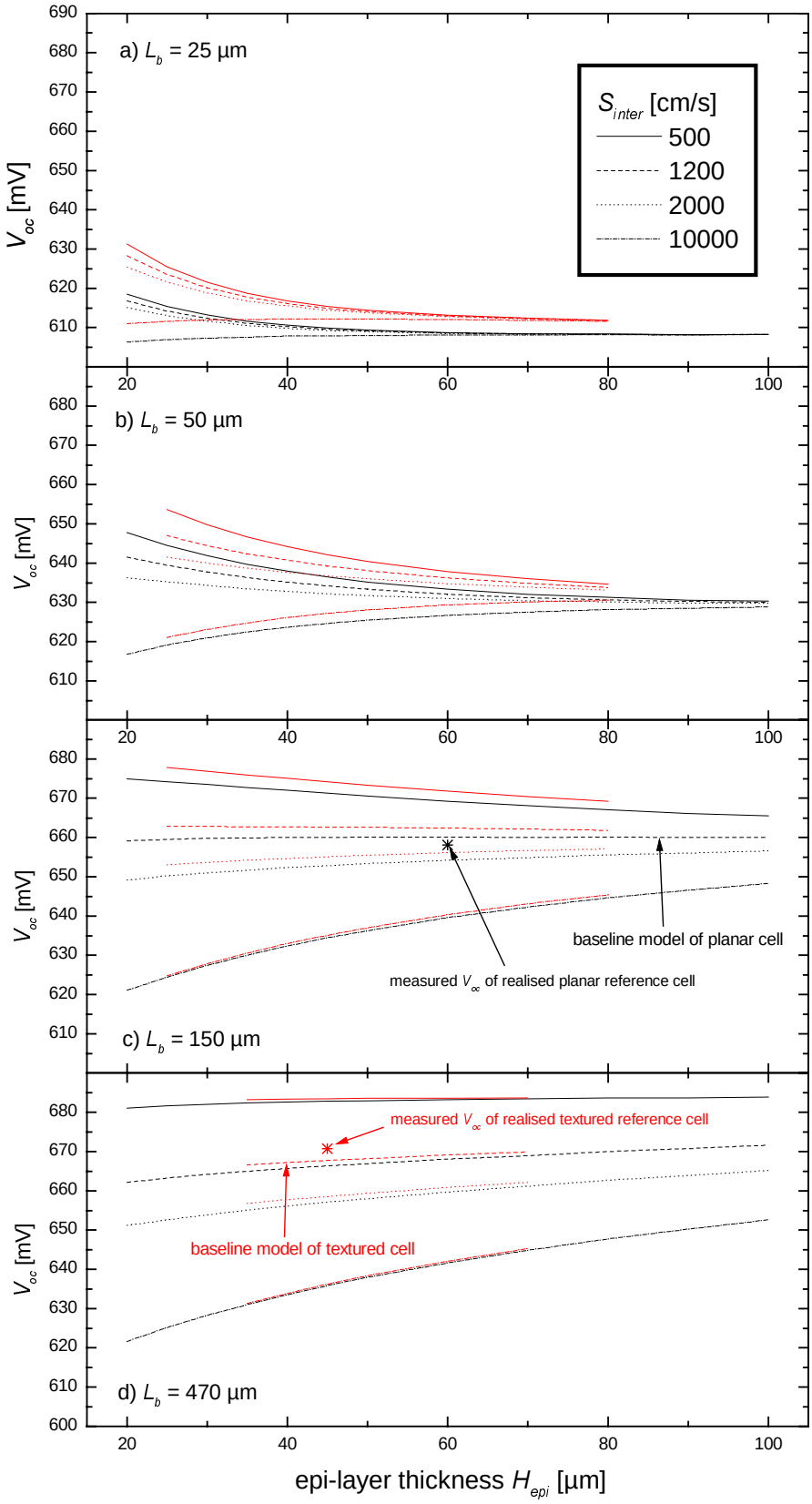

Fig. 6.16: Influence of epi-layer thickness H_{epi} on the open circuit voltage of textured and planar SOI cells for different combinations of the recombination parameters L_b and S_{inter}. The red curves were calculated for a textured front, the black curves for a planar front.

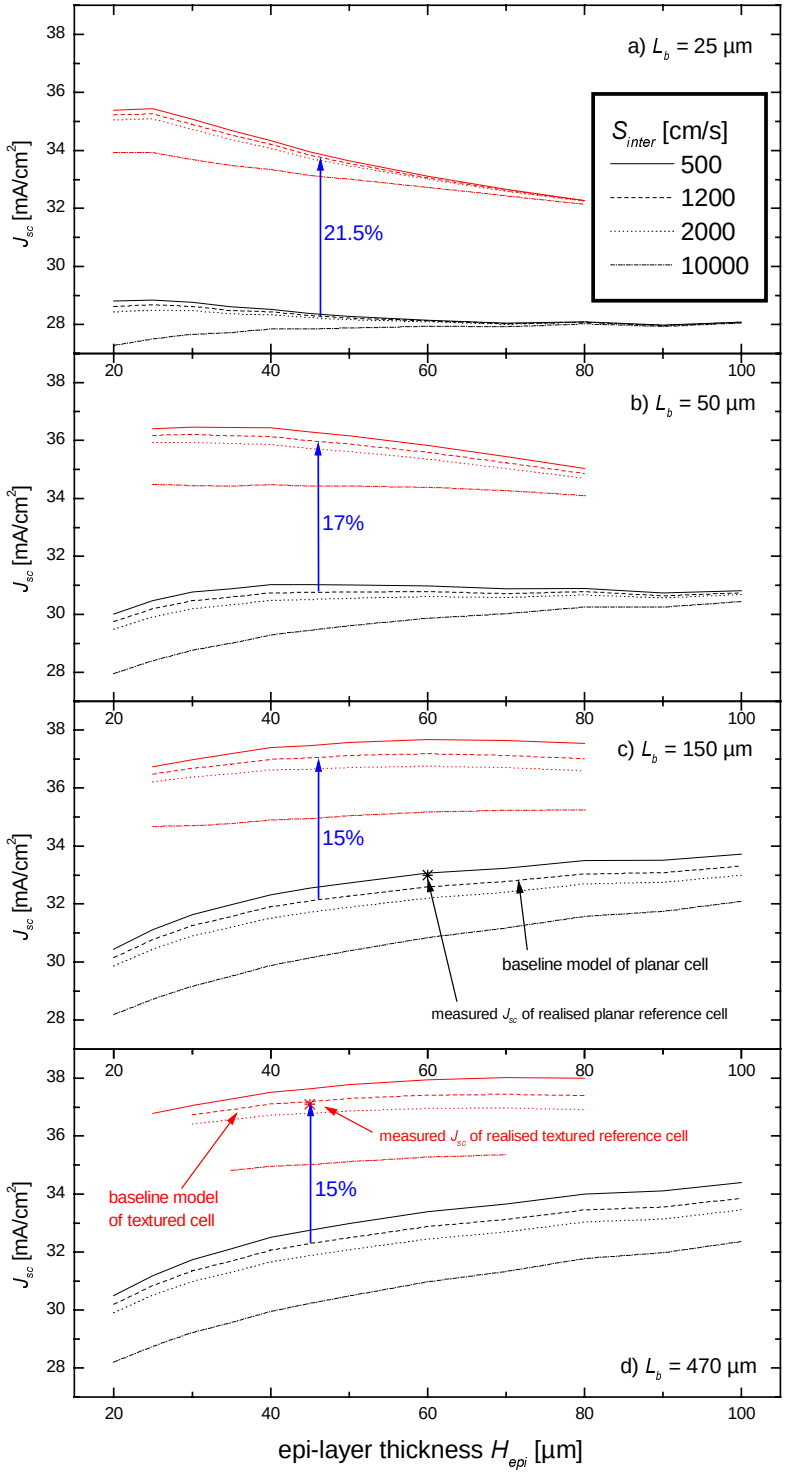

Fig. 6.17: Influence of epi-layer thickness H_{epi} on the short circuit current density of textured and planar SOI cells for different combinations of the recombination parameters L_b and S_{inter}. The red curves were calculated for a textured front, the black curves for a planar front.

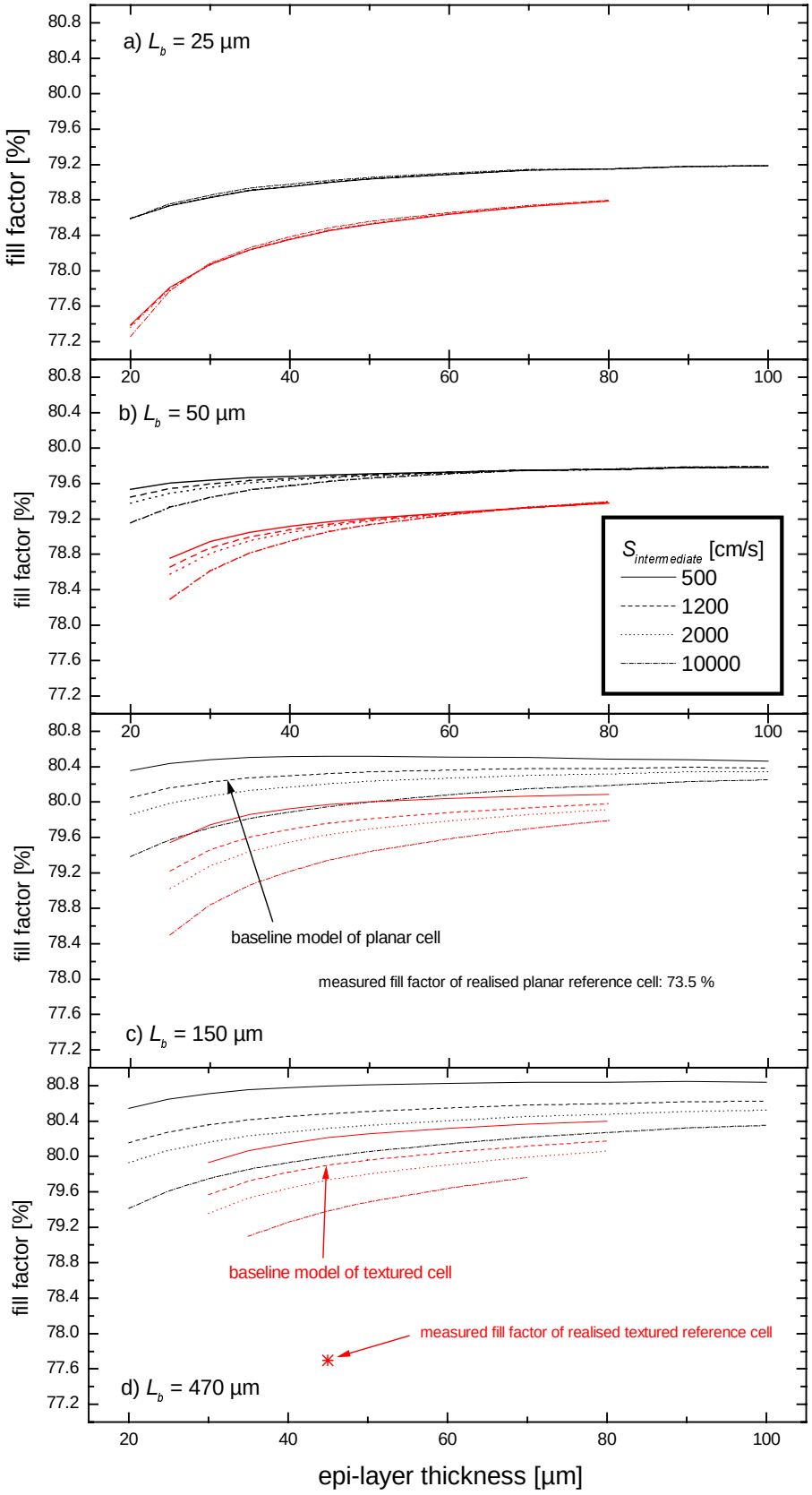

Fig. 6.18: Influence of epi-layer thickness H_{epi} on the fill factor of textured and planar SOI cells for different combinations of the recombination parameters L_b and S_{inter}. The red curves were calculated for a textured front, the black curves for a planar front.

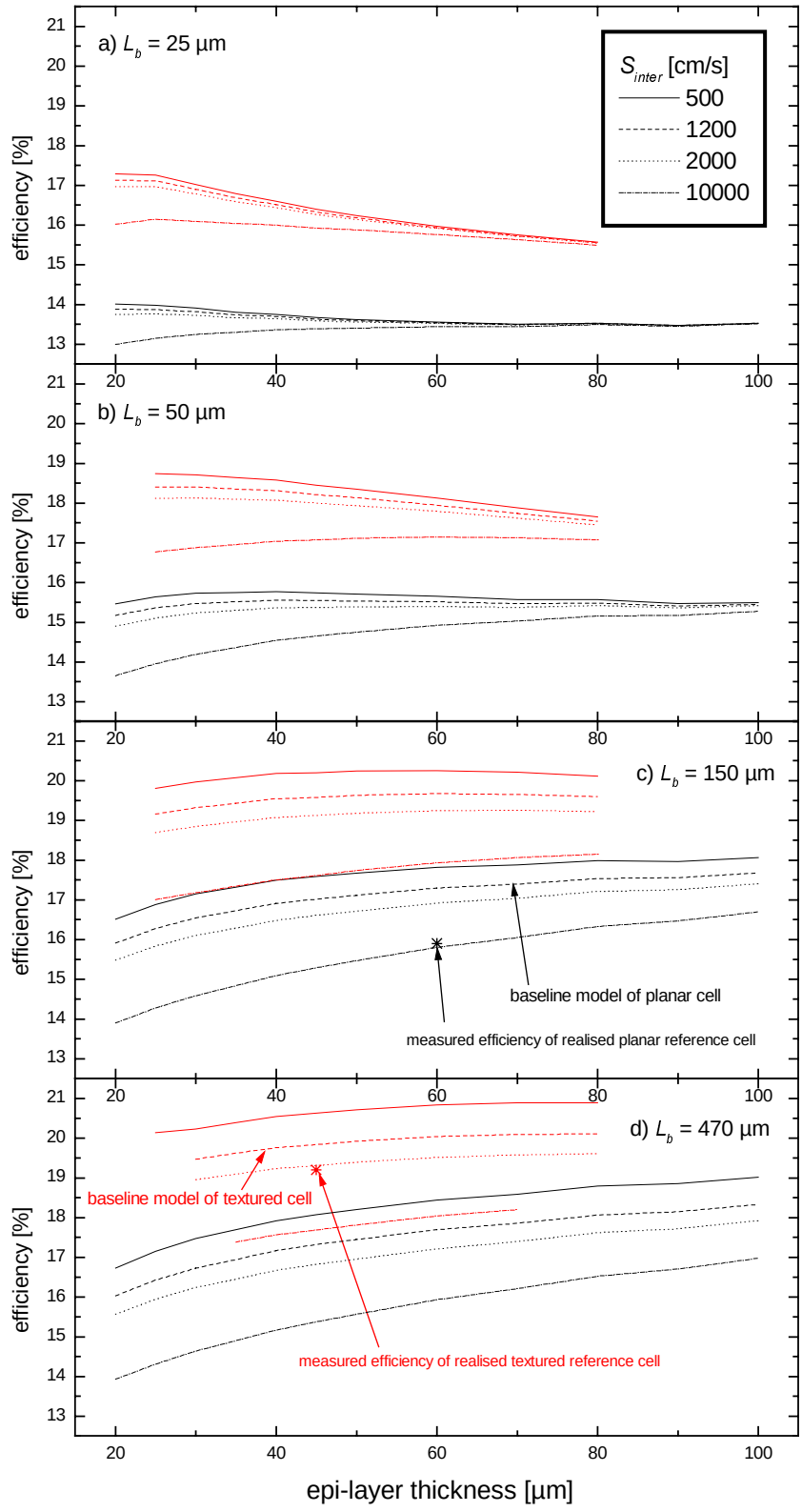

Fig. 6.19: Influence of epi-layer thickness H_{epi} on the conversion efficiency of textured and planar SOI cells for different combinations of the recombination parameters L_b and S_{inter}. The red curves were calculated for a textured front, the black curves for a planar front.

6.6 Comparison of simulated and measured fill factor

In this section we shall compare the measured fill factor values η_{fill} to those obtained by simulation. Despite having been produced using basically uniform conditions a batch of SOI solar cells tends to display substantial variation in the measured fill factor values. The electrical baseline models described in Section 6.4 reproduced the measured V_{oc} and J_{sc} with a high degree of accuracy. However, measuring the planar and the textured reference cells gave 6.7 % and 2.2 % lower absolute values for the fill factor, respectively, compared with the simulation results. The origins of these deviations were investigated by taking measurements from 37 solar cells processed using comparable conditions in two batches.

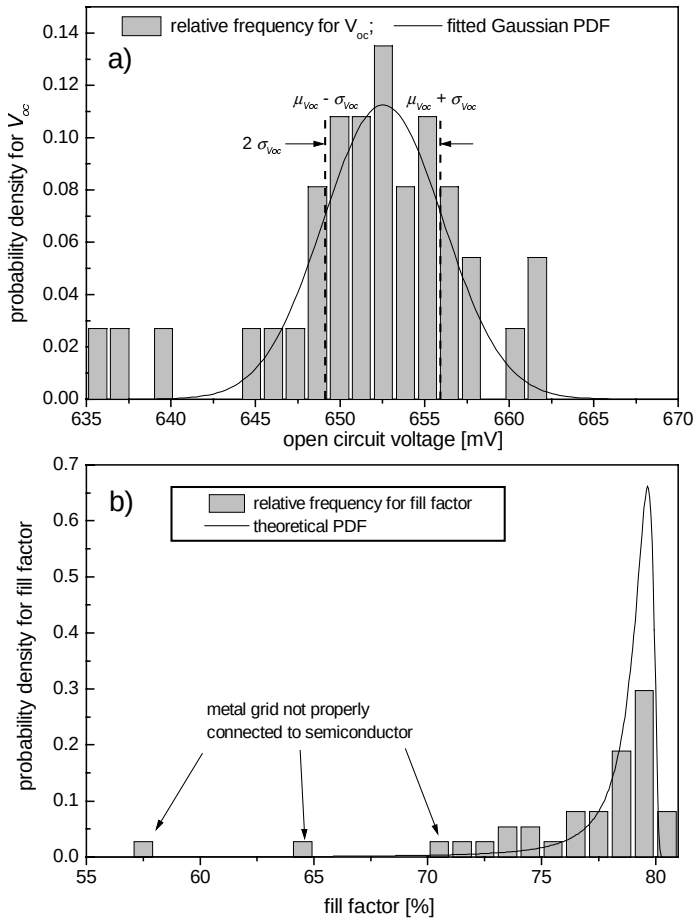

Fig. 6.20: Histograms showing measurement results of 37 solar cells (batches Simox 11 and Simox12). (a) Relative frequency of V_{oc} and fitted Gaussian PDF with mean value μ_{Voc} = 652.5 mV and σ_{Voc} = 3.55 mV; (b) asymmetric relative frequency of fill factor (bars); theoretical PDF, calculated for a *p-n* contact spacing of 715 µm and a standard deviation of σ_f = 6 µm for the finger width (solid line).

The effective base diffusion lengths of the investigated cell batches (Simox 11 and Simox 12) were considerably lower than those of the two reference cells.

V_{oc} is primarily determined by the recombination parameters L_b and S_{inter}. Variations in L_b and S_{inter} are due to the sum of a large number of primarily independent effects. The *Central Limit Theorem* implies that their distribution should approximate a normal distribution.

The relative frequency of the open circuit voltage is plotted in Fig. 6.20a as a bar chart. It can be approximated to a normal distribution using a least squares fit (solid line). The interval [μ_{Voc} - σ_{Voc}, μ_{Voc} + σ_{Voc}] of the Gaussian distribution in Fig. 6.20a corresponds to the area in Fig. 6.21 labelled with 655 mV. The same recombination velocity as used for the baseline model in the previous sections (S_{inter} = 1200 cm/s) was assumed. Hence, L_b-values of 47 µm and 55 µm were extracted from Fig. 6.21. In other words, using these L_b-values for the semiconductor device simulation leads to the V_{oc}-values corresponding to the boundaries μ_{Voc} - σ_{Voc} and μ_{Voc} + σ_{Voc} of the confidence interval, respectively.

Simulating the fill factor as a function of the *p-n* contact finger distance for L_b = 47 µm and L_b = 55 µm results in the dashed lines plotted in Fig. 6.22. Resistive losses in the metal grid are neglected regarding the dashed lines. If a random sample from the batches of solar cells under investigation is taken and its fill factor is simulated based solely on its recombination parameters (L_b and S_{inter}), this simulated fill factor value will have 68 % probability of falling within the interval given by the two dashed lines in Fig. 6.22. This applies because the fill factor has a monotonic relashionship with V_{oc} [20] and the interval boundaries were determined from a V_{oc} confidence interval of width of 2 σ_{Voc} around μ_{Voc}. This provides a measure for the uncertainty in the fill factor simulation, arising from variations in the recombination parameters of the cells.

A highly asymmetric frequency distribution is obtained for the fill factor, with the center of the distribution at 79.5 %, slightly below the maximum realised value of 80.4 % (Fig. 6.20b). The fill factor is mainly effected by the realised cross sectional area of the metal fingers. Variations in the electroplating process, used to increase the cross-sectional area of the contact fingers, cause deviations in the measured fill factor values of different cells.

The asymmetric shape of the relative fill factor frequency distribution can be understood by appeal to a simple statistical approach. The finger width is assumed to follow a Gaussian distribution with probability density function (PDF) *f(w)*, where *w* denotes a realised value of the finger width. An aspect ratio of 3 (finger width to finger height) was determined for the two investigated solar cell batches. This aspect ratio was used in the analytical approach of Serreze to correct for the resistive losses in the metal grid [97]. This leads to the following dependency of fill factor η_{fill} on finger width *w*

$$\eta_{fill}(w) \sim \eta_{fill,sim}\left(1-\frac{c_{finger}}{w^2}-c_{bus}\right)$$

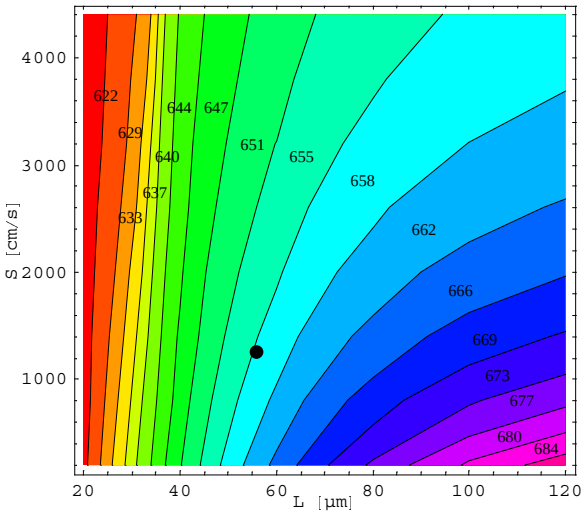

Fig. 6.21: Contours of constant V_{oc} of the textured SOI cell. The black dot indicates the parameter combination which was chosen for the semiconductor device simulation of the fill factor as a function of *p-n* contact spacing (upper dashed line in Fig. 6.22).

where c_{finger} and c_{bus} are constants depending on the metal grid geometry. $\eta_{fill,sim}$ is the upper fill factor limit obtained by semiconductor device simulation using *DESSIS*. $\eta_{fill}(w)$ is shown in Fig. 6.23b as a solid line. The upper fill factor limit $\eta_{fill,sim}$ for a contact finger spacing of 715 µm is indicated in Fig. 6.22 as a black square and as a horizontal dashed line in Fig. 6.23b.

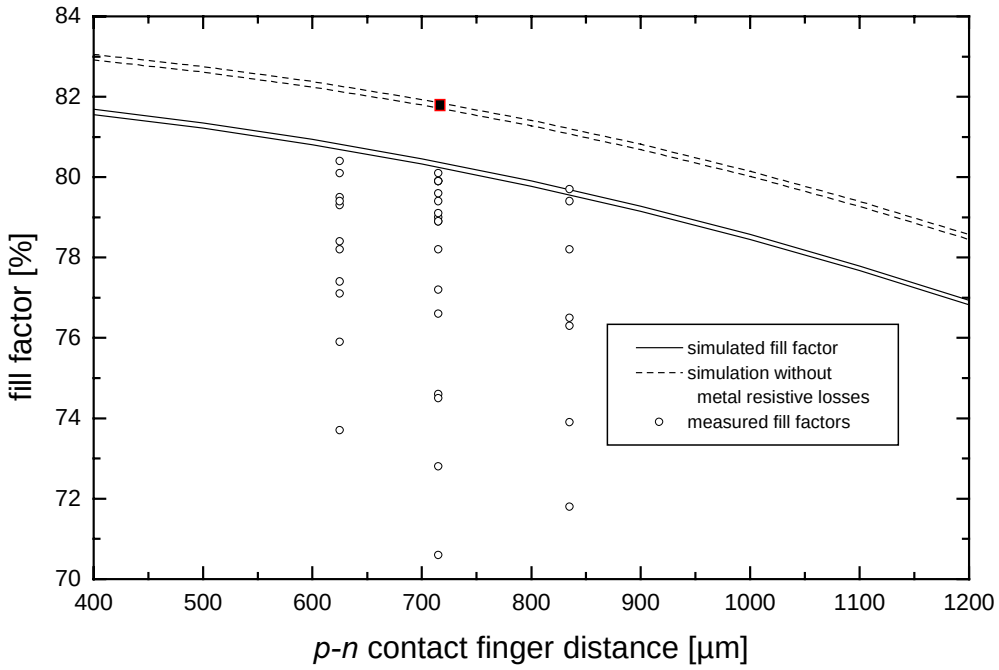

Fig. 6.22: Comparison of simulated and measured fill factor of textured SOI cells. The dashed lines show the fill factor calculated by *DESSIS* as a function of *p-n* contact finger distance. The upper and lower solid curves were simulated for L_b-values of 47 µm and 55 µm, respectively. These two L_b-values give V_{oc} values located within about one standard deviation of the investigated solar cell batches. Accounting for metal resistive losses results in the solid curves.

$\eta_{fill}(w)$ is a monotonic increasing function. Therefore, the PDF $f(\eta_{fill})$ for the fill factor of the SOI cell can be obtained by transformation of the PDF according to the formula

$$f(\eta_{fill}) = \frac{f(w)}{\left|\frac{d\eta_{fill}(w)}{dw}\right|}. \tag{6.5}$$

The resulting PDF is plotted in Fig. 6.23c. The observed relative frequency for the fill factor and this theoretical PDF is compared in Fig. 6.20b for a standard deviation of the finger width of σ_f=6 µm.

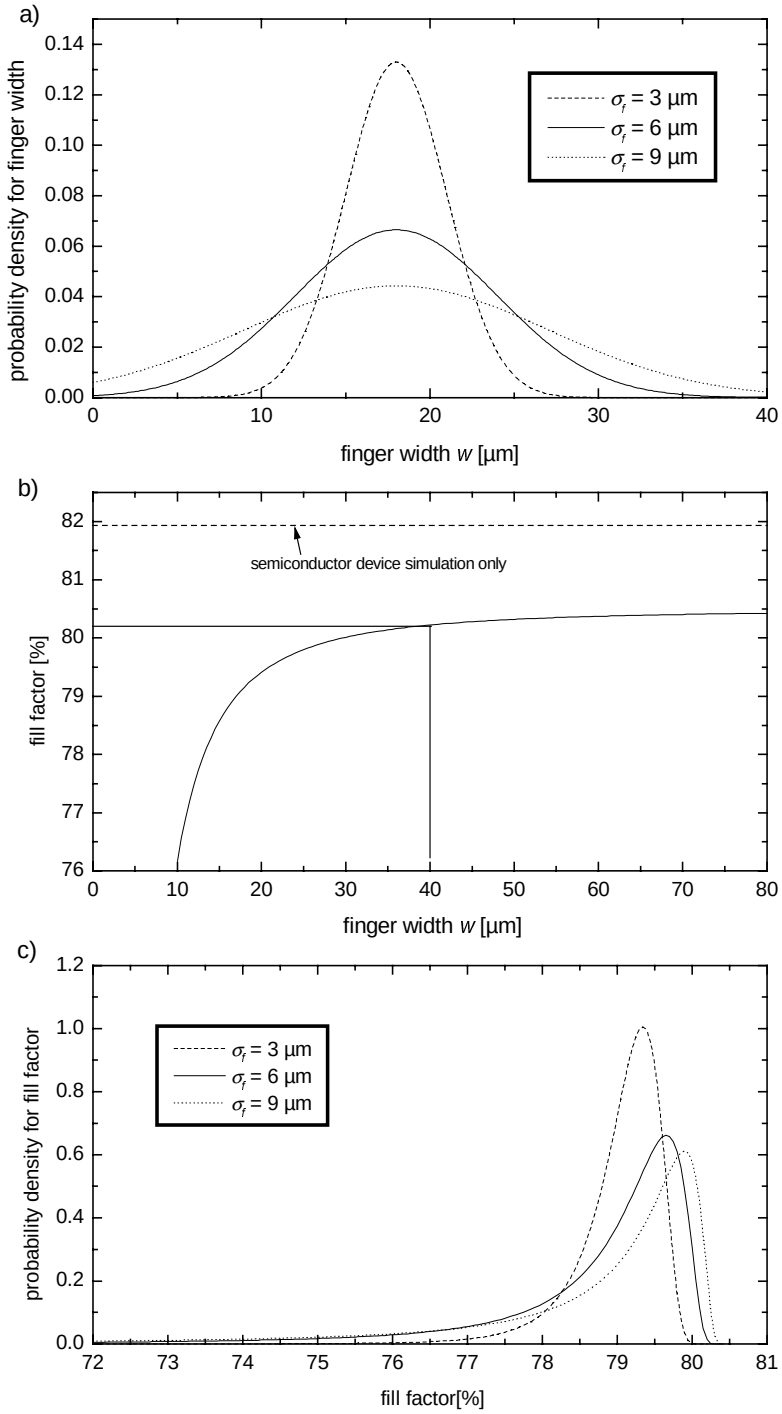

Fig. 6.23: Transformation of probability density function (PDF) for the finger width in order to obtain the PDF for the fill factor. (a) PDF of finger for three different values of the standard deviation σ_f; (b) analytical dependence of fill factor on finger width for a *p-n* contact finger spacing of 715 µm and an aspect ratio of 3; (c) transformed PDF $f(\eta_{fill})$ for fill factor on the basis of the three σ_f values listed in the caption.

The simple statistical approach reproduces the shape of the relative frequency for the fill factor successfully. Moreover, the center of the theoretical PDF is located at the same fill factor value as that observed for the relative frequency. It can be concluded from this discussion that a comparison of simulated fill factor values with measured fill factor values

should be based on a series of measurements. However, a simplified comparison is possible for the *maximum* realised fill factor, which corresponds to the group of cells with constant *p-n* contact finger spacing! These maximum values are plotted in Fig. 6.22 as the three open circles with the highest fill factor values and are in close agreement with the simulated solid curves. These curves have been corrected for the ohmic resistive losses occuring in metal fingers of 40 µm width and 13 µm height. Obviously, this agreement is not affected by possible deviations of the fill factor due to variations in the recombination parameters in the solar cell batch as the two solid lines, side by side, were simulated for the V_{oc} confidence interval with boundaries $[\mu_{Voc} - \sigma_{Voc}, \mu_{Voc} + \sigma_{Voc}]$.

High fill factor values are realised only if the contact resistance is low. The fact that the metal fingers of some SOI cells are not completely connected to the semiconductor can be clearly seen with the naked eye. Consequently, the contact resistance is enhanced and the fill factor is degraded for these cells. This accounts for cases of SOI cells where fill factors of lower than 70 % are observed. These observations do not fit in with the theoretical PDF which does not take this factor into account.

In conclusion, one should, in general, not compare the mean fill factor value from measurements of a solar cell batch to simulation results. As has been demonstrated in this section, such a fill factor comparison should instead be based on the relative frequency of the measurement series.

epi-layer doping concentration	1.35×10^{17} cm^{-3}
L_b-values correspond to $\mu_{Voc} \pm \sigma_{Voc}$ of the Gaussian distribution in Fig. 6.20a	47 µm and 55 µm
S_{inter}	1200 cm/s
finger width	Gaussian distribution with mean value of 18 µm
finger height	1/3 finger width
cell surface	textured

Tab. 6.4: Cell parameters extracted from the batches which were used to investigate the fill factor of textured SOI cells (Simox 11 and Simox12). All other parameters were fixed to the baseline parameters listed in Tab. 6.1 and Tab. 6.3.

6.7 Performance of simplified SOI cells

The metal grid of the high efficiency SOI cells discussed so far was photolithographically defined with a high aspect ratio of the fingers (see Tab. 6.3c). We continue with the discussion of the performance of an industrially manufacturable SOI cell with an interdigitated front grid and front surface texture.

A finger width of 50 µm with full area contact of the metal to the silicon-layer was assumed. The gap between the p-type diffusion and the emitter was chosen to be 40 µm compared to 8 µm for the high efficiency SOI cell. To prevent dominant ohmic losses in the emitter, the emitter sheet resistivity was scaled to lower values with increasing *n-p* contact spacing. The emitter sheet resistivity was decreased from 138 Ω/square for a contact spacing of 700 µm to 70 Ω/square for the 1500 µm contact spacing.

For increasing contact distance the simulation shows an increase of the short circuit current density (Fig. 6.24) due to the decreased shadowing losses from the metal fingers. The open circuit voltage is more or less unaffected by the *n-p* contact spacing whereas the fill factor decreases due to increasing ohmic losses in the base.

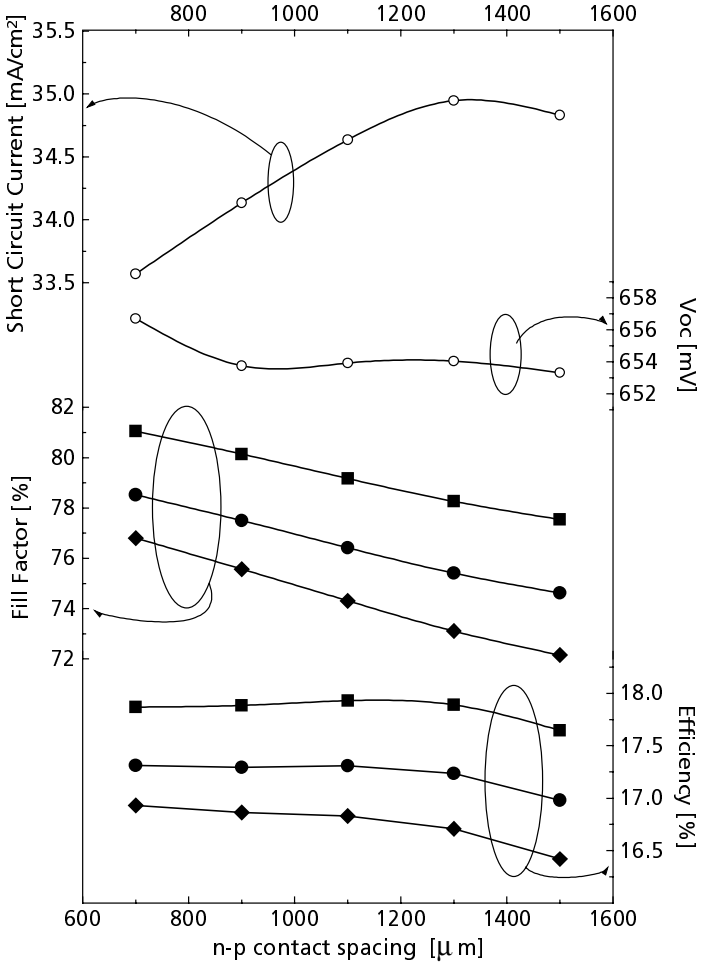

Fig. 6.24: Variation of *n-p* contact spacing for a simplified manufacturable SOI cell.

A correction of the fill factor, calculated by the device simulator for additional ohmic losses in the metal, was performed for three different types of front metal grids (Tab. 6.5). In accordance with the realised SOI cell a finger and bus height of 10 and 20 µm, respectively, and a metal resistivity of $1.6 \cdot 10^{-6}$ Ω cm were taken as the upper limit. The measured values for the metal resistivity of screen printed contacts are found to be around $4.7 \cdot 10^{-6}$ Ω cm. As the lower limit for metal grid quality the height of the fingers was set to be 7 µm and the height of the bus to be 15 µm. This leads to a difference of 1.2 % (absolute) in the cell efficiency between the lower and upper limit as can be seen in Fig. 6.24. Losses due to contact resistance were not included in the modelling.

Symbol	Metal	Resistivity [Ωcm]	Finger height [µm]	Bus height [µm]
■	evaporated	$1.6\ 10^{-6}$	10	20
●	screen printed	$4.7\ 10^{-6}$	15	20
♦	screen printed	$4.7\ 10^{-6}$	7	15

Tab. 6.5: Metal grid parameters for the study of simplified SOI cells.

6.8 Summary of results

The external reflection of planar SOI cells with a double layer antireflection coating can be described analytically. Thereby, escape reflectance in the long wavelength regime is accounted for using a geometric series. The formula reproduces a characteristic hump in the measured reflection at 1030 nm.

The measured external reflection of SOI cells with inverted pyramids can be described with high accuracy using ray tracing. Optical baseline models for a planar and a textured SOI reference cell were established. A detailed quantitative analysis of the optical losses for both cell types is presented revealing that, for illumination with the AM1.5 spectrum, the textured (planar) SOI reference cells absorb 82% (71%) of the incident photon flux in the epi-layer. The lower epi-layer absorption of the planar cell is mostly due to enhanced absorption in the substrate. Whereas 10.5% of the incident photon flux is absorbed in the substrate of the planar cell, only 2.4% is lost in the substrate of the textured cell.

The influence of epi-layer thickness on the reflection and absorption properties of planar and textured SOI cells is investigated utilising the optical baseline models. A strong dependence of the maximum achievable short circuit current density of the planar cell on epi-layer thickness is found. The short circuit current density of a planar SOI cell is limited to $i_{sc,max} = 29.5$ mA/cm^2 for an epi-layer thickness of 15µm. This value increases to $i_{sc,max} = 34.8$ mA/cm^2 for an epi-layer thickness of 100µm. The short circuit current density of the textured cell is limited to $i_{sc,max} = 35.7$ mA/cm^2 for 15µm epi-layer thickness, increasing to $i_{sc,max} = 39.2$ mA/cm^2 for a 100µm thick epi-layer.

For the electrical modelling of thin silicon solar cells it is particularly important to account for the optical carrier generation rates determined by ray tracing. Electrical baseline models for the planar and the textured SOI reference cell were established implementing the optical carrier generation rates determined with the optical baseline models.

The recombination parameters of the reference cells were determined by combining numerical device simulation with measurements of V_{oc} and the effective diffusion length L_{eff} extracted from spectral response measurements. Thereby, it was found that the most sensitive method to determine compatible pairs of the bulk diffusion length and the effective surface recombination velocity at the intermediate oxide are contours of constant $V_{oc.}$ The effective diffusion lengths were determined to be three times the epi-layer thickness for the planar reference cell and four times the epi-layer thickness for the textured reference cell, respectively.

The influence of epi-layer thickness and the recombination parameters on the electrical performance of planar and textured SOI cells was investigated by using the above mentioned combination of optical ray tracing and electrical device simulation. Counteracting optical and electrical losses were identified and quantified.

A gain in V_{oc} can be achieved by a surface texture in comparison to a planar cell front. This gain is due to the increased *p-n* product across the cell, which is a result of enhanced light

absorption. A back surface field is beneficial if the base diffusion length exceeds half the thickness of the epi-layer. Reducing the epi-layer thickness increases V_{oc} if base recombination dominates over surface recombination at the back surface field. In contrary, V_{oc} decreases for a poorly passivated intermediate oxide, *e.g.* if no BSF is present.

J_{sc} of a textured SOI cell can be increased for low minority carrier base diffusion lengths by reducint the epi-layer thickness. This is a result of the efficient light confinement achieved by inverted pyramids on the front side. This effect is not observed for planar cells as a reduction in base recombination is compensated by increasing optical losses.

Opposite trends in the influence of epi-layer thickness on J_{sc} are found comparing planar and textured surfaces for a base diffusion length of L_b = 50 µm. J_{sc} can be slightly increased for reduced epi-layer thickness if the front surface is textured whereas J_{sc} decreases for the planar cell.

Measured fill factor values of a batch of SOI solar cells tend to display substantial variation. The origins of these deviations were investigated by taking measurements from two batches of solar cells processed using comparable conditions.

The relative frequency of the open circuit voltage can be approximated to a normal distribution. This can be explained via the Central Limit Theorem.

In contrast, a highly asymmetric frequency distribution is obtained for the fill factor The realised cross sectional area of the metal fingers plays a dominant role in determining the value of the fill factor. Hence, variations in the electroplating process, used to increase the cross-sectional area of the contact fingers, cause deviations in the measured fill factor values of different cells. The asymmetric shape of the relative fill factor frequency distribution can be understood by appeal to a simple statistical approach. The finger width is assumed to follow a Gaussian distribution. Transformation of this normal distribution using an analytical expression for series resistance losses in the metal grid gives the probability distribution of the fill factor. The obtained probability distribution is in accordance with the frequency distribution of the fill factor. It is concluded that one should not compare the mean fill factor value of solar cell batch to simulation results. Such a fill factor comparison should instead be based on the relative frequency of the measurement series.

7 Analysis of one sun mono-crystalline rear contacted silicon solar cells

7.1 Introduction

Rear-contacted solar cells have their complete metallisation on the rear surface. This decouples the series-resistance versus shadowing loss compromise of conventional solar cells. The sunward side of the cell may be optimised for optical performance and the back side for electrical performance. Thus, rear-contacted cells are especially suitable for concentrator application with its need for very low series resistance. Unlike conventional cells, there is no trade off between increasing cell size decreasing efficiency on account of series resistance losses, because the whole cell surface can be covered by an appropriate metallisation scheme. Moreover, having both contacts on the rear cell side simplifies module assembly significantly. In addition, back-contacted cells offer an easy way of producing bifacial solar cells.

Most of the rear-contacted cells in the past have also been rear-junction cells, *i.e.* the minority carriers generated predominantly at the front surface have to diffuse through the base of the cell to the rear side, where they are collected by the back-side emitter. This cell concept was used mostly for high efficiency approaches, since, unlike conventional cell designs, it requires high quality base material and an excellent front surface passivation. This disadvantage may be partly overcome by a collecting emitter on the front-side of the cell. The emitter-wrap-trough (EWT) cell concept provides an elegant method of connecting the front emitter to the rear emitter [73,98]. The front and rear emitters are connected by emitter-diffused holes from the front to the back.

The cell concept of rear-contacted silicon solar cells with an interdigitated rear-contact metallisation pattern was introduced by Schwartz in 1975 [99]. Conversion efficiencies of 17.5% under 50 suns concentration were reported. In a theoretical study by Lammert [100], it was postulated that with heavier doped junctions, a lower metallisation resistance, reduced reflectance, and improved bulk lifetime it was possible to achieve a cell efficiency of 24% at an illumination intensity of 300 suns. However, severe simplifying assumptions were made in this study, such as neglecting external reflection losses and assuming ideal junctions.

Schwartz [101] compiled a list of approaches to silicon solar cells for use under concentrated sunlight, which includes a discussion of unconventional designs of rear-contacted solar cell structures, such as the polka dot cell [98].

Swanson investigated an improved rear-contacted cell structure in 1986 [36], the point-contact silicon solar cell. At that time, 23% efficiency at 100 suns could be reached using 80 µm thick high resistivity float-zone silicon. Similar to the interdigitated rear-contacted

solar cell in [99], the entire metallisation of the point-contact solar cell is located on the rear surface in the form of an interdigitated grid structure. To reduce contact recombination, the metal contacts the silicon only at small points. These points are opened in the passivation oxide and covered by *n*-type and *p*-type diffusions alternating in a checkerboard fashion. The front surface and the regions between contacts on the rear are covered with SiO_2 for surface passivation. Swanson developed an improved analytical cell model to explain the three-dimensional charge carrier distribution around point contacts. The approach emphasises the accurate determination of the total recombination current rather than carrier densities and fluxes. The semiconductor transport equations are solved using a variational approach to obtain the carrier density in the highly injected base. The recombination activity of the n^+ and p^+ diffusions at the point contacts is modelled using measured values of the diffusion saturation current density. In order to solve the coupled semiconductor equations, Swanson assumed a position-independent diffusion constant in the base, neglected base recombination, and assumed that photogeneration is confined to an infinitesimally thin layer at the front of the device.

Sinton refined Swanson's analytical model by incorporating a numerical solution of the effects of bulk generation and recombination [102]. Sinton analysed 28% (at 100 suns) efficient point-contact cells fabricated on high resistivity silicon (100-400 Ωcm n-type float-zone). He established a baseline model that included a universal set of parameters fixed by independent measurements. The model was shown to be in agreement with measurements to within 1 percent in absolute efficiency for a wide range of illumination intensities.

Research on rear-contacted concentrator cells produced various results that are also relevant to solar cells operating at one sun. King [103] investigated saturation current densities of shallow diffusions for passivating the front surfaces of point-contact solar cells. A one-sun efficiency of 22.3% was reported for a cell with an open-circuit voltage of 706 mV. Verlinden proposed a multilevel metallisation scheme that produces a series resistance independent of the cell size [104].

The above-mentioned solar cell results were obtained with complex processing technology that is too expensive for one-sun application. Sinton [105] proposed a simplified fabrication sequence for rear-contacted cells operating at one sun. A self-aligned metallisation technique proposed in this work allows for the fabrications of rear-contacted cells with only one photolithographic mask step. However, to avoid shunt effects in heavily doped compensated regions, Sinton used a simplified fabrication sequence with two mask steps. Large area cells with 21.9% efficiency for one-sun operation were fabricated on high-resistivity, 390 Ωcm, phosphorous doped silicon wafers that were 130 µm thick.

Matsukuma *et al.* from Hitachi Research laboratories enhanced the analytical point-contact cell model of Swanson to account more accurately for multiple internal reflections and carrier recombination in the base [106]. In this study, simplified large area rear-contacted cells with point and line emitters are investigated. The modeled cell dimensions were adjusted to be achievable using screen printing technology for the contact metallisation.

In 1991, research on one-sun rear-contacted cells at Stanford University resulted in 22.7% efficient cells [107]. The first pilot line production of large-area rear-contacted cells for one-sun operation was started at SunPower in 1993 [108], followed by the fabrication of the 7000 high efficient rear-contacted cells for the winning car, the "Dream", in the 1993 solar car race [109]. At SunPower it was shown that a rear-contacted cell fabrication line can be implemented with a production yield greater than 90% and with an average cell efficiency of 21.1%. A total of five photolithography masks was used in the 1993 production line and the cells were processed on high-resistivity float-zone silicon wafers of 160 µm thickness, *i.e.* the production line was not optimised for low cost.

The cell design was further optimised in order to reduce parasitic perimeter losses [110]. The maximum cell efficiency was enhanced to 23.2% by reducing the carrier recombination at the saw-cut perimeter, by using lower resistivity material [111].

7.2 Rear contact cells for one-sun application at Fraunhofer ISE

Two goals were pursued within the development of rear-contacted cells at Fraunhofer ISE:

1. the utilisation of low-resistivity base material and
2. the optimisation of this cell type for bifacial application.

A set of masks for cells with interdigitated grids was used on 250 µm thick low-resistivity (1.25 Ωcm) p-type FZ-silicon.

The front side of the RCC is textured with random pyramids for optimal optical characteristics, the rear side is planar. An oxide passivated floating emitter is applied to the unmetallised side (bottom side in Fig. 7.1) in order to decrease surface recombination velocity. A thermal oxide alone on a textured surface is known to have a non-optimal surface recombination velocity of more than 1000 cm/s and leads to a decrease of 30 mV in V_{oc} for this cell type [92]. Therefore, the performance of the RCC depends strongly on the minimisation of the front surface recombination, a fact discussed for one-sun rear point-contact cells in Ref. [112].

Since the floating emitter on the unmetallised side is processed in the same step as the one on the metallised side, this additional feature does not make the process more complex. Both emitters have a sheet resistance of 127 Ω/sq. and peak doping concentration of 5×10^{18} cm^{-3}. On the metallised side of the cell nearly the whole surface is a phosphorous diffused area. Only a fraction of around 2% is left undiffused for the base contacts. Local deep diffusions underneath both emitter and base contacts were used. Due to the resulting high surface doping concentration, it is possible to use Ti/Pd/Ag not only for the emitter but also for the base contacts. The distance between the finger lines of one grid type lies between 1000 to 1430 µm.

The RCC investigated in this chapter had an efficiency of 21.4% and was improved in the course of the optimisation studies to 22.1%. A RCC structure optimised for bifacial

application has, for the first time, produced an efficiency of more than 20% for illumination from either front or rear side [112].

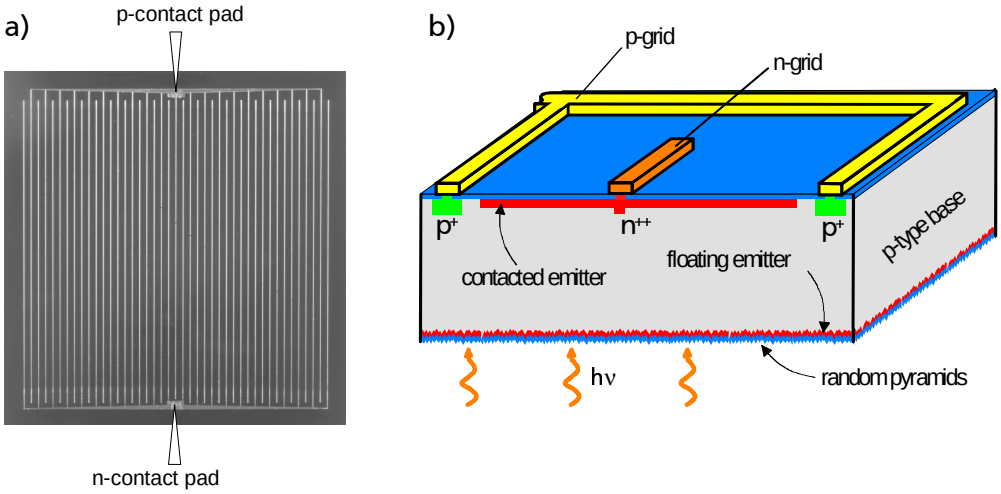

Fig. 7.1: Structure of the rear-contacted cell fabricated at Fraunhofer ISE. (a) View of the rear side of the rear-contacted cell showing the interdigitated contact pattern. (b) Detail, with the cell shown upside down, so that the light illuminates the cell from the bottom. For bifacial application the rear surface is also textured.

7.3 A comprehensive electrical and optical numerical model for the rear-contacted cell

Fig. 7.2 presents a diagram of the simulation steps for a complete device simulation of the RCC. The reflection and absorption properties of textured silicon solar cells can be calculated with the ray tracing program *RAYN* [113]. An optical symmetry element suitable for ray tracing simulation of the random pyramid texture of the rear-contacted cell is shown in Fig. 7.2a. Front side illumination on the random pyramids is approximated by calculating the geometric path of a monochromatic light ray of random incidence on a single upright pyramid [70].

For electrical device simulation the device volume has to be discretised. Fig. 7.3 shows the discretisation mesh of a symmetry element of the rear-contacted cell, including one *n*– to *p*– contact finger distance. In the following this symmetry element of the interior cell region is called an *elementary diode* (Fig. 7.4). A high density of mesh points in device regions with a steep doping gradient is needed for convergence of the iteration scheme used by *DESSIS* [41]. This is shown in Fig. 7.3 in the detail of the discretisation mesh around the *n*-contact region. To calculate a realistic short-circuit current, we need a very high density of mesh points at the illuminate front surface. Thus, the discretisation mesh is adapted to the gradient of the generation function, as shown in the details at the top of (Fig. 7.3).

Ray tracing, construction of a discretisation mesh, and device simulation are performed in an object oriented simulation environment described in Section 4.

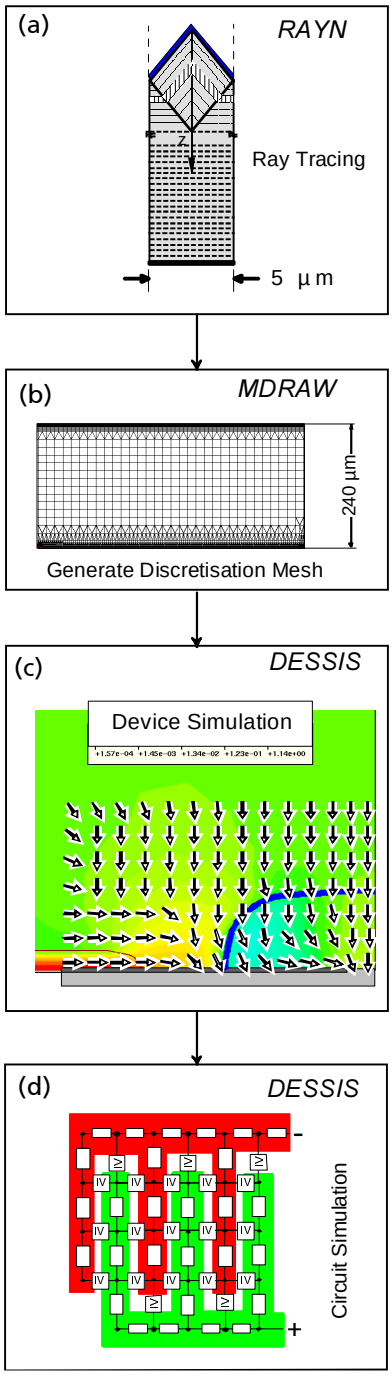

Fig. 7.2: Simulation flow for the numerical calculation of the optical and electrical properties of the RCC. (a) A single upright pyramid of 5 µm width is the symmetry element for the optical ray tracing simulation; (b) the discretisation mesh is generated in the next step; (c) for the electrical device simulation, the optical generation profile and the discretisation mesh calculated in the previous two steps are used; (d) the current-voltage characteristic from the device simulator is used as input for the circuit simulation, taking into account the voltage drops along the metal bus bar and the metal fingers of the solar cell.

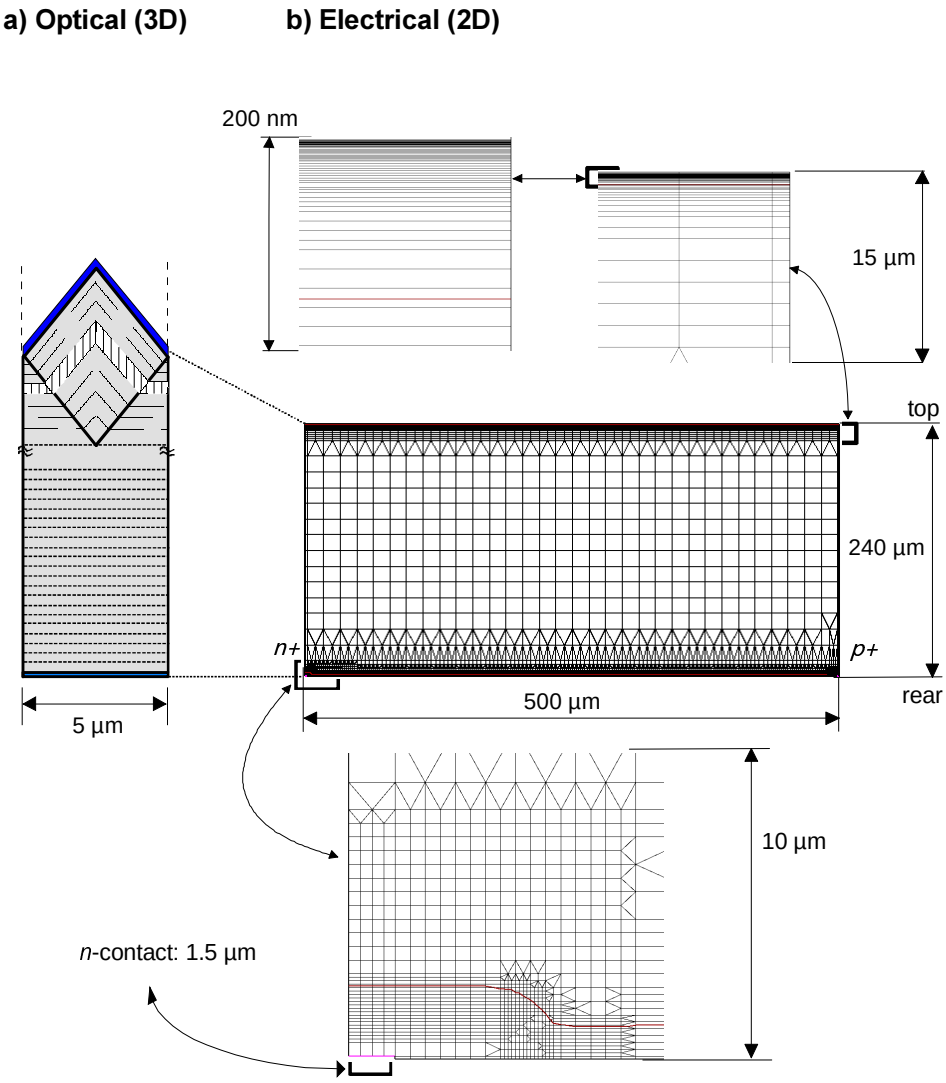

Fig. 7.3: Optical and electrical discretisation of the cell volume.

Till now, the description of device simulations performed with an elementary diode region has ignored resistive metal grid losses and recombination losses at the cell perimeter. Recombination losses at the cell perimeter are a consequence mainly of the unpassivated cut surface of the cell. Perimeter recombination losses also degrade the cell efficiency of cells that remain embedded in the wafer. This is due to outdiffusion of minority carriers into the unilluminated wafer regions outside the cell area.

We shall include the distributed resistive losses of the interdigitated metal grid using the circuit simulation method as introduced in Section 3.6. Losses due to recombination of charge carriers at the device perimeter can also be quantified by introducing *I–V* curves of the perimeter region into the circuit simulation. The perimeter region represented by a perimeter diode is shown at the right side of Fig. 7.4. Half of a *p*-contact, the collecting emitter, and the shaded cell perimeter are included in the perimeter diode.

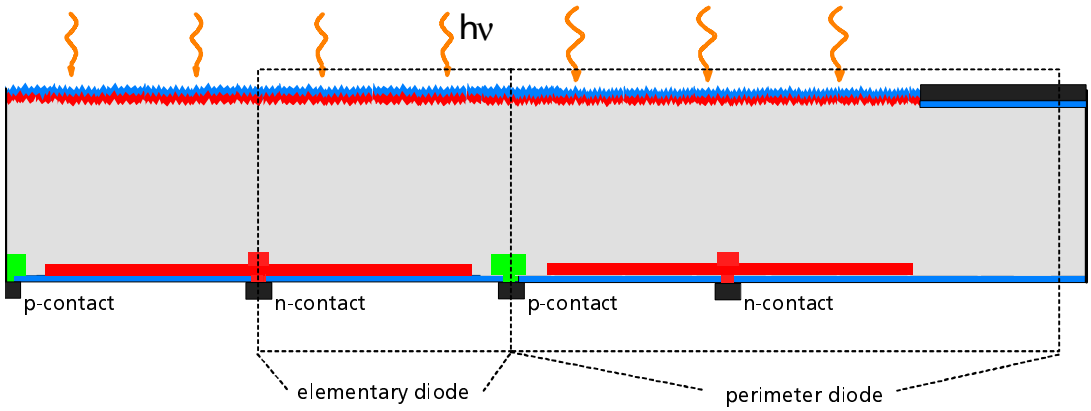

Fig. 7.4: Vertical section through the RCC, including the perimeter region. Dotted lines show the simulation domain of an elementary diode and a perimeter diode.

The electrical circuit representing the entire solar cell comprises elementary diodes and perimeter diodes connected by Ohmic resistors (Fig. 3.10). For reasons of symmetry, only half of the metal grid needs to be resolved in the circuit simulation in order to describe the *I-V* curve of an entire RCC. The elementary diodes of the RCC are modelled in two dimensions in this work. Doing the numerical device simulations in two dimensions allows simulations to be performed within acceptable computing time. Differences arising from three-dimensional current flow patterns in the base were investigated by Ohtsuka [114]. The RCCs investigated by Ohtsuka have a large area fraction of the rear surface that is not covered by the emitter. The third dimension in the simulation of the elementary diodes is neglected here because the rear surface is almost fully covered by the collecting emitter. Therefore, the current flow patterns in the base of our RCC can be approximated by 2D simulations.

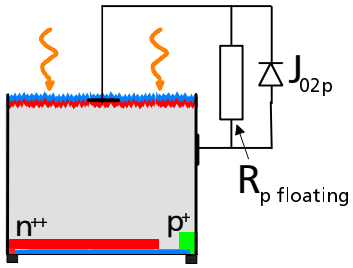

Fig. 7.5: Equivalent circuit for the description of carrier recombination of the floating junction.

To investigate shunt effects on the floating emitter, one-dimensional simulations using PC1D [67] were performed. The equivalent circuit for these calculations is shown in Fig. 7.5 and discussed in Section 7.6.

7.4 Optical properties of random pyramid texture

The random pyramid texturisation is approximated by a symmetry element consisting of one upright pyramid. Fig. 7.6 demonstrates that even the simplified upright pyramid approach provides a good approximation of the measured reflection of a wafer with random pyramid texture at the illuminated surface and a planar rear surface.

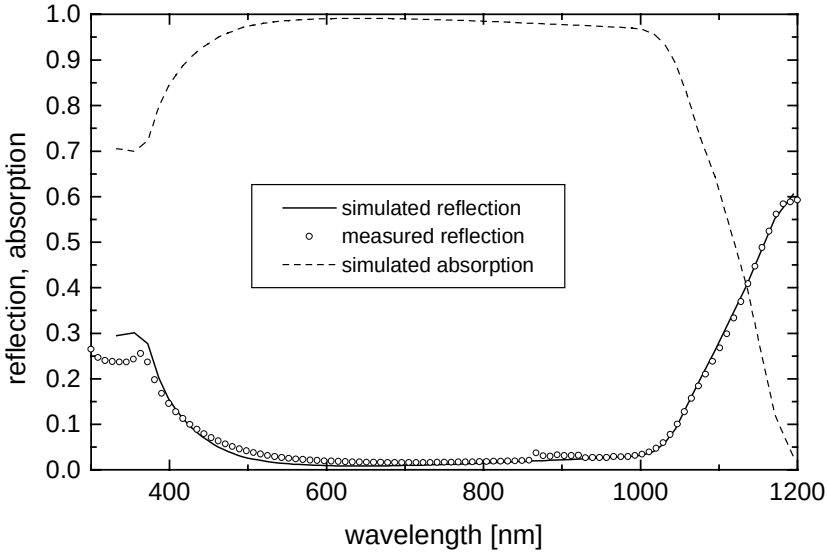

Fig. 7.6: External reflection and absorption of the RCC. The open circles show the measured external reflection of a wafer with random pyramids at the front and planar rear surface. The lines indicate ray tracing results obtained by simulating one upright pyramid.

7.5 Determination of recombination parameters

This section describes a general method to extract the recombination parameters of a high efficiency solar cell by combining numerical device simulation with measurements of open-circuit voltage and microwave-detected photo conductance decay (MW-PCD). In addition, the spatial distribution of excess carrier recombination in the different regions of the RCC for standard AM1.5 global illumination is determined.

The peak doping concentration of the emitter at the planar oxide-passivated rear side is 5×10^{18} cm^{-3}. Various references in the literature give an extracted interface surface recombination velocity of $S_{interface} \approx 500$ cm/s (Fig. 5.8).

The method applied here to determine the bulk diffusion length L_b and the effective surface recombination velocity of the emitter passivated front side $S_{eff,front}$ is the same one as in [70]: to match the overall recombination of the solar cell model and the realised cell, device simulations were performed for different combinations of L_b and $S_{eff,front}$, which reproduce the measured open-circuit voltage. For this purpose, we used an iterative algorithm, determining $S_{eff,front}$ for a given L_b to reproduce the measured V_{oc} by device simulation.

Upper and lower limits for the range of possible recombination parameters are obtained as follows. The solid lines in Fig. 7.7 show different combinations of $S_{eff,front}$ and L_b, resulting in the same open-circuit voltage in a device simulation with *DESSIS* and *RAYN*. The line with the circles was calculated for a measured open-circuit voltage of 689 mV for the cell under investigation. A range of $\pm$ 5 mV in V_{oc} was assumed as an upper limit for the tolerable deviation between measurement and simulation.

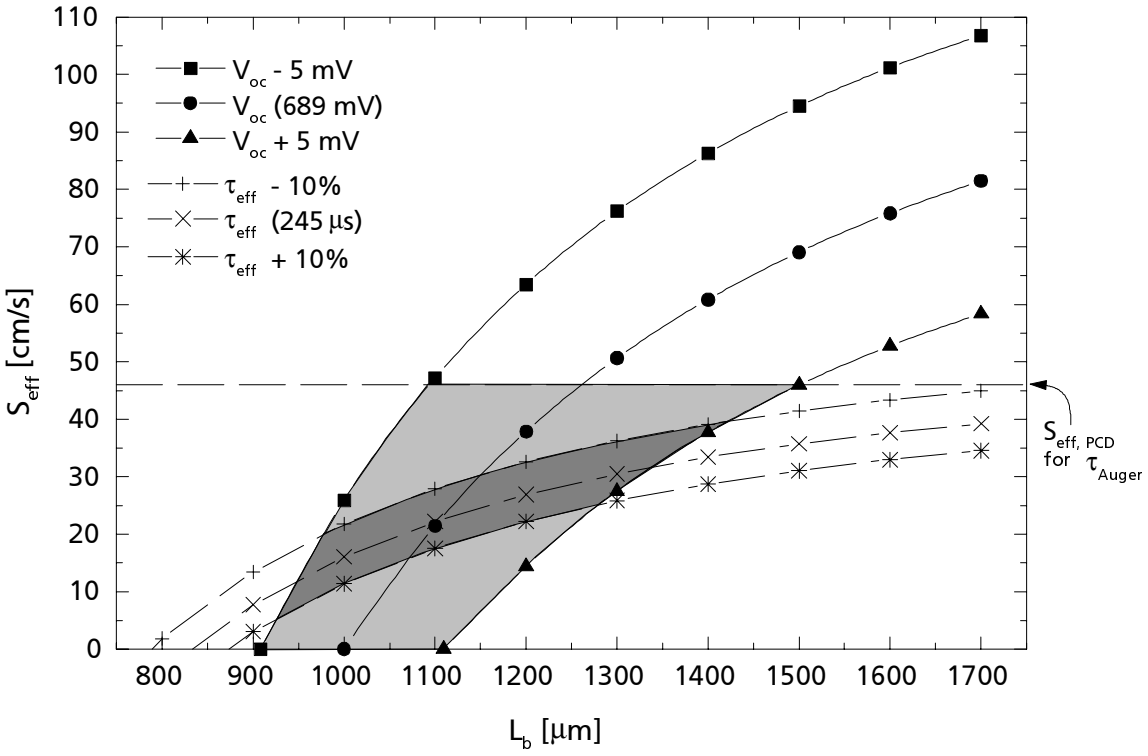

Fig. 7.7: Determination of the recombination parameters of the RCC. Curves of constant open-circuit voltage were simulated with *DESSIS* for different combinations of bulk diffusion length L_b and effective front surface recombination velocity S_{eff}. The range of possible combinations of L_b and S_{eff} can be further constricted applying PCD measurements to the same starting material.

Additional information on $S_{eff,front}$ was obtained from microwave-detected photoconductance decay (MW-PCD) measurements on test structures [92]. The effective minority carrier lifetime at one-sun illumination was determined to be $\tau_{eff} = 245$ µs [115]. An upper limit for $S_{eff,front}$ can be estimated by assuming Auger recombination as the only loss mechanism in the base. This assumption leads to $S_{eff,max} = 46$ cm/s and a range of possible values of L_b and $S_{eff,front}$ shown within the lightly shaded area in Fig. 7.7. The dashed lines in Fig. 7.7 show (L_b, $S_{eff,front}$)-combinations, resulting in the same measured τ_{eff}, including the estimated measurement error.

The intersection of possible (L_b, $S_{eff,front}$)-combinations determined by device simulation and PCD measurement is shown as the dark grey area in Fig. 7.7.

In addition to $S_{eff,front}$, the interface surface recombination velocity of the front surface, $S_{interface}$, was determined by *DESSIS* simulations, including the front n^+-diffused layer. The measured V_{oc} was obtained for $S_{interface} = 1500$ cm/s. As mentioned before, the value deduced from Fig. 5.8 for a planar surface with the same phosphorous peak doping concentration is 500 cm/s. Thus, $S_{interface}$ for the oxide–passivated random pyramid texture is approximately *three times* higher than that for a planar surface. The surface area with random pyramid texture is 1.7 times larger than a planar surface. Therefore, the increase in surface recombination velocity is not merely caused by greater surface area. The same strong increase in $S_{interface}$ was observed for a wide range of emitters in [92].

These recombination parameters are used to calculate the recombination fractions within different cell regions (perimeter losses excluded). This is done by integrating the spatially distributed recombination rates of all recombination channels over different cell regions. In Tab. 7.1 the recombination fractions are given for short circuit, maximum power, and open-circuit conditions.

region	J_{sc}	V_{mpp}	V_{oc}
base	86 %	82 %	70 %
emitter	6 %	6 %	14 %
surfaces	8 %	11 %	15 %
contacts	< 0.05 %	0.5 %	1 %
sum [mA/cm^2]	1	3	41

Tab. 7.1: Recombination distribution in the RCC for different operating conditions.

The light-generated current density in the RCC obtained by ray tracing simulation is 41.0 mA/cm^2. This represents the maximum achievable short circuit current density assuming no recombination losses in the device. Under open-circuit conditions, this current density is identical to the overall recombination current density in the solar cell. Under short circuit conditions, only 1 mA/cm^2 of the generated current density recombines within the cell. The main recombination mechanism, independent of the operating conditions, is Shockley-Read-Hall recombination in the base region. Thus, even when high-quality material is used, it is beneficial to reduce the cell thickness as will be investigated in detail in Section 7.10.1.

The recombination fraction of the emitter under open-circuit conditions is twice the recombination fraction under short circuit and maximum power point conditions. This can be explained by the fact that under open-circuit conditions there is no external current flow. Therefore, the minority carrier density in the emitter, and hence the Auger recombination fraction, is higher under open-circuit conditions.

The surface recombination fraction increases from 8% to 15% under short- and open-circuit conditions, respectively. The surface area of the non-diffused gap region at the rear side contributes only 1.5% to the entire cell area. However, under maximum power point conditions 30 % of the overall surface recombination occurs at the undiffused gap region. This emphasises the surface passivating effect of the floating emitter and the contacted emitter.

Fig. 7.8 shows the influence of the interface recombination velocity at the front surface on the RCC efficiency. The plotted cell efficiencies do not include fill factor losses due to the metal resistance of the grid. The dotted line shows the strong impact of the front surface interface recombination velocity for an RCC without floating emitter passivated front surface. Increasing the front surface interface recombination velocity from 0 to 3000 cm/s completely degrades the cell efficiency. In contrast, an effective front surface passivation can be achieved by a floating emitter: Even an increase in the front surface *interface* recombination velocity, $S_{interface}$, to 10000 cm/s causes an absolute decrease in cell efficiency of only 3%, because the effective front surface recombination velocity, S_{eff}, remains moderate.

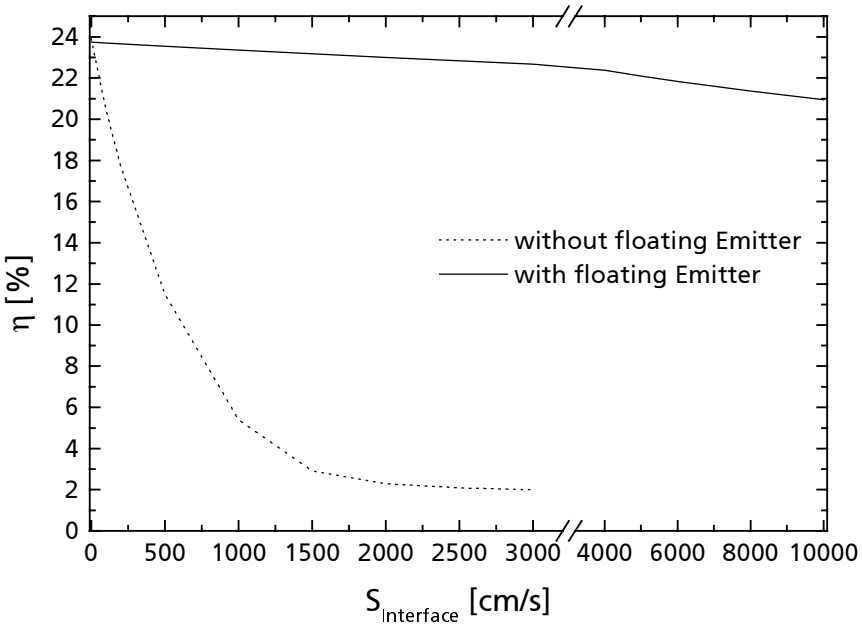

Fig. 7.8: Conversion efficiency of the RCC as a function of recombination velocity at the front surface. Distributed resistive losses and perimeter losses are neglected here.

7.6 Injection level dependence of the floating emitter

RCCs with floating emitter are strongly non-linear, *i.e.* the short circuit current density J_{sc} depends non-linearly on the illumination intensity. A non-linearity was also found for Passivated Emitter and Rear Floating junction (PERF) cells, where shunts of the floating emitter junction to the rear-contacts were found to be an important factor in the interpretation of the *I-V* curves [116]. In contrast to this type of shunt, in the case of the diffused front floating emitter of a RCC, a shunt element constitutes a contribution to the recombination losses at the front surface. This shunt effect might be due to inhomogeneities of the doping profile along the random pyramid texturisation. The passivating property of the floating emitter is weakened where the doping profile is thinner. In other words, a non-negligible minority carrier recombination current towards the less passivated parts of the front surface occurs.

The shunt effect of the floating emitter causes a strongly injection-level-dependent effective front surface recombination velocity. This injection dependence is reflected in a drastic decrease in the measured quantum efficiencies for low illumination intensities (Fig. 7.9)[7].

[7] The measured quantum efficiency without bias light is vanishing between 350 and 650 nm, shows a linear increase from 650 nm to 900 nm and a maximum of 40% at 1050 nm. The increase in quantum efficiency can be explained by an increasing fraction of the generated carriers being able to reach the collecting rear emitter.

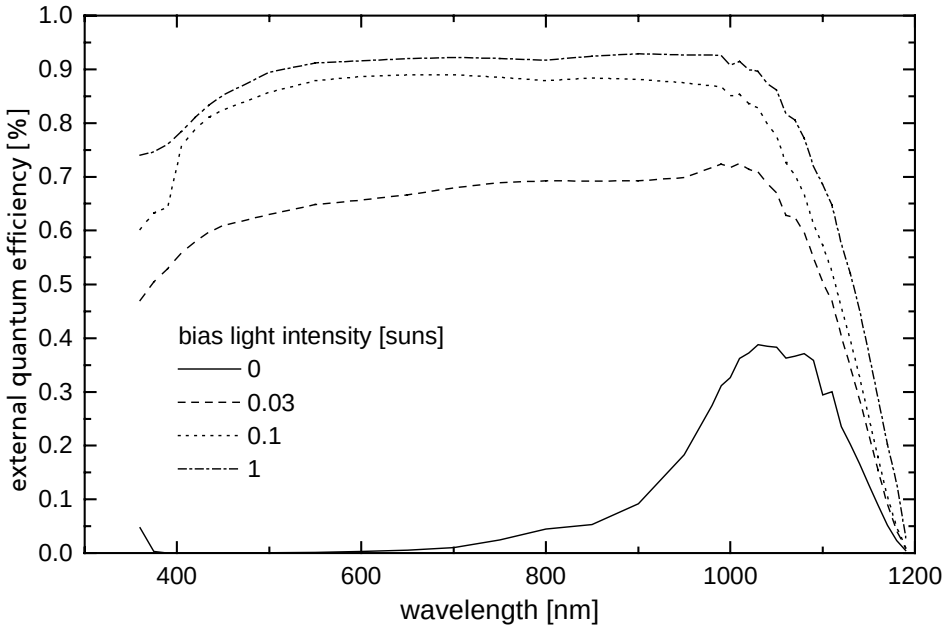

Fig. 7.9: Measured bias light dependence of the external quantum efficiency of the RCC. A strong non-linearity of short circuit current on the bias light is observed.

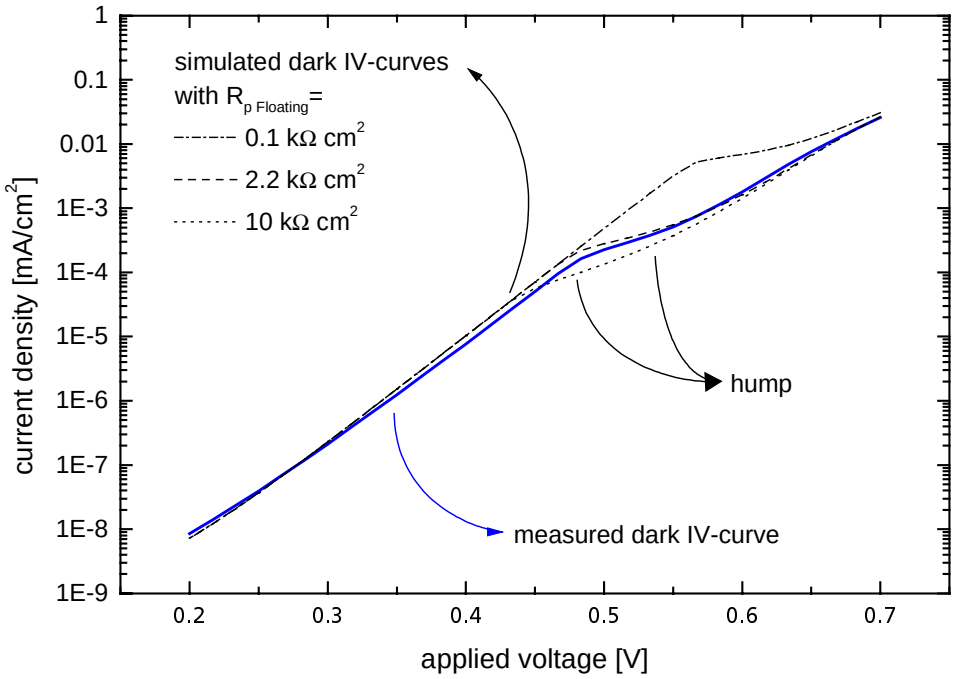

Fig. 7.10: Dark current voltage characteristics of the investigated baseline cell. The hump in the measured dark *I-V* curve is due to increased recombination of charge carriers at the floating junction with decreasing excess carrier density (lower applied voltage). The value of the parallel resistance in the equivalent circuit of the floating junction was quantified using PC1D.

A model for the injection dependence of the recombination at floating emitter passivated surfaces was proposed by Lölgen [117]. Based on this physical background, a shunt resistance, $R_{p,\,floating}$, is introduced as shown in Fig. 7.5. In addition to a shunt resistance, $R_{p,floating}$, the space charge region recombination of the floating emitter is accounted for by introducing a diode with ideality factor 2 and saturation current density J_{02p}. Using PC1D [67], we simulated dark *I-V* curves using the equivalent circuit shown in Fig. 7.5 for different values of $R_{p,floating}$ and J_{02p}. The best fit with the measured dark *I-V* curve was obtained for $R_{p,floating}$ = 2.2 kΩ cm^2 and J_{02p} = 8×10^{-9} A/cm^2, as can be seen in Fig. 7.10.

In analogy to the effective surface recombination velocity S_{eff} of the floating emitter passivated front side described by Lölgen, we define

$$\begin{aligned} S_{\text{eff}} &= S_{\text{eff, J0}} + S_{\text{eff, J02}} + S_{\text{eff, Shunt}} \\ &= \frac{J_{0p}}{q\, n_{0p}} + \frac{J_{02\text{p}}\,(e^{q\,V_{\text{floating}}/(2kT)} - 1)}{q\, n_{0p}\,(e^{q\,V_{\text{floating}}/(kT)} - 1)} + \frac{V_{\text{floating}} / R_{\text{p floating}}}{q\, n_{0p}\,(e^{q\,V_{\text{floating}}/(kT)} - 1)} \end{aligned} \tag{7.1}$$

where q is the elementary charge, k is the Boltzmann constant, T is the cell temperature, n_{0p} is the equilibrium minority carrier density at the edge of the space charge region (8.8×10^3 cm^{-3} for the doping profile of the floating emitter), $V_{floating}$ is the voltage that appears across the junction, and J_{0p} is the saturation current density of the floating emitter. J_{op} was calculated to be 5×10^{-14} A/cm^2 under the assumption of Auger recombination as the limiting recombination mechanism in the floating emitter. The first term in equation Eq. 7.1, $S_{eff,\,J0}$, is due to the current injected into the emitter. The second term, $S_{eff,\,J02}$, is the contribution to S_{eff}, which is due to recombination in the space charge region, and the last term, $S_{eff,\,Shunt}$, accounts for the recombination current due to the shunt effect.

The three components contributing to S_{eff} are shown as a function of $V_{floating}$ in Fig. 7.11.

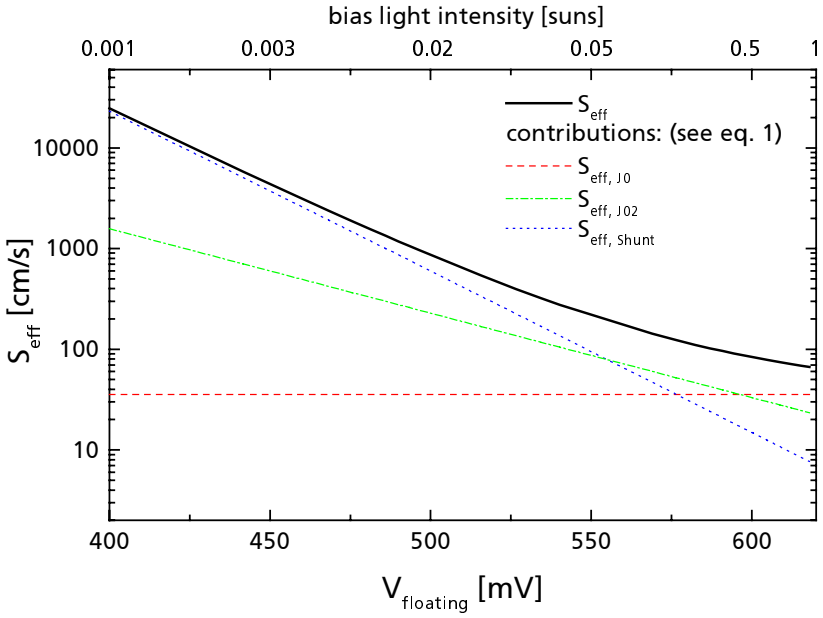

Fig. 7.11: Contributions to the effective recombination velocity of the floating junction at the front surface (Eq. 7.1).

On the upper X-axis, values of the bias light intensity in units of 1 sun (1000 W/m²) are shown. Under short circuit conditions, the bias light intensity corresponds to $V_{floating}$ indicated on the lower X-axis. The second and third terms in Eq. 7.1 are injection-dependent contributions to S_{eff}, whereas $S_{eff,J0}$ is independent of the injection level. At low bias light intensities, there is a strong increase in the front surface recombination owing to the dominating shunt component. This is reflected in the strong injection level dependence of the RCC for low illumination intensities. As illumination intensities increase, S_{eff} approaches a lower limit given by $S_{eff,J0}$.

To further verify the validity of the model, two different measurements were compared with the theoretical predictions:

In a first step, the injection dependence of S_{eff} was determined from spectral response measurements at 600 nm (light absorbed close to the surface) for different bias light intensities (see Fig. 7.12).

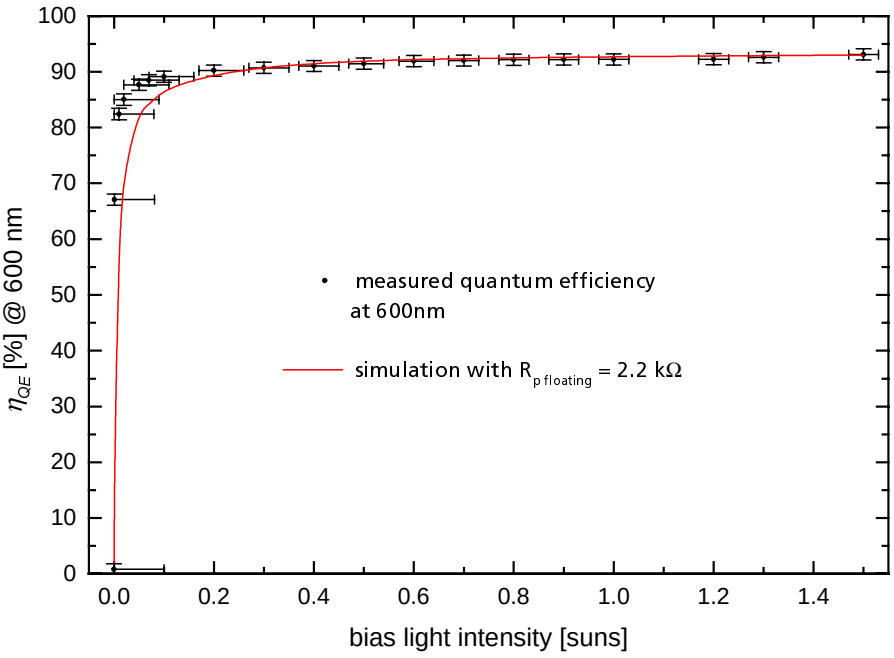

Fig. 7.12: Bias light dependence of the external quantum efficiency for illumination with monochromatic light of 600 nm wavelength. The external quantum efficiency saturates towards one-sun illumination conditions. The solid line shows a PC1D simulation using values for $R_{p,floating}$ and $J_{02,p}$ extracted from the dark *I-V*-curve (see Fig. 7.10).

Then, PC1D simulations of a RCC (modelled without floating emitter) were used to determine the effective surface recombination velocity at the front side, S_{front}, which results in the measured EQE at the given bias light intensities. This S_{front} represents the effective differential surface recombination velocity, $S_{eff,diff}$, of a RCC with floating emitter at the injection levels calculated for the given bias light intensities.

A second independent measurement of $S_{eff,diff}$ was realised by PCD measurements on test samples. Test structures with oxide-passivated floating emitters on both sides were processed from the same starting material and with the same processing conditions for the emitter and the thermal oxides as used in the RCC processing. Therefore, it can be assumed that the test structures and the RCCs have the same bulk lifetime. Furthermore, the test structures were textured with random pyramids in order to establish surface conditions similar to those of the RCCs.

To compare the theoretical predictions with the measurements described above, it is necessary to replace the voltage across the floating emitter, $V_{floating}$, in Eq. 7.1 with the injection level Δn in the base

$$\Delta n = n_{0p}\left(e^{q\,V_{\text{floating}}/(kT)} - 1\right) \tag{7.2}$$

where n_{0p} is the majority carrier density in the base. Applying Eq. 7.2 to Eq. 7.1 gives

$$S_{\text{eff}} = \frac{J_{0p}}{q\,n_{0p}} + \frac{J_{02\text{p}}}{q\,\Delta n}\left(\sqrt{\frac{\Delta n}{n_{0\text{p}}}+1} - 1\right) + \frac{kT}{q^2\,\Delta n\,R_{\text{p floating}}}\ln\left(\frac{\Delta n}{n_{0\text{p}}}+1\right). \tag{7.3}$$

This equation has to be differentiated in order to obtain the differential effective surface recombination velocity [118]

$$\begin{aligned} S_{\text{eff, diff}}(\Delta n) &= \frac{dJ_{\text{S}}}{q\,d\Delta n} = \frac{d(\Delta n\,S_{\text{eff}}(\Delta n))}{d\Delta n} \\ &= \frac{J_{0p}}{q\,n_{0p}} + \frac{J_{02\text{p}}}{2\,q\,n_{0\text{p}}}\left(\frac{\Delta n}{n_{0\text{p}}}+1\right)^{-\frac{1}{2}} + \frac{kT}{q^2\,R_{\text{p floating}}}\;\frac{1}{n_{0\text{p}}+\Delta n} \end{aligned} \tag{7.4}$$

where J_{S} is the fraction of the minority current density from the base recombining at the front surface.

The resulting curves for $S_{eff,\,diff}$ are plotted in Fig. 7.13. As can be seen, there is close agreement between the two independently measured curves and the calculated data.

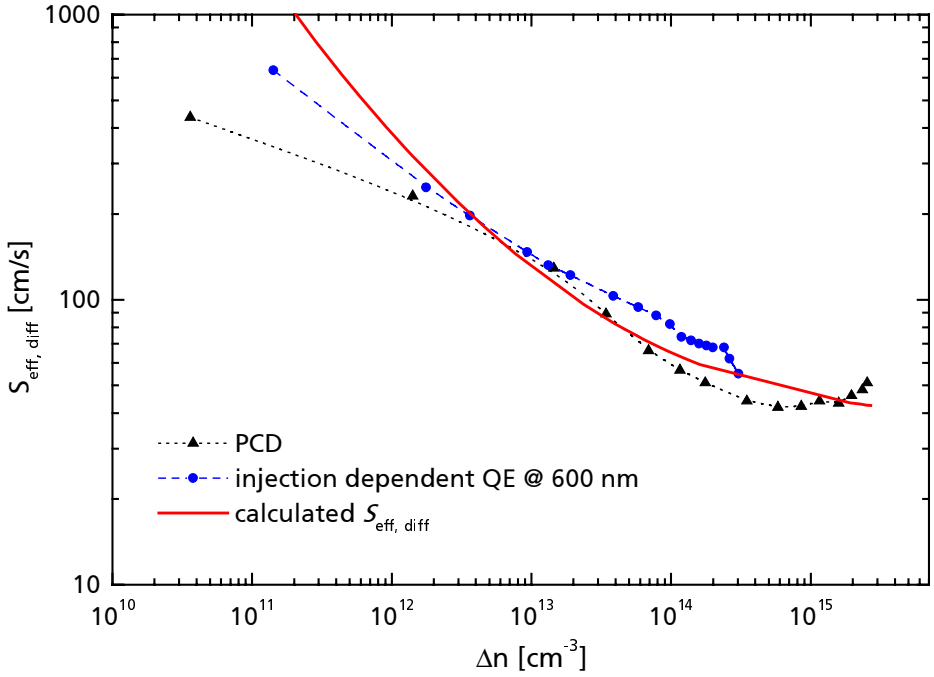

Fig. 7.13: Injection dependence of the effective surface recombination velocity of the floating emitter passivated surface.

7.7 Resistive losses

The total current flow causes a voltage drop along the metal grid. Thus, different cell regions, represented by 2D-symmetry elements in the model, are driven by voltages differing from the voltage at the cell terminals. The losses due to this are known as *non-generation losses* [61]. Non-generation losses of RCCs with interdigitated metal grid are smaller in comparison to conventional solar cells: Fig. 7.14 shows a schematic view of the electrostatic potential distribution along the metal grids under maximum power point conditions at the terminals of the solar cell. The circuit simulation reveals that elementary diodes connected between the same fingers (like the elementary diodes "1" and "2" in Fig. 7.14) work at the same operating point. The voltage drop along one contact finger compensates the voltage drop of the contact finger of opposite type. This is in contrast to a conventional contacted solar cell, where the voltage drop at the back contact is negligible due to the thick metallisation.

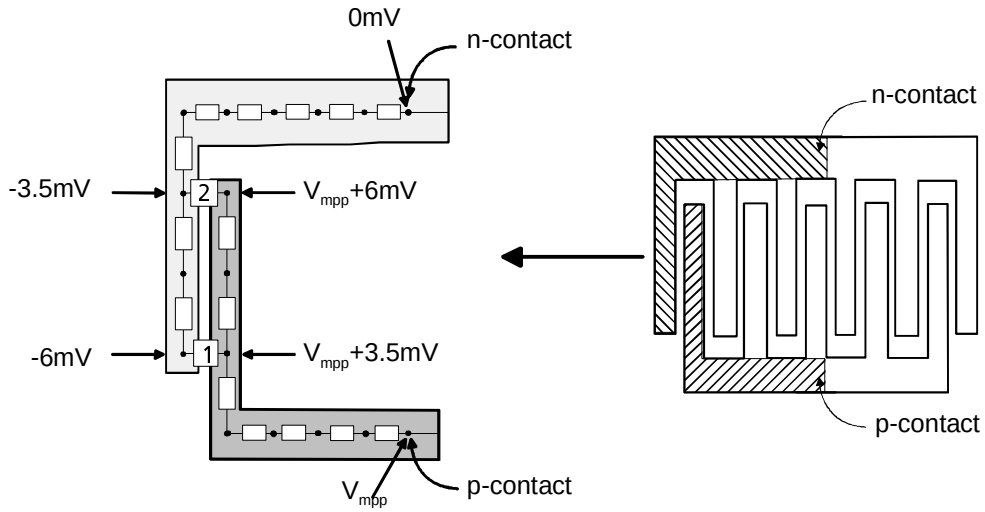

Fig. 7.14: Schematic draw of potential distribution along the interdigitated metal grid. Values were determined by circuit simulation under maximum power conditions.

The distributed Ohmic resistance of the metal grid was measured by three-point probe measurements. Fig. 7.15 shows the resulting metal resistance for the negative contact grid, with the origin set at the contact pad in the middle of the bus bar. The measured metal resistance was compared to the calculated metal resistance, assuming perfectly homogeneous finger shape. Calculations were performed assuming measured finger dimensions and specific metal resistance values (*n*-finger: 30 µm height, 14 µm width, 1.88 cm length; *p*-finger: 30 µm height, 17 µm width, 1.92 cm length; bus-bar: 20 µm height, 158 µm average width, 0.93 cm length; specific metal resistance $\rho_{Ag} = 1.6\times10^{-6}\,\Omega$cm).

The bars at the base of Fig. 7.15 show the absolute difference in resistance between measurement and simulation. Hence, the metal grid of the RCC can be modelled with good accuracy using perfectly shaped fingers and constant specific metal resistance.

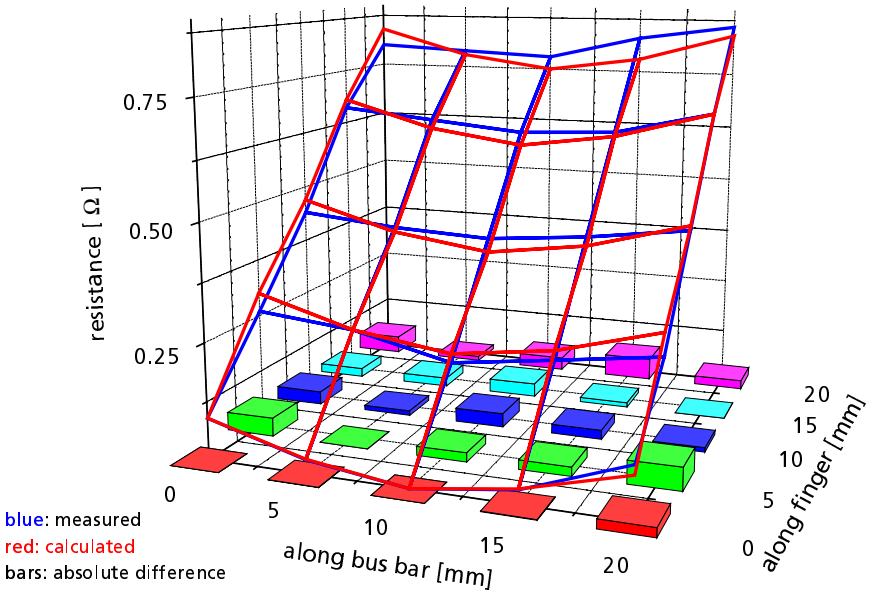

Fig. 7.15: Measured and simulated distribution of the n-contact metal grid resistance. Absolute deviations between simulations and measurements are indicated by the bars at the base of the graph.

The measured distributed voltage drop along the n-contact metal grid was measured as well. The measured data under short circuit conditions and illumination from the metallised rear side are shown in Fig. 7.16. Simulation results obtained with the circuit simulation method are plotted in the same figure. Differences between simulation and measurement are most likely due to technical problems with the adhesion of the metal to the semiconductor. This leads to an inhomogeneous contact resistance along the metal fingers.

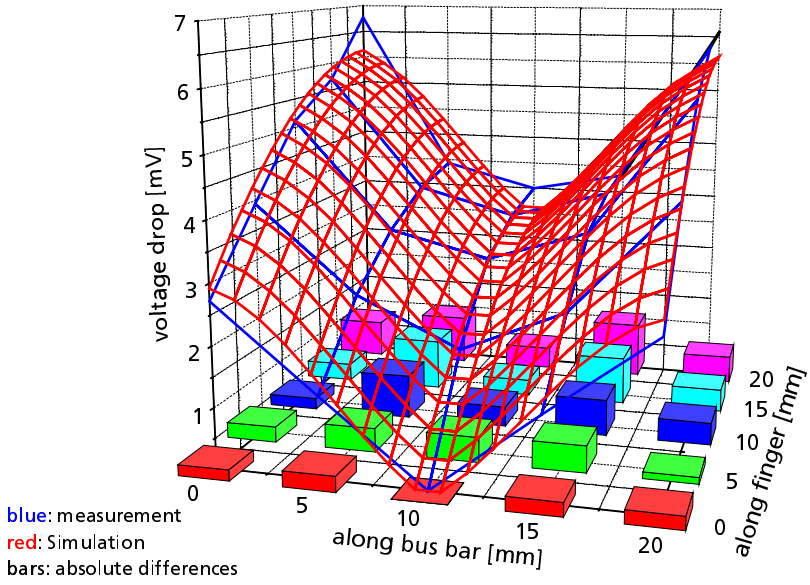

Fig. 7.16: Measured and simulated voltage drop along the n-contact metal grid under short circuit conditions. The origin is located at the contact pad. The cell was illuminated from the metallised rear side.

7.8 Perimeter losses

The investigated RCCs were not separated from the surrounding wafer. Therefore, the symmetry element for device simulation of the perimeter region includes one p- and one n-finger as well as a shaded perimeter region (Fig. 7.4, cf. also Ref. [60]). Simulations revealed that for negligible recombination at the perimeter edge the width of the shaded perimeter region should be one diffusion length. The edge of the emitter diffusions is defined by an area mask. At the non-diffused planar surface a recombination velocity of 1000 cm/s was assumed.

Two methods were worked out to quantify the perimeter losses of the RCC. The first method uses an isolated perimeter diode. For a constant applied voltage, the lateral current density component is integrated along the boundary between the illuminated part and the part of the solar cell shaded by the area definition mask. The resulting current density is denoted $J_{\mathrm{Peri,Int}}(V)$.

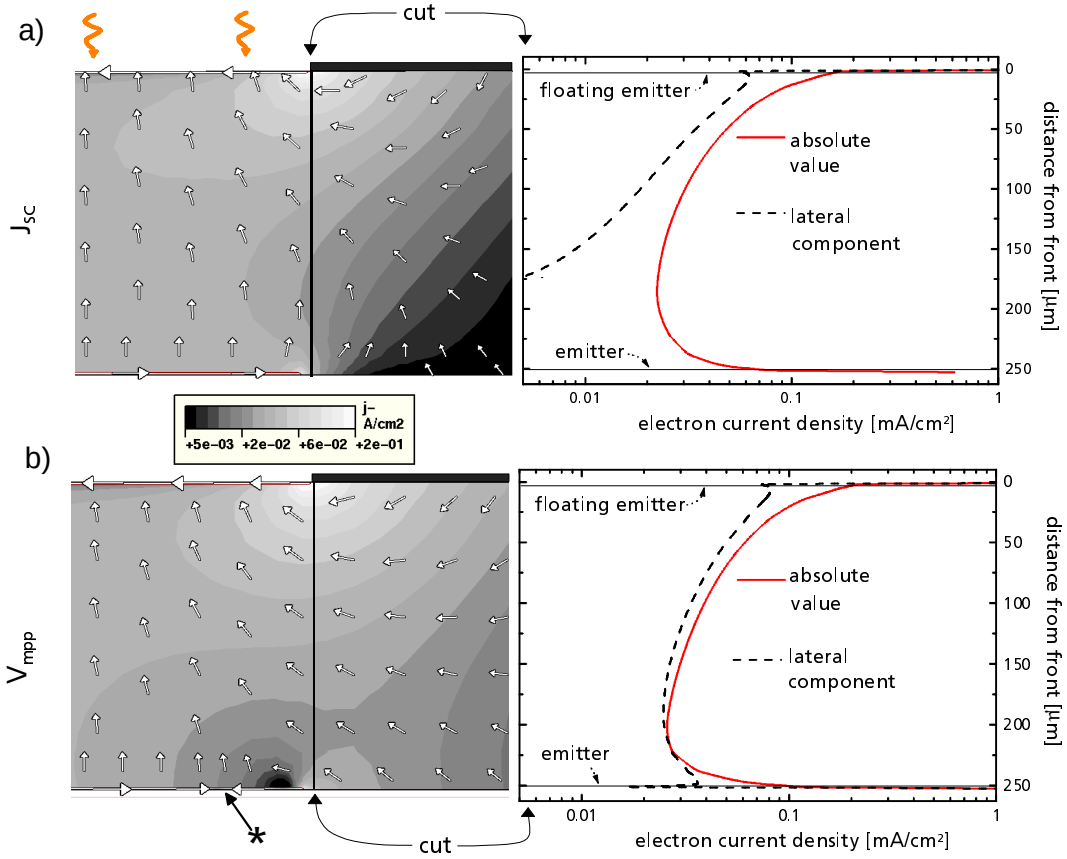

Fig. 7.17: Recombination losses at the cell border can be accounted for by simulation of the perimeter region of the solar cell. The details (Figs. a and b) show the electron density distribution at the cell perimeter under short circuit and maximum power point conditions. Arrows indicate the direction of positive current flow, opposite to the direction of electron flow. The absolute value of the electron current density at the perimeter is shown as solid curves. Dashed curves show the lateral electron current density component along the perimeter (denoted "cut").

The second method employs the circuit simulation technique introduced above. Two different cases are considered. The first case is an RCC with ideal perimeter conditions. This is modelled by inserting elementary diodes at the border positions of the circuit (denoted "*P*"

in Fig. 3.10) as well as at the interior cell positions (denoted "*E*" in Fig. 3.10). The resulting *I-V* curve is termed $I\text{-}V_{Circ,no\_perimeterloss}$. The second case is an RCC modelled with perimeter losses. Simulating the illuminated *I-V* curve of the RCC with perimeter diodes at the cell border yields the *I-V* curve of a RCC, including perimeter losses, termed $I\text{-}V_{\mathrm{Circ}}$. The difference between $I\text{-}V_{\mathrm{Circ}}$ and $I\text{-}V_{Circ,no\_perimeterloss}$ is a current density, $J_{Peri,Circ}(V)$, which can be attributed to the perimeter loss.

The perimeter current $J_{\mathrm{Peri,Int}}(V)$ is plotted in Fig. 7.17 under short circuit (a) and maximum power (b) conditions. Arrows indicate the direction of positive current flow, opposite to the direction of electron flow. The graphs on the right side of Fig. 7.17 show the electron current density along a line at the edge of the area mask. Compared with short circuit conditions, under maximum power point conditions a higher lateral current density can be observed. Under short circuit conditions, the lateral component of the perimeter current changes direction at a distance of 200 µm from the front side, *i.e.*, at the rear side electrons flow from the dark to the illuminated region (Fig. 7.17a). Under maximum power point conditions, the electron current density at the area mask edge is mainly lateral. A width of 150 µm of the contacted emitter does not contribute to the terminal current, but to the perimeter recombination current. In Fig. 7.17b, a star marks the change in direction of the current flow in the contacted emitter.

The perimeter current densities obtained by the two methods are plotted in Fig. 7.18. Method 1 yields a perimeter current density $J_{\mathrm{Peri,Int}}$, which increases monotonically with the applied voltage. This is due to the increase of minority carrier density in the base shown in the upper part of the graph. In contrast, the perimeter current density $J_{\mathrm{Peri,Circ}}$ obtained by the second method shows a maximum.

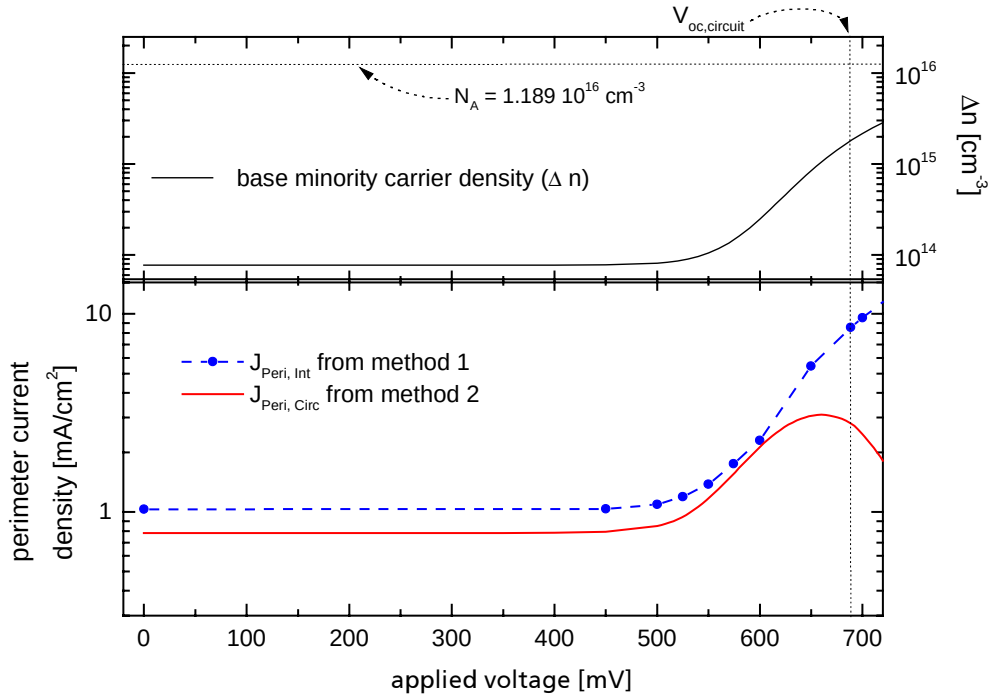

Fig. 7.18. Perimeter current densities obtained by two different methods: Method 1 considers an isolated perimeter diode, whereas method 2 employs circuit simulation of the entire device.

This difference can be explained by investigating the series resistance and its impact on the *I-V* curves. A series resistance leads to an increase in the local ideality factor [116] of the *I-V* curve in the vicinity of V_{oc}, as shown in Fig. 7.19. The series resistance of the perimeter diode is higher than that of the elementary diode, because the mean distance between the generation location of the majority carriers in the base and collection at the positive contact is larger for the perimeter diode (see Fig. 7.4). Fitting the two diode model to simulated *I-V* curves yields $R_S = (0.56 \pm 0.19)\ \Omega\text{cm}^2$ for the perimeter diode and $R_S = (0.39 \pm 0.16)\ \Omega\text{cm}^2$ for the elementary diode. *I-V* curves of both diode types, and the local ideality factors, are plotted in Fig. 7.20. The difference between the two *I-V* curves, $J_{Diff} = J_{PD}(V) - J_{ED}(V)$, is shown as well.

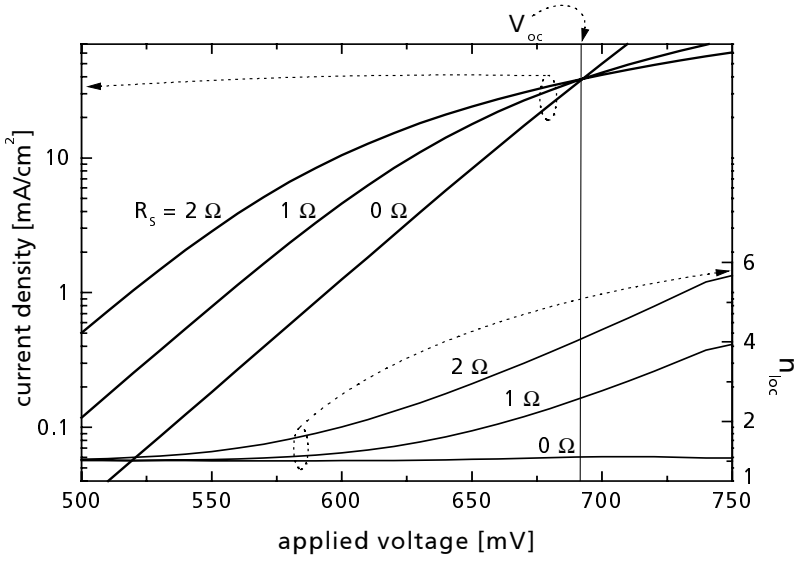

Fig. 7.19: Shifted illuminated *I-V* curves for different series resistance values. As there is no current flow at open-circuit conditions, no voltage drop at the series resistance occurs. Thus, the shifted *I-V* curves intersect at open-circuit conditions. The local ideality factors corresponding to the *I-V* curves are shown as well (right Y-axis).

The behaviour of J_{Diff} can be understood by first order series expansion of the one-diode model, including a local ideality factor:

$$J_{Diff} \approx const + \frac{V}{V_{th}}\left(\frac{J_{0,p}}{n_p(V)} - \frac{J_{0,el}}{n_{el}(V)}\right) \tag{7.5}$$

where V is the applied voltage, V_{th} is the thermal voltage, $J_{0,\text{el}}$, $J_{0,\text{p}}$ are the dark emitter saturation current densities, and n_{el}, n_{p} are the ideality factors for the elementary and the perimeter diode, respectively. The decrease in J_{Diff} is due to the increase of n_p-n_{el} with increasing voltage.

Comparing the circuit simulation results $I\text{-}V_{\text{Circ,no perimeterloss}}$ and $I\text{-}V_{\text{Circ}}$, the same effect is found at a smaller magnitude (Fig. 7.21). In the circuit simulation, the perimeter diodes are

weighted with only 15% of the overall cell area. Therefore, the difference of *I-V*$_{\text{Circ}}$ and *I-V*$_{\text{Circ,no Perimeterloss}}$ is smaller than the difference of the *I-V* curves of the two diode types in isolation.

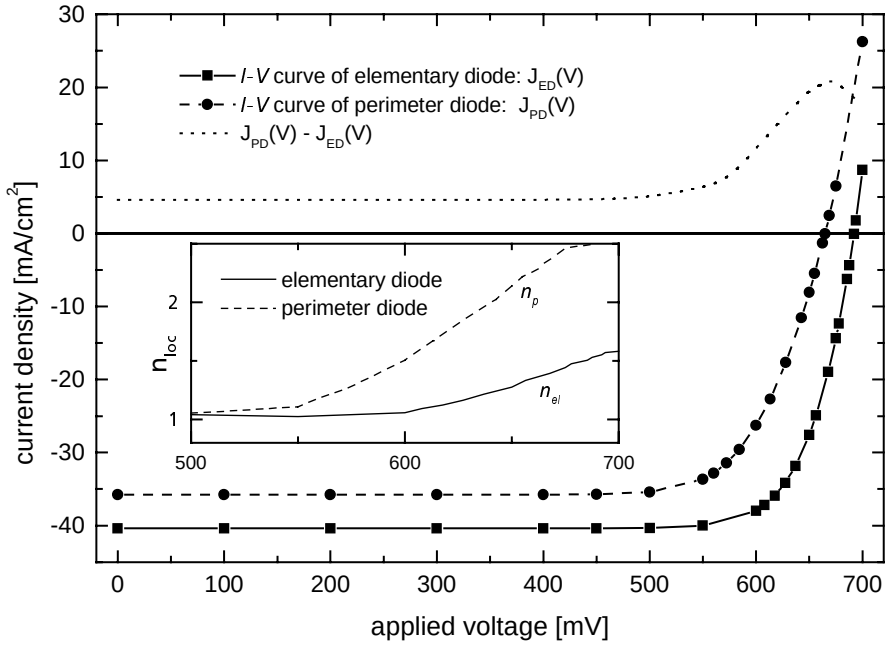

Fig. 7.20: *I-V* curves of the elementary diode (solid) and the perimeter diode (dashed). The difference between the *I-V* curve of the perimeter- and the elementary diode is plotted in the upper graph.

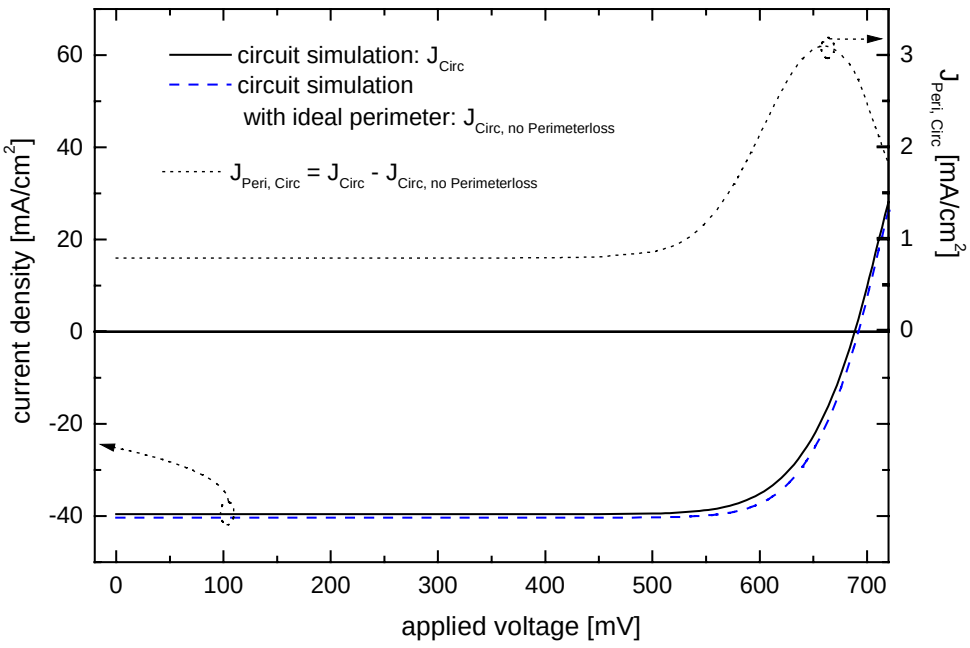

Fig. 7.21: *I-V* curves obtained by circuit simulation. The solid line represents the *I-V* curve of the RCC considering all loss mechanisms. The dashed line was simulated assuming ideal perimeter conditions.

7.9 Comparison of simulated and measured *I-V* output parameters

The measured *I-V* output parameters of a 21.4 % efficient bifacial RCC are listed in the last row of Tab. 7.2. These values can be directly compared with the circuit simulation results listed in row d) of Tab. 7.2, because these simulation results were obtained by a combination of device and circuit simulation that accounts for all known loss mechanisms of the real solar cell. The recombination parameters were chosen to reproduce the measured open-circuit voltage. Due to the realistic optical ray tracing model, the simulated short circuit current density is in excellent agreement with the measured value of 39.2 mA/cm^2. Circuit simulation results in a fill factor that is 1.3 % higher. This difference is most probably due to problems with the metal-semiconductor adhesion, which results in an absolute decrease of 0.2% in cell efficiency.

	J_{sc} [mA/cm^2]	V_{oc} [mV]	J_{mpp} [mA/cm^2]	V_{mpp} [mV]	η_{fill} [%]	η [%]
a) elementary diode	40.4	692.0	38.5	592.5	81.7	22.8
b) perimeter diode	35.8	664.8	34.0	545.6	77.9	18.5
c) circuit, ideal perimeter	40.4	692.0	38.6	584.6	80.8	22.6
d) **circuit (including perimeter)**	39.6	688.7	37.6	574.4	79.3	21.6
e) **measurement (RSK3_5a)**	39.2	688.5	37.7	564.8	78.0	21.4

Tab. 7.2: Comparison of measured and simulated *I-V* output parameters.

Furthermore, Tab. 7.2 reveals the influence of metal resistive losses, non-generation losses, and perimeter losses on cell performance. The results listed in row c) were obtained with a circuit simulation using only elementary diodes, *i.e.*, perimeter losses are neglected, but metal resistive and non-generation losses are taken into account. Comparing rows a) and c), there is a decrease of 0.2% in cell efficiency due to metal resistive and non-generation losses. This corresponds to a difference of 0.9% in the fill factor, which affects neither the output voltage nor the short circuit current.

Recombination losses at the cell perimeter represent a substantial loss in the RCC, as can be seen by comparing rows c) and d): The difference in cell efficiency between circuit simulation with and without perimeter diodes was 1.0%. Perimeter losses also affect the open-circuit voltage and the short circuit current density.

7.10 Parameter studies

The parameter variations presented in this section were obtained from two-dimensional device simulations with one elementary diode. The baseline model for a simulation with one elementary diode yields a cell efficiency of 22.8 %, excluding the metal resistive losses, non-generation losses and perimeter losses that are present in a real RCC. From Tab. 7.2, these additional losses can be found to cause a 5.3 % relative decrease in cell efficiency for a baseline cell.

Normalised values for the *I-V* output parameters are shown on the right y-axis of the following plots; a normalised cell efficiency of 1 corresponds to 22.8 % cell efficiency (baseline, only elementary diode) or 21.6 % including distributed resistive and perimeter losses.

7.10.1 Wafer thickness

The cell thickness was varied for a bulk diffusion length of 1200 µm as determined for the baseline cell. Although this is a high bulk diffusion length of FZ material, base recombination still contributes 70 % of the total recombination losses under open circuit conditions in the RCC. This dominant bulk recombination is the reason for the decrease of V_{oc} with increasing cell thickness, as can be seen in Fig. 7.22.

The short circuit current density increases with increasing cell thickness due to a higher level of light absorption in the cell. Maximum short circuit current density is obtained at a cell thickness of around 170 µm. For thicker cells, a dominant bulk recombination causes a decrease in J_{sc}.

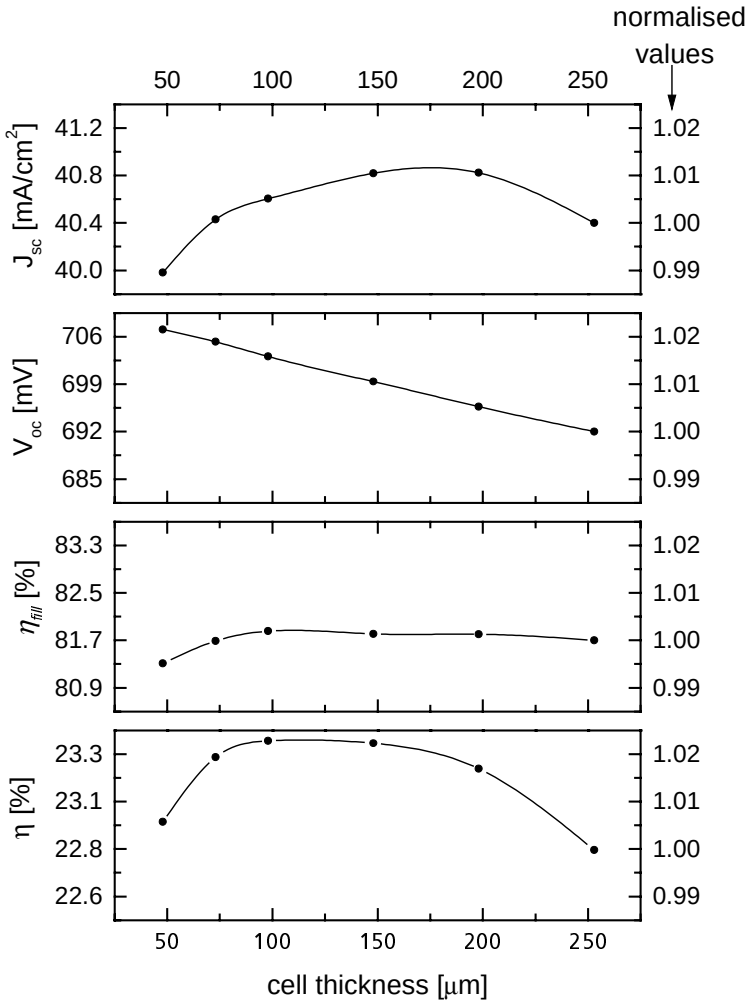

Fig. 7.22: Influence of cell thickness on *I-V* output parameters.

The optimum cell thickness is located in the thickness range from 100 µm to 150 µm. The result is a relative increase of 2% in cell efficiency for this reduced thickness, in comparison to the baseline value of 250 µm for the realised cell.

7.10.2 Metal finger spacing (n-p contact spacing)

With both contacts on the rear side, no shading is caused by the metal grid. Therefore, the short circuit current density is unaffected by the metal finger spacing (Fig. 7.23). A slight increase in the open circuit voltage (< 0.1%) is found at a higher finger spacing. This is due to a decrease in the fraction of the contact area compared to the cell area. However, the effect is negligible because of the effective screening of the metallised cell parts by highly doped areas under the contacts. Internal series resistance losses in the semiconductor cause a 3 % relative drop in the fillfactor by increasing the metal finger spacing from 300 µm to 800 µm. An increased metal finger spacing compared to the baseline value of 500 µm might be needed if screen printing technology is used for the metallisation step. For high efficiency cells fabricated with photolithographically-defined metal fingers, a relative increase in cell efficiency of 1 % can be obtained by reducing the metal finger spacing to 300 µm.

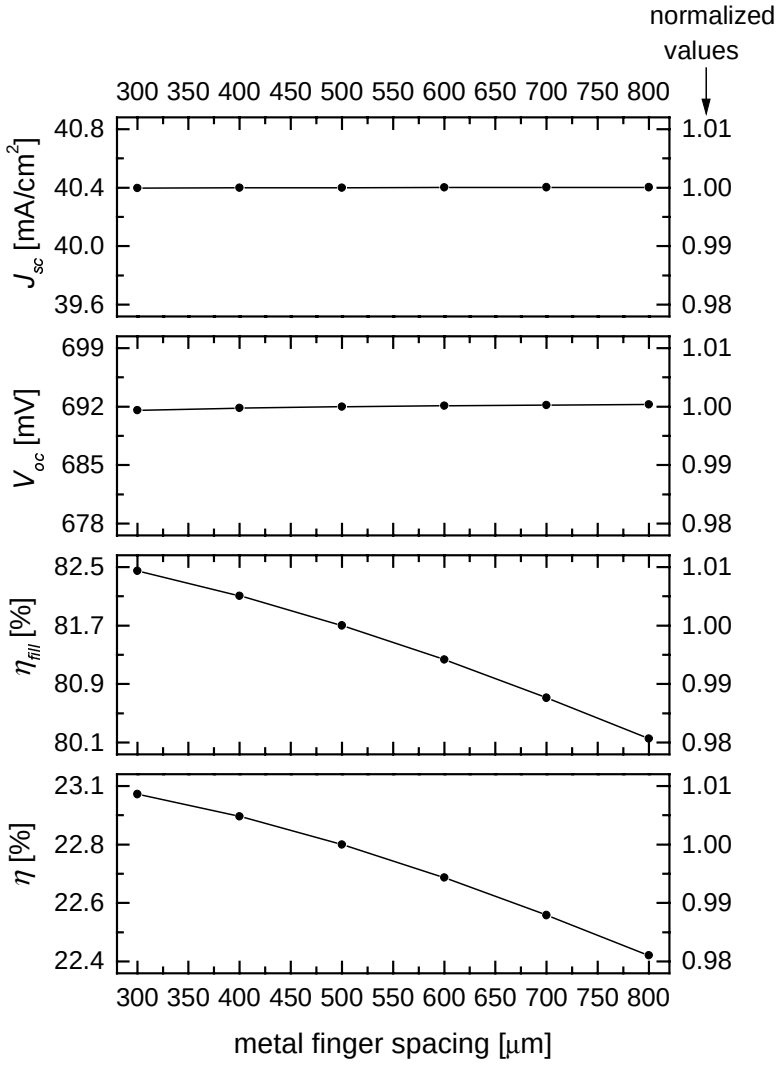

Fig. 7.23: Influence of metal-finger spacing on cell performance.

7.10.3 Emitter coverage fraction

The part of the rear surface not covered by dopant diffusions is called the gap area. Simulations reveal that 30 % of the surface recombination is due to recombination in the gap area, assuming an interface recombination velocity of $S = 100$ cm/s. Fig. 7.24 shows the influence of gap width on the cell performance. The emitter coverage fraction is a critical design parameter for higher surface recombination velocities, *e.g.* for $S = 1000$ cm/s, as found in bifacial cells with a textured rear surface. This case is plotted as solid lines in Fig. 7.24 revealing a 4 % relative drop in cell efficiency for an enhanced gap width of 35 µm compared to the baseline cell.

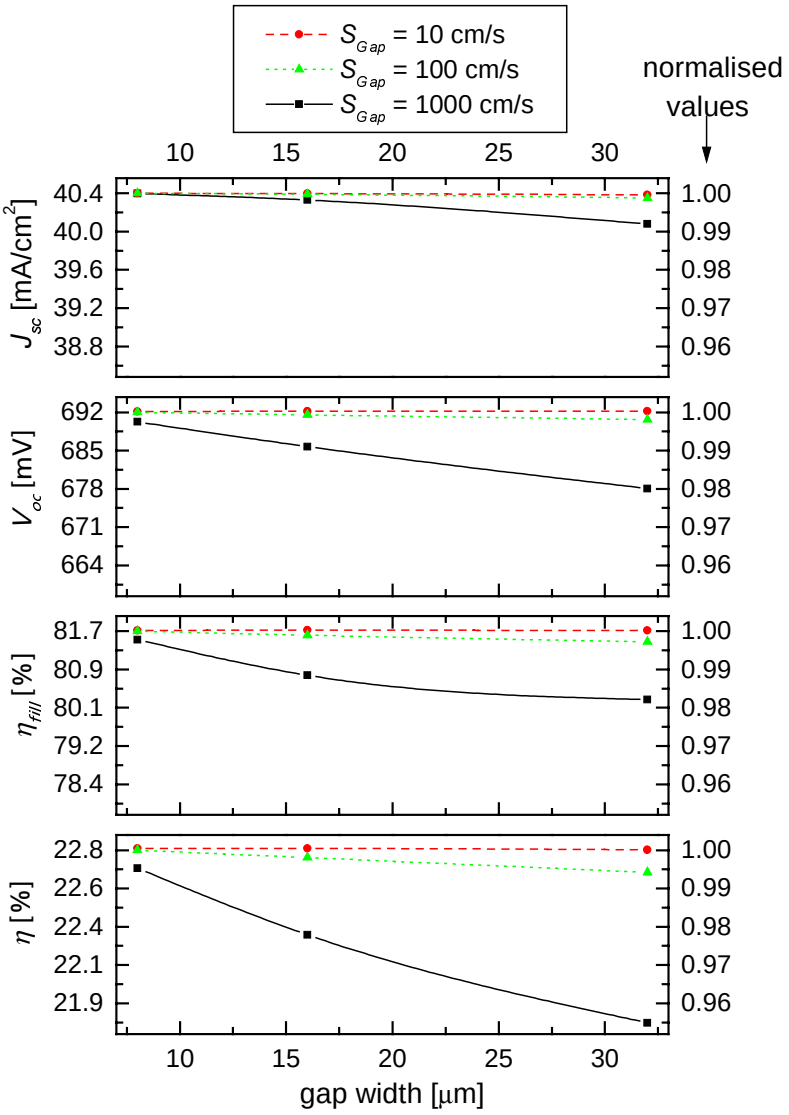

Fig. 7.24: Influence of the width of the gap region on *I-V* output parameters. The gap region is not covered by dopant diffusions, and may degrade the cell's efficiency due to enhanced recombination compared to other surface areas.

7.10.4 Emitter profiles

The n^+ diffusions of the RCC are obtained via the same process step. Therefore, the same n^+ doping profiles have to be assumed on both surfaces. Cell efficiency is very sensitive to the surface recombination velocity S_{int} assumed at the Si/SiO_2 interface beneath the n^+ diffusions.

An empirical expression for S_{int} of oxide passivated diffusions as a function of the peak doping density was given by Cuevas [66]. This expression can be used with good accuracy for peak doping densities $N_{peak} < 10^{19}$ cm^{-3} as for the high efficiency cells investigated here (Fig. 5.8). Four different peak doping values were chosen for the variation of the emitter profiles listed in Fig. 7.25. At the textured front surface S was enhanced by a factor of three, as described previously. The sheet resistance was varied by changing the junction depth. Fig. 7.25 shows the influence of the n^+ diffusion on the RCC's efficiency. An increase in the open circuit voltage and short circuit current density for more shallow diffusions is found for all peak doping density values. This is caused by a decrease in Auger recombination for smaller junction depths. The opposite dependency is found for the fillfactor, due to increasing series resistance losses of the emitter. Maximum cell efficiency is obtained with significant junction depths. Optimum cell performance is achieved for low peak doping concentrations and deep diffusions.

Simulations with one elementary diode reveal a maximum efficiency of 23.5 % for a peak doping concentration of 1×10^{18} cm^{-3}. If we assume a relative correction of 5.3 % due to metal resistive losses, non-generation losses and perimeter losses, as extracted for the baseline cell, then a cell efficiency of 22.3 % results. A 22.1 % efficiency level was realised in a solar cell batch with this peak doping concentration of 1×10^{18} cm^{-3}.

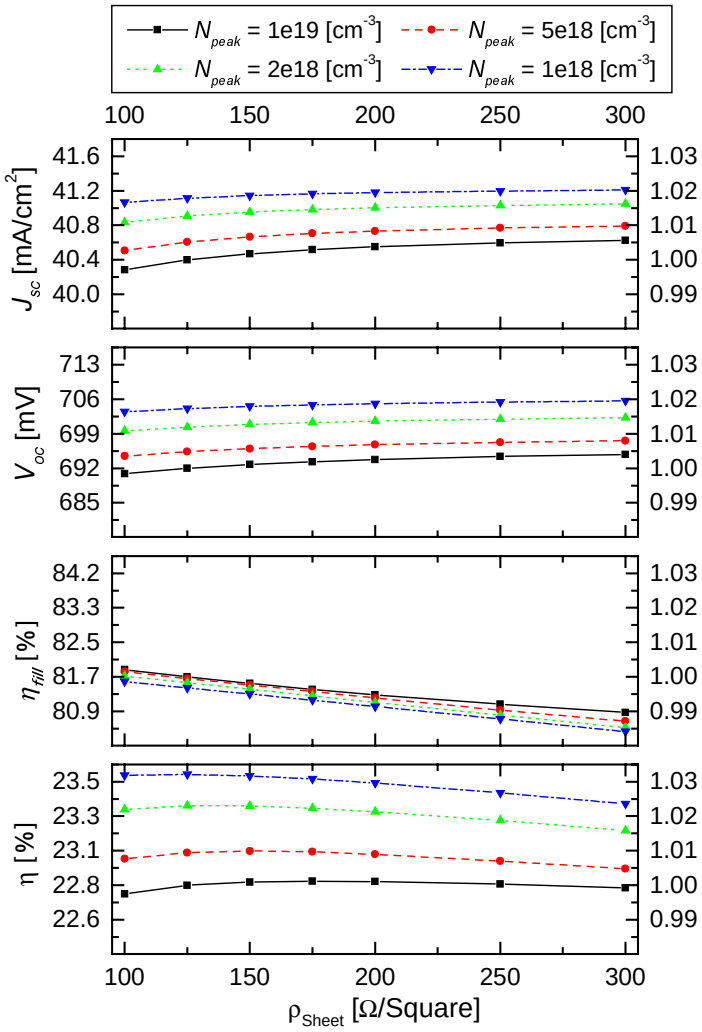

Fig. 7.25: Influence of emitter doping profile on *I-V* output parameters. Optimum efficiency is obtained via a deep diffusion with relatively low surface concentration.

7.10.5 Recombination parameters

Parameter variations were performed to estimate the loss in cell performance for lower quality base material. Therefore, the base diffusion length L_b, cell thickness W and the effective front surface recombination velocity S_{eff} were varied.

The fill factor mainly depends on the cell thickness: values of 79.7 %, 80.7 % and 81.3 % were obtained for cell thicknesses of 50 µm, 100 µm and 200 µm, respectively. One has to keep in mind that these values must be corrected by distributed metal resistive and perimeter losses.

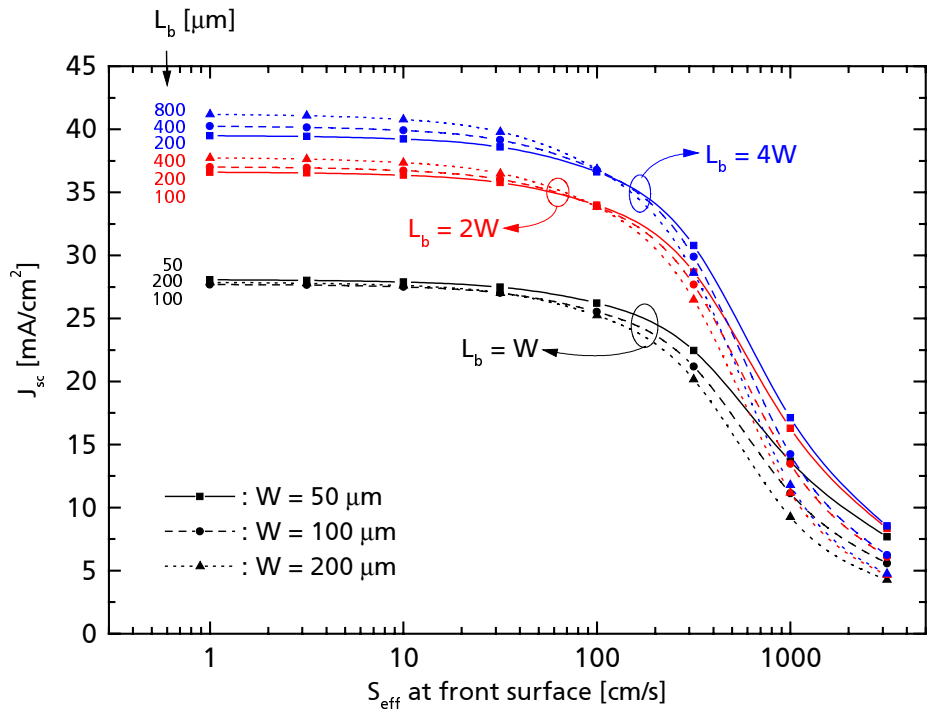

Fig. 7.26: Short circuit current density as a function of the effective recombination velocity of the front surface.

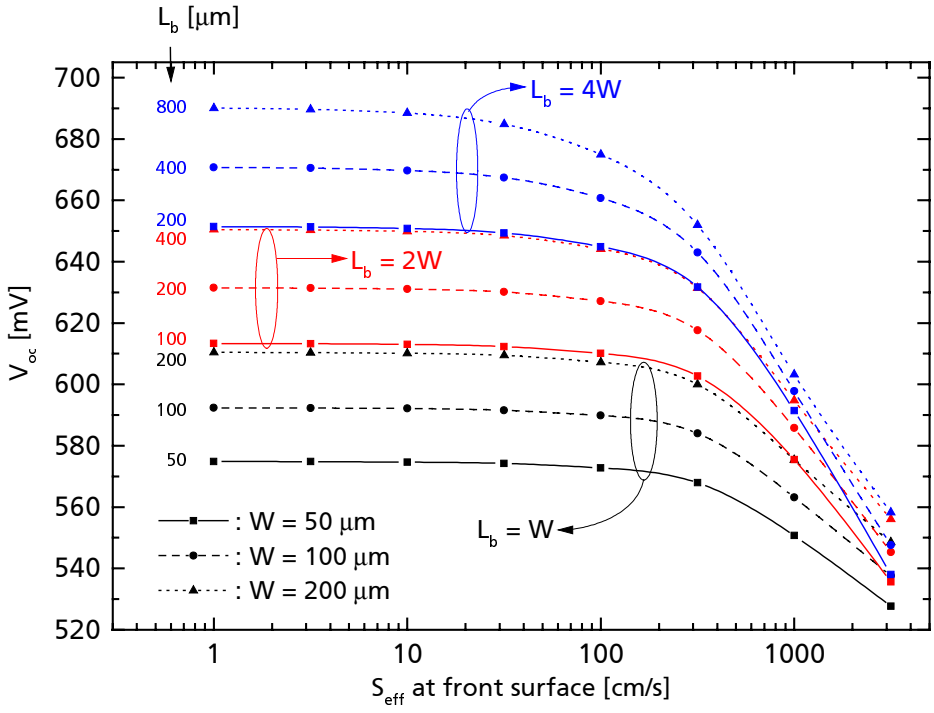

Fig. 7.27: Open circuit voltage as a function of the effective recombination velocity of the front surface.

Fig. 7.26, Fig. 7.27 and Fig. 7.28 show three groups of simulation runs. Each group was calculated for a constant L_b / W ratio. The *I-V* output parameters were calculated as a function

of the effective front surface recombination velocity. The cell performance is merely unaffected for $S_{eff} < 50$ cm/s. At higher values of S_{eff} the cell performance rapidly degrades. In Fig. 7.26 an intersection of the J_{sc}-curves belonging to one group of constant L_b / W ratio can be seen. This can be explained by the fact that the minority carrier density in the vicinity of the contacted emitter at the rear surface is higher in thinner cells. Therefore, the sensitivity of thin RCCs to front surface passivation is lower.

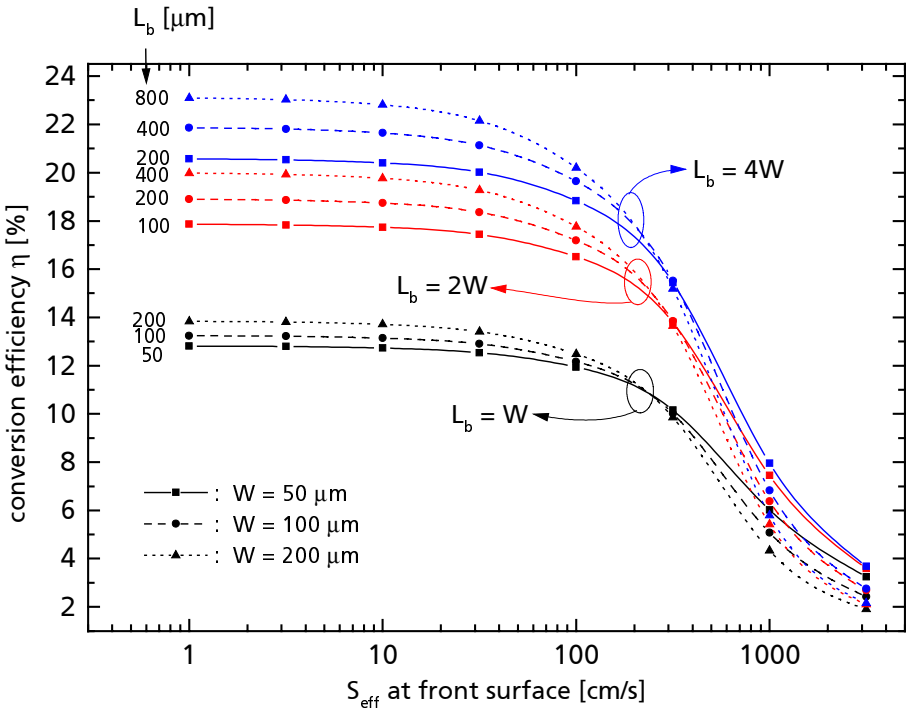

Fig. 7.28: Cell efficiency as a function of the effective recombination velocity of the front surface. A low surface recombination velocity is crucial to the RCC performance.

The situation is different in V_{oc} conditions (Fig. 7.27): The minority carrier density is nearly constant across the cell's depth because no carriers are collected at the rear junction. Consequently, there is no intersection of the curves belonging to one group with a constant L_b / W ratio.

Thinner cells show higher surface recombination fractions. This causes lower open circuit voltages in thin cells compared to thick cells with the same L_b / W ratio.

The following example compares an RCC processed on FZ material ($L_b > 800$ µm) with one processed on Cz material ($L_b \approx 200$ µm). If both cells have a thickness of 200 µm, it can be concluded from Fig. 7.28 that a difference of $\Delta\eta \approx (23\% - 14\ \%) = 9\%$ in cell efficiency has to be expected. If, on the other hand, the Cz cell ($L_b \approx 200$ µm) was processed on a 50 µm thin wafer, an efficiency of 20.5% would be obtained. Thus, in comparison to the thick 23% efficient FZ cell, the efficiency difference would be only $\Delta\eta \approx (23\% - 20.5\ \%) = 2.5\%$.

7.11 Summary of results

A detailed numerical model for the simulation of highly efficient rear-contacted silicon solar cells was developed. The model includes optical ray tracing, two-dimensional electrical device simulation, and circuit simulation. It provides a quantitative treatment of optical carrier generation, distributed metal resistance losses, and perimeter losses. This represents an improvement compared with previous models for rear-contacted cells described in the literature.

A new approach to separate bulk- and surface recombination losses is presented. It sharply reduces the range of combinations of bulk lifetime and surface recombination velocity, resulting in the same overall cell performance. Lifetime measurements on test structures and the open-circuit voltage obtained by measurement and by numerical device simulation are utilised. The most probable values for the interface surface recombination velocity of the thermally oxidised emitter covering the front surface and the bulk diffusion length are 1500 cm/s and 1200 µm, respectively.

Recombination fractions for the different cell regions have been determined under open-circuit, maximum power, and short circuit conditions. At maximum power point, 80 % of the total recombination is due to Shockley-Read-Hall recombination in the base. This demonstrates the potential for thinner RCCs.

Realised RCCs exhibit a strongly reduced spectral response for low illumination levels. This behavior could be modeled quantitatively by introducing a shunt resistance and diode across the floating emitter. The validity of the floating emitter description has been verified by spectral response and photoconductance decay measurements to a high degree of accuracy.

The measured voltage drop along the rear side metallisation was compared to results obtained by circuit simulation. Hence, losses due to the distributed metal resistance (including non-generation losses) can be quantified with our model for interdigitated contact schemes. For the described cell, an absolute fill factor loss of 1% can be attributed to the resistance losses of the grid.

Perimeter losses of the RCC have been quantified using circuit simulations that include symmetry elements representing the device perimeter. A maximum of the perimeter current density (loss current) at 650 mV applied voltage could be explained by the different series resistance of inner and perimeter cell parts. This current flowing out of the cell perimeter leads to an additional absolute fill factor loss of 1.5%. Interestingly, the fill factor loss due to the perimeter current is higher than that due to the resistance loss in the grid described above.

The results of this work establish a numerical baseline model for the high efficiency RCC at Fraunhofer ISE. The model proves to be in very close agreement with measured *I-V* output parameters.

Using this numerical baseline model for the RCC parameter variations were performed. The optimum cell thickness is located in the thickness range from 100 µm to 150 µm. A relative increase of 2% in cell efficiency results for a reduced thickness in comparison to the baseline value of 250 µm for the realised cell. The metal finger spacing of this high efficient

RCC mainly affects the fillfactor. Internal series resistance losses in the semiconductor cause a 3 % relative drop in the fillfactor by increasing the metal finger spacing from 300 µm to 800 µm.

The relative RCC efficiency was predicted to improve by 3% when changing the surface concentration of the front and rear emitter diffusion from 5×10^{18} to 5×10^{18} cm^{-3} for constant sheet resistance. Indeed, this modification has led to an increase in cell efficiency, due mainly to an increase in short current density and open-circuit voltage from 21.4 % to 22.1 %, that is a relative improvement of 3.3 %.

List of symbols

Symbol	Usual Unit	Name or description
A	cm^{-2}	area
A_{metal}	–	metal coverage fraction
c	$m\ s^{-1}$	speed of light
$C_{n,p}$	$cm^6\ s^{-1}$	band-to-band Auger recombination rate constant
$C_{n,lli}$	$cm^6\ s^{-1}$	C_n under low injection conditions
$D_{e,h}$	$cm^2\ s^{-1}$	diffusion coefficient of electron, hole
E	$W\ m^{-2}$	total irradiance
$E_{c,v}$	eV	conduction or valence band energy
E_F	eV	Fermi level
E_{fc}	eV	electron quasi-Fermi level
E_{fv}	eV	hole quasi-Fermi level
E_λ	$W\ m^{-2}\ nm^{-1}$	spectral irradiance per unit wavelength
f	–	probability density function (PDF)
f_{abs}	–	fraction of light absorbed in active silicon layer
$F_{1/2}$	–	Fermi integral of order 1/2
$g(\lambda,x)$	μm^{-1}	normalised generation rate function
G	$s^{-1}\ cm^{-3}$	generation rate
G_λ	$s^{-1}\ cm^{-4}$	spectral generation rate
h	Js	Planck constant
H_{epi}	µm	thickness of epitaxially grown layer
$H_{n,p}$	µm	thickness of *n*- or *p*-doped region
j_λ	photons $m^{-2}\ s^{-1}$	spectral photon flux
J	$A\ cm^{-2}$	current density
$J_{e,h}$	$A\ cm^{-2}$	electron or hole current density
J^{Lt}	$A\ cm^{-2}$	light-generated current density
J_{ph}	$A\ cm^{-2}$	photocurrent density
J_{sc}	$A\ cm^{-2}$	short circuit current density

$J_{sc,max}$	A cm^{-2}	max. achievable short circuit current density (no recombination)
J_{surf}	A cm^{-2}	recombination current density at surface
J_0	A cm^{-2}	saturation current density
J_{0b}	A cm^{-2}	base saturation current density
J_{0e}	A cm^{-2}	emitter saturation current density
k	J K^{-1}	Boltzmann constant
k^T	cm^3 s^{-1}	Shockley-Read-Hall trap recombination constant
L_D	µm	Debye length
$L_{e,h}$	µm	minority carrier diffusion length of an electron or hole
L_b	µm	minority carrier diffusion length in the base
L_{eff}	µm	effective minority carrier diffusion length
n	cm^{-3}	electron concentration in the conduction band
n_0	cm^{-3}	electron concentration at thermal equilibrium
n_i	cm^{-3}	intrinsic carrier density
$n_{i,eff}$	cm^{-3}	effective intrinsic carrier density
$N_{A,D}$	cm^{-3}	density of acceptor or donor impurities
$N_{c,v}$	cm^{-3}	effective density of states of conduction or valence band
N_{peak}	cm^{-3}	peak doping concentration
p	cm^{-3}	hole concentration in the valence band
p_0	cm^{-3}	hole concentration at thermal equilibrium
P	W m^{-2}	power density
q	C	magnitude of the elementary charge
Q	µm	thickness of quasineutral region
$r_{e,h}$	cm^{-3} s^{-1}	volume rate of recombination of electrons or holes
R	–	reflectivity
R_b	–	internal reflectivity at rear surface of solar cell
R_{ext}	–	external reflectivity of a solar cell
R_{ext}^{nm}	–	external reflectivity of a solar cell excluding metal reflection
R_{fi}	–	internal reflectivity at front surface of solar cell

R_{metal}	–	metal reflectivity
R_p	Ω cm^2	shunt resistance
R_s	Ω cm^2	series resistance
s	A/W	spectral response
$\tilde{s}$	A/W	differential spectral response
S	cm/s	surface recombination velocity
$S_{e0,h0}$	cm/s	recombination velocity of electrons or holes at surface
S_{eff}	cm/s	effective surface recombination velocity
S_{inter}	cm/s	effective surface recombination velocity at intermediate oxide
$\tilde{S} \equiv D_e / L_b$	cm/s	S_{eff} for balancing surface and bulk components
T	K	temperature
$T_{fe,fi}$	–	front external or front internal transmissivity
V	V	voltage
V_D	V	diffusion voltage (or built-in potential)
V_j	V	potential difference at the depletion region edges
V_{ja}	V	portion of the applied voltage that appears across the junction
V_{oc}	V	open circuit voltage
V_{mpp}	V	voltage at maximum power point
V_{th}	V	thermal voltage
W	µm	wafer- or substrate thickness
$W_{n,p}$	µm	n-type or p-type space charge layer thickness
x_e	µm	edge of space charge region
x_j	µm	junction position
α	µm^{-1}	absorption coefficient
α_t	–	emitter transparency factor
β	–	diode ideality factor
ΔE_g	eV	band gap narrowing
ϵ_0	A s V^{-1} m^{-1}	permittivity of free space
ϵ_s	–	static relative permittivity of a medium

$\mathcal{E}$	kV cm^{-1}	electric field strength
ϕ	V	electrostatic potential
γ_{deg}	–	degeneracy factor
γ_{BGN}^{2}	–	band gap narrowing factor
η	–	energy conversion efficiency
η_c	–	carrier collection efficiency
η_{fill}	%	fill factor
η_{QE}	–	external quantum efficiency
λ	nm	wavelength of light
μ		mean value
$\mu_{e,h}$	cm^2 s^{-1} V^{-1}	electron or hole mobility
ν	s^{-1}	frequency of light
ρ	C cm^{-3}	space-charge density
σ		standard deviation
τ	s	lifetime
τ_{eff}	s	effective lifetime
Ξ	–	geometry factor

Author's publications

J. O. Schumacher and W. Wettling: "Device physics of silicon solar cells", in Photoconversion of Solar Energy; Vol. 3, edited by M. Archer (Imperial College Press, London, 2000, ISBN 1-860-94161-3).

J. O. Schumacher, P. P. Altermatt, G. Heiser, and A. G. Aberle: "Application of an improved band gap narrowing model to the numerical simulation of recombination properties of phosphorous doped silicon emitters", accepted for publication in Solar Energy Materials and Solar Cells (2000).

J. O. Schumacher, J. Dicker, J. Sölter, and D. Biro: "An object oriented approach for the analytical and numerical modelling of silicon solar cells", submitted to Progress in Photovoltaics: Research and Applications (2000).

J. O. Schumacher, C. Hebling, and W. Warta: "Analysis and design of a thin film silicon solar cell on an insulating substrate", 14th EC-PVSEC, Barcelona (1997) 1467-1471.

J. O. Schumacher, J. Dicker, S. Glunz, C. Hebling, J. Knobloch, W. Warta, and W. Wettling: "Characterisation of silicon solar cells with interdigitated contacts", Proceedings of the 26th IEEE Photovoltaic Specialists Conference, Anaheim, California, USA (1997) 71-74.

J. O. Schumacher, S. Sterk, B. Wagner, and W. Warta: "Quantum efficiency analysis of high efficiency solar cells with textured surfaces", 13th EC-PVSEC, Nice (1995) 96-99.

P. P. Altermatt, J. O. Schumacher, A. Cuevas, S. W. Glunz, R. R. King, G. Heiser, and A. Schenk: "The extraction of the surface recombination velocity of Si:P emitters using advanced silicon models", Proceedings of the 16th European Photovoltaic Solar Energy Conference, Glasgow, Scotland (2000).

J. Dicker, J. O. Schumacher, J. Sölter, W. Zimmermann, S. Bau, and W. Warta: "Numerical analysis of crystalline silicon thin film solar cells on perforated SiO2 barrier layers", Proceedings of the 16th European Photovoltaic Solar Energy Conference, Glasgow, Scotland (2000).

J. Dicker, J. O. Schumacher, S. W. Glunz, and W. Warta: "Characterisation of high-efficiency silicon solar cells with rear side contacts", Proceedings of the 2nd World Conference on Photovoltaic Energy Conversion, Vienna, Austria (1998) 95-99.

R. Preu, J. O. Schumacher, P. Hahne, H. Lautenschlager, I. Reis, S. W. Glunz, and W. Wettling: "Screen printed and RT-processed emitters for crystalline silicon solar cells", Proceedings of the 2nd World Conference on Photovoltaic Energy Conversion, Vienna, Austria (1998) 1503-1506.

S. W. Glunz, J. O. Schumacher, W. Warta, J. Knobloch, and W. Wettling: "Optimisation of mesh-structured emitters", Proceedings of the 14th European Photovoltaic Solar Energy Conference, Barcelona, Spain (1997) .

C. Hebling, S. W. Glunz, J. O. Schumacher, and J. Knobloch: "High-efficiency (19.2%) silicon thin-film solar cells with interdigitated emitter and base front-contacts", Proceedings of the 14th European Photovoltaic Solar Energy Conference, Barcelona (1997) 2318-2321.

S. W. Glunz, J. O. Schumacher, W. Warta, J. Knobloch, and W. Wettling: "Solar cells with mesh-structured emitter", Progr. Photovolt. 4 (1996) 415-424.

C. Hebling, S. W. Glunz, J. O. Schumacher, and J. Knobloch: "Variation of the back surface field in silicon thin-film solar cells with interdigitated front grid", Proceedings of the 2nd World Conference on Photovoltaic Energy Conversion, Vienna, Austria (1998) 1786-1789.

B. F. Wagner and J. O. Schumacher: "Light confinement and influence of electrical parameters on thin silicon solar cells", 13th EC-PVSEC, Nice (1995) 465-468.

J. Dicker and J. O. Schumacher: "Halbleitersimulation von Solarzellen", in Design und Elektronik (1998), p. 57-62.

U. Blieske, S. Sterk, A. Bett, J. Schumacher, and W. Wettling: "LPE-GaAs and LBSF-Si solar cells for tandem concentrator application", Proceedings of the 1st World Conference on Photovoltaic Energy Conversion, Hawaii, USA (1994) 1902-1905.

Bibliography

[1] *Climate Change 1995: The science of climate change; Contribution of Working Group I to the Second Assessment Report of the Intergovernmental Panel on Climate Change;* edited by J. T. Houghton (Cambridge University Press, Cambridge, 1996).

[2] *Report of Working Group II: Scientific-Technical Analysis of Impacts, Adaptations, and Mitigation of Climate Change; Intergovernmental Panel on Climate Change;* edited by R. T. Watson, M. C. Zinyowera, and R. H. Moss (Cambridge University Press, Cambridge, 1996).

[3] C. Flavin and S. Dunn: "A new energy paradigm for the 21st century", Journal of International Affairs 53 (1999) 167-190.

[4] A. Lovins and C. Lotspeich: "Energy surprises for the 21st cenury", Journal of International Affairs 53 (1999) 191-208.

[5] P. Kassler: "Energy for Development", Shell International Petroleum Company, London, England (1994) .

[6] S. H. Kim, C. MacCracken, and J. Edmonds: "Solar energy technologies and stabilizing atmospheric CO2 concentrations", Progr. Photovolt. 8 (2000) 3-15.

[7] *Climate change 1994: Radiative forcing of climate change and an evaluation of the IPCC IS92 emissions scenarios;* edited by J. T. Houghton, L. G. M. Filho, J. Bruce, H. Lee, and B. A. Callander (Cambridge University Press, Cambridge, 1995).

[8] T. Bruton, G. Luthardt, K. D. Rasch, K. Roy, I. A. Dorrity, B. Garrard, L. Teale, J. Alonso, U. Ugalde, K. Declerq, J. Nijs, J. Szlufcik, A. Räuber, W. Wettling, and A. Vallera: "A study of the manufacture at 500 MWp p.a. of crystalline silicon photovoltaic modules", Proceedings of the 14th European Photovoltaic Solar Energy Conference, Barcelona, Spain (1997) 11-16.

[9] M. A. Green, *Silicon solar cells: Advanced principles and practice* (Bridge printery, Sydney, NSW, 1995).

[10] M. A. Green: "The future of crystalline silicon solar cells", Progr. Photovolt. 8 (2000) 127-139.

[11] S. Reber and W. Wettling: "High-temperature processing of crystalline silicon thin-film solar cells", Appl. Phys. A 69 (1999) 215-220.

[12] R. B. Bergmann, J. Köhler, R. Dassow, C. Zaczek, and H. J. Werner: Phys. Stat. Sol. 166 (1998)

[13] S. Guha, J. Yang, and A. Banerjee: "Amorphous silicon alloy photovoltaic research - present and future", Progr. Photovolt. 8 (2000) 141-150.

[14] P. V. Meyers and S. P. Albright: "Technical and economic opportunities for CdTe PV at the turn of the millenium", Progr. Photovolt. 8 (2000) 161-169.

[15] H. W. Schock and R. Noufi: "CIGS-based solar cells for the next millennium", Progr. Photovolt. 8 (2000) 151-160.

[16] A. W. Bett, F. Dimroth, G. Stollwerck, and O. V. Sulima: "III-V compounds for solar cell applications", Appl. Phys. A 69 (1999) 119-129.

[17] W. Shockley: "The theory of p-n junctions in semiconductors and p-n junction transistors", Bell System Tech. J. 28 (1949) 435-489.

[18] A. H. Marshak and K. M. Vliet: "On the separation of quasi-Fermi levels and the boundary conditions for junction devices", Solid-State Electron. 23 (1980) 1223-1228.

[19] M. D. Archer, B. J. R., and S. T. C. Siklos: "A review of analytic solutions for a model p-n junction cell under low-injection conditions", Sol. Ener. Mater. Sol. Cells 40 (1996) 133-176.

[20] M. A. Green, *Solar cells: operating principles, technology and system applications* (UNSW, Kensington, New South Wales, 1986).

[21] C. T. Sah, R. N. Noyce, and W. Shockley: "Carrier generation and recombination in p-n junctions and p-n junction characteristics", Proceedings of the IRE 45 (1957) 1228-1243.

[22] A. L. Fahrenbruch and R. H. Bube, *Fundamentals of solar cells* (Academic Press, New York, 1983).

[23] A. G. Aberle, S. J. Robinson, A. Wang, J. Zhao, S. R. Wenham, and M. A. Green: "High-efficiency silicon solar cells: fill factor limitations and non-ideal diode behaviour due to voltage-dependent rear surface recombination velocity", Progr. Photovolt. 1 (1993) 133-143.

[24] S. M. Sze, *Physics of Semiconductor Devices*, 2nd ed. (John Wiley & Sons, New York, 1981).

[25] D. K. Schroder, R. N. Thomas, and J. C. Swartz: "Free carrier absorption in silicon", IEEE Trans. Electron Devices 25 (1978) 254-261.

[26] J. O. Schumacher, *Charakterisierung texturierter Silicium-Solarzellen;* Diploma Thesis, Albert-Ludwigs Universität, Freiburg, Germany, 1994.

[27] J. O. Schumacher, S. Sterk, B. Wagner, and W. Warta: "Quantum efficiency analysis of high efficiency solar cells with textured surfaces", 13th EC-PVSEC, Nice (1995) 96-99.

[28] J. Metzdorf: "Calibration of solar cells. 1: the differential spectral responsivity method", Appl. Opt. 26 (1987)

[29] J. S. Park, A. Neugroschel, and F. A. Lindholm: "Systematic analytical solutions for minority-carrier transport in semiconductors with position-dependent composition, with application to heavily doped silicon", IEEE Trans. Electron Devices 33 (1986) 240-249.

[30] R. R. King, R. A. Sinton, and R. M. Swanson: "Studies of diffused phosphorus emitters: saturation current, surface recombination velocity, and quantum efficiency", IEEE Trans. Electron Devices 37 (1990) 365-371.

[31] R. Preu, J. O. Schumacher, P. Hahne, H. Lautenschlager, I. Reis, S. W. Glunz, and W. Wettling: "Screen printed and RT-processed emitters for crystalline silicon solar cells", Proceedings of the 2nd World Conference on Photovoltaic Energy Conversion, Vienna, Austria (1998) 1503-1506.

[32] A. G. Aberle, G. Heiser, and M. A. Green: "Two-dimensional numerical optimization study of the rear contact geometry of high-efficiency silicon solar cells", J. Appl. Phys. 75 (1994) 5391-5405.

[33] P. P. Altermatt, G. Heiser, and M. A. Green: "Numerical quantification and minimization of perimeter losses in high-efficiency silicon solar cells", Progr. Photovolt. 4 (1996) 355-367.

[34] P. P. Altermatt, G. Heiser, A. G. Aberle, A. Wang, J. Zhao, S. J. Robinson, S. Bowden, and M. A. Green: "Spatially resolved analysis and minimization of resistive losses in high-efficiency Si solar cells", Progr. Photovolt. 4 (1996) 399-414.

[35] C. Zechner, P. Fath, G. Willeke, and E. Bucher: "Two- and three-dimensional optical carrier generation determination in crystalline silicon solar cells", Sol. Ener. Mater. Sol. Cells 51 (1998) 255-267.

[36] R. M. Swanson: "Point-contact solar cells: modelling and experiment", Sol. Cells 17 (1986) 85-118.

[37] B. Kuhlmann, A. G. Aberle, R. Hezel, and G. Heiser: "Simulation and optimization of metal-insulator-semiconductor inversion layer silicon solar cells", submitted to IEEE Trans. Electron Devices (1999)

[38] S. Selberherr, *Analysis and simulation of semiconductor devices* (Springer-Verlag, Vienna, 1984).

[39] J. F. Bürgler, *Discretisation and grid adaption in semiconductor device modeling;* PhD Thesis, ETH-Zürich, Konstanz, 1990.

[40] G. Heiser, *Design and implementation of a three-dimensional general purpose semiconductor device simulator;* PhD Thesis, ETH-Zürich, Konstanz, 1991.

[41] "Development, modeling and optimization of microelectronics processes, devices and systems", Vers. 6.0.5, ISE Integrated Systems Engineering, Zurich, (1999), http://www.ise.ch

[42] D. T. Rover and P. A. Basore: "Solar cell modeling on personal computers", Proceedings of the 18th IEEE Photovoltaic Specialists Conference, Las Vegas, Nevada, USA (1985) 703-709.

[43] P. A. Basore and D. A. Clugston: "PC1D Version 5: 32-BIT solar cell modelling on personal computers", Proceedings of the 26th IEEE Photovoltaic Specialists Conference, Anaheim, California, USA (1997) 207-210.

[44] P. A. Basore, D. T. Rover, and A. W. Smith: "PC1D: Enhanced numerical solar cell modelling", Proceedings of the 20th IEEE Photovoltaic Specialists Conference, Las Vegas, Nevada, USA (1988) 389-396.

[45] A. W. Smith, A. Rohatgi, and S. C. Neel: "TEXTURE: A ray tracing program for the photovoltaic community", Proceedings of the 21st IEEE Photovoltaic Specialists Conference, Florida (1990) 426-431.

[46] R. Brendel: "Sunrays: A versatile ray tracing program for the photovoltaic community", Proceedings of the 14th European Photovoltaic Solar Energy Conference, Amsterdam, The Netherlands (1994) 1339-1342.

[47] A. Goetzberger: "Optical confinement in thin Si-solar cells by diffuse back reflectors", Proceedings of the 15th IEEE Photovoltaic Specialists Conference, Kissimimee, Florida, USA (1981) 867-870.

[48] E. Yablonovitch: "Statistical ray optics", J. Opt. Soc. A. 72 (1982) 899-907.

[49] P. Campbell and M. A. Green: "Light trapping properties of pyramidally textured surfaces", J. Appl. Phys. 62 (1987) 243-249.

[50] D. Thorp*;* PhD Thesis, University of New South Wales, Sydney, 1998.

[51] B. F. Wagner and J. O. Schumacher: "Light confinement and influence of electrical parameters on thin silicon solar cells", 13th EC-PVSEC, Nice (1995) 465-468.

[52] W. Winkler, *Untersuchung des räumlichen und spektralen Reflexionsverhaltens von strukturierten Si/Metall-Grenzflächen;* Diploma Thesis, Albert-Ludwigs-Universität, Freiburg, 1984.

[53] B. F. Wagner, *Dünnschichtsolarzellen aus rekristallisiertem Silicium;* PhD Thesis, Technische Hochschule Darmstadt, Darmstadt, Germany, 1995.

[54] R. Preu, P. Koltay, H. Schmidhuber, and K. Bücher: "Optimisation of cell interconnectors for PV module performance enhancement", Proceedings of the 14th European Photovoltaic Solar Energy Conference, Barcelona, Spain (1997) 278-281.

[55] P. Koltay, H. Schmidhuber, and K. Bücher: "Decreasing PV-module reflection losses under realistic irradiation conditions", Proceedings of the 2nd World Conference on Photovoltaic Energy Conversion, Vienna, Austria (1998) 2198-2202.

[56] B. L. Sopori and T. Marshall: "Optical confinement in thin silicon films: a comprehensive ray optical theory", Proceedings of the 23rd IEEE Photovoltaic Specialists Conference, Louisville, Kentucky, USA (1993) 127-132.

[57] M. Born and E. Wolf, *Principles of optics* (Pergamon Press, New York, 1959).

[58] J. Foley, A. van Dam, S. Feiner, and J. Hughes, *Computer graphics: Principles and Practice* (Addison Wesley, 1990).

[59] *Designation: E 892 -87, Standard Tables for Terrestrial Solar Spectral Irradiance at Air Mass 1.5*; *Vol. 12.02;* edited by P. C. Fazio (American society for testing and materials, Philadelphia, USA, 1993).

[60] G. Heiser, P. P. Altermatt, and J. Litsios: "Combining 2D and 3D device simulation with circuit simulation for optimising high-efficiency silicon solar cells", in *Simulation of Semiconductor Devices and Processes*; *Vol. 6*, edited by H. Ryssel and P. Pichler (Springer, Vienna/New York, 1995), p. 348-351.

[61] J. E. Mahan and G. M. Smirnov: "A new perspective on distributed series resistance effects in photovoltaic devices", Proceedings of the 14th IEEE Photovoltaic Specialists Conference, San Diego (1980) 612-618.

[62] T. Budd, *An introduction to object-oriented programming* (Addison-Wesley Publishing Company, 1991).

[63] S. Wolfram, *The Mathematica Book*, Vol. 4 (Cambridge University Press, Cambridge, 1999).

[64] R. Maeder, *The Mathematica Programmer* (AP Professional, Cambridge, 1994).

[65] G. Masetti, M. Severi, and S. Solmi: "Modelling of carrier mobility against carrier concentration in arsenic-, phosphorus- and boron-doped silicon", IEEE Trans. on Electron Devices 30 (1983) 764-769.

[66] A. Cuevas, G. Giroult-Matlakowski, P. A. Basore, C. DuBois, and R. R. King: "Extraction of the surface recombination velocity of passivated phosphorus-doped silicon emitters", Proceedings of the 1st World Conference on Photovoltaic Energy Conversion, Hawaii, USA (1994) 1446-1449.

[67] D. A. Clugston and P. A. Basore: "PC1D version 5: 32-bit solar cell modeling on personal computers", Proceedings of the 26th IEEE Photovoltaic Specialists Conference, Anaheim, California, USA (1997) 207-210.

[68] A. Schenk: "Finite-temperature full random-phase approximation model of band gap narrowing for silicon device simulation", J. Appl. Phys. 84 (1998) 3684-3695.

[69] J. del Alamo, S. Swirhun, and R. M. Swanson: "Simultaneous measuring of hole lifetime, hole mobility and bandgap narrowing in heavily doped n-type silicon", IEDM Tech. Digest, December (1985) 290-293.

[70] J. O. Schumacher, J. Dicker, S. Glunz, C. Hebling, J. Knobloch, W. Warta, and W. Wettling: "Characterization of silicon solar cells with interdigitated contacts", Proceedings of the 26th IEEE Photovoltaic Specialists Conference, Anaheim, California, USA (1997) 71-74.

[71] J. O. Schumacher, C. Hebling, and W. Warta: "Analysis and design of a thin film silicon solar cell on an insulating substrate", 14th EC-PVSEC, Barcelona (1997) 1467-1471.

[72] C. Hebling, S. W. Glunz, J. O. Schumacher, and J. Knobloch: "High-efficiency (19.2%) silicon thin-film solar cells with interdigitated emitter and base front-contacts", Proceedings of the 14th European Photovoltaic Solar Energy Conference, Barcelona (1997) 2318-2321.

[73] J. M. Gee, W. K. Schubert, and P. A. Basore: "Emitter wrap-through solar cell", Proceedings of the 23rd IEEE Photovoltaic Specialists Conference, Louisville, Kentucky, USA (1993) 265-270.

[74] J. Dicker, J. O. Schumacher, J. Sölter, W. Zimmermann, S. Bau, and W. Warta: "Numerical analysis of crystalline silicon thin film solar cells on perforated SiO2

barrier layers", Proceedings of the 16th European Photovoltaic Solar Energy Conference, Glasgow, Scotland (2000) .

[75] W. Zimmermann, F. Haas, K. Schmidt, and A. Eyer: "Silicon sheets from powder as low cost substrates for crystalline silicon thin film solar cells", Proc. 2nd WCPEC, Vienna (1998) 1790-1793.

[76] A. G. Aberle, S. R. Wenham, and M. A. Green: "A new method for accurate measurements of the lumped series resistance of solar cells", Proceedings of the 23rd IEEE Photovoltaic Specialists Conference, Louisville, Kentucky, USA (1993) 133-139.

[77] R. Maeder, *Programming in Mathematica* (Addison Wesley, 1997).

[78] P. P. Altermatt, A. Schenk, G. Heiser, and M. A. Green: "The influence of a new band gap narrowing model on measurements of the intrinsic carrier density in crystalline silicon", to be published in Solar Energy Materials and Solar Cells (1999)

[79] A. B. Sproul, M. A. Green, and J. Zhao: "Improved value for the silicon intrinsic carrier concentration at 300 K", Appl. Phys. Lett. 57 (1990) 255-257.

[80] D. B. M. Klaassen: "A unified mobility model for device simulation - I. Model equations and concentration dependence", Solid-State Electron. 35 (1992) 953-959.

[81] R. A. Sinton, A. Cuevas, and M. Stuckings: "Quasi-steady-state photoconductance, a new method for solar cell material and device characterization", Proceedings of the 25th IEEE Photovoltaic Specialists Conference, Washington DC, USA (1996) 457-460.

[82] H. Nagel, C. Berge, and A. G. Aberle: "Generalized analysis of quasi-steady state and quasi-transient measurements of carrier lifetimes in semiconductors", J. Appl. Phys. 86 (1999) 6218-6221.

[83] J. del Alamo, F. van Meerbergen, F. D‘Hoore, and J. Nijs: "High-low junctions for solar cell applications", Solid-State Electron. 24 (1981) 533-538.

[84] J. A. del Alamo and R. M. Swanson: "The Physics and modeling of heavily doped emitters", IEEE Trans. Electron Devices 31 (1984) 1878-1888.

[85] A. B. Sproul and M. A. Green: "Improved value for the silicon intrinsic carrier concentration from 275 to 375 K", J. Appl. Phys. 70 (1991) 846-854.

[86] P. P. Altermatt, J. O. Schumacher, A. Cuevas, S. W. Glunz, R. R. King, G. Heiser, and A. Schenk: "The extraction of the surface recombination velocity of Si:P emitters using advanced silicon models", Proceedings of the 16th European Photovoltaic Solar Energy Conference, Glasgow, Scotland (2000) .

[87] J. S. Blakemore, *Semiconductor statistics* (Pergamon Press, New York, 1962).

[88] A. Schenk, *Advanced physical models for silicon device simulation* (Springer Verlag, Wien, New York, 1998).

[89] R. King, *Studies of oxide-passivated emitters in silicon and applications to solar cells;* PhD Thesis, Stanford University, California, 1990.

[90] J. del Alamo*;* PhD Thesis, Stanford University, Stanford, 1985.

[91] A. Cuevas, P. A. Basore, G. Giroult-Matlakowski, and C. Dubois: "Surface recombination velocity of highly doped n-type silicon", J. Appl. Phys. 80 (1996) 3370-3375.

[92] S. W. Glunz, S. Sterk, R. Steeman, W. Warta, J. Knobloch, and W. Wettling: "Emitter dark saturation currents of high efficiency solar cells with inverted pyramids", Proceedings of the 13th European Photovoltaic Solar Energy Conference, Nice (1995) 409-412.

[93] H. V. Gassel, *Untersuchung der SIMOX-Technologie zur Erzeugung anwendungsspezifischer SOI-Substrate;* PhD Thesis, Gerhard-Mercator-Universität, Dortmund, Germany, 1995.

[94] C. Hebling, *Die kristalline Silicium-Dünnschichtsolarzelle auf isolierenden Substraten;* PhD Thesis, Universität Konstanz, Konstanz, Germany, 1998.

[95] J. Knobloch, A. Noel, E. Schäffer, U. Schubert, F. J. Kamerewerd, S. Klußmann, and W. Wettling: "High-efficiency solar cells from FZ, Cz and Mc-silicium material", 23rd IEEE PVSC, Louisville (1993) 271-276.

[96] P. A. Basore: "Extended spectral analysis of internal quantum efficiency", Proceedings of the 23rd IEEE Photovoltaic Specialists Conference, Louisville, Kentucky, USA (1993) 147-152.

[97] H. B. Serreze: "Optimizing solar cell performance by simultaneous consideration of grid pattern design and interconnect configurations", Proceedings of the 13th IEEE Photovoltaic Specialists Conference, Washington DC, USA (1978) 609-614.

[98] R. N. Hall and T. J. Soltys: "Polka-dot solar cell", Proceedings of the 14th IEEE Photovoltaic Specialists Conference, San Diego, California, USA (1980) 550-553.

[99] R. J. Schwartz and M. D. Lammert: "Silicon solar cells for high concentration applications", Internat. Electron Devices Meeting, Washington, DC (1975) 350-351.

[100] M. D. Lammert and R. J. Schwartz: "The interdigitated back contact solar cell: a silicon solar cell for use in concentrated sunlight", IEEE Trans. Electron Devices 24 (1977) 337-342.

[101] R. J. Schwartz: "Review of silicon solar cells for high concentrations", Sol. Cells 6 (1982) 17-38.

[102] R. A. Sinton and R. M. Swanson: "Design criteria for Si point-contact concentrator solar cells", IEEE Trans. Electron Devices 34 (1987) 2116-2123.

[103] R. R. King, R. A. Sinton, and R. M. Swanson: "Front and back surface fields for point-contact solar cells", Proceedings of the 20th IEEE Photovoltaic Specialists Conference, Las Vegas, Nevada, USA (1988) 538-544.

[104] P. Verlinden, R. A. Sinton, and R. M. Swanson: "High efficiency large area back contact concentrator solar cells with a multilevel interconnection", Int. J. Solar Energy 6 (1988) 347-366.

[105] R. A. Sinton and R. M. Swanson: "Simplified backside-contact solar cells", IEEE Trans. Electron Devices 37 (1990) 348-352.

[106] K. Matsukuma, H. Yagi, Y. Kida, T. Takahashi, K. Nishinoiri, T. Warabisako, T. Uematsu, and K. Morita: "Exact analytical simulation for large area simplified backside-contact silicon solar cells", Proceedings of the 5th International Photovoltaic Science and Engineering Conference, Kyoto, Japan (1990) 505-508.

[107] R. R. King, R. A. Sinton, and R. M. Swanson: “One-Sun, Single-Crystalline Silicon Solar Cell Research,” Report No. SAND91-7003 (1991).

[108] R. A. Sinton, P. J. Verlinden, R. A. Crane, R. M. Swanson, C. Tilford, J. Perkins, and K. Garrison: "Large-area 21% efficient Si solar cells", Proceedings of the 23rd IEEE Photovoltaic Specialists Conference, Louisville, Kentucky, USA (1993) 157-161.

[109] P. J. Verlinden, R. M. Swanson, and R. A. Crane: "7000 high efficiency cells for a dream", Progr. Photovolt. 2 (1994) 143-152.

[110] R. A. Sinton, P. J. Verlinden, R. M. Swanson, R. A. Crane, K. Wickham, and J. Perkins: "Improvements in Si backside-contact solar cells for high-value one-sun applications", Proceedings of the 13th European Photovoltaic Solar Energy Conference, Nice, France (1995) 1586-1589.

[111] P. J. Verlinden, R. A. Sinton, K. Wickham, R. A. Crane, and R. M. Swanson: "Backside-contact silicon solar cells with improved efficiency for the '96 world solar challenge", Proceedings of the 14th European Photovoltaic Solar Energy Conference, Barcelona, Spain (1997) 96-99.

[112] S. W. Glunz, J. Knobloch, C. Hebling, and W. Wettling: "The range of high-efficiency silicon solar cells fabricated at Fraunhofer ISE", Proceedings of the 26th IEEE Photovoltaic Specialists Conference, Anaheim, California, USA (1997) 231-234.

[113] J. O. Schumacher, J. Dicker, J. Sölter, and D. Biro: "An object oriented approach for the analytical and numerical modelling of silicon solar cells", submitted to Progress in Photovoltaics: Research and Applications (2000)

[114] H. Ohtsuka, Y. Ohkura, T. Uematsu, and T. Warabisako: "Three-dimensional numerical analysis of contact geometry in back-contact solar cells", Progr. Photovolt. 2 (1994) 275-285.

[115] J. Dicker, J. O. Schumacher, S. W. Glunz, and W. Warta: "Characterization of high-efficiency silicon solar cells with rear side contacts", Proceedings of the 2nd World Conference on Photovoltaic Energy Conversion, Vienna, Austria (1998) 95-99.

[116] P. P. Altermatt, G. Heiser, D. Ximing, J. Jurgens, A. G. Aberle, S. J. Robinson, T. Young, S. R. Wenham, and M. A. Green: "Rear surface passivation of high-efficiency silicon solar cells by a floating junction", J. Appl. Phys. 80 (1996) 3574-3586.

[117] P. Lölgen, *Surface and volume recombination in silicon solar cells;* PhD Thesis, CIP-Gegevens Koninklijke Bibliotheek, Den Haag, 1995.

[118] R. Brendel: "Note on the interpretation of injection level dependent surface recombination velocities", Applied Physics A 60 (1995) 523.